

ABSTRACT

Title of Dissertation: **INVESTIGATION ON REFRIGERANT DISTRIBUTION
IN EVAPORATOR MANIFOLDS**

Dae-Hyun Jin, Doctor of Philosophy, 2006

Dissertation directed by: Professor Reinhard Radermacher, Ph.D.
Department of Mechanical Engineering

To provide essential design information of microchannel evaporators, an experimental study was conducted on the effects of geometry, operating conditions and fluid properties on the distribution of refrigerant and pressure drop in horizontal heat exchanger manifolds. An experimental facility with a visualization section for mimicking a real heat exchanger manifold geometry was developed. Under realistic operating conditions, measurements of refrigerant distribution were conducted by measuring mass flow rates and vapor quality of all branch tube groups (individual adjacent heat exchanger tubes were grouped in groups) for a total of 60 test cases. The flow direction within the heat exchangers is vertically upward.

Stratified flow is observed for the end inlet case of the dividing manifold due to the gravitational effect. The liquid level increases along the dividing manifold because the liquid is traveling farther than the vapor due to inertia difference. Near the end of the manifold, the liquid level is almost constant. For the side inlet case, it is observed that the incoming refrigerant impinges on the inner side wall of the manifold, and is divided

symmetrically near the inlet, and the interface between the vapor and the liquid has a V-shaped form near the inlet.

Based on the measurements, it is observed that for the end inlet case, the profile of the branch tube inlet vapor quality is of a “stepwise” shape. There exist two almost constant value regions, one of about 100% vapor quality near the inlet and the remainder of about 12% vapor quality with a very short transition region. For the end inlet case, as the manifold inlet mass flow rate increases, the number of branch tube groups having almost 100% tube inlet vapor quality increases also because the vapor-liquid interface is moving farther towards the end of the manifold due to the increased momentum. However, for the side inlet case, there is no such region having 100% branch tube inlet vapor quality. For the side inlet case, the profile of the branch tube inlet vapor quality is symmetric. Near the inlet, the branch tube inlet vapor quality is about 60 ~ 70%, and near the end of the manifold, the branch tube inlet vapor quality is about 20%. In between two regions, the branch tube inlet vapor quality decreases monotonously along the manifold. The flow distribution is strongly affected by the manifold inlet location and/or manifold inlet geometry and manifold inlet vapor mass flux.

Correlations are proposed using the T-junction concept in a modified form from Watanabe et al.’s method (1995). For R-410A and R-134a tests with both inlet cases, 90% of measured vapor inlet quality data and 90% of measured liquid fraction of taken off data are within predicted values ± 0.1 . To investigate the effect of refrigerant maldistribution on the performance of the tested heat exchangers, heat exchanger simulations were conducted. Based on the heat exchanger simulation results using test results for the refrigerant distribution, for the side inlet case, the capacity degradation

based on the uniform distribution at the tested inlet manifold mass flow rates (at 30, 45 and 60 g/s) is 5 ~ 8%. For the end inlet case, as the inlet manifold mass flow rate increases, the capacity degradation based on the uniform distribution ranges from 4% to 15% as a function of the manifold inlet mass flow rate. Therefore, the side inlet is preferred for a wide range of mass flow rates compared to the end inlet.

**INVESTIGATION ON REFRIGERANT DISTRIBUTION
IN EVAPORATOR MANIFOLDS**

by

Dae-Hyun Jin

Dissertation submitted to the Faculty of the Graduate School of the University
of Maryland, College Park in partial fulfillment
of the requirements for the degree of
Doctor of Philosophy
2006

Advisory Committee:

Professor Reinhard Radermacher, Ph.D., Chair / Advisor
Associate Professor Jungho Kim, Ph.D.
Assistant Professor Elias Balaras, Ph.D.
Assistant Professor Bao Yang, Ph.D.
Associate Professor Gary Pertmer, Ph.D.

©Copyright by
Dae-Hyun Jin
2006

ACKNOWLEDGEMENTS

I would first like to express my thanks to my advisor, Dr. Reinhard Radermacher, for his generous support, advice, and guidance.

I would thank the American Society of Heating, Refrigerating and Air-Conditioning Engineers, Inc (ASHRAE) and the Center for Environmental Energy Engineering (CEEE) for providing funding for this project.

I also would like to thank Dr. Yunho Hwang who continuously provided the advice and guidance for my research.

Many people have contributed and helped me during this study, thank you: Xudong Wang, Ahmet Örs, Cara Sanderson, Tolga Aynur, and Magnus Eisele for your sincere help and the time you spent in discussion. Special thanks go to John Linde for his great work with the test section design and machining, and to Jan Muehlbauer for his wonderful work with the transparent manifolds machining.

I want to express my warm thanks to Dr. Brian Na for his advice, help, and the time he spent in our discussions.

I want to thank my father, brother, and sisters for prayer and support. In addition, I greatly miss my mother in heaven.

Lastly, to my wife Grace and amazingly loving son, Joey, I would like to express my gratitude for your patience and help.

I want to dedicate this work to my wife, with my love and respect.

TABLE OF CONTENTS

ACKNOWLEDGMENTS	ii
TABLE OF CONTENTS.....	iii
LIST OF TABLES	v
LIST OF FIGURES	vi
NOMENCLATURE	xiv
LIST OF FINDINGS	xvi
1. INTRODUCTION	1
2. LITERATURE REVIEW	4
2.1 Microchannel tube manifolds	4
2.2 Plate heat exchanger manifolds	6
2.3 Round tube heat exchanger manifolds	7
2.4 Two-phase flow in T-junctions.....	9
2.5 Two-phase flow patterns in horizontal tube.....	11
2.6 Two-phase flow distribution model in T-junctions	14
2.7 Two-phase flow distribution model in manifolds.....	19
2.8 Summary of Literature Review.....	22
3. EXPERIMENTAL METHODS.....	23
3.1 Test Section.....	23
3.2 Experimental Parameters	32
3.3 Experimental Test Setup.....	32
3.4 Instrumentation	38
3.5 Data Reduction.....	43
3.6 Experimental Uncertainty Analysis	49
4. EXPERIMENTAL RESULTS.....	55
4.1 Overview.....	55
4.2 Flow Visualization in Dividing Manifold.....	57
4.3 Measured Inlet and Outlet Conditions	65
4.3.1 Effect of Manifold Inlet Mass Flow Rate	65
4.3.2 Effect of Heat Load	80
4.3.3 Effect of Manifold Inlet Vapor Quality	92

4.3.4 Effect of Branch Tube Number (Manifold Length with fixed Tube Pitch)...	97
4.3.5 Effect of Tube Pitch.....	110
4.3.6 Effect of Oil Mass Fraction.....	119
4.4 Flow pattern map	126
5. MODELING OF REFRIGERANT DISTRIBUTION.....	128
5.1 Overview.....	128
5.2 Modeling of Refrigerant Distribution	128
5.3 Comparison to existing two-phase distribution model	131
5.3.1 Comparison to models using h/h_b	131
5.3.2 Comparison to Seeger et al. model and Sivert Vist model	136
5.3.3 Comparison to the Model of Watanabe	140
5.4 Model	151
5.5 Parameters Affecting Refrigerant Flow Distribution.....	170
6. HEAT EXCHANGER SIMULATIONS	172
7. CONCLUSIONS.....	176
8. FUTURE WORK.....	179
9. REFERENCES	182

LIST OF TABLES

Table 3.1: Experimental parameters	32
Table 3.2: Detailed information for the differential pressure transducers	41
Table 3.3: List of the wattmeters	42
Table 3.4: Information for the mass flow meters.....	42
Table 3.5: Calculated heat gain for the preheater	45
Table 3.6: Uncertainty of the preheater inlet enthalpy	51
Table 3.7: Uncertainty of vapor quality at the inlet of the dividing manifold enthalpy	52
Table 3.8: Uncertainty of the post heater outlet enthalpy.....	53
Table 3.9: Uncertainty of the branch tube group inlet vapor quality.....	54
Table 4.1: Test matrix conducted in this study	56
Table 4.2 Normalized standard deviation of the mass flow rate at the branch tube groups for the vapor and liquid phase for various branch tube group numbers ($\dot{m}_{dm,In} = 30$ g/s , and 55 g/s).....	105
Table 4.3 Normalized standard deviation of the mass flow rate at the branch tube groups for the vapor and liquid phase with various branch tube pitches ($\dot{m}_{dm,In} = 30$ g/s , and 55 g/s).....	114
Table 5.1 Comparison of manifold geometry	141
Table 6.1 Heat exchanger geometry and operating conditions for heat exchanger simulations	172
Table 6.2 Heat exchanger simulations results.....	173

LIST OF FIGURES

Figure 1 Schematic diagram of the manifold for end inlet and side inlet.....	xvii
Figure 2.1 Schematic diagram of a T-junction	9
Figure 2.2 Typical pressure gradients in a T-junctions (Lahey, 1986).....	11
Figure 2.3 Flow patterns in horizontal flow.....	13
Figure 2.4 Flow pattern map in horizontal flow (from Thome and El Hajal (2002))	14
Figure 2.5 Off-take and liquid entrainment (Moon et al. (2003)).....	16
Figure 2.6 Liquid entrainment in stratified flow with upward branch tube and gas pull-through in stratified flow with downward branch (Castiglia and Giardina(2002b))	18
Figure 3.1 Multiport heat exchanger assembly	24
Figure 3.2 Cross section of multiport flat tube with dimensions in millimeters	25
Figure 3.3 Exploded view of the visualization section assembly	26
Figure 3.4 Variation of tube number (tube group number) for the end inlet case	28
Figure 3.5 Variation of tube number (tube group number) for the side inlet case	29
Figure 3.6 Drawing for a transparent manifold with dimensions in millimeters.....	31
Figure 3.7 Process and instrumentation diagram of the experimental test setup.....	34
Figure 3.8 Positions of the differential pressure transducers	40
Figure 3.9 Mass and energy balance across the preheater	45
Figure 3.10 Mass and energy balance across the post heater	46
Figure 3.11 Heat loss through the insulation on the post heater.....	48
Figure 3.12 Mass and energy balance across the branch tube group.....	49
Figure 4.1 Refrigerant distribution in the dividing manifold with 10 mm tube pitch and 10 tube groups for the end inlet (R-410A, Heat load: 5 kW, $x_{dm,In} = 0.3$, $\dot{m}_{dm,In} = 30$ g/s)	58
Figure 4.2 Refrigerant distribution in the dividing manifold with 10 mm tube pitch and 10 tube groups for the side inlet (R-410A, Heat load: 5 kW, $x_{dm,In} = 0.3$, $\dot{m}_{dm,In} = 60$ g/s)	59
Figure 4.3 Refrigerant distribution in the dividing manifold with 10 mm tube pitch and 10 tube groups (R-410A, Heat load: 0 kW, $x_{dm,In} = 0.3$)	60

Figure 4.4 Refrigerant distribution in the dividing manifold with various tube pitches (R-410A, End inlet, Tube group No.: 10 ea, Heat load: 5 kW, $x_{dm,In} = 0.3$)	62
Figure 4.5 Refrigerant distribution in the dividing manifold with different heat load (R-410A, End inlet, Tube pitch: 10 mm, Tube group No.: 10 ea, $x_{dm,In} = 0.3$)	63
Figure 4.6 Refrigerant distribution in the dividing manifold with different refrigerant (End inlet, Tube pitch: 10 mm, Tube group No.: 10 ea, $x_{dm,In} = 0.3$)	64
Figure 4.7 Branch tube group inlet vapor quality at varying inlet mass flow rate with 5 kW heat load for R-410A and R-134a (Tube pitch: 10 mm, Tube group No.: 10 ea, $x_{dm,In} = 0.3$)	68
Figure 4.8 Mass flow rate ratio with various manifold inlet mass flow rates with 5 kW heat load for R-410A and R-134a (Tube pitch: 10 mm, Tube group No.: 10 ea, $x_{dm,In} = 0.3$)	70
Figure 4.9 Vapor mass flow rate ratio with various manifold inlet mass flow rates with 5 kW heat load for R-410A and R-134a (Tube pitch: 10 mm, Tube group No.: 10 ea, $x_{dm,In} = 0.3$)	71
Figure 4.10 Liquid mass flow rate ratio with various manifold inlet mass flow rates with 5 kW heat load for R-410A and R-134a (Tube pitch: 10 mm, Tube group No.: 10 ea, $x_{dm,In} = 0.3$)	73
Figure 4.11 Pressure drop along the branch tube group with various manifold inlet mass flow rates with 5 kW heat load for R-410A and R-134a (Tube pitch: 10 mm, Tube group No.: 10 ea, $x_{dm,In} = 0.3$)	74
Figure 4.12 Pressure drop along the manifold with various manifold inlet mass flow rates with 5 kW heat load for R-410A and R-134a (Tube pitch: 10 mm, Tube group No.: 10 ea, $x_{dm,In} = 0.3$)	75
Figure 4.13 Power input with various manifold inlet mass flow rates with 5 kW heat load for R-410A and R-134a (Tube pitch: 10 mm, Tube group No: 10 ea, $x_{dm,In} = 0.3$)	76

Figure 4.14 Branch tube group outlet temperature with various manifold inlet mass flow rates with 5 kW heat load for R-410A and R-134a (Tube pitch: 10 mm, Tube group No.: 10 ea, $x_{dm,In} = 0.3$)	78
Figure 4.15 Branch tube group inlet and outlet vapor quality at varying heat load for R-410A (Tube pitch: 10 mm, Tube group No.: 10 ea, $x_{dm,In} = 0.3$)	81
Figure 4.16 Mass flow rate ratio with various heat loads for R-410A (Tube pitch: 10 mm, Tube group No.: 10 ea, $x_{dm,In} = 0.3$)	82
Figure 4.17 Vapor mass flow rate ratio with various heat loads for R-410A (Tube pitch: 10 mm, Tube group No.: 10 ea, $x_{dm,In} = 0.3$)	84
Figure 4.18 Liquid mass flow rate ratio with various heat loads for R-410A (Tube pitch: 10 mm, Tube group No.: 10 ea, $x_{dm,In} = 0.3$)	86
Figure 4.19 Pressure drop along the branch tube group at varying heat load for R-410A (Tube pitch: 10 mm, Tube group No.: 10 ea, $x_{dm,In} = 0.3$)	88
Figure 4.20 Power input with various heat loads for R-410A (Tube pitch: 10 mm, Tube group No.: 10 ea, $x_{dm} = 0.3$)	89
Figure 4.21 Branch tube group outlet temperature with various heat loads for R-410A (Tube pitch: 10 mm, Tube group No.: 10 ea, $x_{dm,In} = 0.3$)	91
Figure 4.22 Branch tube group inlet and outlet vapor quality at varying inlet quality for R-134a with the end inlet (Tube pitch: 10 mm, Tube group No.: 10 ea, $\dot{m}_{dm,In} = 45$ g/s)	92
Figure 4.23 Mass flow rate ratio at varying inlet quality for R-134a with the end inlet (Tube pitch: 10 mm, Tube group No.: 10 ea, $\dot{m}_{dm,In} = 45$ g/s)	94
Figure 4.24 Vapor and liquid mass flow rate ratio at varying inlet quality for R-134a with the end inlet (Tube pitch: 10 mm, Tube group No.: 10 ea, $\dot{m}_{dm,In} = 45$ g/s)	95
Figure 4.25 Pressure drops along the branch tube groups and the manifold at varying inlet quality for R-134a with the end inlet (Tube pitch: 10 mm, Tube group No.: 10 ea, $\dot{m}_{dm,In} = 45$ g/s)	95

Figure 4.26 Power input and the branch tube outlet temperature with varying inlet quality for R-134a with end inlet (Tube pitch: 10 mm, Tube group No.: 10 ea, $\dot{m}_{dm,in} = 45$ g/s)	96
Figure 4.27 Branch tube group inlet vapor quality with various branch tube group numbers for R-410A (Tube pitch: 10 mm, Heat load: 5 kW)	98
Figure 4.28 Mass flow rate ratio with various branch tube group numbers for R-410A (Tube pitch: 10 mm, Heat load: 5 kW)	99
Figure 4.29 Vapor mass flow rate ratio with various branch tube group numbers for R-410A (Tube pitch: 10 mm, Heat load: 5 kW)	100
Figure 4.30 Normalized vapor mass flow rate ratio with various branch tube group numbers for R-410A (Tube pitch: 10 mm, Heat load: 5 kW)	101
Figure 4.31 Liquid mass flow rate ratio with various branch tube group numbers for R-410A (Tube pitch: 10 mm, Heat load: 5 kW)	102
Figure 4.32 Normalized liquid mass flow rate ratio with various branch tube group numbers for R-410A (Tube pitch: 10 mm, Heat load: 5 kW)	104
Figure 4.33 Pressure drop along the branch tube group with various branch tube group numbers for R-410A (Tube pitch: 10 mm, Heat load: 5 kW)	107
Figure 4.34 Power input with various branch tube group numbers for R-410A (Tube pitch: 10 mm, Heat load: 5 kW)	108
Figure 4.35 Branch tube outlet temperature with various branch tube group numbers for R-410A (Tube pitch: 10 mm, Heat load: 5 kW)	109
Figure 4.36 Mass flow rate ratio with various tube pitches for R-410A (Tube number: 30 ea, Heat load: 5 kW)	111
Figure 4.37 Vapor mass flow rate ratio with various tube pitches for R-410A (Tube number: 30 ea, Heat load: 5 kW)	112
Figure 4.38 Liquid mass flow rate ratio with various tube pitches for R-410A (Tube number: 30 ea, Heat load: 5 kW)	113
Figure 4.39 Pressure drop along the branch tube group with various tube pitches for R-410A (Tube number: 30 ea, Heat load: 5 kW)	115
Figure 4.40 Power input with various tube pitches for R-410A (Tube number: 30 ea, Heat load: 5 kW)	117

Figure 4.41 Branch tube outlet temperature with various tube pitches for R-410A (Tube number: 30 ea, Heat load: 5 kW)	118
Figure 4.42 Branch tube group inlet vapor quality with 0 and 2 wt. % OMF for R-410A ($\dot{m}_{dm,in} = 45$ g/s , Tube number: 30 ea, Heat load: 5 kW)	121
Figure 4.43 Mass flow rate for tube group No. 10 with 0 and 2 wt. % OMF for R-410A, end inlet ($\dot{m}_{dm,in} = 45$ g/s , Tube number: 30 ea, Heat load: 5 kW)	121
Figure 4.44 Mass flow rate ratio with 0 and 2 wt. % OMF for R-410A ($\dot{m}_{dm,in} = 45$ g/s , Tube number: 30 ea, Heat load: 5 kW)	122
Figure 4.45 Vapor mass flow rate ratio with 0 and 2 wt. % OMF for R-410A ($\dot{m}_{dm,in} = 45$ g/s , Tube number: 30 ea, Heat load: 5 kW)	123
Figure 4.46 Liquid mass flow rate ratio with 0 and 2 wt. % OMF for R-410A ($\dot{m}_{dm,in} = 45$ g/s , Tube number: 30 ea, Heat load: 5 kW)	123
Figure 4.47 Pressure drop along the branch tube group with 0 and 2 wt. % OMF for R- 410A ($\dot{m}_{dm,in} = 45$ g/s , Tube number: 30 ea, Heat load: 5 kW)	124
Figure 4.48 Power input with 0 and 2 wt. % OMF for R-410A ($\dot{m}_{dm,in} = 45$ g/s , Tube number: 30 ea, Heat load: 5 kW)	125
Figure 4.49 Branch tube outlet temperature with 0 and 2 wt. % OMF for R-410A ($\dot{m}_{dm,in} = 45$ g/s , Tube number: 30 ea, Heat load: 5 kW)	126
Figure 4.50 Flow pattern map for R-134a based on Thome, J. R. and Hajal, J. E. (2002)	127
Figure 4.51 Flow pattern map for R-410A based on Thome, J. R. and Hajal, J. E. (2002)	127
Figure 5.1 Schematic diagram of the dividing manifold	129
Figure 5.2 Comparison of void fraction for R-134a	133
Figure 5.3 Comparison of void fraction for R-410A	133
Figure 5.4 Comparison of T-junction models (branch tube vapor quality vs. h/h_b)	134
Figure 5.5 Comparison of test results with T-junction models (R-134a, End inlet, $\dot{m}_{dm,in} = 30$ g/s)	135

Figure 5.6 Comparison of test results with T-junction models (R-134a, End inlet, $\dot{m}_{dm,In} = 60$ g/s)	135
Figure 5.7 Comparison of test results with Seeger model and Vist model (R-134a, End inlet, $\dot{m}_{dm,In} = 30$ g/s)	138
Figure 5.8 Comparison of test results with Seeger model and Vist model (R-134a, End inlet, $\dot{m}_{dm,In} = 60$ g/s)	138
Figure 5.9 Comparison of test results with Seeger model and Vist model (R-410A, End inlet, $\dot{m}_{dm,In} = 30$ g/s)	139
Figure 5.10 Comparison of test results with Seeger model and Vist model (R-410A, End inlet, $\dot{m}_{dm,In} = 60$ g/s)	139
Figure 5.11 Branch tube vapor mass flux ($G_{bt,In,vap}(i)$) vs. the vapor mass flux at the inlet of the manifold T-junction ($G_{dm,vap}(i)$) for R-410A, side inlet	143
Figure 5.12 Branch tube vapor mass flux ($G_{bt,In,vap}(i)$) vs. the vapor mass flux at the inlet of the manifold T-junction ($G_{dm,vap}(i)$) for R-134a, side inlet	143
Figure 5.13 Branch tube liquid fraction taken off ($\dot{m}_{bt,In,liq}(i) / \dot{m}_{dm,liq}(i)$) vs. $\sqrt{\text{Re}_{dm,vap}(i)}$ for R-410A, side inlet	145
Figure 5.14 Branch tube liquid fraction taken off ($\dot{m}_{bt,In,liq}(i) / \dot{m}_{dm,liq}(i)$) vs. $\sqrt{\text{Re}_{dm,vap}(i)}$ for R-134a, side inlet	145
Figure 5.15 Branch tube vapor mass flux ($G_{bt,In,vap}(i)$) vs. the vapor mass flux at the inlet of the manifold T-junction ($G_{dm,vap}(i)$) for R-410A, end inlet	148
Figure 5.16 Branch tube vapor mass flux ($G_{bt,In,vap}(i)$) vs. the vapor mass flux at the inlet of the manifold T-junction ($G_{dm,vap}(i)$) for R-134a, end inlet	148
Figure 5.17 Branch tube liquid fraction taken off ($\dot{m}_{bt,In,liq}(i) / \dot{m}_{dm,liq}(i)$) vs. $\sqrt{\text{Re}_{dm,vap}(i)}$ for R-410A, end inlet	150
Figure 5.18 Branch tube liquid fraction taken off ($\dot{m}_{bt,In,liq}(i) / \dot{m}_{dm,liq}(i)$) vs. $\sqrt{\text{Re}_{dm,vap}(i)}$ for R-134a, end inlet	150

Figure 5.19 Comparison of correlation with measured data based on the relationship between the branch vapor mass flux ($G_{bt,In,vap}(i)$) and the vapor mass flux at the inlet of the manifold T-junctions ($G_{dm,vap}(i)$) for R-410A, side inlet	153
Figure 5.20 Comparison of correlation with measured data based on the relationship between the branch vapor mass flux ($G_{bt,In,vap}(i)$) and the vapor mass flux at the inlet of the manifold T-junctions ($G_{dm,vap}(i)$) for R-134a, side inlet	153
Figure 5.21 Measured branch tube inlet vapor quality ($x_{bt,In}(i)$) vs. the normalized vapor mass flux ($G_{dm,vap}(i)/G_{dm,In,vap}$) for R-410A, side inlet	155
Figure 5.22 Measured branch tube inlet vapor quality ($x_{bt,In}(i)$) vs. the normalized vapor mass flux ($G_{dm,vap}(i)/G_{dm,In,vap}$) for R-134a, side inlet	155
Figure 5.23 Branch tube liquid fraction taken off ($\dot{m}_{bt,In,liq}(i)/\dot{m}_{dm,liq}(i)$) vs. the normalized Reynolds number ($\sqrt{\text{Re}_{dm,vap}(i)}/\sqrt{\text{Re}_{dm,In,vap}}$) for R-410A, side inlet	157
Figure 5.24 Branch tube liquid fraction taken off ($\dot{m}_{bt,In,liq}(i)/\dot{m}_{dm,liq}(i)$) vs. the normalized Reynolds number ($\sqrt{\text{Re}_{dm,vap}(i)}/\sqrt{\text{Re}_{dm,In,vap}}$) for R-134a, side inlet	157
Figure 5.25 Measured branch tube inlet vapor quality ($x_{bt,In}(i)$) vs. the normalized vapor mass flux ($G_{dm,vap}(i)/G_{dm,In,vap}$) for R-410A, end inlet	160
Figure 5.26 Measured branch tube inlet vapor quality ($x_{bt,In}(i)$) vs. the normalized vapor mass flux ($G_{dm,vap}(i)/G_{dm,In,vap}$) for R-134a, end inlet	160
Figure 5.27 Branch tube liquid fraction taken off ($\dot{m}_{bt,In,liq}(i)/\dot{m}_{dm,liq}(i)$) vs. the normalized Reynolds number ($\sqrt{\text{Re}_{dm,vap}(i)}/\sqrt{\text{Re}_{dm,In,vap}}$) for R-410A, end inlet	163
Figure 5.28 Branch tube liquid fraction taken off ($\dot{m}_{bt,In,liq}(i)/\dot{m}_{dm,liq}(i)$) vs. the normalized Reynolds number ($\sqrt{\text{Re}_{dm,vap}(i)}/\sqrt{\text{Re}_{dm,In,vap}}$) for R-134a, end inlet	163
Figure 5.29 Measured branch tube inlet vapor quality ($x_{bt,In}(i)$) vs. the normalized vapor mass flux ($G_{dm,vap}(i)/G_{dm,In,vap}$) for R-410A and $\dot{m}_{dm,In} = 30 \text{ g/s}$, end inlet	168

Figure 5.30 Measured branch tube inlet vapor quality ($x_{bt,In}(i)$) vs. the normalized vapor mass flux ($G_{dm,vap}(i)/G_{dm, half-In,vap}$) for R-410A and $\dot{m}_{dm,In} = 60$ g/s , side inlet168

Figure 5.31 Branch tube liquid fraction taken off ($\dot{m}_{bt,In,liq}(i)/\dot{m}_{dm,liq}(i)$) vs. the normalized Reynolds number ($\sqrt{Re_{dm,vap}(i)}/\sqrt{Re_{dm,In,vap}}$) for R-410A and $\dot{m}_{dm,In} = 30$ g/s , end inlet169

Figure 5.32 Branch tube liquid fraction taken off ($\dot{m}_{bt,In,liq}(i)/\dot{m}_{dm,liq}(i)$) vs. the normalized Reynolds number ($\sqrt{Re_{dm,vap}(i)}/\sqrt{Re_{dm, half-In,vap}}$) for R-410A and $\dot{m}_{dm,In} = 60$ g/s , side inlet.....169

Figure 6.1 Simulated cooling capacity vs. branch tube group number for R-410A for R-410A and $\dot{m}_{dm,In} = 30$ g/s174

Figure 6.2 Simulated cooling capacity vs. branch tube group number for R-410A for R-410A and $\dot{m}_{dm,In} = 45$ g/s175

Figure 6.3 Simulated cooling capacity vs. branch tube group number for R-410A for R-410A and $\dot{m}_{dm,In} = 60$ g/s175

NOMENCLATURE

a	Parameter
AMFR	Average Mass Flow Rate
b	Parameter
CEEE	Center for Environmental Energy Engineering
FMT	Flat Multiport Tube
GWP	Global Warming Potential
G	Mass Flux
HTC	Heat Transfer Coefficient
h	Enthalpy, Distance
K	Parameter
L	Length
LOCA	Loss of Coolant Accident
MFR	Mass Flow Rate
\dot{m}	Refrigerant mass flow rate
NR	Normalized Mass Flow Rate Ratio
SG	Sight Glass
STD	Standard Deviation
T	Temperature
OMF	Oil Mass Fraction
P	Pressure
\dot{Q}	Heat transfer rate
\dot{W}	Power input

x	Vapor Quality, Parameter
y	Parameter
ω	Uncertainty

Subscripts

b	Beginning of entrainment
bt	Branch tube
c	Cross Section
dm	Dividing manifold
f	Saturated liquid
g	Saturated vapor
$half-In$	Half side inlet of the manifold for the side inlet
In	Inlet
liq	Liquid
$loss$	Loss of heat
m	Manifold
max	Maximum
mh	Main heaters
Out	Outlet
ph	Phase of refrigerant
poh	Post heater
prh	Preheater
vap	Vapor

LIST OF FINDINGS

- For all entire test conditions, both non-uniform distribution of the mass flow rate and non-uniform distribution of the vapor and liquid phases were found, and in the current study, the degree of non-uniform distribution of the vapor and liquid phases was more severe than that of the mass flow rate.
- The differences between R-410A and R-134a are minor.
- The refrigerant distribution is little affected by the variation of heat load, tube pitch, and number of parallel tubes.
- The refrigerant distribution is strongly affected by the manifold inlet location and/or inlet geometry and manifold inlet vapor mass flux (total mass flux and vapor quality).
- The profile of the branch tube inlet vapor quality depends on the manifold inlet location and/or the manifold inlet geometry. For the end inlet case, the profile of the branch tube inlet vapor quality is of a “stepwise” shape. There exist two almost constant value regions, one of about 100% vapor quality, one of about 12% vapor quality with a very short transition region. Near the inlet, the branch tube inlet vapor quality is almost 100%, and near the end of the manifold, the branch tube inlet vapor quality is about 12%. In between two regions, there is a short transition area. For the side inlet case, the incoming refrigerant impinges on the manifold wall, and is divided symmetrically near the inlet. As a result, the profile of the branch tube inlet vapor quality is symmetric. The interface between the vapor and liquid has a V-shape near the inlet. Near the inlet, the branch tube inlet vapor quality is about 60 ~ 70%, and near the end of the manifold, the branch tube inlet vapor quality is about 20%. In

between two regions, the branch tube inlet vapor quality decreases monotonously along the manifold.

- For the end inlet case, as the manifold inlet mass flow rate increases, the number of branch tube groups having almost 100% tube inlet vapor quality is increasing because the vapor-liquid interface is moving farther towards the end of the manifold due to the increased momentum.
- Based on the heat exchanger simulation results using test results for the refrigerant distribution, for the side inlet case, the capacity degradation as compared to the uniform distribution at the tested inlet manifold mass flow rates (at 30, 45 and 60 g/s) is 5 ~ 8%. For the end inlet case, as the inlet manifold mass flow rate increases, the capacity degradation as compared to the uniform distribution is larger. The capacity degradation ranges from 4% to 15% as a function of the manifold inlet mass flow rate. The side inlet refrigerant supply is preferred to the end inlet since the capacity degradation is less for a wide range of mass flow rates.

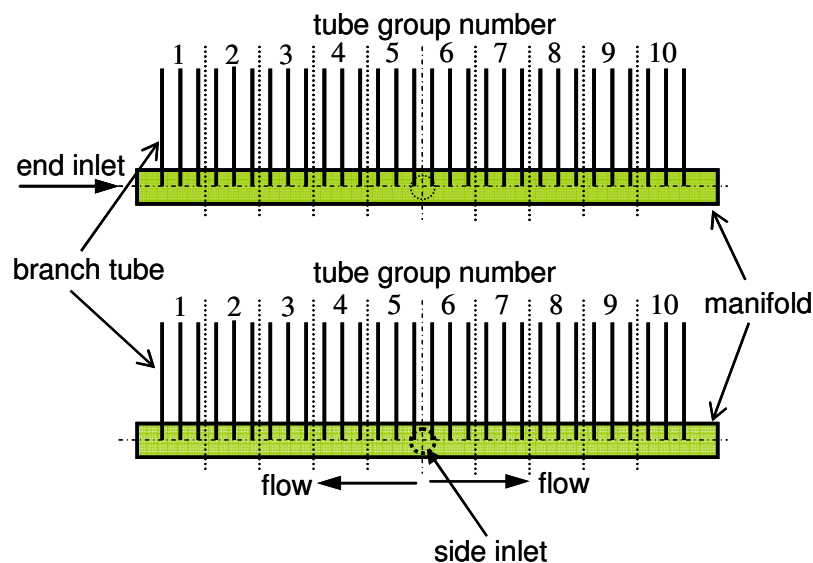


Figure 1 Schematic diagram of the manifold for end inlet and side inlet

1 INTRODUCTION

1.1 Background

The two basic demands for air-conditioning and refrigeration products are higher efficiency and compact size. Past energy crises and recent international concerns about climate change or global warming potential (GWP) have garnered public attention on improving energy efficiency of air-conditioning and refrigeration systems. Both system manufacturers and users want a size reduction of the system to reduce shipping and handling costs and to save installation space. Compact heat exchangers meet these demands very well, and the number of their applications increased during the last decade. Automotive climate control systems are a good example of an application of compact heat exchangers since they have to provide improved thermal comfort against increased thermal load and need a reduced component weight. These demands have resulted in aluminum brazed compact heat exchangers (termed here microchannel heat exchangers or multiport heat exchangers). As the technology in aluminum brazed compact heat exchangers advances, the hydraulic diameter of the tube channel is reduced to a size of less than 1 mm. This reduced cross sectional area of each tube requires many parallel tubes to maintain the pressure drop across heat exchangers in a reasonable range. This leads to refrigerant mal-distribution issues, especially in evaporators. Refrigerant flow maldistribution can be defined as non-uniform distribution of the mass flow rate, and/or non-uniform distribution of the individual phases.

1.2 Description of Challenges

In the refrigeration cycle, the condensed liquid refrigerant is expanded to a two-phase fluid entering the evaporator. In many applications, the evaporator paths are divided into a number of parallel sections to keep the pressure drop across the evaporator within a reasonable range and to maximize overall heat exchanger performance. Since the state of the refrigerant entering the evaporator is two-phase and its quality changes depending upon the operating conditions, the proper refrigerant distribution to individual sections is not an easy task. Non-uniform distribution will cause dry out at the sections of lesser mass flow rate and/or of higher vapor inlet quality by superheating the refrigerant vapors due to smaller cooling capacity. This can result in non-uniform heat exchanger surface temperature distribution and poor utilization of available heat transfer area. Since single phase heat transfer coefficients (HTCs) are much lower than those for two-phase flow, both refrigerant-side HTCs and air-side HTCs are lower than those of surfaces with two-phase flow. In addition to this, the temperature difference between the air and refrigerant decreases due to the increased refrigerant temperature. Therefore, refrigerant maldistribution results in an overall deterioration of heat exchanger performance.

1.3 Objective

It is the objective of this work to provide essential design information of microchannel evaporators (or multiport evaporators) by conducting an experimental study on the effects of geometry, operating conditions, and fluid properties on the distribution of refrigerant and pressure drops in heat exchanger manifolds. In order to achieve the proposed

objective, experiments and numerical analysis are needed. For the experimental work, the following approach is taken: to visualize the flow through a dividing manifold (or dividing header, or distributing header) of a microchannel heat exchanger (or a multiport heat exchanger), to measure the refrigerant mass flow rate and vapor quality for each branch tube group (As shown in Figure 3.1, three branch tubes are grouped together as one branch tube group using baffles in the combining manifold), and measure the pressure drops along the dividing manifold and the vertical branch tubes of the heat exchanger.

2 LITERATURE REVIEW

Refrigerant mal-distribution in the evaporator is not a new problem. Many engineers have tackled this issue in conventional heat exchangers with an experimental and numerical approach. Recently researchers conducted experimental and numerical work in microchannel heat exchangers. The following summary provides highlights of previous studies.

2.1 Microchannel Tube Manifolds

Sivert Vist (2003) investigated two-phase refrigerant flow distribution in microchannel tube heat exchanger manifolds with 16mm inner diameter having ten parallel microchannel tubes with 21 mm tube pitch. The dimension of the microchannel is as follows: the thickness is 1.65 mm, and the width is 13.3 mm. In his study, CO₂ and HFC-134a were used as refrigerants. It was found that for the upward flow experiments, vapor was taken off in the first branch tubes, while liquid was taken off in the last branch tubes of the manifold. More liquid was taken off in the first branch tubes with reduced hydraulic diameter of the manifold. For the downward branch tubes, liquid was preferentially taken off in the first branch tubes, and vapor was traveling to the last branch tubes. It was shown that more vapor entered the first branch tubes and more of the liquid was transported to the last branch tubes with the reduced hydraulic diameter of the manifold and the reduced hydraulic diameter of the manifold by introducing tube protrusion. For upward flow, it was shown that the branch tube heat transfer uniformity

was improved only by using spiral mixer at the inlet of the manifold among the geometric modifications of the manifold. However, for the downward branch tubes, it was found that only minor changes were seen by the manifold modifications. Based on the test results, he suggested an empirical correlation.

Hrnjak (2004) investigated the refrigerant distribution issues in parallel flow heat exchangers. In his study, some major distribution situations and approaches were presented for single-phase (opposite position of inlet and outlet pipe) and two-phase flow (distribution in homogeneous zone and separation of the phases with separate distribution). In addition, for a horizontal header and downward flow in branches, five flow regimes were identified and a new two-phase flow map was presented. Using standard deviation from the average value of liquid flow rates, zones of good distribution for the case of a horizontal downward flow header were indicated.

Sa et al. (2003) investigated the refrigerant maldistribution in microchannel evaporators for residential air-conditioners. The two headers of the evaporator were located horizontally, and the branch tubes connecting the headers were vertically positioned. The outer diameter of the manifold is 27 mm, and the width and the height of the microchannel is 20 mm and 2 mm, respectively. In order to take the thermal images on the evaporators, an infrared camera was used. Based on the test results, it was found that the thermal performance was strongly influenced by refrigerant maldistribution, and the performance of well-designed evaporator could be twice as much as that of the worst one.

Cho et al. (2003) studied two-phase R-22 maldistribution in a vertical manifold with fifteen horizontal microchannel tubes under adiabatic test conditions. The inner diameter of the manifold is 19.4 mm. The microchannel has 8 rectangular ports with 1.32

hydraulic diameter. It was found that the effect of inlet vapor quality on the mass flow rate distribution and phase separation in the microchannel tubes was negligible, and that the effect of the orientation of the header on the mass flow rate distribution and phase separation was largest among the test parameters. In addition, a horizontal header showed better mass flow rate distribution and phase separation characteristics than a vertical header.

Kulkarni et al. (2003) investigated the refrigerant mal-distribution in microchannel evaporators. In their study, a simulation model was used to quantify design tradeoffs related to refrigerant maldistribution caused by header pressure gradients in microchannel evaporators. Mass flow maldistribution was investigated by using well-known pressure drop and heat transfer correlations for two-phase, chosen after comparing with the experimental results obtained by using different correlations. It was shown that mass flow maldistribution cannot be controlled by changing either port/header diameter or the refrigerant state at the inlet to the ports, only by minimizing pressure gradients along header. In addition, based on parametric analyses, a fundamentally different concept for header design was identified and characterized.

2.2 Plate Heat Exchanger Manifolds

Rong et al. (1995) conducted an adiabatic experiment to study two-phase flow distribution in a stacked plate heat exchanger. Air/water two-phase flow was used in the experiment. They found that the flow distribution was highly non-uniform under most conditions and the vertical upward flow and the flow at low gas flow rates showed a

better flow distribution. They also identified the most important parameters affecting flow distribution: flow pattern in the inlet tube (inlet flow rate and quality), flow channel orientation, and geometry of the channel inlet port.

2.3 Round Tube Heat Exchanger Manifolds

Vist and Petterson (2004) investigated two-phase refrigerant flow distribution in round tube heat exchanger manifolds with 8 and 16mm inner diameter having ten parallel inner diameter 4mm upward oriented heat exchanger tubes. In their study, CO₂ and R-134a were used as refrigerants. It was found that for the upward flow experiments, the vapor phase flow distributes much easier into the most adjacently located tubes, and the liquid flows down the manifold and is preferentially distributed to the last tubes of the heat exchanger. In their work, experiments with varying total mass flow rate (0.023, 0.028, and 0.0033 kg/s) and constant inlet vapor fraction showed small deviation in the two-phase distribution. In addition, changes in heat load on the heat exchanger tube showed small effect on the two-phase distribution. The experimental data were compared to existing semi-empirical models for phase split in T-junctions.

Watanabe et al. (1995) observed the flow distribution of R-11 two-phase flow in the 20 mm inner diameter manifold having four vertically upward branches at 40 mm intervals with thermal loads to simulate a serpentine-type evaporator. They found that the flow pattern at the header inlet dominated the flow distribution for adiabatic conditions; the pressure drop along the pass affected the flow distribution when the heat load was applied; the uniform flow distribution was observed when the heat load was applied; and the T-junction data could be used to predict the flow distribution and pressure drop in the

manifold. In addition, for vapor phase, a correlation between the vapor mass flux at the branch tube inlet and at the manifold inlet was proposed, and for liquid phase, the liquid fraction taken off was selected as a variable, and was correlated with vapor Reynolds number in the manifold.

Asoh et al. (1991) observed the flow pattern of R-113 two-phase flow in a manifold having three vertically downward branches. Thermal loads were used to simulate a serpentine-type evaporator. The flow pattern in the main pipe was set as either a slug or froth flow. They found that the flow pattern in branch pipes was not uniform, the liquid flow rate in the header greatly affected the flow distribution, and the slip flow model was more appropriate than the homogeneous model.

Wang et al. (1988) conducted numerical analysis and verified it with experiments. Water was used for the experiments. It was found that the header system can be categorized as pressure regain type and pressure decrease type, and the flow distribution of pressure regain header system is more uniform than that of pressure decrease one. In addition, it was shown that the branch interval was very important parameter.

Bajura and Jones (1976) studied the flow distribution of the air in the four types of manifold. They found that the uniform flow distribution in the laterals is attained only when the headers act as infinite reservoirs, and they identified the most important parameters affecting flow distribution: manifold area ratio (total lateral tube area/inlet tube area), lateral flow resistance, header length/diameter ratio, diameter ratio between headers, and friction factor of the tube.

2.4 Two-Phase Flow In T-Junctions

A review of the previous work on the two-phase flow in T-junctions is provided in this Section because the manifolds of the current study can be considered as a series of T-junctions. For better understanding of T-junctions, the schematic diagram of a T-junction is shown in Figure 2.1. The T-junctions considered in the current review has one inlet and two outlets. The T-junctions are composed of a main tube and a branch tube. The angle between the main tube and the branch tube is a right angle. One of the outlet tubes is inline with the inlet tube, and it is called run. The other tube meets the main tube in a right angle. The angle θ in the Figure 2.1 represents the angle between the axial direction of the branch and the horizontal plane.

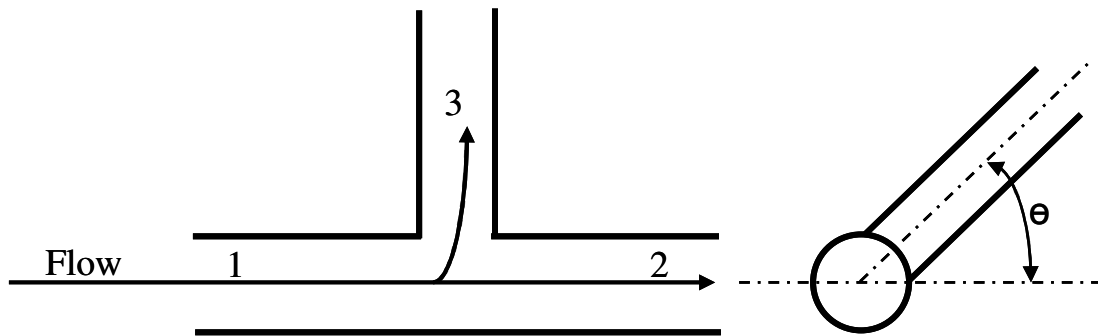


Figure 2.1 Schematic diagram of a T-junction

Most previous studies have been done to either try to quantify the amount of phase separation which takes place in branch tubes or try to devise methods to reduce it.

Collier (1975) presented the data of St Pierre taken in a horizontal T-junction in which the diameter of the inlet tube and run was 38 mm, while that of the branch tube was 25

mm. It was shown that almost complete phase separation occurred (i.e. $x_3/x_1 = [\dot{m}_3/\dot{m}_1]^{-1}$) over a wide range of mass extraction rates (\dot{m}_3/\dot{m}_1). From the results, it can be expected that due to far less inertia of the vapor than that of the liquid, the vapor easily turn the corner into the side branch.

Azzopardi and Whalley (1982) took annular flow data in T-junctions for horizontal and vertical orientations. They found that the phase separation was strongly affected by the mass extraction rate (\dot{m}_3/\dot{m}_1), flow regime, operating conditions and test section geometry and orientation.

Reimann and Seeger (1983) took data for stratified horizontal flows. They found that phase separation depended strongly on the mass extraction rate, flow regime and test section geometry.

Smoglie et al. (1987) investigated the flow distribution through small breaks at the bottom, the top and the side of a horizontal coolant pipe with stratified flow. Experiments were performed with air-water flows through breaks simulated by pipe stubs of various diameters, perpendicular to a horizontal main pipe. The flow phenomena observed were illustrated with photographs. Correlations were provided for the beginning of entrainment. A model was developed to predict the break quality and mass flux.

Typical pressure distribution in T-junctions is shown in Figure 2.2. Data trends of this type were measured for both single and two-phase flows. The upper profile in Figure 2.2 shows the characteristic pressure undershoot and recovery that occurs when the fluid turns a sharp 90° bend. In contrast, the lower profile in Figure 2.2 shows the pressure recovery that occurs in the run of the test section due to the reduced mass flux when fluid is extracted out the branch tube.

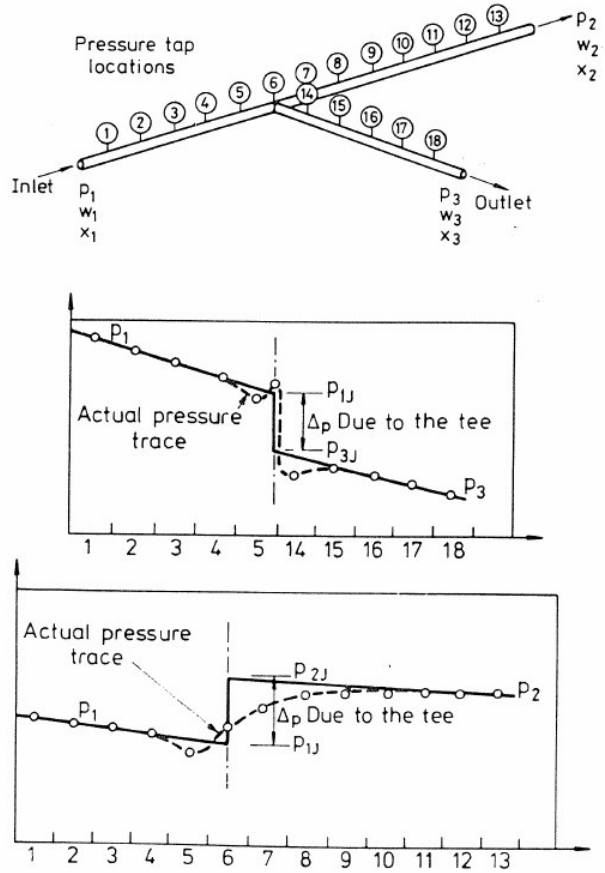


Figure 2.2 Typical pressure gradients in a T-junctions (Lahey, 1986)

2.5 Two-Phase Flow Patterns In Horizontal Tube

Many researchers mentioned that the flow pattern at the inlet of a manifold and along the manifold length significantly affected the two-phase flow distribution. Therefore, it is useful to consider two-phase flow patterns in horizontal tubes for understanding the flow patterns in horizontal manifolds. Figure 2.3 shows the two-phase flow pattern in a horizontal tube.

As the quality is gradually increased from zero, the flow patterns obtained are:

- (a) Bubbly flow: In bubbly flow the vapor phase is distributed as discrete bubbles in a continuous liquid phase. The vapor bubbles tend to flow along the top of the tube.
- (b) Plug flow: The individual small vapor bubbles have coalesced to produce long plugs. The vapor bubbles tend to travel in the upper half of the tube.
- (c) Stratified flow: The two phases flow separately with a relatively smooth interface.
The liquid is flowing in the lower part of the tube.
- (d) Wavy flow: As the vapor velocity increases, the interface becomes disturbed by waves travelling in the direction of flow.
- (e) Slug flow: The wave amplitude is so large that the wave touches the top of the tube.
- (f) Annular flow: A liquid film forms at the tube wall with a continuous central vapor core. The liquid film is much thicker at the bottom of the tube than at the top.

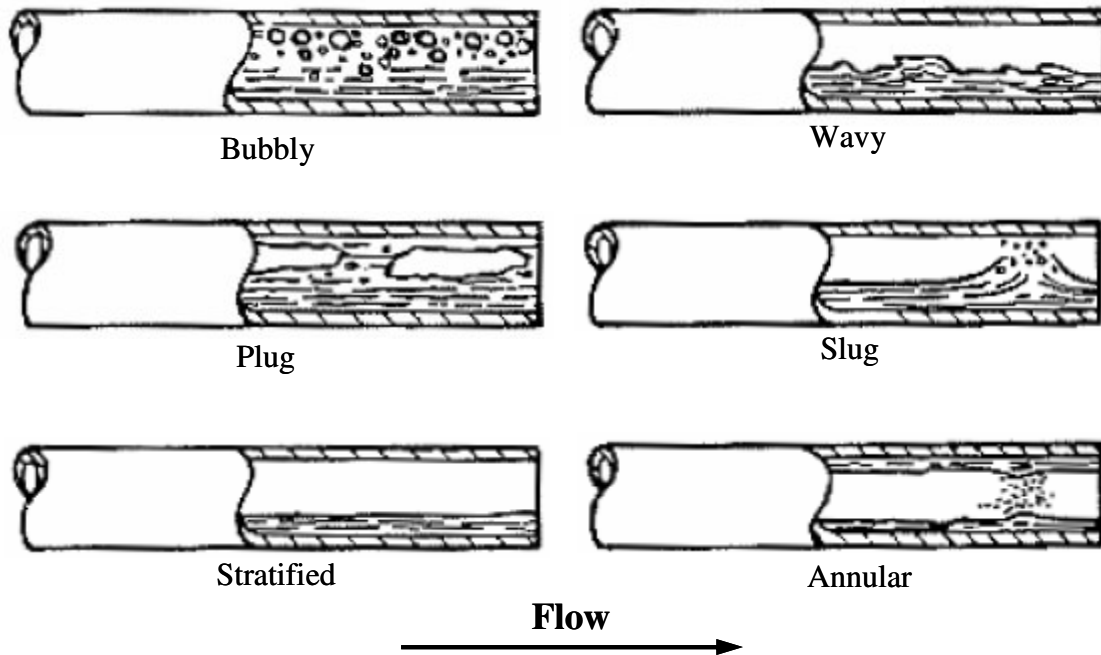


Figure 2.3 Flow patterns in horizontal flow
 (Reproduced from Collier and Thome (1994))

Flow pattern maps are an attempt to divide the space on a two-dimensional graph into areas corresponding to the various flow patterns. The flow patterns are represented as areas on the map divided by transition lines. Many flow pattern maps have been suggested. Kattan et al. (1998) developed a diabatic two-phase flow pattern map modified from the Steiner (1998) map, which in turn is a modification of the original Taitel and Dukler (1976) map. Zürcher, Thome and Favrat (1999) have proposed an updated version of this map with two minor adjustments based on new flow pattern observations for ammonia taken at mass velocities down to about $16 \text{ kg/m}^2\text{s}$. Recently, Thome and El Hajal (2002) have simplified implementation of the map by bringing the Rouhani-Axelsson void fraction equation into the method to remove its iterative solution scheme.

As an example of the flow pattern maps, Figure 2.4 shows a flow pattern map produced with the transition equations given by Thome and El Hajal (2002).

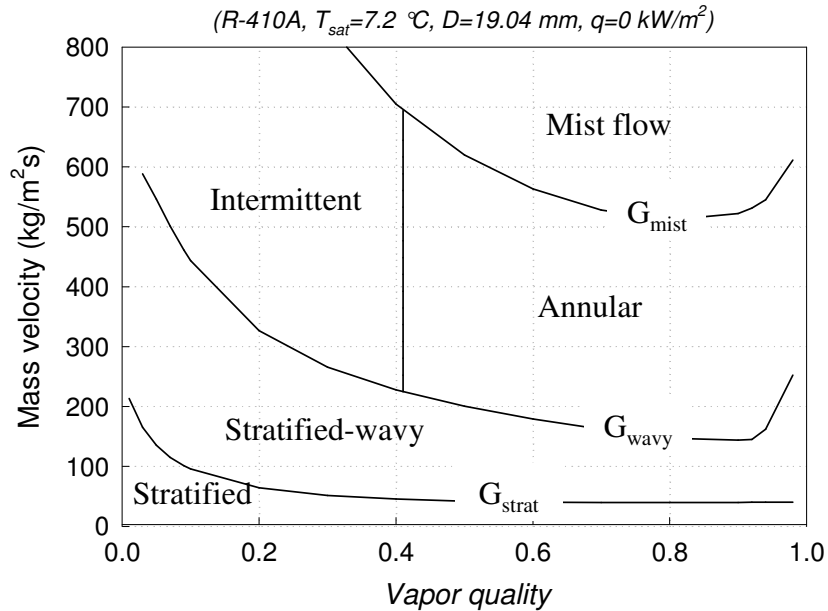


Figure 2.4 Flow pattern map in horizontal flow
(from Thome and El Hajal (2002))

2.6 Two-Phase Flow Distribution Model In T-Junctions

Seeger et al. (1986) performed experiments with T-junctions of equal diameters ($D1 = D3 = 50$ mm), a horizontal inlet flow, and a horizontal, vertical upward or downward orientation of the branch. The experiments were conducted with air-water flow (maximum pressure was smaller than 1 MPa), steam-water flow (maximum pressure was smaller than 10 MPa) and an inlet mass flux $500 < G_1 < 7,000$ kg/m²s including different flow patterns. They developed an empirical correlation. For upward branch tube, the correlation is shown in Equation 2.1.

$$x_3/x_1 = (G_3/G_1)^{-0.8} \quad (2.1)$$

Equation 2.1 is not valid for very low values of G_3/G_1 . In this range the branch quality x_3 is equal to 1, because liquid carryover does not occur. For estimating the maximum value of G_3 with $x_3 = 1$, Equation 2.2 was suggested.

$$G_{3\max, x=1} = A \cdot 0.23 [gD(\rho_l - \rho_g)\rho_g]^{0.5} \quad (2.2)$$

In Equation 2.2, $A = 0.5$ for inlet conditions with the dispersed bubble flow regime and $A = 1$ for other inlet flow patterns.

In the field of nuclear reactor safety the loss of coolant accident (LOCA) caused by a small break in a coolant pipe is very important. During such a LOCA, a stratified flow may occur in the horizontal pipe, which severely affects the mass flow rate through the break. Breaks were usually simulated by T-junctions with a small ratio d/D of branch tube to main tube diameter. An off-take is the entrainment or pull-through of liquid on the vapor-liquid interface by the vapor flow into the upward branch as shown in Figure 2.5. In previous studies, the break flows at the T-junction of horizontal tube were experimentally performed to investigate the small break loss of coolant accident and their

correlations were implemented into thermal-hydraulic codes (e.g., RELAP5/MOD3 or CATHARE).

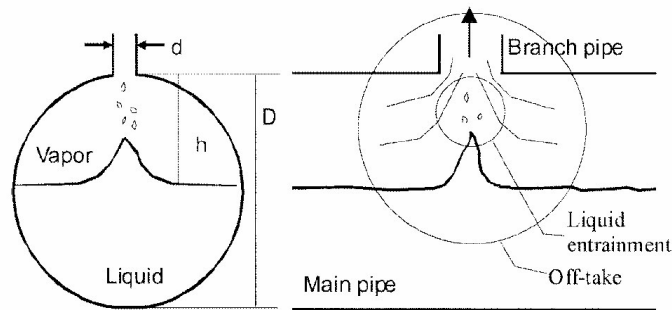


Figure 2.5 Off-take and liquid entrainment (Moon et al. (2003))

Smoglie et al. (1987) investigated small breaks at the bottom, the top or the side of a horizontal coolant tube with stratified flow. They conducted the experiment for high vapor quality which is over 0.95 in the main tube having 205 mm diameter. Based on the extensive test results, they developed a phase distribution correlation in upward branch tubes as shown in Equation 2.3.

$$x = 1 - \left(\frac{1.15}{1 + \sqrt{\rho_l / \rho_g}} \right)^{2 \frac{h}{h_b}} \left[1 - \frac{1}{2} \frac{h}{h_b} \left(1 + \frac{h}{h_b} \right) \left(\frac{1.15}{1 + \sqrt{\rho_l / \rho_g}} \right)^{1 - \frac{h}{h_b}} \right]^{0.5} \quad (2.3)$$

In Equation 2.3, h represents the distance between the branch tube inlet and the liquid level. In addition, h_b denotes h at beginning of liquid entrainment, and can be calculated using Equation 2.4 which was produced from the test results.

$$h_b = \frac{1.67 \dot{m}_{b3}^{0.4}}{[g \rho_b (\rho_l - \rho_g)]^{0.2}} \quad (2.4)$$

In Equation 2.4, the parameters ρ_b and \dot{m}_{b3} represent the density and the mass flow rate of the continuous phase at beginning of entrainment (for upward flow, vapor phase).

Schrock et al. (1986) conducted the experiment using air-water and steam water at the maximum pressure of 1Mpa. They developed a phase distribution correlation based on their test results and high quality data by Smoglie et al. (1987). The correlation is shown in Equation 2.5.

$$x_{bt} = \left(\frac{h}{h_b} \right)^{3.25 \left(1 - \frac{h}{h_b} \right)^2} \quad (2.5)$$

This correlation is implemented into the horizontal stratification entrainment model that simulates the off-take at T-junction geometry in RELAP5/MOD3.

Castiglia and Giardina (2002a) introduced a new semi-empirical model which produced a single expression for the branch tube vapor quality for both upward and downward branch tubes. The model was based on the assumption of a region of branch interest in the main tube. The region was bounded by the horizontal surface at a distance h_b from the branch tube inlet and the main tube wall as shown in Figure 2.6. They introduced a slip parameter to represent the velocity difference between the vapor and liquid phase. The

slip parameter was included in parameter K, and Equation 2.6 was produced. The values of K and n were suggested based on the fitting to test datas of the previous studies.

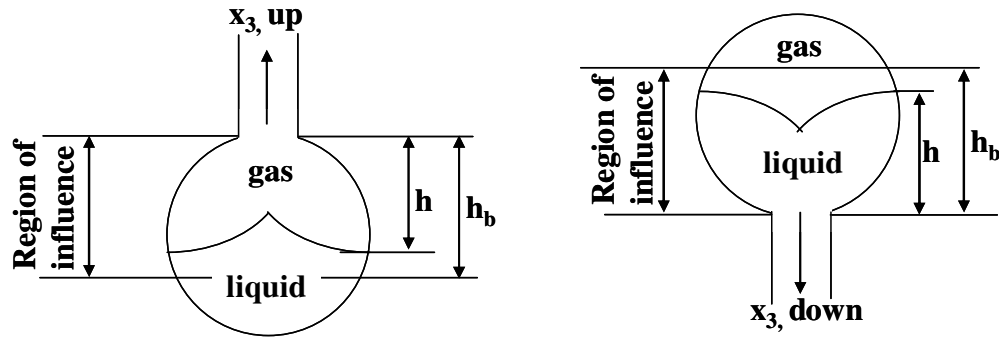


Figure 2.6 Liquid entrainment in stratified flow with upward branch tube and gas pull-through in stratified flow with downward branch (Castiglia and Giardina(2002b))

$$\frac{h}{h_b - h} = K \left(\frac{x_3}{1 - x_3} \right)^n \quad (2.6)$$

In Equation 2.6, for upward branch tube, the values of K and n are 0.62 and 0.3, respectively. In addition, for downward branch tube, the values of K and n are 0.12 and -0.65, respectively.

2.7 Two-Phase Flow Distribution Model In Manifolds

Watanabe et al. (1995) developed an empirical correlation based on the experiments in a 20 mm inner diameter manifold with four upward 6 mm inner diameter branch tubes using R-11. In their study, under no heating mode, the manifold inlet mass flow rate was 12.6, 25.1 and 37.7 g/s (these mass flow rates were expressed in mass flux as 40, 80 and 120 kg/m²s). The manifold inlet vapor quality was varied from the subcooled state to 0.4. A correlation between the vapor mass flux at the branch tube ($G_{bt,In,vap}(i)$) and at the dividing manifold ($G_{dm,vap}(i)$) was proposed as follows:

$$G_{bt,In,vap}(i) = 6.07G_{dm,vap}(i) \quad (2.7)$$

Based on this correlation, the vapor mass flux at the branch tube No. (i) depends on only vapor mass flux at the inlet of the junction (i) in the manifold. For the liquid phase, the fraction of liquid taken off in the branch tube was selected as a variable representing the flow split characteristics at a junction. The liquid fraction depends on the vapor Reynolds number at the inlet of the corresponding branch tube junction in the manifold as shown in Equation 2.8.

$$\frac{\dot{m}_{bt,In,liq}(i)}{\dot{m}_{dm,liq}(i)} = 2.74 \times 10^{-5} \eta^2 - 0.0124\eta + 1.37, \text{ where } \eta = \sqrt{\text{Re}_{dm,vap}(i)} \quad (2.8)$$

Sivert Vist (2003) investigated two-phase refrigerant flow distribution in microchannel tube heat exchanger manifolds and in round tube heat exchanger manifolds. In his study, CO₂ and HFC-134a were used as refrigerants. Based on the extensive test results, he developed an empirical correlation. To cover wide range of mass flux by using wide range of manifold diameter (8 ~ 16 mm), the correlation was divided into two regions depending on the mass flux at the inlet of the manifold T-junction. The two regions are high mass flux region and low mass flux region. The transition criterion is shown in Equation 2.9.

$$\left(\frac{G_m}{G_{m,wavy}} \right)_{tc} = \frac{148.7}{1 + 14.89A_c \times 10^5} \quad (2.9)$$

In Equation 2.9, A_c represents the manifold free-flow cross sectional area. At mass flux above the transition criterion, the constant liquid take-off fraction was developed independently of the two-phase flow properties. The developed correlation is shown in Equation 2.10.

$$CLTF = (\dot{m}_{l,t} / \dot{m}_{l,m})_{const} = -1.055 + e^{\frac{1.450}{A_c \times 10^5 + 7.248}} \quad (2.10)$$

At mass flux below the transition criterion, a linear curve was suggested. The criterion at the low mass flux is shown in Equation 2.11.

$$G_{g,m,\text{lim}} = 4.471 + e^{\frac{103.4}{A_c \times 10^5 + 18.07}} \quad (2.11)$$

The branch tube vapor quality in the low mass flux region is predicted by Equation 2.12.

$$G_{g,m} < G_{g,m,\text{lim}} : x_t = \frac{G_{g,m}}{G_{g,m,\text{lim}}} \quad (2.12)$$
$$G_{g,m} > G_{g,m,\text{lim}} : x_t = 1$$

2.8 Summary of Literature Review

Based on the literature survey, observations are summarized as follows:

- Many studies have been done for simple T-type or Y-type branches by using air-water mixture or steam-water mixture. Even though some studies have been done for multi-branches, there are only few test results for the real microchannel type heat exchangers having headers and microchannel tubes connecting headers.
- Although it has been reported that the flow pattern was the one of the most important parameters for the flow distribution, there have been rare visualization results for the real geometry.
- Even though R-410A is mostly being used for the residential air-conditioning system, there are sparse test results for the refrigerant. In the previous studies, R-22, R-134a, R-11, and CO₂ were used.
- For the distribution of refrigerant, pressure drop measurement is very important information, but there are few published test results for the real microchannel type heat exchangers.
- Two-phase refrigerant distribution for the microchannel type heat exchangers could be anticipated from the previous studies summarized above. However, most previous studies are regarding the flow distribution in plate or serpentine heat exchangers. Since the geometry of the microchannel type heat exchangers is different from ones that have been studied previously, the two-phase flow distribution in microchannel type heat exchangers needs to be studied.

3 EXPERIMENTAL METHODS

3.1 Test Section

3.1.1 General requirements

The first task was the design and construction of the test section for measuring the distribution of refrigerant in heat exchanger manifolds. An experimental facility was designed to have a visualization section while mimicking a real heat exchanger manifold geometry to simulate a realistic situation. The factors that may significantly affect the flow pattern and distribution were carefully considered not to deviate from the real heat exchangers. Figure 3.1 shows the following geometric factors accounted for:

- The length of the inlet tube to the manifold should be at least 10 straight tube diameters to ensure a fully developed flow to minimize the impact of upstream obstructions on the flow patterns.
- Flat multiport tubes should be inserted into the manifold with a tube insertion depth of 1/2 the inside diameter.
- The manifold geometry should be circular with inner diameter of the manifold large enough for tube insertion (measured value: 19.04mm).
- The manifold should be installed in horizontal position with multiport flat tubes oriented in the vertical upward flow configuration.
- The overall length of the heat exchanger tubes is 1m.
- End inlet is simply left end of the manifold.

- Side inlet is located at the middle of the manifold.

In order to distinguish between the top and bottom manifolds, hereafter the top- and bottom-manifolds are referred to as “combining manifold”, or “collecting manifold” and “dividing manifold”, or “distributing manifold”, respectively. Since measuring physical quantities for all multiport flat tubes is not practical, three tubes are grouped together at the combining manifold using baffles as shown in Figure 3.1. Figure 3.1 shows a heat exchanger having 30 microchannel tubes. Therefore, there are 10 branch tube groups in the heat exchanger.

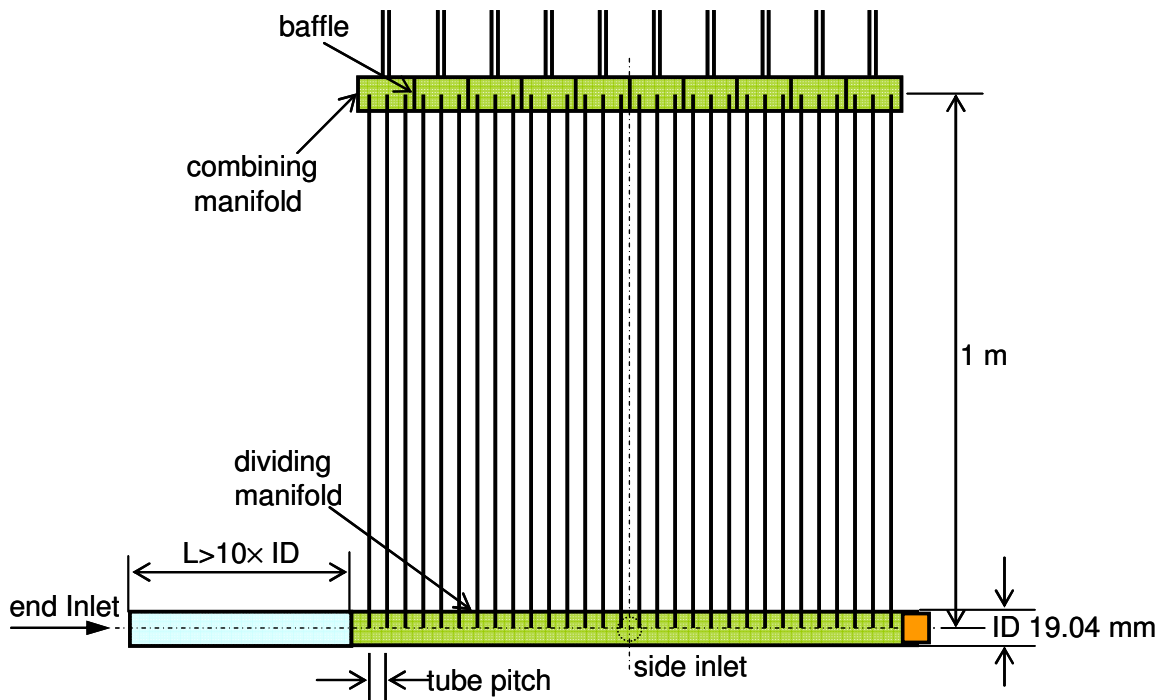


Figure 3.1 Multiport heat exchanger assembly

3.1.2 Multiport flat tube

Figure 3.2 shows a drawing of the cross section of the multiport flat tube used in the current study. The multiport flat tube has six ports with hydraulic diameter of each port of about 1.70 mm.

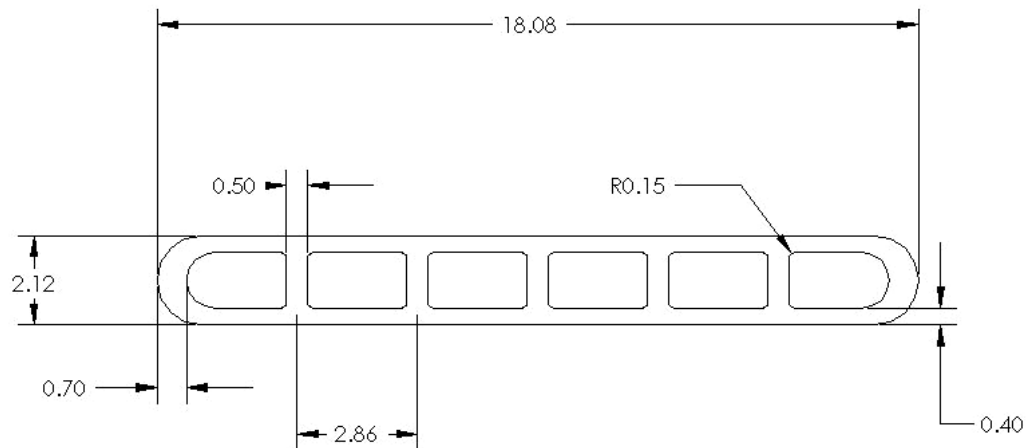


Figure 3.2 Cross section of multiport flat tube with dimensions in millimeters

3.1.3 Visualization section

An experimental facility should not only mimic a real heat exchanger manifold geometry but also provide the flexible, independent variable variations and flow visualization to better understand and document two-phase flow patterns inside the manifold. To meet these requirements, the visualization section was designed as shown in Figure 3.3. A specially designed main body houses all components. Multiport flat tubes are brazed to the top cover, and pressure taps at the bottom cover are equally spaced to measure the pressure drop along the manifold. They are threaded into the bottom cover. A transparent manifold (or transparent tube) is installed on top of the bottom cover. Each pressure hole

at the bottom cover shown in Figure 3.3 and a matching pressure hole in the transparent manifold shown in Figure 3.6 are lined up for the accurate measurements. Multiport flat tubes are inserted into matching slots on the transparent manifold. Since the side inlet tube is threaded in, there is a gap between the transparent manifold and the side inlet tube. This gap is filled by the side block, which is assembled first. Then the inlet tubes at left and middle of the manifold and the end block at the right of the manifold are assembled into the main body. After positioning o-rings and flat sight glasses, two side plates are tightened to prevent any leakage from the main body.

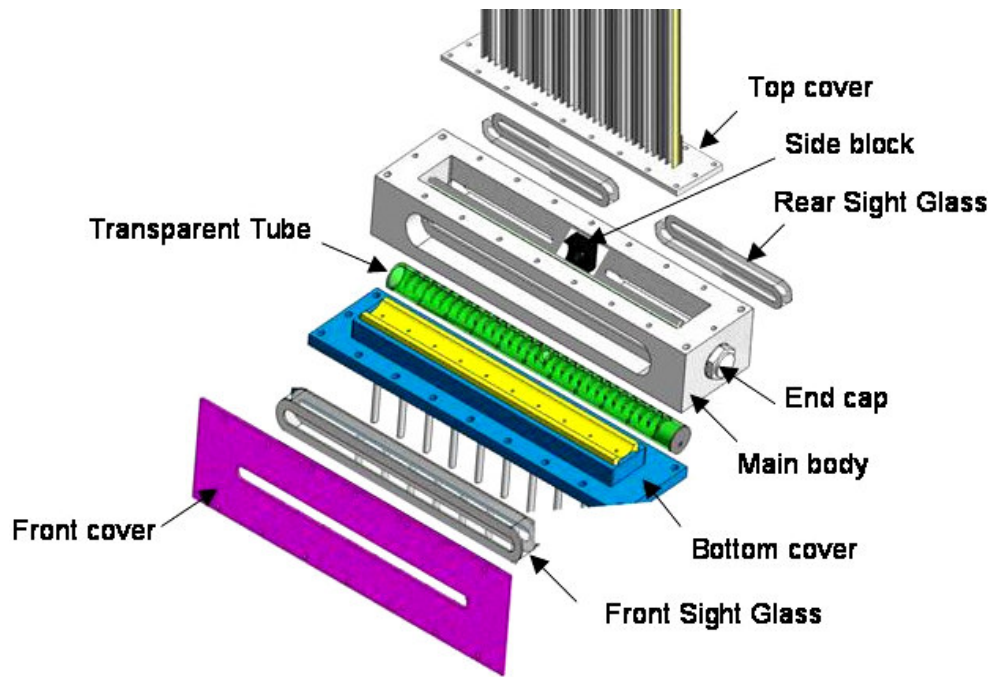


Figure 3.3 Exploded view of the visualization section assembly

The end inlet is simply the left end of the manifold in Figures 3.3 and 3.6. As shown in Figure 3.6, a 5/8" (15.875 mm) circular port is machined into the side of the transparent tube halfway along its length. This port is used as the side inlet to the transparent

manifold. In the current study, three microchannel heat exchangers were used for investigating the effect of tube pitch on the flow distribution. The tube pitch of each heat exchanger is 8, 10 and 12 mm, respectively. To vary tube pitch in the test section, it is needed to replace the top cover, the bottom cover and the transparent manifold with other top covers, bottom covers and transparent manifolds for other tube pitches. For the tests with various tube numbers, 10mm tube pitch heat exchanger was used. By blocking a certain number of tubes with dead blocks, the tube numbers (or tube group numbers) were varied. As shown in Figures 3.4 and 3.5, for both inlet locations, three different tube numbers (or three different tube group numbers) were used for investigating the effect of tube numbers. With this approach, the test heat exchanger can provide the flexibility of independent variables and visualization of flow patterns while keeping the flow dynamics realistic. In addition, shut-off valves were installed as well at the outlet of individual tube groups to make sure that there was no flow through the branch tube groups that were supposed to be blocked.

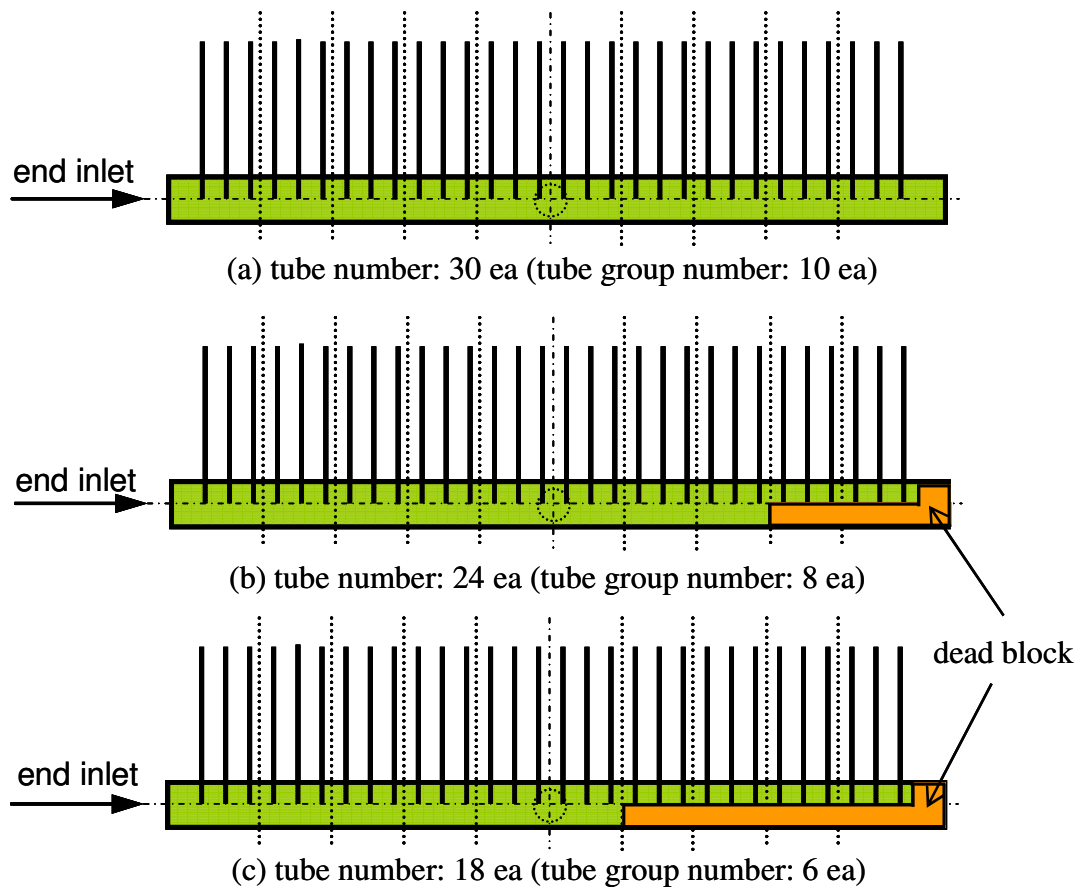


Figure 3.4 Variation of tube number (tube group number) for the end inlet case

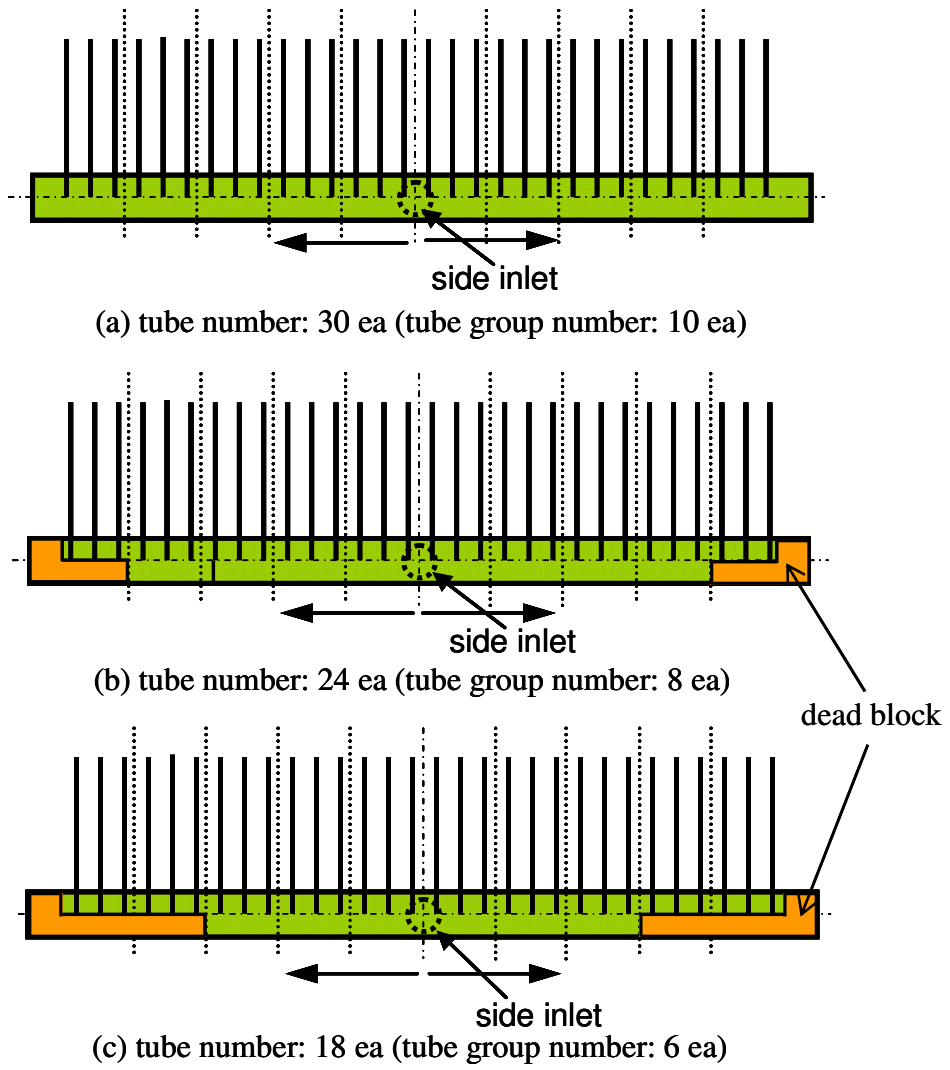


Figure 3.5 Variation of tube number (tube group number) for the side inlet case

3.1.4 Transparent manifolds

A transparent manifold is at the heart of the visualization section. Figure 3.6 shows a drawing of a transparent manifold with dimensions in millimeters. The transparent manifold has 30 slots along the top of its length. These slots are sized to match the cross section of the multiport flat tubes used in this experimental work. In the current study, for investigating the effect of tube pitch on the flow distribution, three microchannel heat exchangers were used. The tube pitch of each heat exchanger is 8, 10 and 12 mm, respectively. To match the heat exchangers, three transparent manifolds were made. Each manifold has 8, 10 and 12 mm, respectively, for the spacing between two slots shown in Figure 3.6. When the visualization section is fully assembled, the bottom edges of the multiport flat tubes are one radius inside the transparent manifolds. In addition to the slots made along the top of the manifold for the multiport flat tubes, a 5/8" (15.875 mm) circular port is machined into the side of the tube halfway along its length. This port is used as the side inlet to the transparent manifold. For the variation of tube number, the manifold having 10 mm slot spacing was used. As shown in Figures 3.4 and 3.5, the tube number is adjusted by blocking a certain number of tubes with dead blocks. 10 pressure taps (1/8" (3.175 mm) circular holes) were drilled into the lengthwise bottom of the manifold as pressure taps. These pressure taps are located directly under the second of three multiport flat tube slots for each tube group.

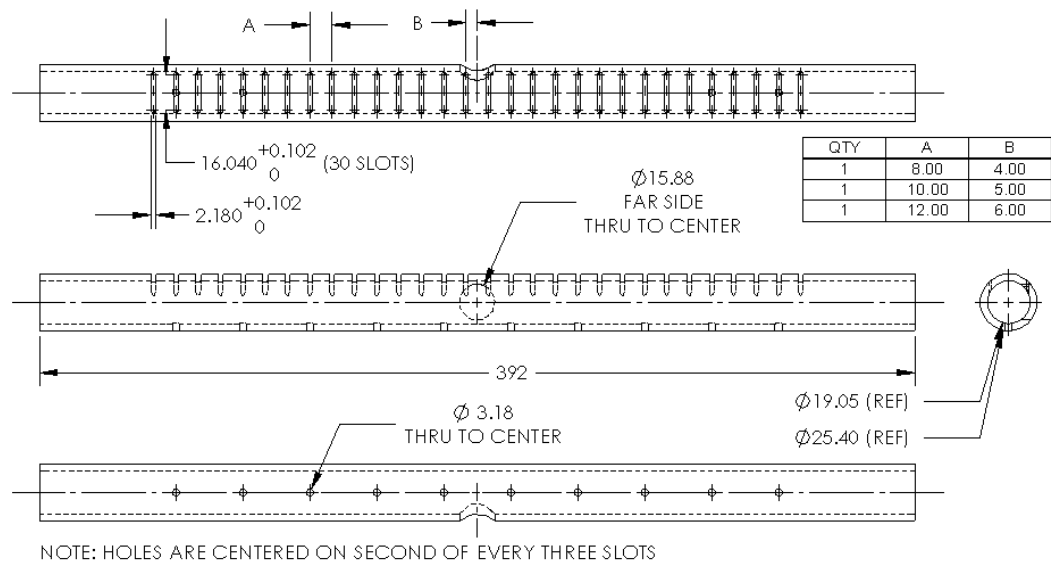


Figure 3.6 Drawing for a transparent manifold with dimensions in millimeters

3.2 Experimental Parameters

Table 3.1 shows the experimental parameters. In order to consider a representative application, the inlet temperature and inlet quality are fixed, which are 7.2 °C and 0.3, respectively. Only the tube pitch variable requires changes in the test heat exchanger, but other variables, which are refrigerant, manifold inlet mass flow rate, heat load, inlet location and tube numbers in parallel, can be varied without changing the test heat exchanger.

Table 3.1 Experimental parameters

Variable	Range
Inlet temperature	7.2 °C
Inlet quality	0.3
1. Refrigerant	R-134a / R-410A
2. Manifold inlet mass flow rate (g/s)	30 / 45 / 60
3. Heat load (kW)	0 / 5 / 10
4. Heat exchanger tube pitch (mm/tube)	8 / 10 / 12
5. Location of inlet	End / Side
6. Number of heat exchanger tubes in parallel	End inlet 18 / 24 / 30, Side inlet 18 / 24 / 30

3.3 Experimental Test Setup

To provide various test conditions and to measure flow rates and vapor qualities for individual tube groups, the new test facility using the previously described test heat exchanger was designed and constructed.

3.3.1 Test facility

Figure 3.7 shows the process and instrumentation diagram of the experimental test setup.

The test setup is composed of four major parts: main refrigerant circuit, post-heater

section to measure mass flow rate and vapor quality for the individual tube groups, test heat exchanger section with visualization section, and condensing unit circuit to control inlet condition of the visualization section. A gear pump delivers liquid refrigerant to the test heat exchanger after passing a main mass flow meter and pre-heater. For measuring the main mass flow rate, a Coriolis-type mass flow meter was used. The pre-heater was used to heat the subcooled liquid refrigerant to the desired inlet vapor quality (0.3) at the inlet of the test section. In the dividing manifold of the heat exchanger, the refrigerant was distributed into either 6, 8 or 10 branch tube groups, which were heated by tape heaters applied to individual tubes. In order to measure power input for each branch tube group, ten power meters were installed. The refrigerant flow of each branch tube group in the heat exchanger could be redirected by three-way valves either to the collecting tube or to the post heater section. The outlet state of refrigerant flow for each branch tube group of the tested heat exchanger could be two-phase or superheated vapor, depending upon the heat load. Vapor quality for the outlet of the individual branch tube group can be calculated through measurements of the post heater section, which are measurements of temperature and pressure for the outlet of the post heater section, mass flow rate, and power input for the post heaters. The power input to these post heaters is adjusted such that the exiting refrigerant flow for the post heater section is always superheated. To measure the mass flow rate through the post heater section, a second Coriolis-type mass flow meter was used. The superheated vapor from the post heater section enters the condenser and is condensed by the refrigerant from the condensing unit. Inlet temperature of the dividing manifold could be controlled to the desired condition, which is 7.2°C by

controlling the cooling capacity of the condensing unit by adjusting either the expansion device or bypass valve.

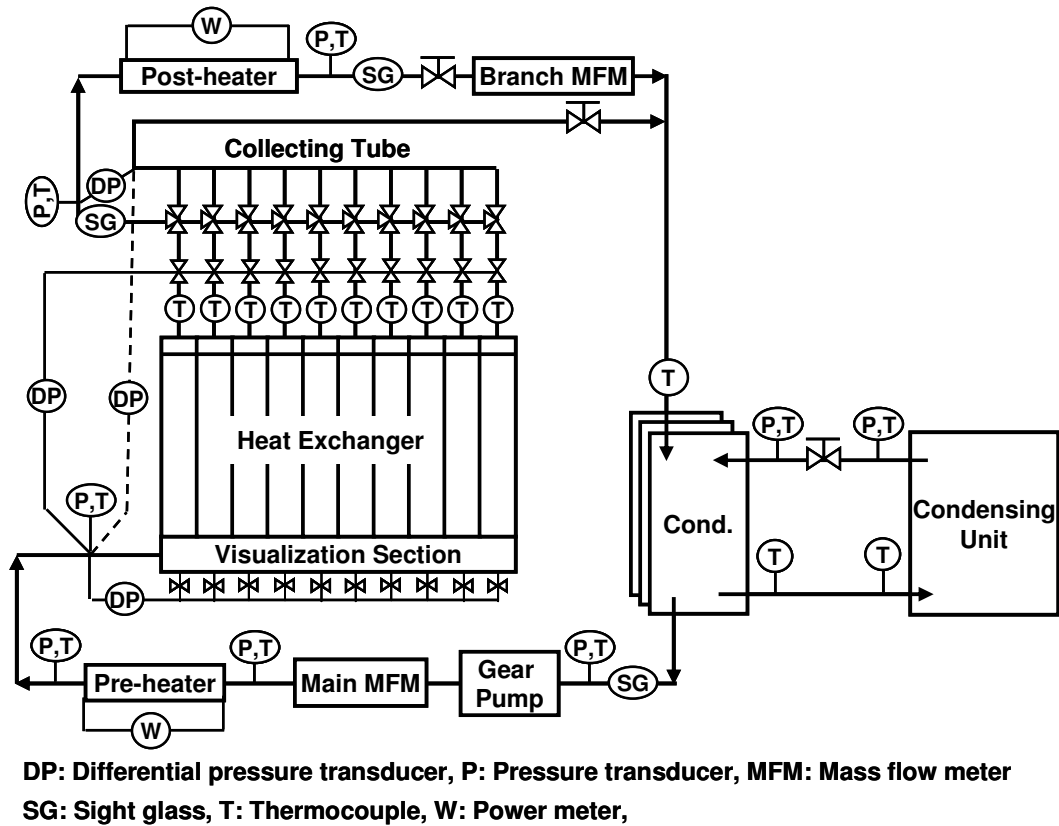


Figure 3.7 Process and instrumentation diagram of the experimental test setup

3.3.2 Refrigerant

The fluids under test are R-134a and R-410A. R-134a is commonly used in refrigeration and automotive air-conditioning systems, and R-410A is mostly being used for residential air-conditioning systems. Corresponding saturation pressures of the inlet temperature, 7.2°C are 377 kPa for R-134a and 998 kPa for R-410A.

3.3.3 Gear pump

A gear pump used in this work is a series 200 Micropump, P/N GB-P35PVSKP4. The pump is oil-less, and is magnetically driven by a 1/2 horsepower (373 W), 208 volt single phase, 3450 rpm AC motor. Therefore, the system was operated oil-free. The mass flow rate was controlled by adjusting the bypass valve. The pump is installed at the lowest part in the system to prevent cavitation.

3.3.4 Preheater

The pre-heater consists of a cylindrical vessel with a 2-1/2" (63.5 mm) NPT threaded end, and an immersion heater cap. The heater cap is comprised of two 2.2 kW stainless steel immersion heating elements, the element's electrical connections, and a 2-1/2" (63.5 mm) NPT threaded male connection. The heating elements are contained in a 36" (0.91 m) long cylindrical steel enclosure, with 3/4" (19.05 mm) NPT threads at each end, extending radially from the cylinder. The heating elements were used to heat the subcooled liquid refrigerant from the pump into a two-phase flow with 30% vapor quality. The exact power input for the preheater was adjusted by a voltage transformer. For the safety control of the preheater, a control box was installed. It consists of a

controller and two relays. The controller is an on-off controller which is produced by Omega, P/N CN76000, and given a setting temperature by the user. The controller output is connected to two 25 amp solid state relays which are also produced by Omega, P/N SSR330DC25. Each of the relays is mounted on a heat sink to ensure that overheating of the relays does not occur. When the refrigerant temperature at the outlet of the heater exceeds a set temperature, the relay terminals are automatically disconnected by the output of the controller. When the temperature is below the setting temperature, a 9 volt DC signal is sent to the relays, and the relay terminals connect.

3.3.5 Main heaters

In order to meet the given test conditions, 30 tape heaters were installed on the multiport flat tubes. To provide equal heating on individual multiport flat tube, a tape heater was attached on both sides of a given multiport flat tube. The electrical characteristics of the tape heaters are as follows: each tape heater has a resistance of approximately 30 ohms, draws 3.9 amperes of 120 VAC, and provides 468 W of heating to individual multiport flat tubes. Based on the test conditions, it was necessary to vary heat load on the tested heat exchanger. The exact power input for the main heaters was controlled by a voltage transformer. In addition, the tape heaters were controlled by 12 solid state relays in order to reflect operating conditions for real applications. For real applications at which air is used as a secondary fluid for evaporation, the refrigerant temperatures at the outlet of heat exchanger cannot exceed air temperature. For considering the ideal case, the cut-off temperature was set to 27 °C assuming the maximum refrigerant temperature being the inlet air temperature. The solid state relays were contained in one electrical control box,

and each of the relays had its own heat sink, and its own DC control voltage line which connected to a Hewlett-Packard data acquisition system, controlled by Q-basic program. This was used only to control the tape heaters on the evaporator. This system reads the temperatures at the outlet of the multiport flat tube heat exchanger. If any of the temperatures exceed the set temperature, the heating tapes for that particular group are shut off. This is done with an actuator card, which either opens or closes the DC power circuit to that particular tape heater group's solid state relay. Each of the 12 relays can be turned on or off independently, and once the temperatures return below the setting temperature, the relay operates as usual.

3.3.6 Post heater

In order to calculate the vapor quality at the outlet of the individual branch tube groups, and measure mass flow rate for the individual branch tube groups, six tape heaters were installed on the post heater section. The electrical characteristics of the tape heaters are same as those of the main heaters. In order to vary input power for the post heaters to make sure the outlet state of the refrigerant flow being superheated vapor, two voltage transformers were used.

3.3.7 Plate heat exchanger

Once the refrigerant flow from the collecting tube and the superheated gas flow are merged, the combined flow is flowing to a plate heat exchanger which is shared by the condensing unit cycle and the main refrigerant cycle as an evaporator and a condenser, respectively. The function of the heat exchanger is to condense and subcool the combined

refrigerant flow from the collecting tube and from the post heater section of the main refrigerant cycle. In order to make sure that subcooled liquid refrigerant is coming out of the heat exchanger, a sight glass is installed at the exit of the condenser.

3.4 Instrumentation

To evaluate the refrigerant distribution in the dividing manifold of the test setup, it was needed to measure temperatures, pressures (differential pressures), mass flow rates and power inputs.

3.4.1 Temperature measurement

Most of temperature measurements in this study were made using T-type in-stream shielded thermocouple probes (Copper/Constantan). The accuracy of the in-stream thermocouples is ± 0.5 °C. For measuring surface temperatures, conventional T-type thermocouples were used. The conventional thermocouples are accurate to within ± 1 °C.

3.4.2 Absolute pressure measurement

For measuring absolute pressures in the main refrigerant circuit and the condensing unit circuit, Setra type P/N 280E and C207 pressure transducers were used. These transducers have $\pm 0.11 \sim 0.13\%$ ($\pm 1.90 \sim 2.24$ kPa) accuracies. The output of the transducers is 4 ~ 20 mA or 0 ~ 5V depending on the type, corresponding to 0 ~ 250 psia (0 ~ 1,724 kPa). Each of the pressure transducers used in this study have been calibrated with a digital pressure calibrator over the entire measurement range of 0 ~ 250 psia (0 ~ 1,724 kPa).

3.4.3 Pressure difference measurement

Figure 3.8 shows the positions of the differential pressure transducers. As shown in the Figure, a total of four differential pressure transducers were used in the main refrigerant circuit. In order to avoid liquid column effect due to gravity, the pressure transducer to measure pressure difference between the visualization section inlet and the heat exchanger outlet was located at the same level as that for the heat exchanger outlet. In the same way, the pressure transducer to measure pressure difference between the visualization section inlet and the collecting tube outlet was installed at the same level as that for the collecting tube outlet. The sensors are all 230 series wet-wet transducers manufactured by Setra. The sensors are powered through the data acquisition system's 24 volt DC power supply. The output of the sensors is a 4-20 mA signal which is read into the data acquisition system. The detailed information for the differential pressure transducers is shown in Table 3.2. The pressure transducers are connected to the data acquisition system and calibrated by a water U-tube manometer having a 0.098 kPa accuracy. At the outlet of each branch tube group, as shown in Figure 3.8, there was a three way valve, which could redirect the refrigerant flow of each tube group at a time to the post heater section. The post heater section was built in the test setup for measuring refrigerant mass flow rate and vapor quality for the each branch tube group at the outlet of the heat exchanger. Even though the top manifold in the tested heat exchanger is intended to operate as a combining manifold, the top manifold cannot function as a combining manifold because each baffle is inserted and brazed into each slot located at every three tubes in the top manifold due to handling every three tubes as one tube group for the measurement of the refrigerant mass flow rate. Instead, the collecting tube is

functioning as a combining manifold. Therefore it is necessary to set up test guidelines in order that those factors may not affect significantly the flow pattern and distribution. Differential pressure measurement was used as a measure for reflecting real operating conditions of the heat exchangers. Pressure taps were made at the outlet of the collecting tube and at the inlet of the post heater section to measure the pressure difference between the two points. This pressure difference was used to control refrigerant flow in the post heater section. Due to the two-phase flow being so unsteady, time-averaged measurements were used. The pressure difference between the two points was adjusted to reach approximately zero by controlling the valve located at the outlet of the post heater section. When the two pressures at the outlet of the collecting tube and at the inlet of post heater section are the same, the measurements of vapor quality and mass flow rate at the post heater section represent the measurements of the respective tube group when it is connected to the collecting tube.

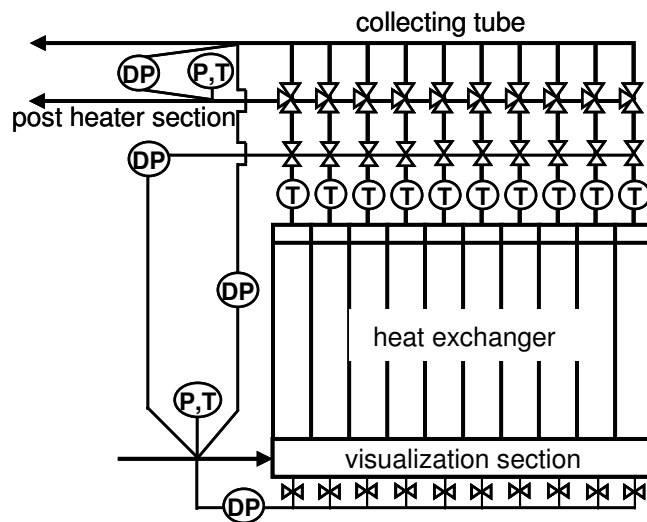


Figure 3.8 Positions of the differential pressure transducers

Table 3.2 Detailed information for the differential pressure transducers

Location	Range (kPa)	Accuracy (kPa)
Between the visualization section inlet and the collecting tube outlet	0 ~ 172.4	±0.43
Between the visualization section inlet and the pressure ports in the dividing manifold	± 6.9	±0.017
Between the post heater section inlet and the collecting tube outlet	± 6.9	±0.017
Between the visualization section inlet and each pressure port at the heat exchanger outlet	± 34.5	±0.086

3.4.4 Power input measurement

The electrical power inputs to the preheater, main heaters, and post heaters were measured using wattmeters manufactured by Ohio Semitronics Inc. They are accurate to within ±0.5% of full scale. The preheater consists of two heating elements and circuits, and each of these circuits is connected to a wattmeter. For measuring power input for the main heaters, 10 wattmeters were used. In addition, two wattmeters were used to measure power inputs for the post heater section. The detailed information for them is shown in Table 3.3.

Table 3.3 List of the wattmeters

Location	No	Range	Output	Accuracy
Preheater	1	0 ~ 4 kW	0 ~ 10 V	±20 W
	2	0 ~ 4 kW		±20 W
Main heater	1	0 ~ 2 kW		±10 W
	2	0 ~ 4 kW		±20 W
	3	0 ~ 4 kW		±20 W
	4	0 ~ 2 kW		±10 W
	5	0 ~ 4 kW		±20 W
	6	0 ~ 4 kW		±20 W
	7	0 ~ 4 kW		±20 W
	8	0 ~ 2 kW		±10 W
	9	0 ~ 2 kW		±10 W
	10	0 ~ 2 kW		±10 W
Post heater	1	0 ~ 1 kW	±5 W	
	2	0 ~ 1 kW	±5 W	

3.4.5 Mass flow rate measurement

The mass flow meters used in this study are all Coriolis-type mass flow meters, produced by Micromotion. The two mass flow meters were calibrated using tap water, bucket and scale, and stopwatch. Table 3.4 shows detailed information for the mass flow meters.

Table 3.4 Information for the mass flow meters

Location	Range	Output	Accuracy
Main flow	0 ~ 75 g/s	0 ~ 5 V	±0.1% (±0.075 g/s)
Branch tube group	0 ~ 60 g/s		±0.35% (±0.21 g/s)

3.4.6 Data acquisition system

Signals from all instruments were provided to a LabView data acquisition software package through the use of National Instruments' FieldPoint data acquisition modules

connecting to a network module. The network module is a FP-1000, with a RS-232 serial connection that transmits all data to the data acquisition computer. Among the eight input modules, four are AI-110 modules, which are used for reading analog voltage or current input signals. The remaining four input modules are TC-120 models, which are used to record temperature measurements, in addition to an ambient temperature measurement. Each of the modules has a terminal base with either 16 or 32 screw connections for input wiring. The modules are powered with a 24 volt DC power supply, and this power source is also used for the four AI-110 modules. Each of the modules then provides power to individual sensors and measures their output. The thermocouple modules do not require power. A total of 64 channels of data were collected (32 thermocouples and 32 analog inputs) and sent to the computer for collection and instantaneous on-screen visualization of system parameters (e.g. pressures, temperatures, mass flow rates, etc.). The sampling interval of this system was 1 second. A GUI was written for this experiment, allowing the user quick access to data from the system while it was in operation. The graphical portion of the program monitored the history of many of these measurements. When all measured data reached steady state, the data collection was started for 10 minutes at a second interval.

3.5 Data Reduction

Measured data from the experiments were logged and processed as explained in section 3.4.6. Based on the measured data, the dividing manifold inlet vapor quality, branch tube

inlet vapor quality and branch tube outlet vapor quality were calculated as described below.

3.5.1 Dividing manifold inlet vapor quality

For calculating vapor quality at the dividing manifold inlet, the following measured values were used:

- Total refrigerant mass flow rate ($\dot{m}_{prh,In} = \dot{m}_{dm,In}$)
- Preheater power input (\dot{W}_{prh})
- Refrigerant temperature at the inlet of the preheater ($T_{prh,In}$)
- Refrigerant pressure at the inlet of the preheater ($P_{prh,In}$)
- Refrigerant pressure at the inlet of the dividing manifold ($P_{dm,In}$)

Figure 3.9 shows the mass and energy balance across the preheater. The subcooled liquid refrigerant always enters the preheater. The subcooled liquid enthalpy was calculated using REFPROP 7.0 based on the measured temperature and pressure at the inlet of the preheater ($h_{prh,In}(P_{prh,In}, T_{prh,In})$). From the energy balance equation, the refrigerant enthalpy at the inlet of the dividing manifold ($h_{dm,In}$) was determined from the preheater inlet enthalpy ($h_{prh,In}$), preheater power input (\dot{W}_{prh}) and total refrigerant mass flow rate ($\dot{m}_{prh,In} = \dot{m}_{dm,In}$) as shown in Equation 3.1.

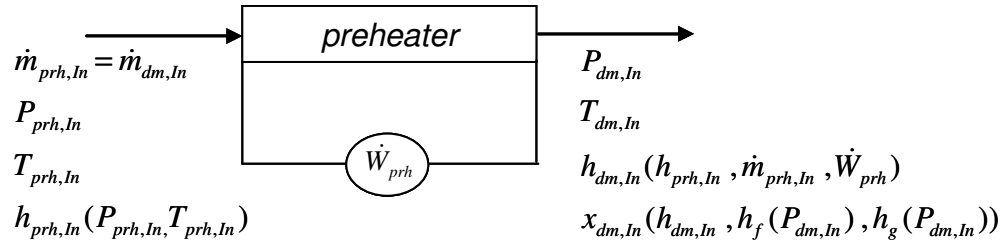


Figure 3.9 Mass and energy balance across the preheater

(*prh,In*: preheater inlet, *dm,In*: dividing manifold inlet)

$$h_{dm,In} = h_{prh,In} + \frac{\dot{W}_{prh}}{\dot{m}_{prh,In}} \quad (3.1)$$

Based on the determined enthalpy, the vapor quality at the dividing manifold inlet was calculated using Equation 3.2.

$$x_{dm,In} = \frac{h_{dm,In} - h_f(P_{dm,In})}{h_{fg}(P_{dm,In})} \quad (3.2)$$

When the refrigerant enthalpy at the inlet of the dividing manifold ($h_{dm,In}$) was calculated, heat gain through insulation was ignored since the maximum calculated heat gain based on the temperature measurements was 8.5 W (less than 0.5% of power input) as shown in Table 3.5.

Table 3.5 Calculated heat gain for the preheater

Mass flow rate (g/s)	30.9	46.4	60.6
Power input (W)	1,814	3,221	4,080
Heat gain (W)	8.4	8.3	8.5
(%)	0.46	0.26	0.21

3.5.2 Branch tube group outlet enthalpy and vapor quality

In the same way to calculate the dividing manifold inlet vapor quality, the measured values in the calculation of the branch tube group outlet enthalpy and vapor quality are summarized as follows;

- Branch tube group refrigerant mass flow rate ($\dot{m}_{bt}(i)$)
- Post heater power input (\dot{W}_{poh})
- Refrigerant temperature at the outlet of the post heater ($T_{poh,Out}$)
- Refrigerant pressure at the outlet of the post heater ($P_{poh,Out}$)
- Refrigerant temperature at the inlet of the post heater ($T_{poh,In}$)
- Refrigerant pressure at the inlet of the post heater ($P_{poh,In}$)

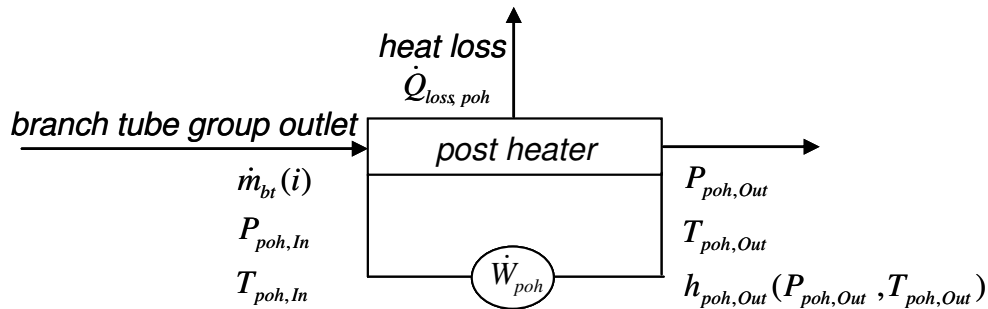


Figure 3.10 Mass and energy balance across the post heater

(*bt*: branch tube, *poh,In*: post heater inlet, *poh,Out*: post heater outlet)

The state of refrigerant at the outlet of the post heater was always kept as superheated vapor. Therefore the enthalpy at the outlet of the post heater was calculated using REFPROP based on the measured temperature and pressure at the outlet of the post

heater ($h_{poh,Out}(P_{poh,Out}, T_{poh,Out})$). From the energy balance equation, the refrigerant enthalpy at the outlet of the branch tube group, which is the refrigerant enthalpy at the inlet of the post heater ($h_{bt,Out}$) was determined from the Equation 3.3 while considering the heat loss of the post heater through insulation.

$$h_{bt,Out}(i) = h_{poh,Out} - \frac{\dot{W}_{poh} - \dot{Q}_{loss,poh}}{\dot{m}_{bt}(i)} \quad (3.3)$$

Figure 3.11 shows the heat loss through the insulation installed on the post heater. The heat loss through the insulation was calculated based on the temperature measurements on the insulation. The calculated value is about 3.3% of the input power. For calculating vapor quality at the outlet of the branch group, Equation 3.4 was used while considering this heat loss.

$$x_{bt,Out}(i) = \frac{h_{bt,Out}(i) - h_f(P_{poh,In})}{h_{fg}(P_{poh,In})} \quad (3.4)$$

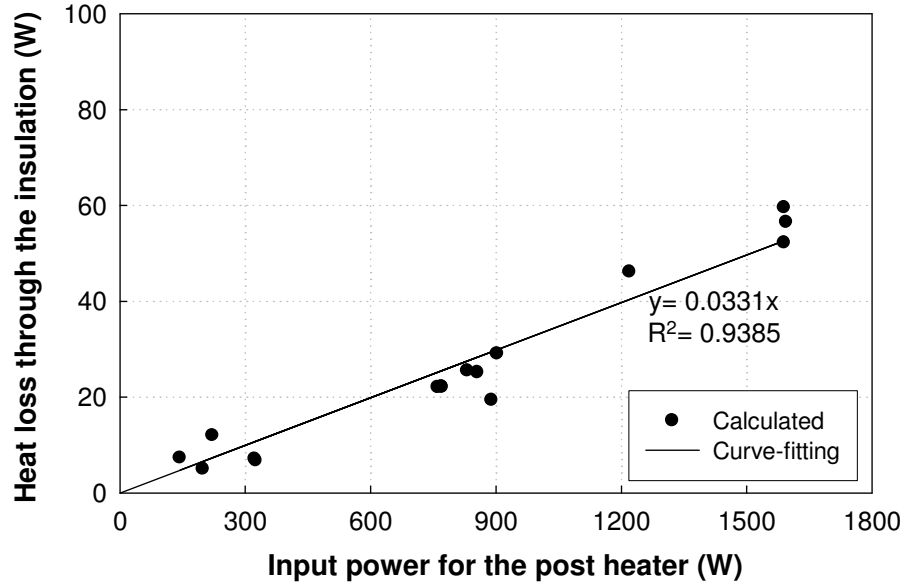


Figure 3.11 Heat loss through the insulation on the post heater

3.5.3 Branch tube group inlet enthalpy and vapor quality

Figure 3.12 shows mass and energy balance across the branch tube group. From the energy balance and property equations, the refrigerant enthalpy and vapor quality at the inlet of the branch tube group were calculated using Equations 3.5 and 3.6.

$$h_{bt,ln}(i) = h_{bt,Out}(i) - \frac{\dot{W}_{mh}}{\dot{m}_{bt}(i)} \quad (3.5)$$

$$x_{bt,ln}(i) = \frac{h_{bt,ln}(i) - h_f(P_{bt,ln})}{h_{fg}(P_{bt,ln})} \quad (3.6)$$

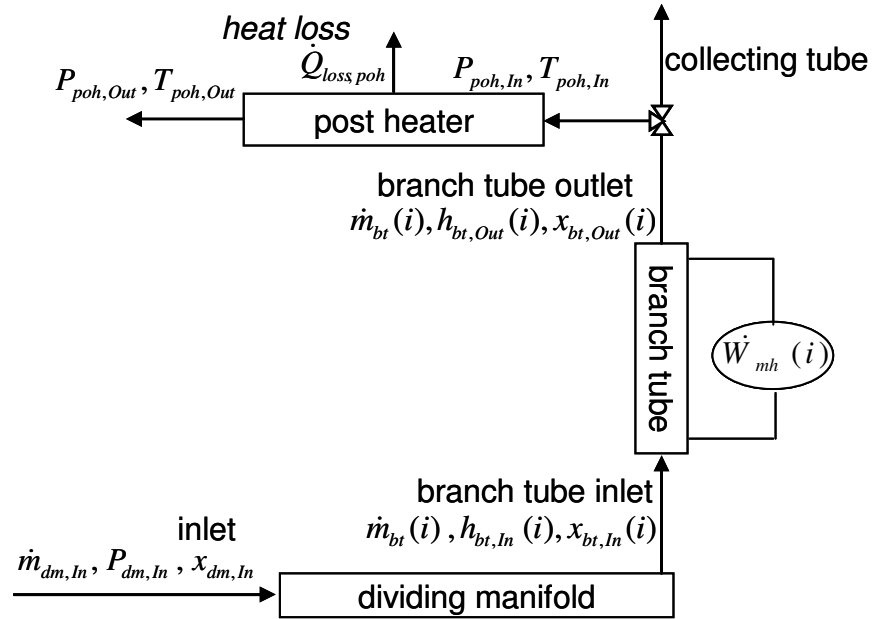


Figure 3.12 Mass and energy balance across the branch tube group

When the refrigerant enthalpy at the inlet of the branch tube group ($h_{bt,In}$) was calculated, heat loss was not included since the calculated heat loss was less than 1% of power input.

3.6 Experimental Uncertainty Analysis

3.6.1. Kline and McClintock method

For estimating the uncertainties, the method presented by Kline and McClintock (Holman, 2001) was used. The result R may be expressed based on the independent variables as:

$$R = R(x_1, x_2, x_3, \dots, x_n) \tag{3.7}$$

In order to quantitatively analyze the uncertainty, Kline and McClintock (Holman, 2001) developed a statistical method, and proposed an equation for the uncertainty as shown in Equation 3.8:

$$\omega_R = \left[\left(\frac{\partial R}{\partial x_1} \omega_{x_1} \right)^2 + \left(\frac{\partial R}{\partial x_2} \omega_{x_2} \right)^2 + \left(\frac{\partial R}{\partial x_3} \omega_{x_3} \right)^2 + \dots + \left(\frac{\partial R}{\partial x_n} \omega_{x_n} \right)^2 \right]^{0.5} \quad (3.8)$$

ω_R is the absolute uncertainty of the result R, and $\omega_{x_1}, \omega_{x_2}, \dots, \omega_{x_n}$ are the uncertainties in the independent variables x_1, x_2, \dots, x_n . For analyzing the uncertainties of the experimental results, it is necessary to analyze the uncertainty of each measurement. The uncertainty of each sensor was described in section 3.4 Instrumentation. In the following sections, two important uncertainties will be discussed: (1) the uncertainty of the vapor quality at the inlet of the dividing manifold, (2) the uncertainty of the vapor quality at the inlet of the individual branch tube group.

3.6.2. Uncertainty of the dividing manifold inlet vapor quality

First, the uncertainty of the vapor quality at the inlet of the dividing manifold will be presented in this section. To measure the refrigerant flow distribution, the vapor quality at the inlet of the dividing manifold was determined using the Equation 3.2. Using Equation 3.8, the uncertainty of the vapor quality at the inlet of the dividing manifold was calculated by Equation 3.9:

$$\omega_{x_{dm,In}} = \left[\left(\frac{\partial x_{dm,In}}{\partial h_{dm,In}} \omega_{h_{dm,In}} \right)^2 + \left(\frac{\partial x_{dm,In}}{\partial P_{dm,In}} \omega_{P_{dm,In}} \right)^2 \right]^{0.5} \quad (3.9)$$

Based on the Equation 3.1, the following equations are needed to calculate Equation 3.9.

$$\omega_{h_{dm,In}} = \left[(\omega_{h_{prh,In}})^2 + \left(\frac{\partial h_{dm,In}}{\partial \dot{W}_{prh}} \omega_{\dot{W}_{prh}} \right)^2 + \left(\frac{\partial h_{dm,In}}{\partial \dot{m}_{dm,In}} \omega_{\dot{m}_{dm,In}} \right)^2 \right]^{0.5} \quad (3.10)$$

$$\omega_{h_{prh,In}} = \left[\left(\frac{\partial h_{prh,In}}{\partial P_{prh,In}} \omega_{P_{prh,In}} \right)^2 + \left(\frac{\partial h_{prh,In}}{\partial T_{prh,In}} \omega_{T_{prh,In}} \right)^2 \right]^{0.5} \quad (3.11)$$

The uncertainty of the preheater inlet enthalpy was determined at typical temperatures and pressures where the experiments were conducted, and calculated uncertainty was shown in Table 3.6.

Table 3.6 Uncertainty of the preheater inlet enthalpy

	R-134a	R-410A
$\omega_{h_{prh,In}}$	$\pm 1.4\%$	$\pm 1.4\%$

For calculating the uncertainty of the vapor quality at the inlet of the dividing manifold, uncertainties of the measurements for temperature (± 0.5 °C), pressure (± 2.4 kPa),

preheater power input ($\pm 20 \sim 40$ W) and refrigerant mass flow rate (± 0.075 g/s) were used. The calculated uncertainties were shown in Table 3.7.

Table 3.7 Uncertainty of vapor quality at the inlet of the dividing manifold

	R-134a			R-410A		
$\dot{m}_{dm,In}$ (g/s)	30.2	44.7	60.0	30.1	44.9	59.9
\dot{W}_{prh} (W)	1,830	2,780	3,756	2,443	3,465	3,830
$\omega_{x_{dm,In}}$	± 0.0051	± 0.0060	± 0.0051	± 0.0070	± 0.0055	± 0.0048

3.6.3. Uncertainty of the branch tube group inlet vapor quality

In order to calculate vapor quality at the inlet of the branch tube group, Equation 3.12 was used based on Equation 3.3, 3.5, and 3.6 as described before.

$$x_{bt,In}(i) = \frac{h_{poh,Out} - \frac{\dot{W}_{mh} + \dot{W}_{poh} - \dot{Q}_{loss,poh}}{\dot{m}_{bt}(i)} - h_f(P_{bt,In})}{h_{fg}(P_{bt,In})} \quad (3.12)$$

By using Equation 3.8, the uncertainty of the branch tube group inlet vapor quality was calculated by the following equation:

$$\begin{aligned} (\omega_{x_{bt,In}})^2 = & \left(\frac{\partial x_{bt,In}}{\partial h_{poh,Out}} \omega_{h_{poh,Out}} \right)^2 + \left(\frac{\partial x_{bt,In}}{\partial \dot{W}_{mh}} \omega_{\dot{W}_{mh}} \right)^2 + \left(\frac{\partial x_{bt,In}}{\partial \dot{W}_{poh}} \omega_{\dot{W}_{poh}} \right)^2 + \left(\frac{\partial x_{bt,In}}{\partial \dot{Q}_{loss,poh}} \omega_{\dot{Q}_{loss,poh}} \right)^2 \\ & + \left(\frac{\partial x_{bt,In}}{\partial \dot{m}_{bt}} \omega_{\dot{m}_{bt}} \right)^2 + \left(\frac{\partial x_{bt,In}}{\partial P_{bt,In}} \omega_{P_{bt,In}} \right)^2 \end{aligned} \quad (3.13)$$

$$\omega_{h_{poh,Out}} = \left[\left(\frac{\partial h_{poh,Out}}{\partial P_{poh,Out}} \omega_{P_{poh,Out}} \right)^2 + \left(\frac{\partial h_{poh,Out}}{\partial T_{poh,Out}} \omega_{T_{poh,Out}} \right)^2 \right]^{0.5} \quad (3.14)$$

The uncertainty of the post heater outlet enthalpy was calculated by Equation 3.14 at typical temperatures and pressures where the experiments were conducted, and calculated uncertainties are shown in Table 3.8.

Table 3.8 Uncertainty of the post heater outlet enthalpy

	R-134a	R-410A
$\omega_{h_{poh,Out}}$	$\pm 0.17\%$	$\pm 0.16\%$

Using Equation 3.12, the uncertainty of vapor quality at the inlet of the branch tube group was calculated, and is shown in Table 3.9. As shown in the Table, as the mass flow rate at the branch tube group decreases, the uncertainty increases due to higher uncertainty of mass flow rate measurement. The maximum uncertainty of vapor quality at the inlet of the branch tube group for R-410A and R-134a is ± 0.063 and ± 0.085 , respectively.

Table 3.9 Uncertainty of the branch tube group inlet vapor quality

	R-410A					
	Low vapor quality region			High vapor quality region		
$x_{bt,In}$	0.088	0.092	0.093	0.950	0.958	0.968
$\dot{m}_{bt}(i)$ (g/s)	3.1	4.6	6.0	3.5	4.9	5.5
\dot{W}_{mh} (W)	446	451	494	65	101	105
\dot{W}_{poh} (W)	288	549	771	155	127	144
$\omega_{x_{dm,In}}$	± 0.063	± 0.058	± 0.034	± 0.058	± 0.017	± 0.015

	R-134a					
	Low vapor quality region			High vapor quality region		
$x_{bt,In}$	0.123	0.083	0.081	0.967	0.965	0.945
$\dot{m}_{bt}(i)$ (g/s)	3.0	4.2	6.3	3.3	4.2	5.1
\dot{W}_{mh} (W)	494	503	499	58	82	135
\dot{W}_{poh} (W)	145	359	761	140	151	147
$\omega_{x_{dm,In}}$	± 0.085	± 0.051	± 0.037	± 0.059	± 0.024	± 0.020

4. Experimental Results

4.1 Overview

In this section, the experimental results will be presented. The flow visualization will be shown in section 4.2. In order to figure out the effects of the individual parameters on the flow distribution, the test results for the mass flow rate and vapor quality for the individual tube groups will be provided from section 4.3 to section 4.8.

4.1.1 Test matrix

Table 4.1 shows the test matrix for this study. Two refrigerants were used as working fluids in this study. Three different heat exchangers were used in order to figure out the effects of tube pitch on the flow distribution. In addition, for the tests with various tube numbers, the 10 mm tube pitch heat exchanger was used by blocking a certain number of tube groups using dead blocks, and shut-off valves were installed as well at the outlet of individual tube groups to make sure no flow through the branch tube groups supposed to be blocked. The total number of the test was 60.

Table 4.1 Test matrix

No	Refrigerant	TP (mm)	TN	$x_{dm,ln}$	Heat Load (kW)	Inlet	MFR (g/s)
1	R-134a	10	30	0.3	0	End	30, 45, 60
2						Side	30, 45, 60
3					5	End	30, 45, 60
4				Side		30, 45, 60	
5				0.15	5	End	45
6						0.45	Side
7	R-410A	10	30	0.3	0	End	30, 45, 60
8						Side	30, 45, 60
9					5	End	30, 45, 55, 60
10				Side		30, 45, 55, 60	
11				10	End	30, 45, 60	
12					Side	30, 45, 60	
13		10	24	0.3	5	End	30, 45, 55
14						Side	30, 45, 55
15		10	18	0.3	5	End	30, 45, 55
16						Side	30, 45, 55
17		8	30	0.3	5	End	30, 45, 55
18						Side	30, 45, 55
19		12	30	0.3	5	End	30, 45, 55
20						Side	30, 45, 55
21	R-410A + Oil	10	30	0.3	5	Side	45
22						End	45

4.1.2 Refrigerant distribution parameters

For presenting the results of the refrigerant distribution in the dividing manifold, the mass flow rate ratio, the vapor phase, and the liquid phase in the i^{th} branch tube group is presented in percentage as follows:

$$R_{bt,ph}(i)(\%) = \frac{\dot{m}_{bt,ph}(i)}{\sum_{i=1}^N \dot{m}_{bt,ph}(i)} \times 100 \quad (4.1)$$

where $ph = vap$ (vapor) and liq (liquid).

In addition, for better understanding of the degree of maldistribution, the normalized form was used as follows:

$$\text{average mass flow rate: } AMFR_{ph} = \frac{\sum_{i=1}^{N_{bt}} \dot{m}_{bt,ph}(i)}{N_{bt}} \quad (4.2)$$

$$\text{normalized mass flow rate ratio: } NR_{bt,ph}(i) = \frac{\dot{m}_{bt,ph}(i)}{AMFR_{ph}} \quad (4.3)$$

where N_{bt} is indicating the number of branch tube groups,

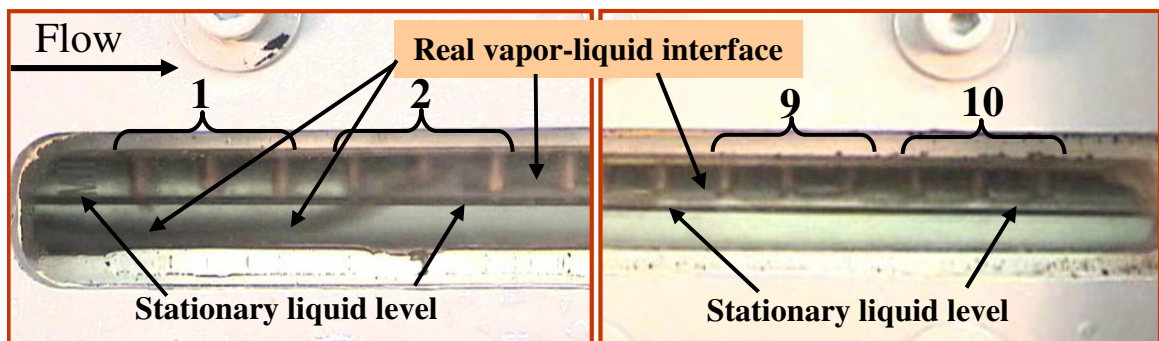
and $ph = vap$ (vapor) and liq (liquid).

4.2 Flow Visualization In Dividing Manifold

4.2.1 Overview

The visualization section was built using transparent tubes as dividing manifolds. Since it is very important to observe the refrigerant flow patterns visually for the understanding of the refrigerant distribution, the refrigerant flow was recorded in digital format for all the test conditions for this study using a digital camcorder while testing. Figure 4.1 shows a flow visualization for the R-410A test with the end inlet, especially for 30 g/s of the manifold inlet mass flow rate. The numbers in Figure 4.1 indicate are the branch tube group number. While assembling the visualization section, the multiport flat tubes were simply inserted into the slots in the transparent manifold with very small gaps. Due to such an assembling method, in the beginning of running the system, some of refrigerant

flowed into the region between the outer transparent wall surface and the inner surfaces of the sight glasses shown in Figure 3.3 by the pressure difference between inside and outside the manifold. After the system reached a steady state, the refrigerant stayed in the space between the outer transparent wall surface and the inner surfaces of the sight glasses as a stationary fluid. Therefore, this stationary refrigerant does not affect the refrigerant distribution in the transparent manifold. In Figure 4.1, the stationary liquid level is clearly seen. For the end inlet case, the refrigerant flows into the manifold from the left. In Figure 4.1, it is shown that near the inlet, the liquid is flowing at the lower part of the dividing manifold, and the vapor is flowing at the upper part of the manifold due to the gravitational effect. In addition, it is shown that the liquid level increases along the dividing manifold up to a certain length of it because the liquid is traveling farther than the vapor due to inertia difference, and near the right end, the liquid level is kept almost constant. Based on the flow pattern map from Kattan et al. (1998) and Thome et al. (2002), the flow pattern can be considered as stratified flow or stratified-wavy flow.

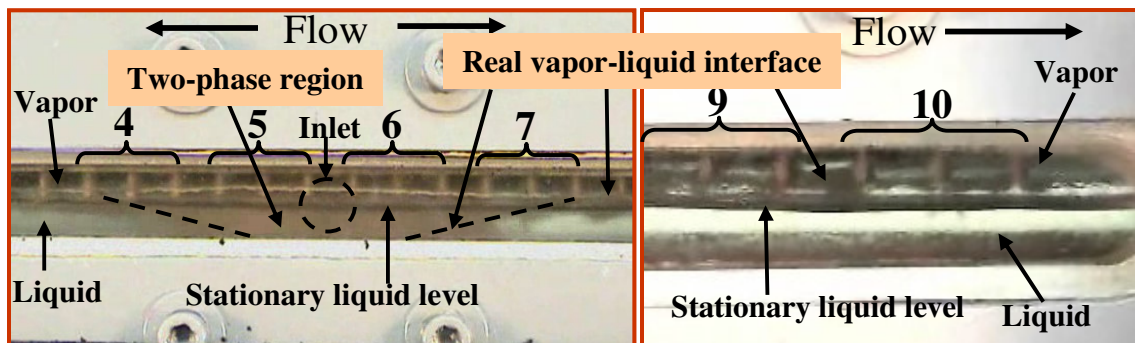


(a) near the inlet

(b) near the right end

Figure 4.1 Refrigerant distribution in the dividing manifold with 10 mm tube pitch and 10 tube groups, end inlet (R-410A, Heat load: 5 kW, $x_{dm,In} = 0.3$, $\dot{m}_{dm,In} = 30$ g/s)

Figure 4.2 shows a flow visualization for the R-410A test with the side inlet, especially for 60 g/s of the manifold inlet mass flow rate. The refrigerant flows into the dividing manifold from the middle located at the rear side. The numbers in the Figure indicate the branch tube group number. In Figure 4.2, it is cleared that the refrigerant impinges on the inner side wall of the manifold, and is divided symmetrically near the inlet. The interface between the vapor and the liquid has a V-shaped form near the inlet, which means the interface has a slope. At the lower mass flow rate, the vapor is mostly flowing near the inlet. As the refrigerant mass flow rate increases, the slope is getting smaller, which means the vapor is traveling farther towards the manifold ends due to the bigger momentum flux. In addition, at the far ends of the manifold, a pool of liquid is seen in Figure 4.2. In order to understand the effects of the parameters on the refrigerant distribution, some snapshots of the refrigerant flow in the dividing manifold are presented in the following sections.



(a) Near the inlet

(b) Near the right end

Figure 4.2 Refrigerant distribution in the dividing manifold with 10 mm tube pitch and 10 tube groups, side inlet (R-410A, Heat load: 5 kW, $x_{dm,In} = 0.3$, $\dot{m}_{dm,In} = 60$ g/s)

4.2.2 Effect of manifold inlet mass flow rate

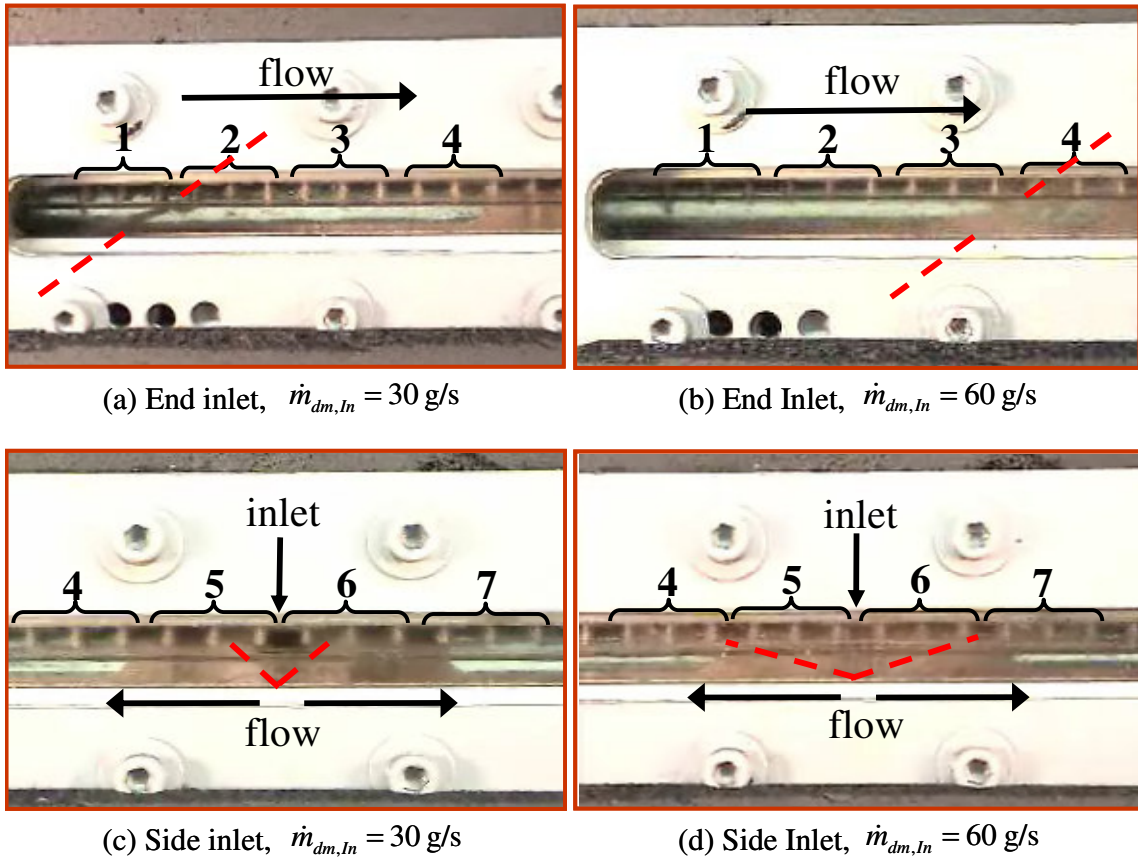


Figure 4.3 Refrigerant distribution in the dividing manifold with 10 mm tube pitch and 10 tube groups (R-410A, Heat load: 0 kW, $x_{dm,in} = 0.3$)

Figure 4.3 shows the flow visualization in the dividing manifold with 10 mm tube pitch and 10 tube groups for the R-410A test with both inlets and 0 kW heat load at varying refrigerant mass flow rates. Figure 4.3 (a) and (b) show the visualization for the end inlet case, and (c) and (d) show the flow visualization for the side inlet case. The dashed lines in the Figure indicate the location for the vapor-liquid interface. For the end inlet case, it is shown that as the refrigerant mass flow rate increases, the vapor-liquid interface is traveling farther downstream due to higher momentum of the liquid. Based on the

measurement of the branch tube group inlet vapor quality, it was shown that the vapor-liquid interface for the $\dot{m}_{dm,in} = 30$ g/s, 45 g/s and 60 g/s was located at right after branch tube group number 1, 2 and 3, respectively. For the side inlet case, the refrigerant is symmetrically divided near the inlet. As the refrigerant mass flow rate increases, the vapor is traveling farther towards both ends of the manifold.

4.2.3 Effect of tube pitch

The refrigerant flow in the dividing manifold with various tube pitches for the R-410A test is shown in the Figure 4.4. The Figure shows refrigerant flow visualization for the end inlet case, where refrigerant flows into the manifold from the left. Figure 4.4 (a) and (b) show the flow visualization for 8 mm tube pitch, and (c) and (d) show the flow visualization for 10 mm tube pitch, and (e) and (f) show the flow visualization for 12 mm tube pitch. The dashed lines in the Figure indicate the location for the vapor-liquid interface. For the manifold with 12 mm tube pitch, two tubes cannot be seen in the visualization because the manifold is wider than those for other tube pitches for limited sight glass section. However, the hidden tubes can be seen through the rear sight glasses because two short sight glasses are installed at the rear side. Based on the snapshots, the locations of the vapor-liquid interface for the three tube pitches are almost same. For the mass flow rate 30 g/s, each vapor-liquid interface is located approximately under tube group No. 2 even though the interface is fluctuating because of unstable two-phase flow. For the mass flow rate 55 g/s, each vapor-liquid interface is located approximately under tube group No. 4. These visual observations are well matched with measurements results shown in the section 4.3.

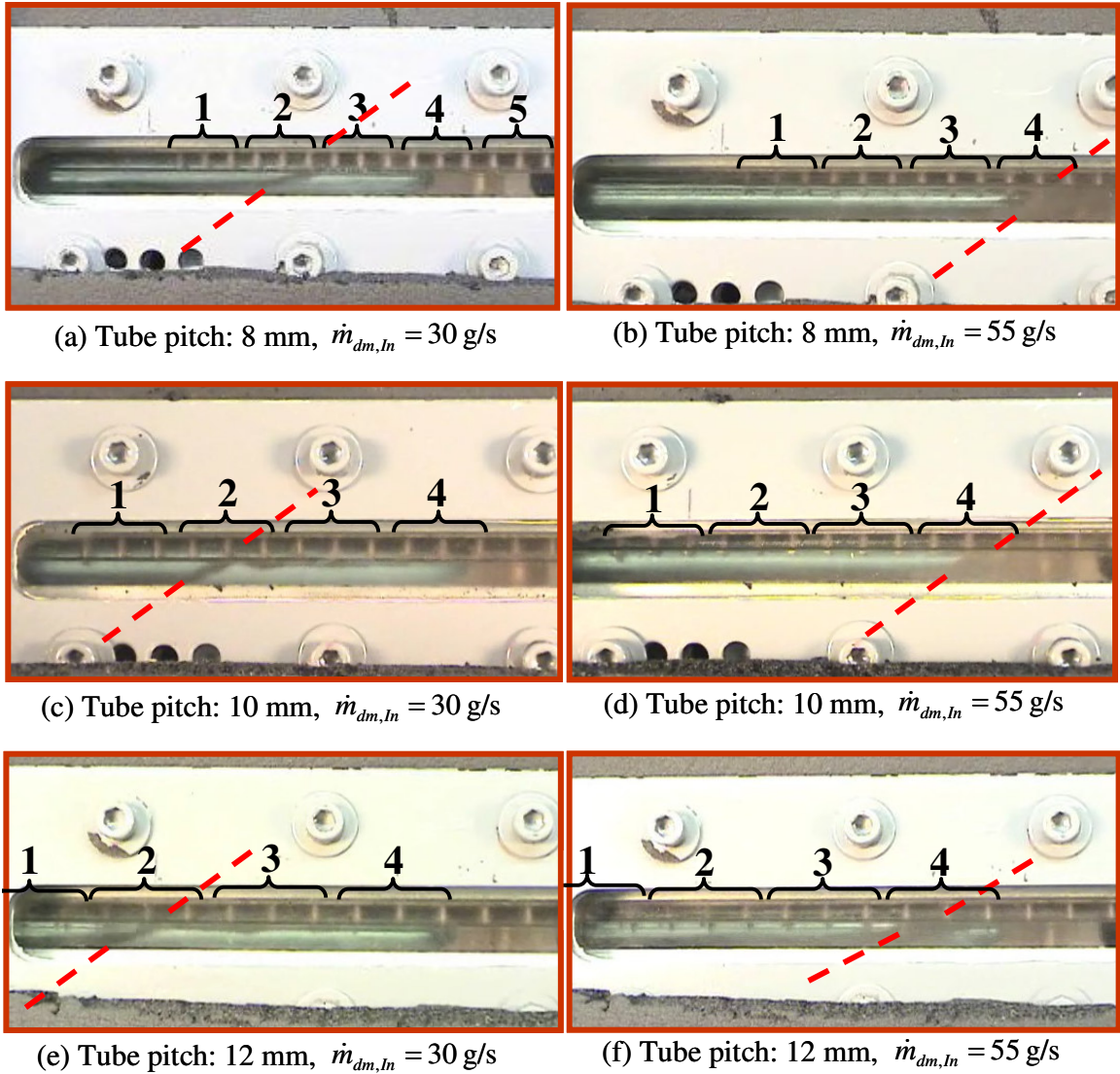


Figure 4.4 Refrigerant distribution in the dividing manifold with various tube pitches (R-410A, End inlet, Tube group No.: 10 ea, Heat load: 5 kW, $x_{dm,in} = 0.3$)

4.2.4 Effect of heat load

The refrigerant flow pattern in the dividing manifold with different heat load for the R-410A test with the end inlet is shown in the Figure 4.5. As explained before, for the end inlet, the refrigerant flows into the manifold from the left. Figure 4.5 (a) and (b) show the visualization for $\dot{m}_{dm,in} = 30$ g/s , and (c) and (d) show the flow visualization for

$\dot{m}_{dm,in} = 60 \text{ g/s}$. Based on the Figure 4.5, it can be seen that as heat load increases, the vapor-liquid interface is traveling farther for both mass flow rates. The difference between the locations of the interfaces for both heat loads is approximately two tube pitches, but it should be considered that the vapor-liquid interface is fluctuating because of the unstable two-phase flow. As the heat load increases, the pressure drops along the branch tubes at the far end decrease due to the reduced gravity effect as the pressure drop measurements show. Therefore, it can be said that as the heat load increases the vapor-liquid interface is traveling farther due to the reduced pressure drop through the branch tubes especially located at the far end of the manifold because the gravity effect for the tube groups at the far end is greater than those for the branch tube groups at the near inlet.

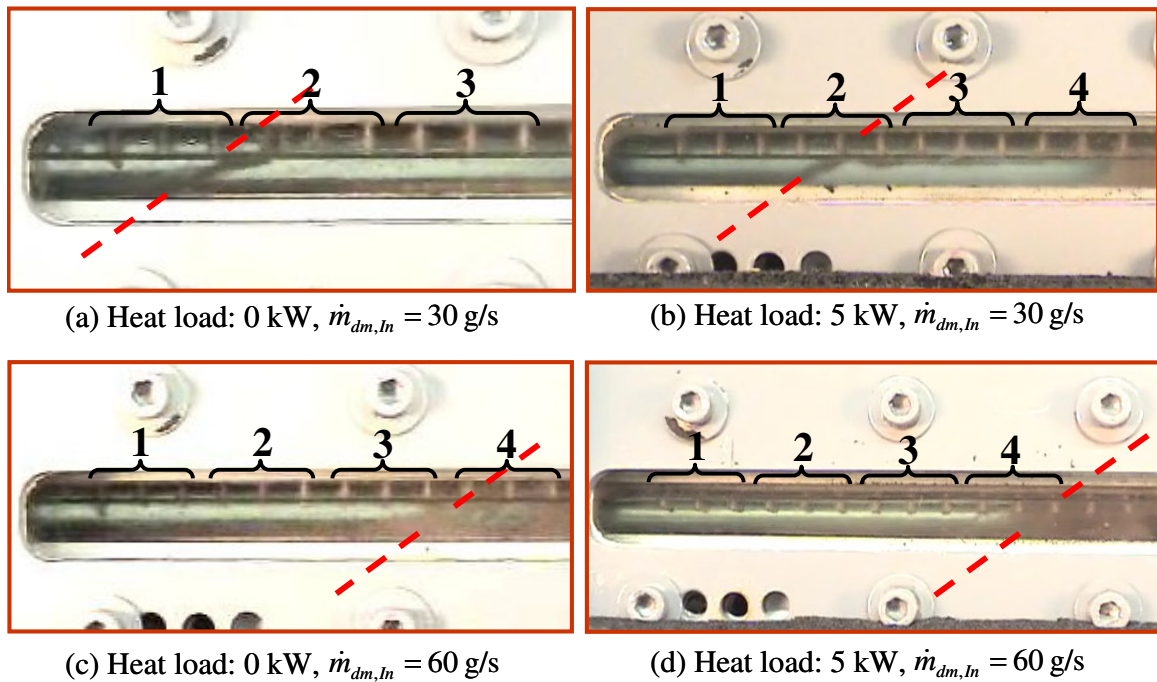


Figure 4.5 Refrigerant distribution in the dividing manifold with different heat loads (R-410A, End inlet, Tube pitch: 10 mm, Tube group No.: 10 ea, $x_{dm,in} = 0.3$)

4.2.5 Effect of refrigerant property

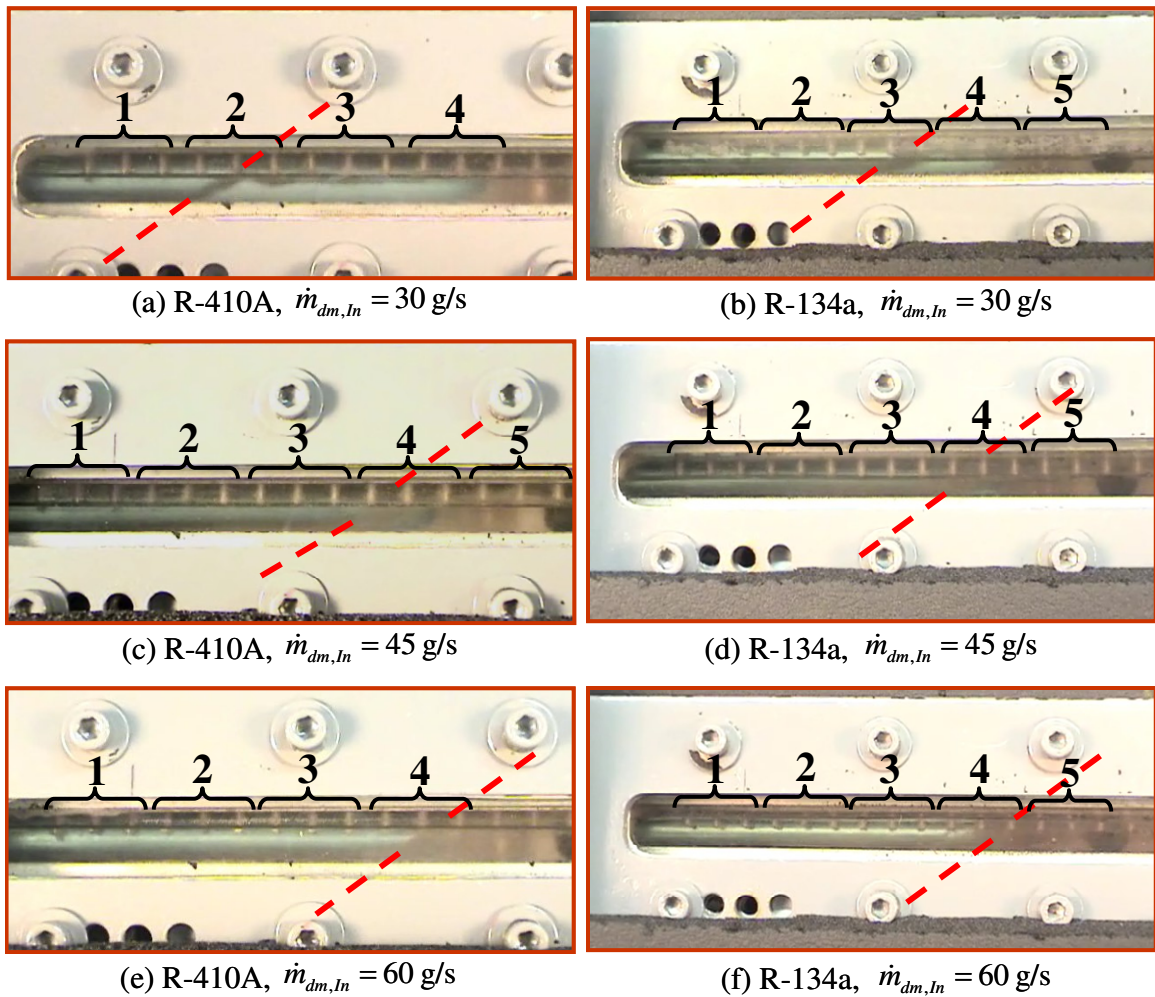


Figure 4.6 Refrigerant distribution in the dividing manifold with different refrigerants (End inlet, Tube pitch: 10 mm, Tube group No.: 10 ea, $x_{dm,In} = 0.3$)

The refrigerant flow in the dividing manifold with different refrigerant for the end inlet is shown in Figure 4.6. For this comparison, the manifold with 10 mm tube pitch and 30 tubes was used. Figure 4.6 (a) and (b), (c) and (d), and (e) and (f) show the flow visualization for $\dot{m}_{dm,In} = 30$ g/s , 45 g/s, and 60 g/s, respectively. Based on the snapshots, the vapor-liquid interface for R-134a is traveling farther than that for R-410A

especially at $\dot{m}_{dm,in} = 30$ g/s . For $\dot{m}_{dm,in} = 45$ g/s and 60 g/s, the locations of the vapor-liquid interfaces for both refrigerants are almost same even though the vapor-liquid interface for R-134a is moving a little towards the far end side of the manifold.

4.3 Measured Inlet and Outlet Conditions

In this section, a summary of test results obtained for the effect of various parameters is described.

4.3.1 Effect of manifold inlet mass flow rate

In this section, test results of the dividing manifold with 10 mm tube pitch and 30 tubes (10 tube groups) for R-410A and R-134a are shown. Especially the effect of manifold inlet mass flow rate is investigated based on test results with 5 kW heat load.

4.3.1.1 The branch tube inlet vapor quality

Figure 4.7 shows branch tube group inlet vapor quality at varying manifold inlet mass flow rate with 5 kW heat load for R-410A and R-134a as a function of the branch tube group number. Figure 4.7 (a) and (b) show the branch tube group inlet vapor quality for the R-410A with the end and the side inlet, respectively, as a function of the branch tube group number, and (c) and (d) show the branch tube group inlet vapor quality for R-134a with the end and the side inlet, respectively, as a function of the branch tube group number. The branch tube group number is named for every three tubes from the left end of the dividing manifold along the manifold. As shown in Figure 4.7, the number of branch tube groups is 10. For the end inlet case with both refrigerants, the branch tube

group inlet vapor quality for the tube groups near the inlet is much higher than that for the tube groups located at after branch tube group No. 5 depending upon the manifold inlet mass flow rate. In the flow visualization for the end inlet case shown in Figure 4.6, near the inlet, the liquid is flowing at the bottom side of the manifold, whereas the vapor is flowing at the upper part of the manifold. In addition, the liquid level near the inlet is much lower than the very end position of the branch tubes. Therefore, the vapor is easily flowing through the branch tubes near the inlet. Unlike near the inlet, the liquid level at the far end is above the very end position of the branch tubes. Therefore, the liquid is easily flowing through the branch tubes located at the far end. In addition, the liquid level at the far end is fluctuating up and down depending on the test conditions, and the vapor can flow through the branch tubes while the liquid level is staying below a certain level, for instance, the very end position of the branch tubes. As shown in Figure 4.7 (a) and (c), the distribution of the branch tube inlet vapor quality along the manifold reflected well the flow visualization shown in Figure 4.6. For the R-410A test with $\dot{m}_{dm,ln} = 30$ g/s (manifold inlet mass flow rate), the branch tube group inlet vapor quality for the tube group No. 1 and No. 2 is about 96% and 80%, respectively, and the branch tube group inlet vapor quality for the tube group No. 3 through 10 is almost constant, about 10 ~ 20%. As the mass flow rate increases, the number of branch tube groups having high inlet vapor quality, which is close to 100%, increases. For the R-410A test with $\dot{m}_{dm,ln} = 60$ g/s, the branch tube group inlet vapor quality for the tube group No. 1 through No. 2 is about 96%, and the branch tube group inlet vapor quality for the tube group No. 3 and No. 4 is about 90% and 30%, respectively. At the branch tube group No. 4 through 10, the branch tube group inlet vapor quality is almost constant, about 10 ~

20%. For the R-134a test, the overall trend is almost the same. However, as shown in the flow visualization in Figure 4.6, the vapor-liquid interface of the R-134a is moving farther towards the end of the manifold than that for the R-410A due to greater momentum. Therefore, for $\dot{m}_{dm,In} = 30$ g/s, the branch tube group inlet vapor quality of the tube group No. 2 for the R-134a is higher than that for the R-410A. For the R-134a, the branch tube group inlet vapor quality for the tube group No. 2 is about 96% compared to 80% for the R-410A. For the side inlet, the distribution of the branch tube inlet vapor quality is almost symmetric. Due to the inertia difference between the liquid and the vapor, the liquid is flowing farther than the vapor. For both refrigerants, the branch tube inlet vapor quality for the tube group No. 5 and 6, which are near the inlet, is about 0.7 depending upon the mass flow rate. The branch tube inlet vapor quality along the manifold towards the both ends gradually decreases. In addition, there exist constant vapor quality regions at the tube groups near the ends of the manifold.

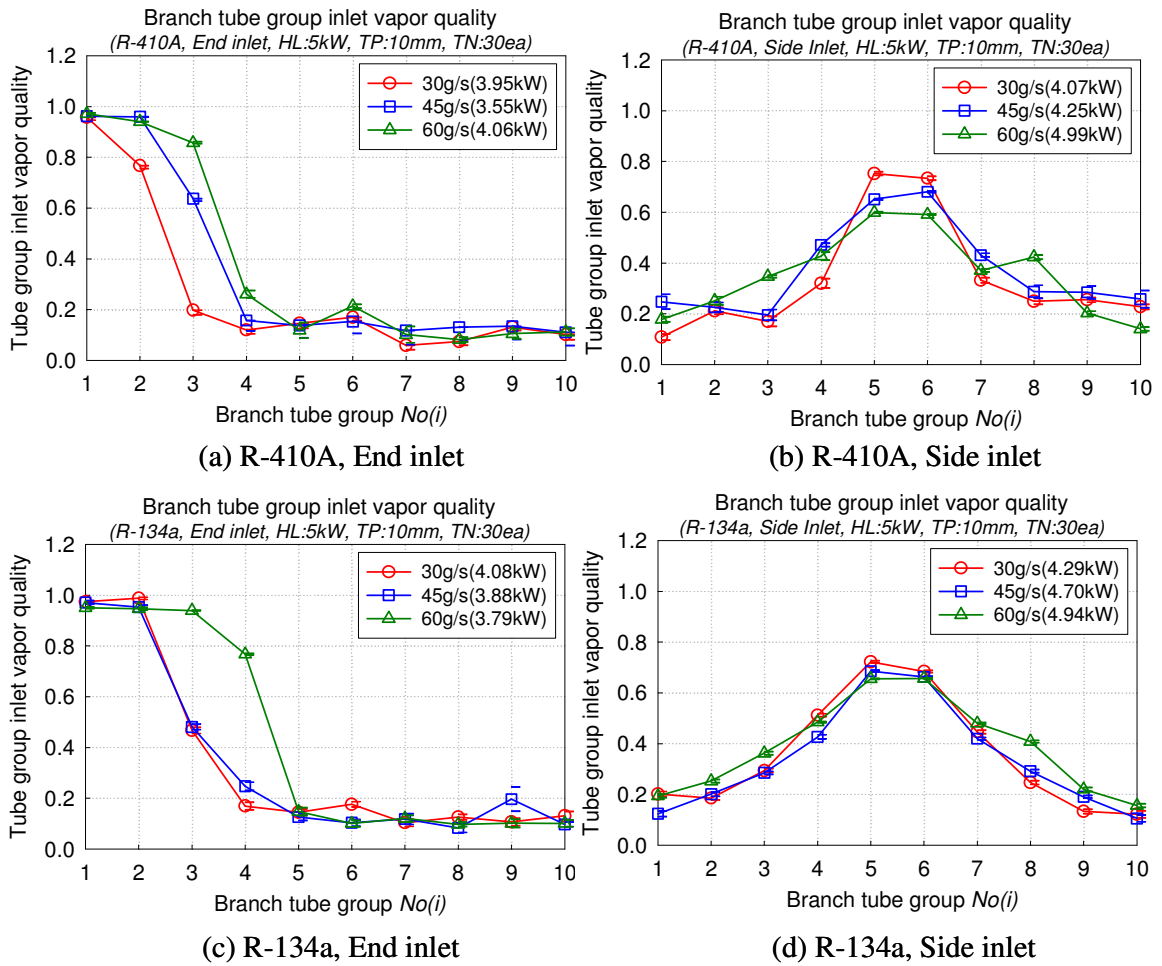


Figure 4.7 Branch tube group inlet vapor quality at varying inlet mass flow rate with 5 kW heat load for R-410A and R-134a (Tube pitch: 10 mm, Tube group No.: 10 ea, $x_{dm,in} = 0.3$)

4.3.1.2 Refrigerant distribution

Figure 4.8 shows the mass flow rate ratio at varying inlet mass flow rate with 5 kW heat load for R-410A and R-134a as a function of the branch tube group. Figure 4.8 (a) and (b) show the mass flow rate ratio for R-410A with the end inlet and side inlet, respectively, as a function of the branch tube group, and (c) and (d) show the mass flow rate ratio for R-134a with the end inlet and side inlet, respectively, as a function of the branch tube group. For both end inlet and side inlet, as the manifold inlet mass flow rate increases, the mass flow rate ratio for the branch tube groups near the manifold inlet is decreasing, whereas the mass flow rate ratio for the branch tube groups near the end of the manifold is increasing because the liquid is traveling farther due to the higher momentum. As shown in Figure 4.8, such a trend is more obvious in the R-134a results than in the R-410A results because the inertia ratio between vapor and liquid for the R-134a is greater than that for the R-410A. For the manifold with 10 tube groups, the average mass flow rate ratio is 10% based on the assumption of equal refrigerant distribution. Based on the measurements as shown in the Figure 4.8, the maximum deviation is 2% from the average mass flow rate ratio.

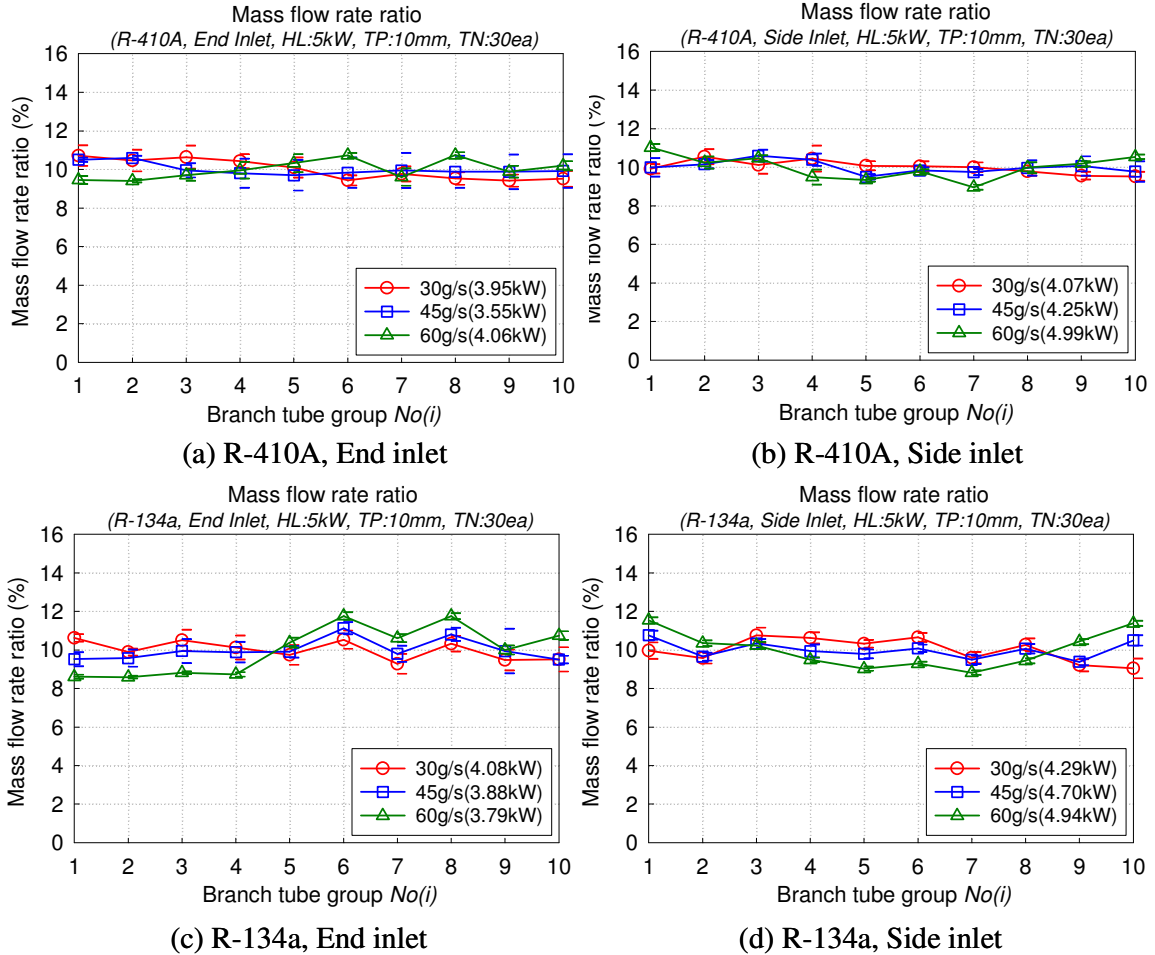


Figure 4.8 Mass flow rate ratio with various manifold inlet mass flow rates with 5 kW heat load for R-410A and R-134a (Tube pitch: 10 mm, Tube group No.: 10 ea, $x_{dm,In} = 0.3$)

Figure 4.9 shows the vapor mass flow rate ratio at varying inlet mass flow rate with 5 kW heat load for R-410A and R-134a as a function of the branch tube group number. Figure 4.9 (a) and (b), and (c) and (d) show the vapor mass flow rate ratio for R-410A and R-134a, respectively, as a function of the branch tube group number. Figure 4.9 shows the exact trend of the branch tube group inlet vapor quality. For the end inlet, it is shown that approximately 65 ~ 75% vapor mass flow rate of the manifold inlet vapor mass flow rate

is flowing through the first three branch tube groups near the inlet depending upon the mass flow rate. For the side inlet, about 50 ~ 65% vapor mass flow rate of the manifold inlet vapor mass flow rate is flowing through the four branch tube groups near the inlet depending upon the mass flow rate.

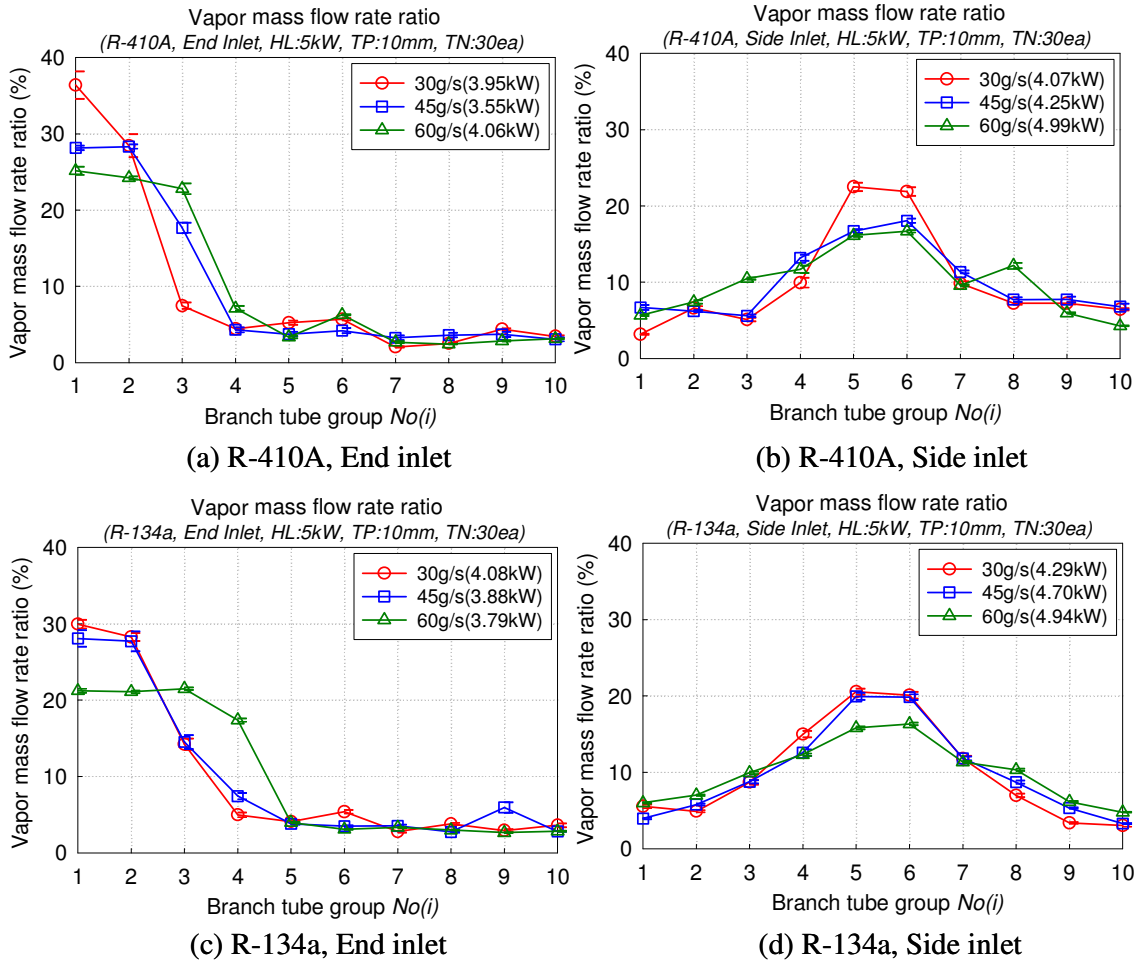


Figure 4.9 Vapor mass flow rate ratio with various manifold inlet mass flow rates with 5 kW heat load for R-410A and R-134a (Tube pitch: 10 mm, Tube group No: 10 ea, $x_{dm,In} = 0.3$)

The liquid mass flow rate ratio at varying inlet mass flow rate with 5 kW heat load for R-410A and R-134a is shown in Figure 4.10 as a function of the branch tube group number. Figure 4.10 (a) and (b), and (c) and (d) show the liquid mass flow rate ratio for R-410A and R-134a, respectively, as a function of the branch tube group number. Figure 4.10 shows that the liquid mass flow rate ratio for the branch tube groups near the inlet is much lower than that for the branch tube groups located at the far end of the manifold. For the end inlet, approximately 7 ~ 15% liquid mass flow rate of the inlet manifold liquid mass flow rate is flowing through the first three branch tube groups near the inlet depending upon the mass flow rate. For the side inlet, about 25% liquid mass flow rate of the inlet manifold liquid mass flow rate is flowing through the four branch tube groups near the inlet.

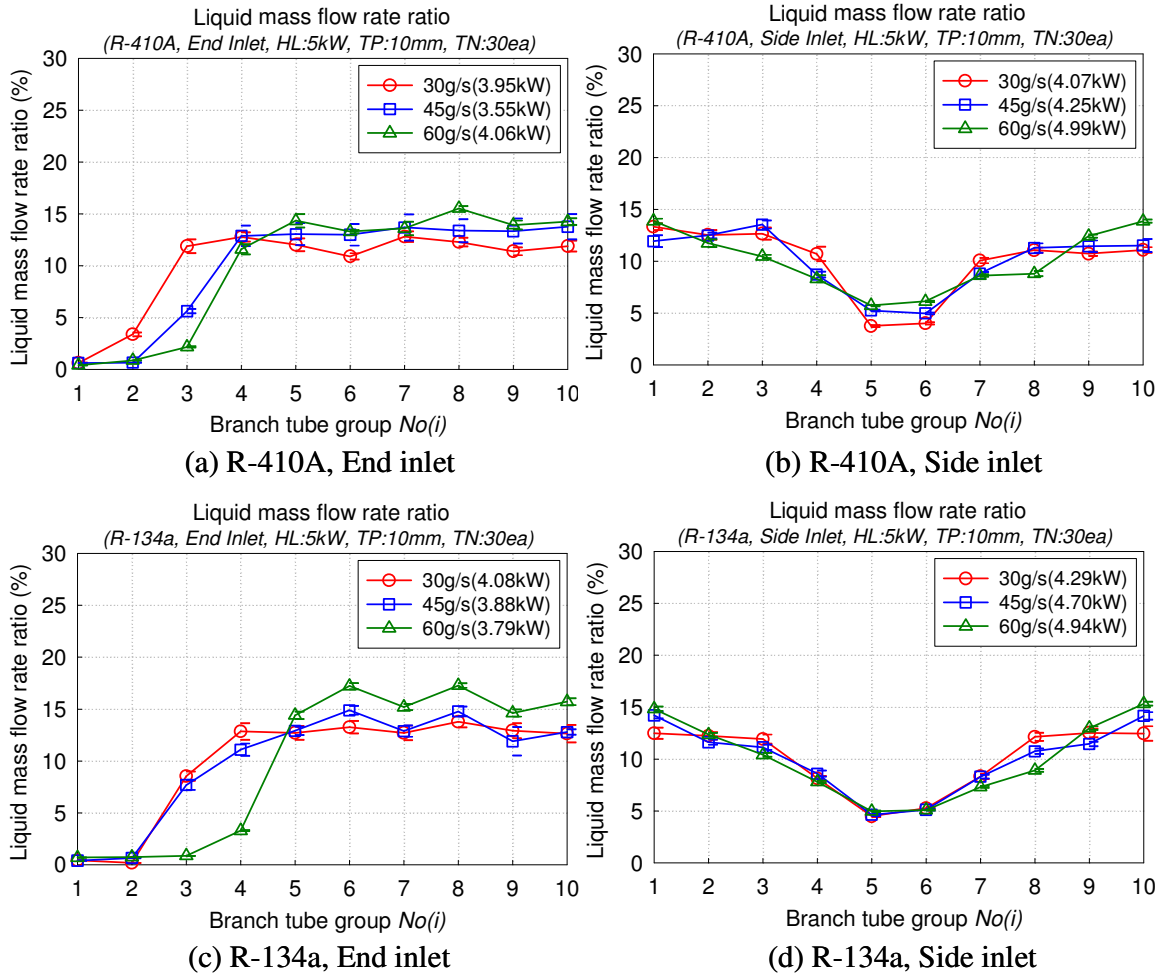


Figure 4.10 Liquid mass flow rate ratio with various manifold inlet mass flow rates with 5 kW heat load for R-410A and R-134a (Tube pitch: 10 mm, Tube group No.: 10 ea, $x_{dm,In} = 0.3$)

4.3.1.3 Pressure drop measurements

Figure 4.11 shows the pressure drop measurements along the branch tube groups at varying inlet mass flow rates with 5 kW heat load for R-410A and R-134a as a function of the branch tube group number. Figure 4.11 (a) and (b), and (c) and (d) show the pressure drop measurements along the branch tube groups for R-410A and R-134a,

respectively, as a function of the branch tube group number. Figure 4.11 shows that in overall, the pressure drop increases for the increasing manifold inlet mass flow rate.

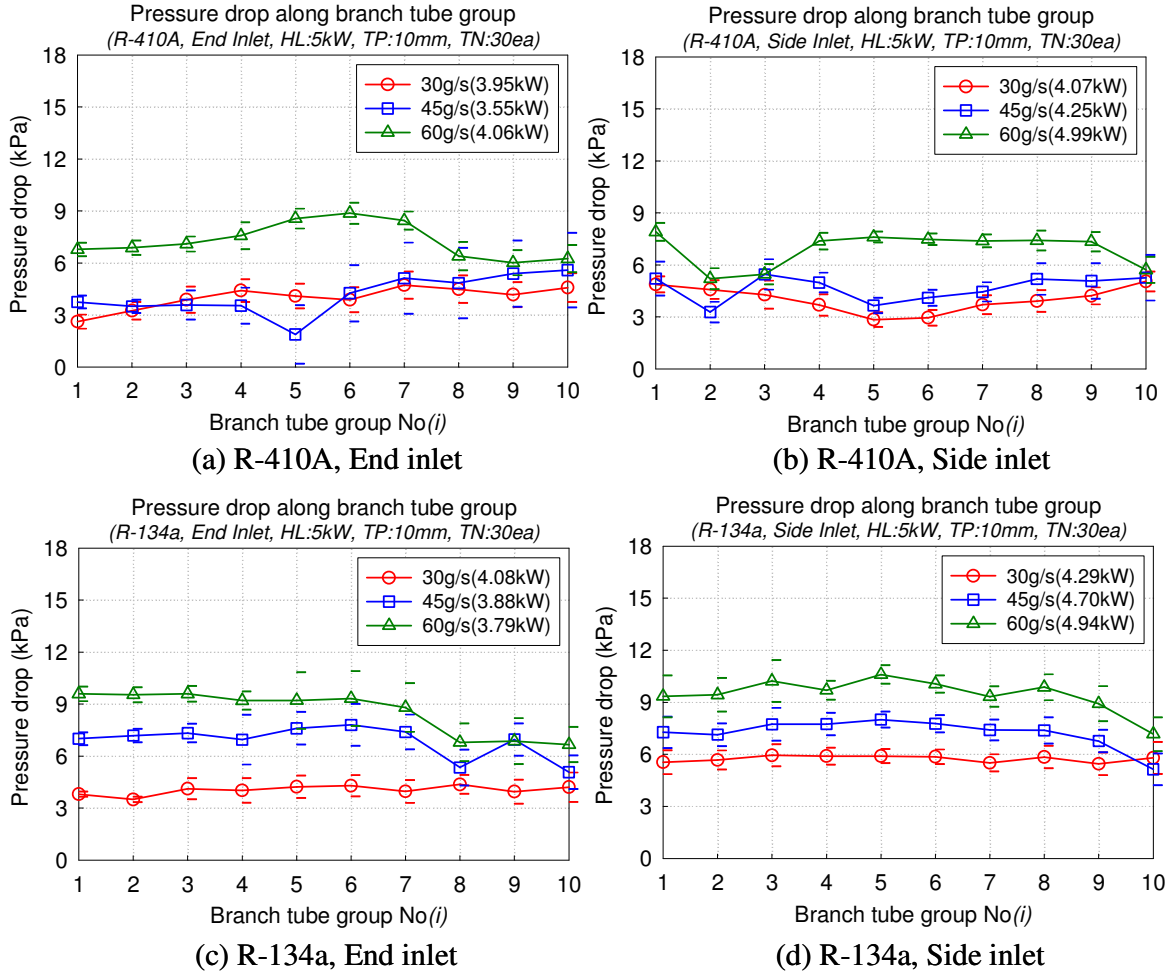


Figure 4.11 Pressure drop along the branch tube group with various manifold inlet mass flow rates with 5 kW heat load for R-410A and R-134a (Tube pitch: 10 mm, Tube group No.: 10 ea, $x_{dm,In} = 0.3$)

Figure 4.12 shows the pressure drop measurements along the dividing manifold at varying inlet mass flow rates with 5 kW heat load for R-410A and R-134a as a function of the branch tube group number. Figure 4.12 (a) and (b), and (c) and (d) show the

pressure drop measurements along the dividing manifold for R-410A and R-134a, respectively, as a function of the branch tube group number. Figure 4.12 shows that in overall, the pressures in the manifold are higher than the manifold inlet pressure due to Bernoulli effects because the mass flux along the manifold decreases due to losing mass flow rate through individual tube groups.

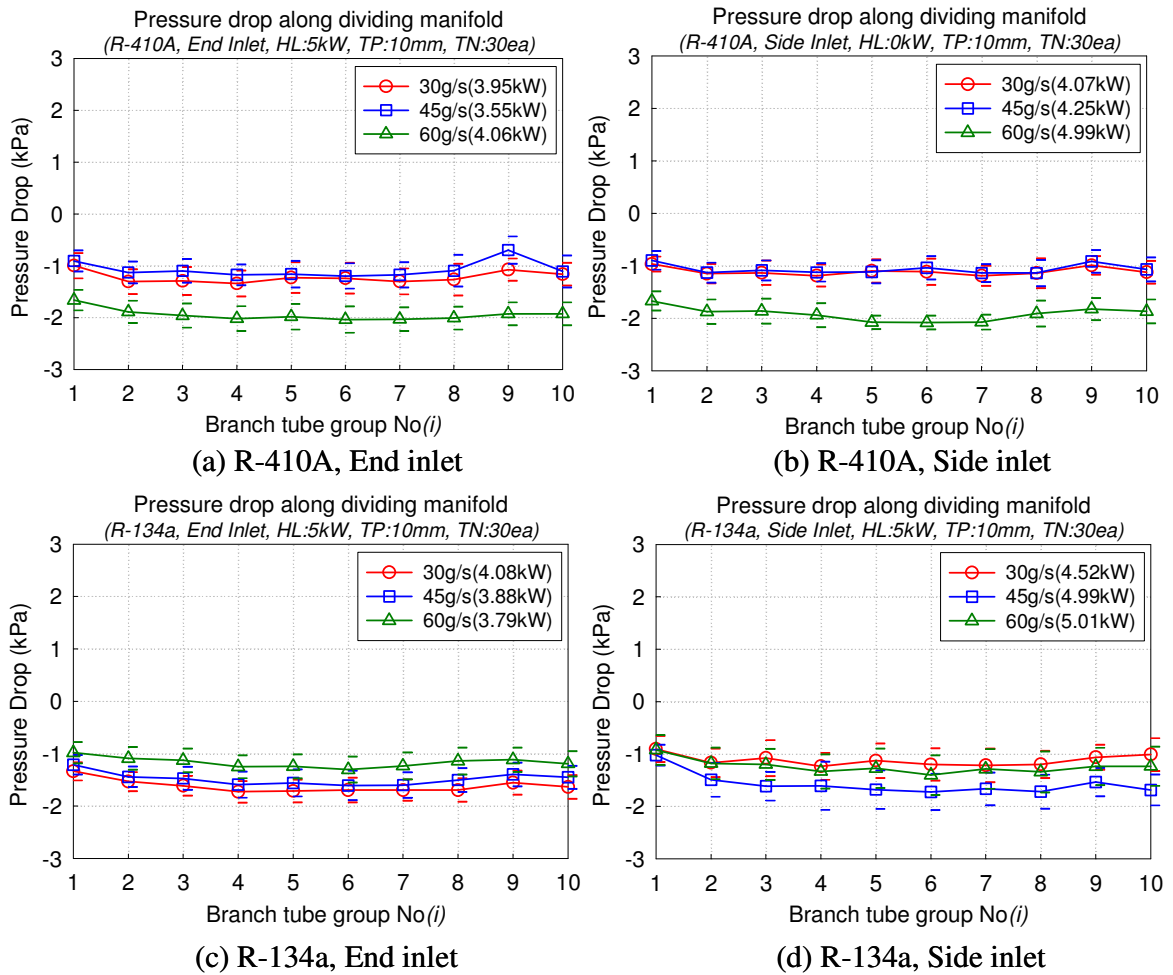


Figure 4.12 Pressure drop along the manifold with various manifold inlet mass flow rates with 5 kW heat load for R-410A and R-134a (Tube pitch: 10 mm, Tube group No.: 10 ea, $x_{dm,In} = 0.3$)

4.3.1.4 Power input and temperature measurements

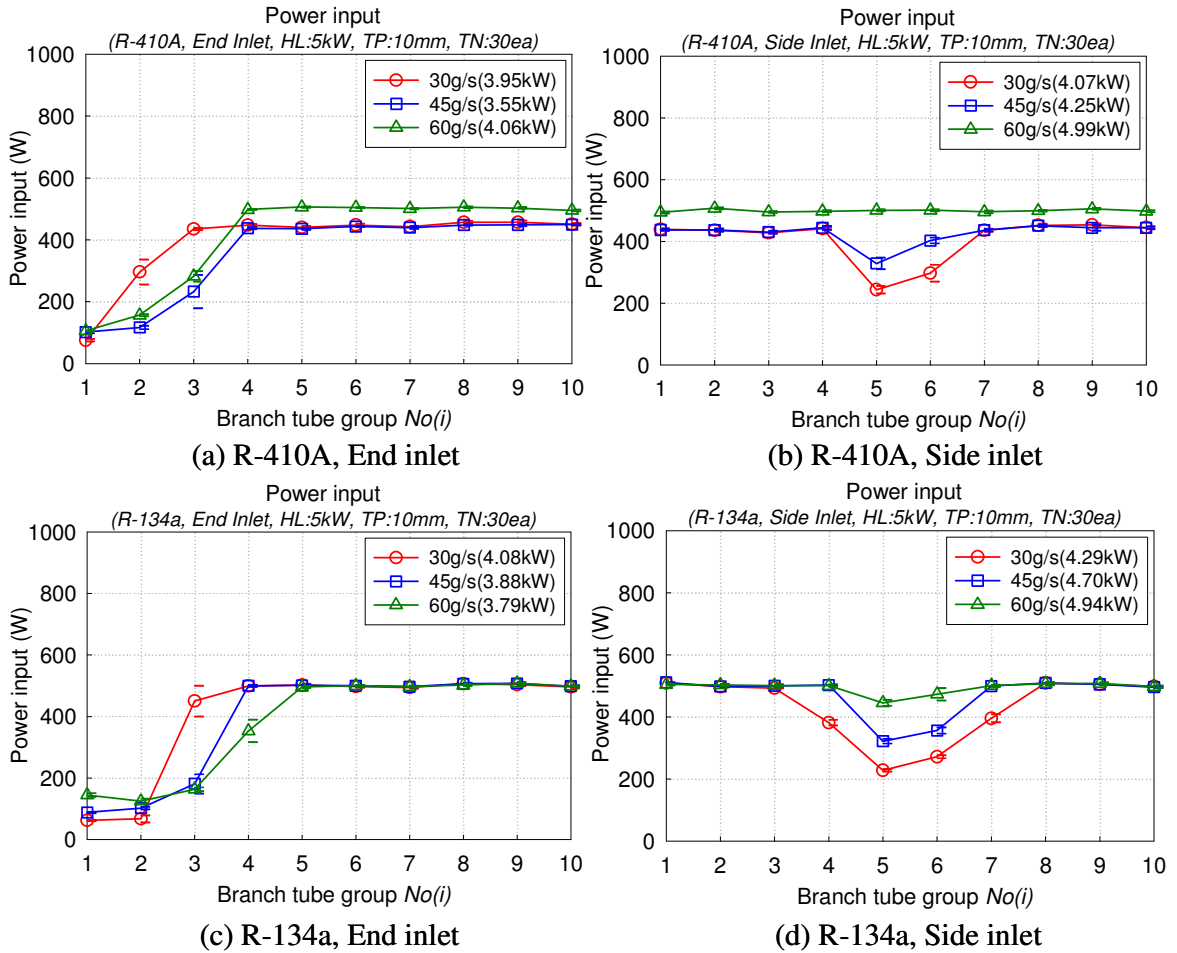


Figure 4.13 Power input with various manifold inlet mass flow rates with 5 kW heat load for R-410A and R-134a (Tube pitch: 10 mm, Tube group No: 10 ea, $x_{dm,In} = 0.3$)

Figure 4.13 shows the power input for the main heaters installed on the branch tubes at varying inlet mass flow rate with 5 kW heat load for R-410A and R-134a as a function of the branch tube group number. Figure 4.13 (a) and (b), and (c) and (d) show the power input for R-410A and R-134a, respectively, as a function of the branch tube group number. For the end inlet, the power input for the tube groups near the inlet is much lower because available cooling capacity is small due to higher branch tube inlet vapor

quality. For the side inlet, the power input for the tube groups near the inlet is lower because available cooling capacity is small due to higher branch tube inlet vapor quality. However, as the mass flow rate increases, the available cooling capacity increases. Therefore, as the mass flow rate decreases, the power input is getting smaller.

As shown in Figure 4.13, for the R-410A tests at $\dot{m}_{dm,in} = 30$ g/s and 45 g/s, the power inputs for the tube groups with lower tube inlet vapor qualities are 10% less than those for 60 g/s. This is not because of heater cut-off, but because of a different heater control scheme. In the beginning of this study, the heaters were controlled by time fraction on-off using Q-basic program to meet the test conditions because the installed heaters have 1.4 kW per tube group. Using that scheme, it's not possible to provide the exact power inputs. After conducting these four experiments, the heater control was implemented using voltage transformers for accurate control. However, as shown in section 4.3.2 (the heat load effect), this difference does not affect this parametric study.

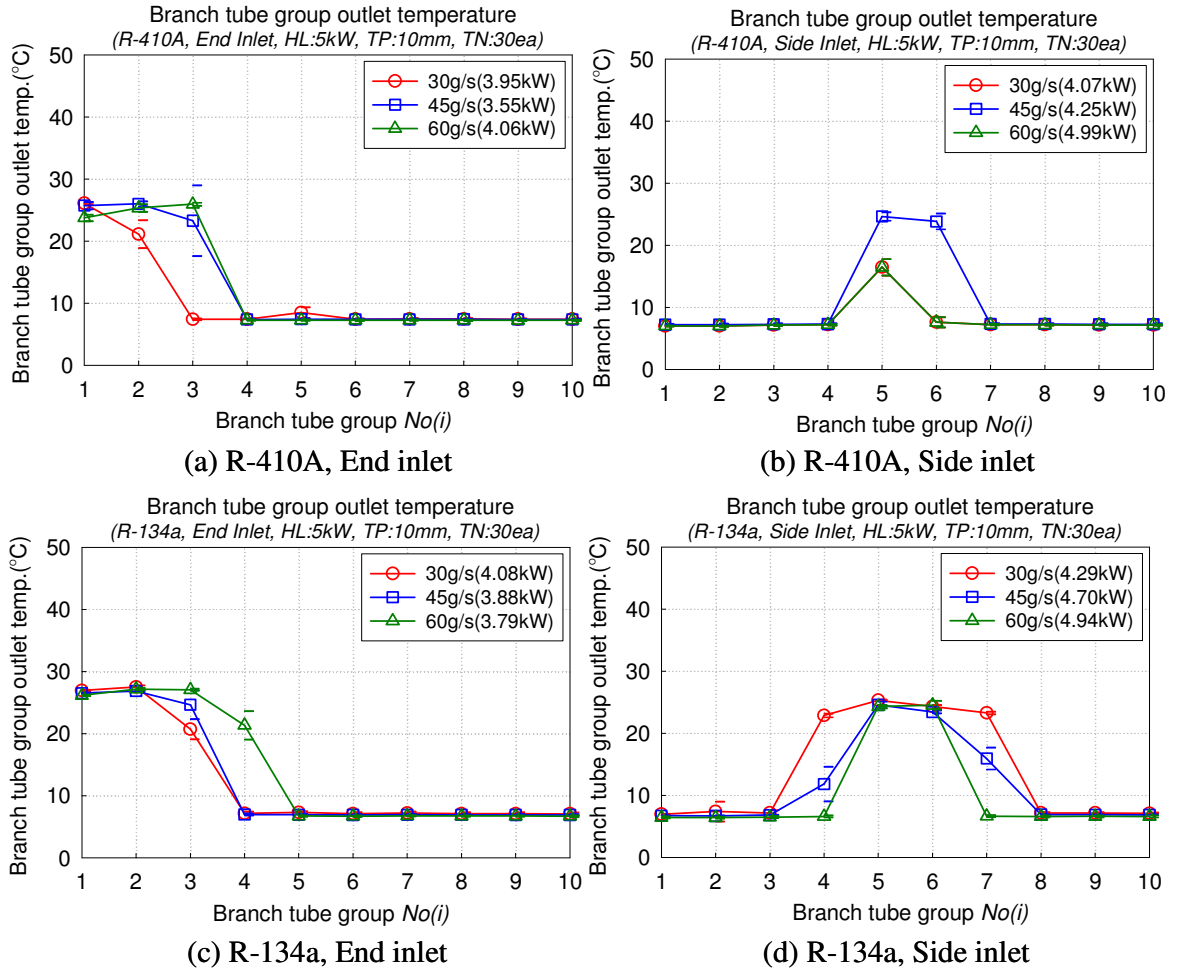


Figure 4.14 Branch tube group outlet temperature with various manifold inlet mass flow rates with 5 kW heat load for R-410A and R-134a (Tube pitch: 10 mm, Tube group No.: 10 ea, $x_{dm,In} = 0.3$)

Figure 4.14 shows the branch tube group outlet temperature at varying inlet mass flow rate with 5 kW heat load for R-410A and R-134a as a function of the branch tube group number. Figure 4.14 (a) and (b), and (c) and (d) show the branch tube group outlet temperature for R-410A and R-134a, respectively, as a function of the branch tube group number. The main heaters installed on the branch tubes were controlled by the voltage transformers and the branch tube group outlet temperature in order to simulate real heat

exchanger operating conditions. For considering ideal operating conditions, the cut-off temperature was set to 27°C, which represents the room temperature. For the end inlet, the branch tube group outlet temperatures for the tube groups near the inlet are representing cut-off temperature because of the smaller available cooling capacity due to higher branch tube inlet vapor quality. For the tube groups No. 4 through 10, the branch tube group outlet temperatures represent saturation temperature which is close to the manifold inlet temperature. For the side inlet, the branch tube group outlet temperature profile is almost symmetric depending upon the mass flow rate. In the same way, the branch tube group outlet temperature for the tube groups near the inlet represents the cut-off temperature because available cooling capacity is small due to higher branch tube inlet vapor quality. For the branch tube groups located near the ends of the manifold, the branch tube group outlet temperatures represent saturation temperature which is close to the manifold inlet temperature.

4.3.2 Effect of heat load

In this section, test results of the dividing manifold with 10 mm tube pitch and 30 tubes for R-410A are presented.

4.3.2.1 The branch tube inlet and outlet vapor quality

Figure 4.15 shows the branch tube group inlet and outlet vapor quality at varying heat load for R-410A as a function of the branch tube group number. Figure 4.15 (a) and (b), and (c) and (d) show the branch tube group inlet and outlet vapor quality for $\dot{m}_{dm,in} = 30$ g/s and 60 g/s, respectively, as a function of the branch tube group number.

The filled symbols indicate the branch tube group outlet vapor quality, and for no heat load, the outlet quality is same as the branch tube inlet vapor quality. As the heat load increases, the branch tube outlet qualities for the tube groups increase. For $\dot{m}_{dm,in} = 30$ g/s , it is shown that the outlet quality for about 5 kW heat input is approximately 100%. However, for $\dot{m}_{dm,in} = 60$ g/s , it is shown that for the end inlet with about 8 kW heat input, the outlet quality for the tube groups near the far end is still under 100%, and for the side inlet with about 9 kW heat input, the outlet quality for the tube groups located near the far end is under 100% too because available cooling capacity is large due to increased mass flow rate. For the end inlet, it is shown that the branch tube inlet vapor quality for No. 2 for $\dot{m}_{dm,in} = 30$ g/s , and the branch tube inlet vapor quality for No. 3 for $\dot{m}_{dm,in} = 60$ g/s increase with the increased heat load. Other than that, in overall, the branch tube inlet vapor quality is little affected by the heat load.

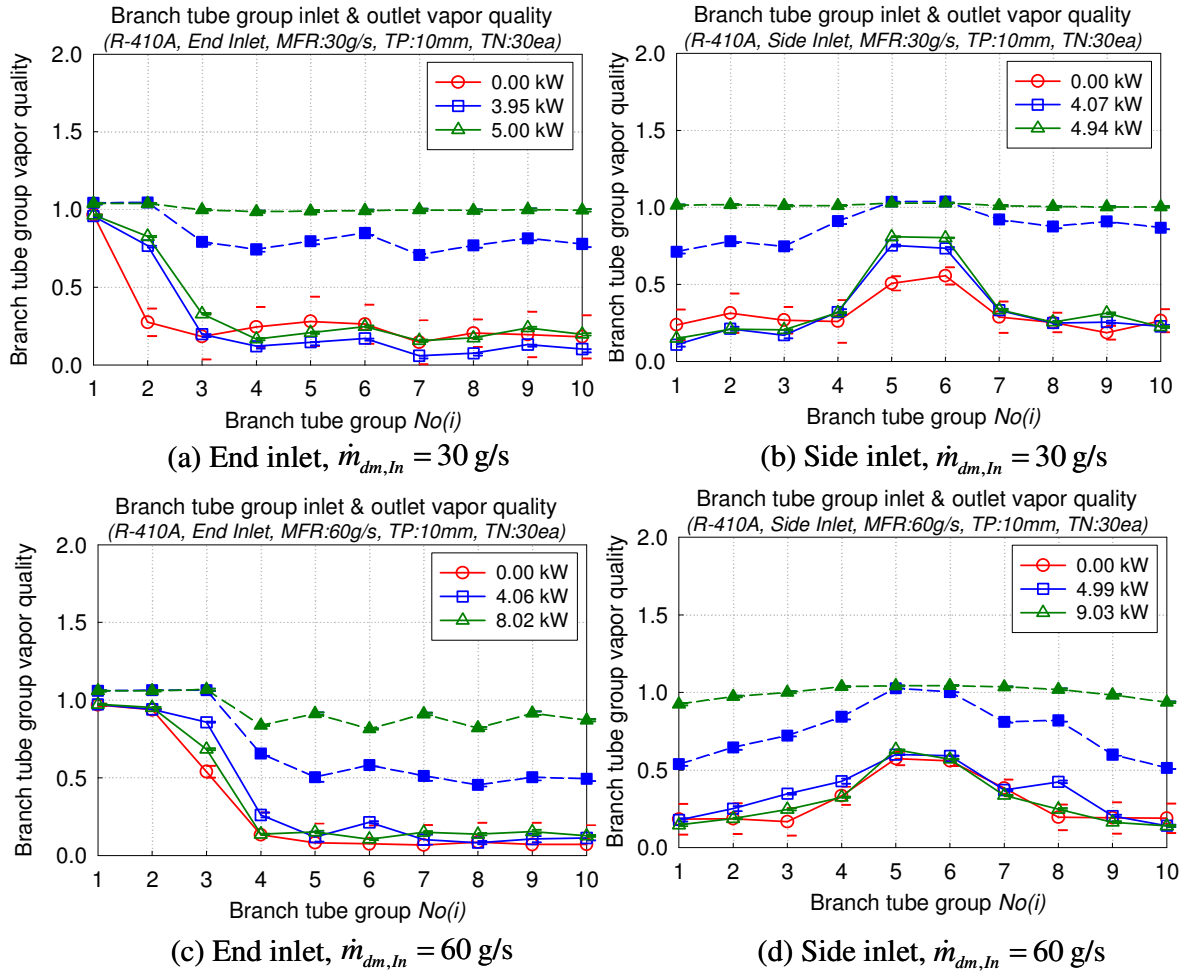


Figure 4.15 Branch tube group inlet and outlet vapor quality at varying heat load for R-410A (Tube pitch: 10 mm, Tube group No.: 10 ea, $x_{dm,In} = 0.3$)

4.3.2.2 Refrigerant distribution

Figure 4.16 shows the mass flow rate ratio at varying heat loads for R-410A as a function of the branch tube group number. Figure 4.16 (a) and (b), and (c) and (d) show the mass flow rate ratio for $\dot{m}_{dm,In} = 30 \text{ g/s}$ and 60 g/s , respectively, as a function of the branch tube group number. For both end inlet and side inlet, it is shown that as the heat load increases, the mass flow rate ratio is getting more uniform for both inlet mass flow rates.

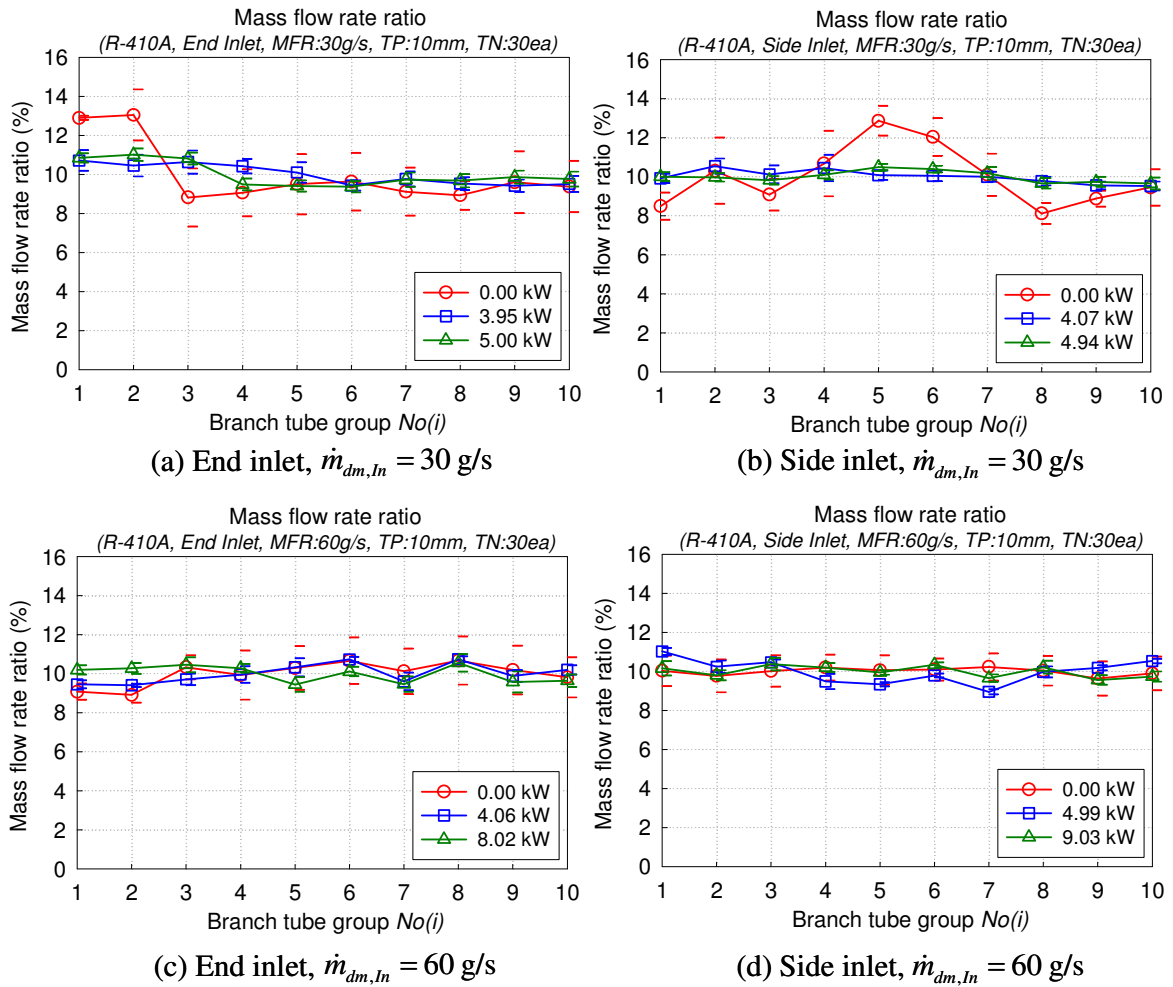


Figure 4.16 Mass flow rate ratio with various heat loads for R-410A

(Tube pitch: 10 mm, Tube group No.: 10 ea, $x_{dm,In} = 0.3$)

Figure 4.17 shows the vapor mass flow rate ratio at varying heat loads for R-410A as a function of the branch tube group number. Figure 4.17 (a) and (b), and (c) and (d) show the vapor mass flow rate ratio for $\dot{m}_{dm,ln} = 30$ g/s and 60 g/s, respectively, as a function of the branch tube group number. The trend reflects the vapor inlet quality distribution. For the end inlet, it can be seen that for $\dot{m}_{dm,ln} = 30$ g/s, approximately 50 ~ 65% of the manifold inlet vapor mass flow rate is flowing through the first two branch tube groups near the inlet depending upon the heat load. In addition, for $\dot{m}_{dm,ln} = 60$ g/s, about 80% of the manifold inlet vapor mass flow rate is flowing through the first three branch tube groups near the inlet depending upon the heat load. For the side inlet, it is shown that for $\dot{m}_{dm,ln} = 30$ g/s, about 60 ~ 65% of the manifold inlet vapor mass flow rate is flowing through the four branch tube groups near the inlet, and for $\dot{m}_{dm,ln} = 60$ g/s, about 50 ~ 60% of the manifold inlet vapor mass flow rate is flowing through the four branch tube groups near the inlet depending upon the heat load.

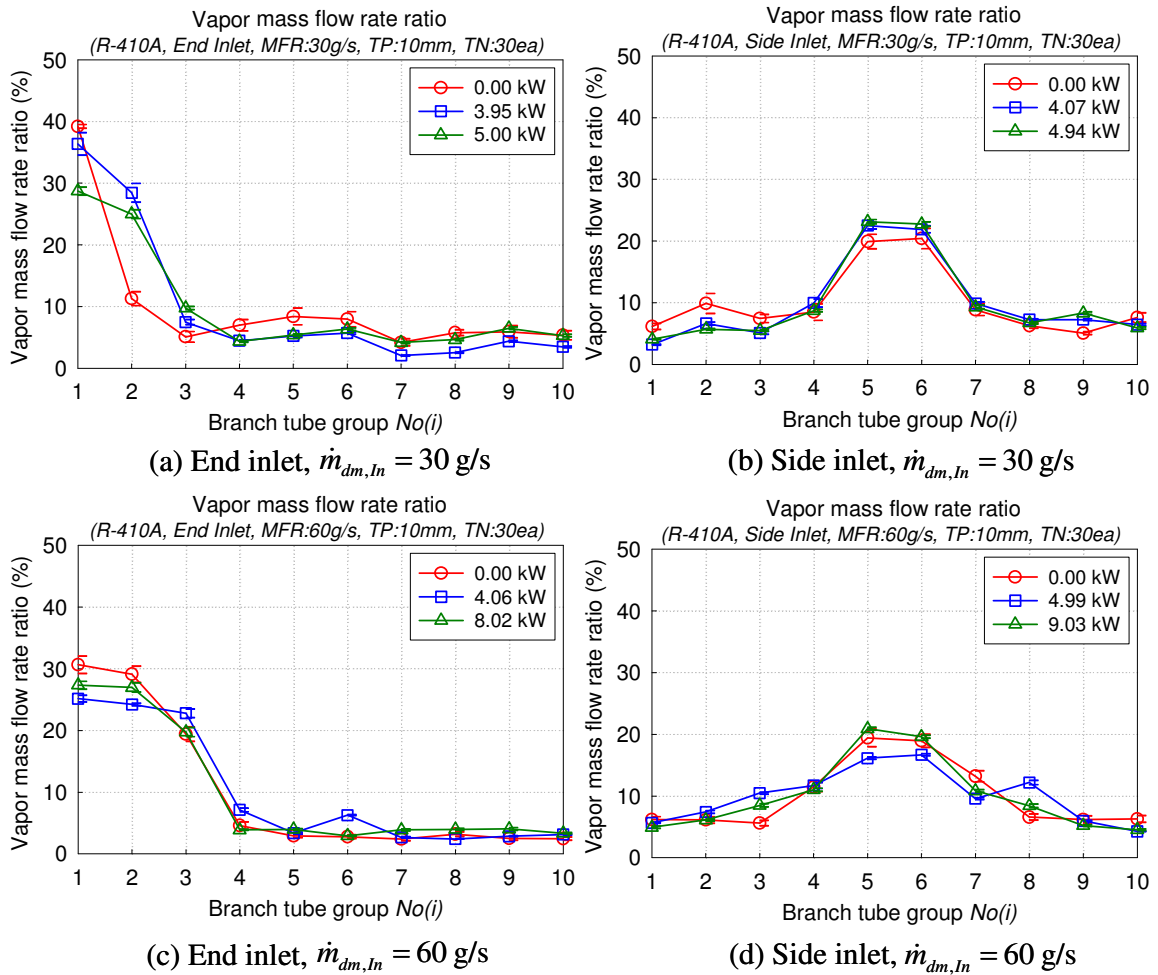


Figure 4.17 Vapor mass flow rate ratio with various heat loads for R-410A

(Tube pitch: 10 mm, Tube group No.: 10 ea, $x_{dm,In} = 0.3$)

Figure 4.18 shows the liquid mass flow rate ratio at varying heat load for R-410A as a function of the branch tube group number. Figure 4.18 (a) and (b), and (c) and (d) show the liquid mass flow rate ratio for $\dot{m}_{dm,ln} = 30 \text{ g/s}$ and 60 g/s , respectively, as a function of the branch tube group number. For $\dot{m}_{dm,ln} = 30 \text{ g/s}$, the liquid mass flow rate ratio for the branch tube groups near the inlet decreases as the heat load increases up to a certain heat load, and beyond the heat load, the liquid mass flow rate ratio is insignificantly affected by the heat load. This can be explained by the pressure drop variation along the branch tubes. As shown in section 4.3.2.3, Figure 4.19 clearly shows that as the heat load increases up to a certain heat load, the pressure drop along the branch tube group drastically decreases, and with the additional increasing heat load, the pressure drop variation is getting smaller. Therefore, the liquid is traveling farther with the increased heat load due to the reduced resistance through the branch tube groups. However, for $\dot{m}_{dm,ln} = 60 \text{ g/s}$, the variation of the liquid mass flow rate for the varying heat load is less than that for $\dot{m}_{dm,ln} = 30 \text{ g/s}$. In Figure 4.19, it is shown that the pressure drop variation with the varying heat load is less than that for $\dot{m}_{dm,ln} = 30 \text{ g/s}$.

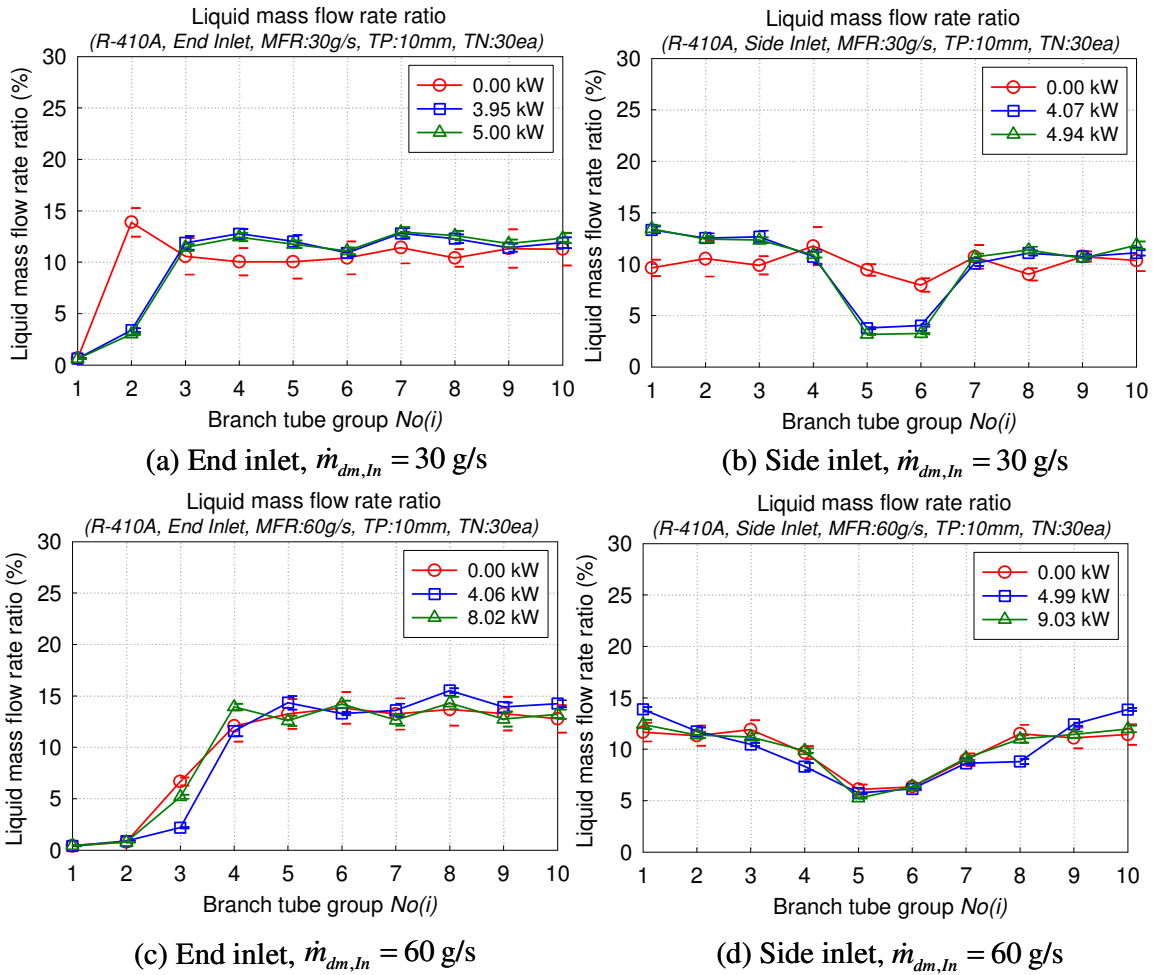


Figure 4.18 Liquid mass flow rate ratio with various heat loads for R-410A
 (Tube pitch: 10 mm, Tube group No.: 10 ea, $x_{dm,ln} = 0.3$)

4.3.2.3 Pressure drop measurements

Figure 4.19 shows the pressure drop measurements along the branch tube groups at varying heat load for R-410A and R-134a as a function of the branch tube group number. Figure 4.19 (a) and (b), and (c) and (d) show the pressure drop along the branch tube group for $\dot{m}_{dm,In} = 30$ g/s and 60 g/s, respectively, as a function of the branch tube group number. As shown in Figure 4.19, the pressure drop profile for the side inlet is almost symmetric. In Figure 4.19, especially the pressure drop along the branch tube groups near the manifold inlet is smaller than that for other branch tube groups because of the smaller gravitational effect due to the higher inlet vapor quality. Based on the calculation, the pressure drop for the branch tube groups located near the far end, which means the branch tube groups with lower vapor quality, is almost similar to the pressure drop calculated from a liquid column with the same height as that for the heat exchanger. It is clearly shown that as heat load increases, the pressure drop decreases due to the reduced gravity effect because the vapor quality along the branch tube increases as shown in the section 4.4.1. For the higher mass flow rate, the effect of the heat load on the pressure drop is less than that for the lower mass flow rate.

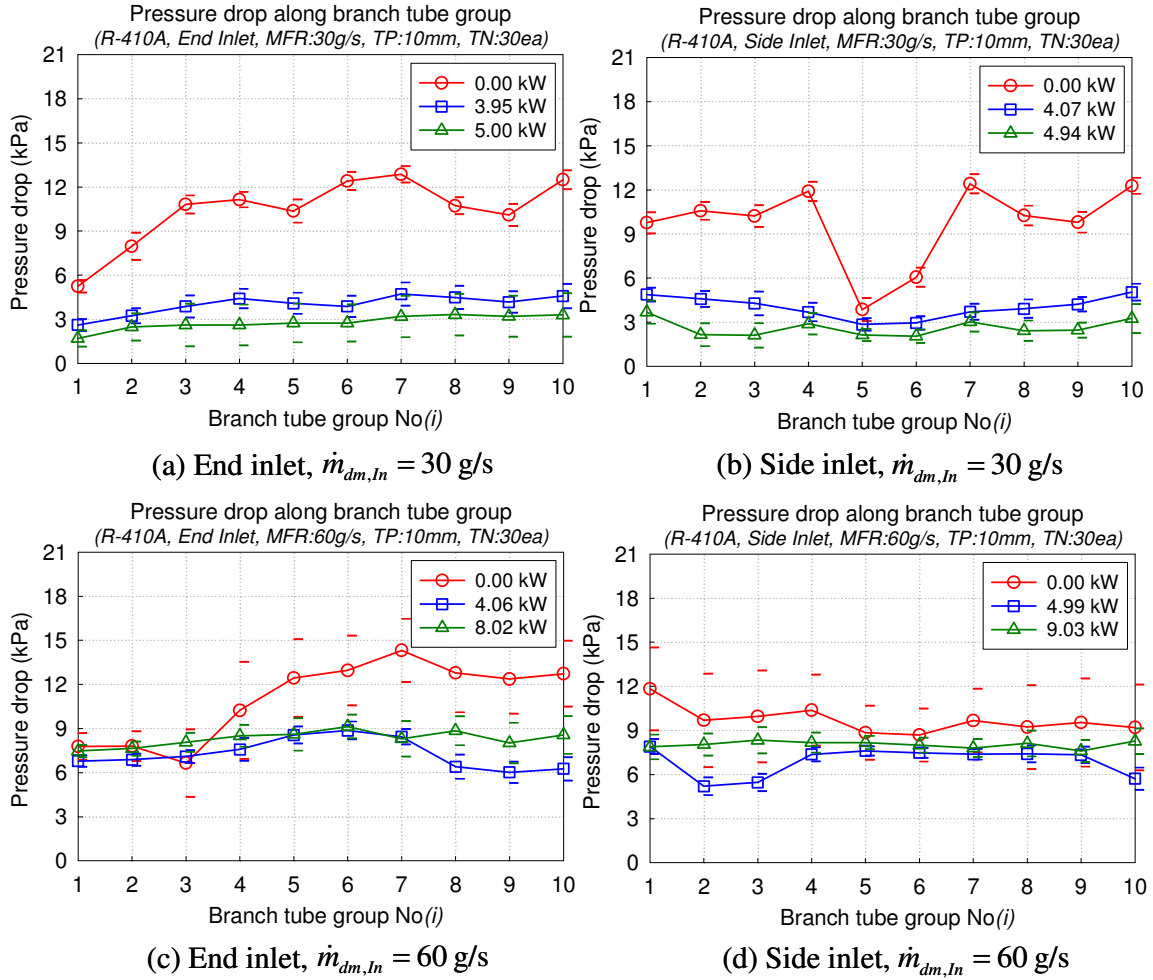


Figure 4.19 Pressure drop along the branch tube group at varying heat load for R-410A (Tube pitch: 10 mm, Tube group No.: 10 ea, $x_{dm,In} = 0.3$)

4.3.2.4 Power input and temperature measurements

Figure 4.20 shows the power input for the main heaters at varying heat load for R-410A as a function of the branch tube group number. Figure 4.20 (a) and (b), and (c) and (d) show the power input for $\dot{m}_{dm,In} = 30$ g/s and 60 g/s, respectively, as a function of the branch tube group number. For both inlet mass flow rates, the maximum intentional power input was 10 kW, but for $\dot{m}_{dm,In} = 30$ g/s, the power input was reduced by

temperature control because of less cooling capacity due to smaller mass flow rate compared to 60 g/s. For 60 g/s, the actual power input is about 8 ~ 9 kW depending upon the inlet position because of the temperature control. As explained earlier, the power input for the branch tube groups near the inlet is less than that for those located at far end due to higher inlet vapor quality.

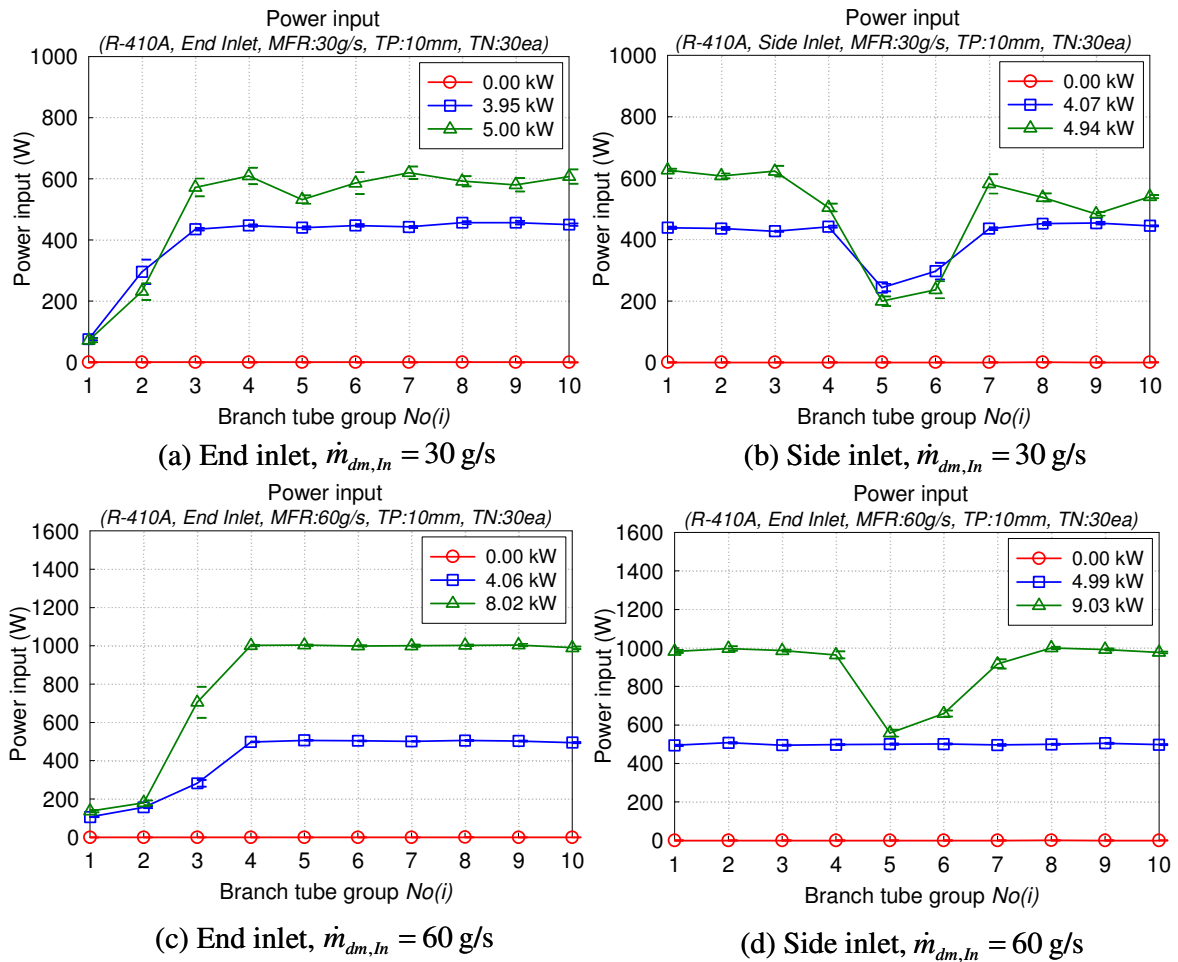


Figure 4.20 Power input with various heat loads for R-410A

(Tube pitch: 10 mm, Tube group No.: 10 ea, $x_{dm} = 0.3$)

Figure 4.21 shows the branch tube group outlet temperature at varying heat load for R-410A as a function of the branch tube group number. Figure 4.21 (a) and (b), and (c) and (d) show the branch tube group outlet temperature for $\dot{m}_{dm,ln} = 30$ g/s and 60 g/s, respectively, as a function of the branch tube group number. As shown in Figure 4.21, for $\dot{m}_{dm,ln} = 30$ g/s, the branch tube group outlet temperature with about 5 kW heat input is above 20°C, which represents superheated vapor at the outlet of the branch tube. With less power input, the branch tube group outlet temperature near the far end represents saturation temperature. For $\dot{m}_{dm,ln} = 60$ g/s, the branch tube group outlet temperature near the far end represents saturation temperature even though the provided total power input is about 8 ~ 9 kW depending upon inlet position because of the larger cooling capacity due to higher mass flow rate compared to inlet mass flow rate 30 g/s.

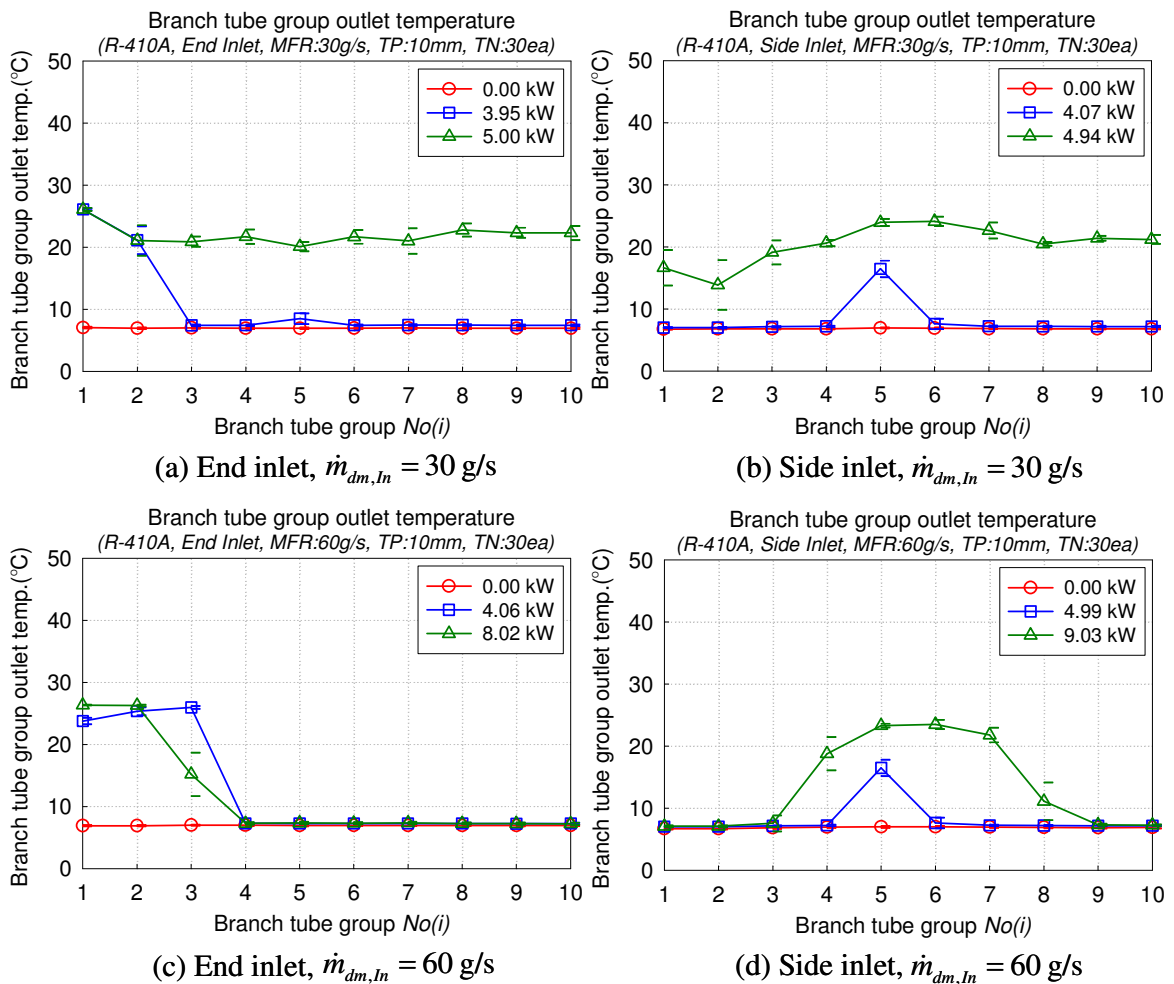


Figure 4.21 Branch tube group outlet temperature with various heat loads for R-410A (Tube pitch: 10 mm, Tube group No.: 10 ea, $x_{dm,In} = 0.3$)

4.3.3 Effect of manifold inlet vapor quality

In this section, test results of the dividing manifold with 10 mm tube pitch and 30 tubes at varying manifold inlet vapor quality for R-134a, $\dot{m}_{dm,In} = 45 \text{ g/s}$, and the end inlet are presented.

4.3.3.1 The branch tube inlet and outlet vapor quality

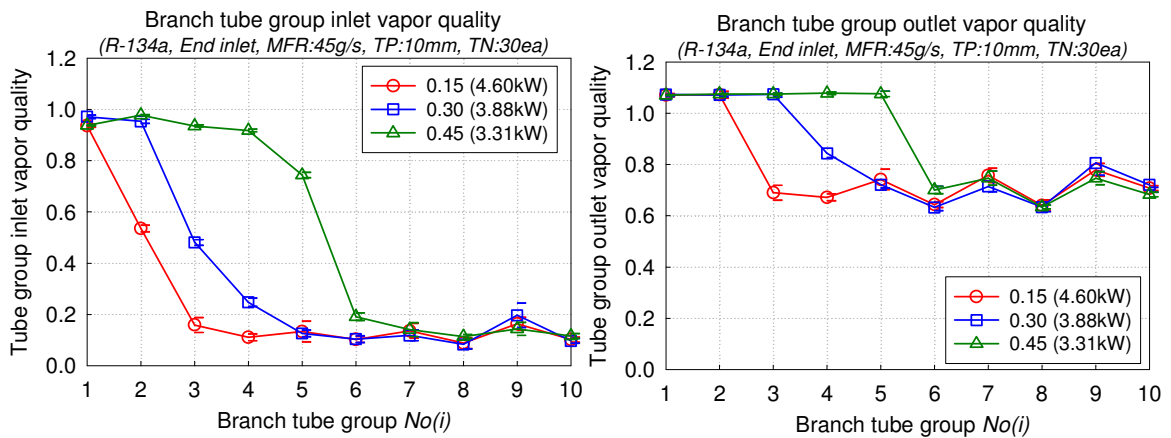


Figure 4.22 Branch tube group inlet and outlet vapor quality at varying inlet quality for R-134a with the end inlet (Tube pitch: 10 mm, Tube group No.: 10 ea, $\dot{m}_{dm,In} = 45 \text{ g/s}$)

Figure 4.22 shows the branch tube group inlet and outlet vapor quality at varying manifold inlet vapor quality for R-134a, $\dot{m}_{dm,In} = 45 \text{ g/s}$, and the end inlet as a function of the branch tube group number. As shown in Figure 4.22, the vapor phase is distributed into the first tube groups, and the liquid phase is distributed into the tube groups close to the end of the manifold. As the manifold inlet vapor quality increases, the number of branch tube groups with higher inlet vapor quality, which is close to 100%, is increasing because the vapor-liquid interface is moving farther towards the end of the manifold

because of the increased vapor momentum due to the increased vapor fraction with the fixed manifold inlet mass flow rate. For the manifold inlet vapor quality 0.45, the outlet vapor quality for the tube group No. 1 through 5 is above 100%, which means that superheated vapor is flowing out of the tube groups because of the smaller cooling capacity due to the higher branch tube inlet vapor quality. For the tube group No. 6 through 10, the branch inlet vapor quality is less than 20%, and the outlet vapor quality is around 70%.

4.3.3.2 Refrigerant distribution

Figure 4.23 shows the mass flow rate ratio at varying inlet vapor quality for R-134a, $\dot{m}_{dm,ln} = 45 \text{ g/s}$, and the end inlet as a function of the branch tube group number. In Figure 4.23, for the inlet vapor quality 0.15, the mass flow rate ratio for the tube group No. 3 through 4 is a little higher than that for other inlet qualities. For the inlet vapor quality 0.45, the mass flow rate ratio for the tube group No. 6 and 8 is a little higher than that for other inlet qualities. Other than that, in overall, the mass flow rate ratio profiles for the inlet vapor qualities show the same trend.

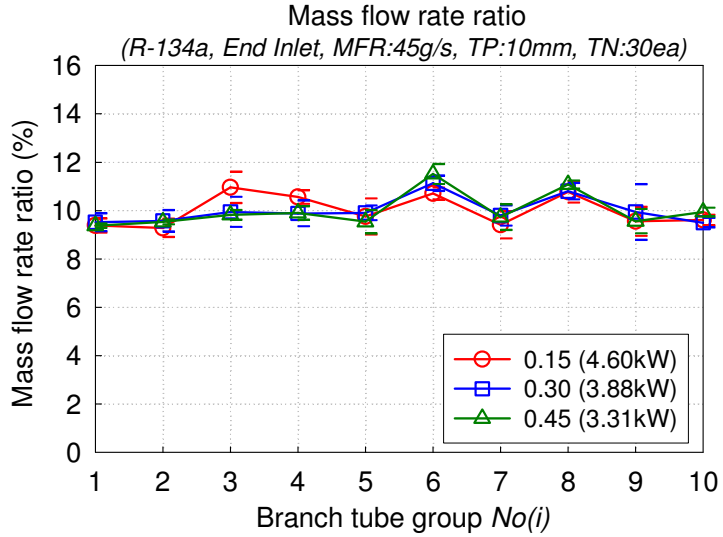


Figure 4.23 Mass flow rate ratio at varying inlet quality for R-134a, end inlet

(Tube pitch: 10 mm, Tube group No.: 10 ea, $\dot{m}_{dm,ln} = 45 \text{ g/s}$)

Figure 4.24 shows the vapor and liquid mass flow rate ratio at varying inlet vapor quality for R-134a, $\dot{m}_{dm,ln} = 45 \text{ g/s}$, and the end inlet as a function of the branch tube group number. At increasing inlet vapor quality, the liquid mass flow rate ratio in the branch tube group No. 6 through 10 increases. For the inlet quality 0.15, it can be seen that about 55% vapor mass flow rate of the manifold inlet vapor mass flow rate is flowing through the first two branch tube groups near the inlet. For the inlet quality 0.45, it can be seen that about 70% vapor mass flow rate of the manifold inlet vapor mass flow rate is flowing through the first four branch tube groups near the inlet. In addition, for the inlet quality, about 75% liquid mass flow rate of the manifold inlet liquid mass flow rate is flowing through the tube group No. 6 through 10.

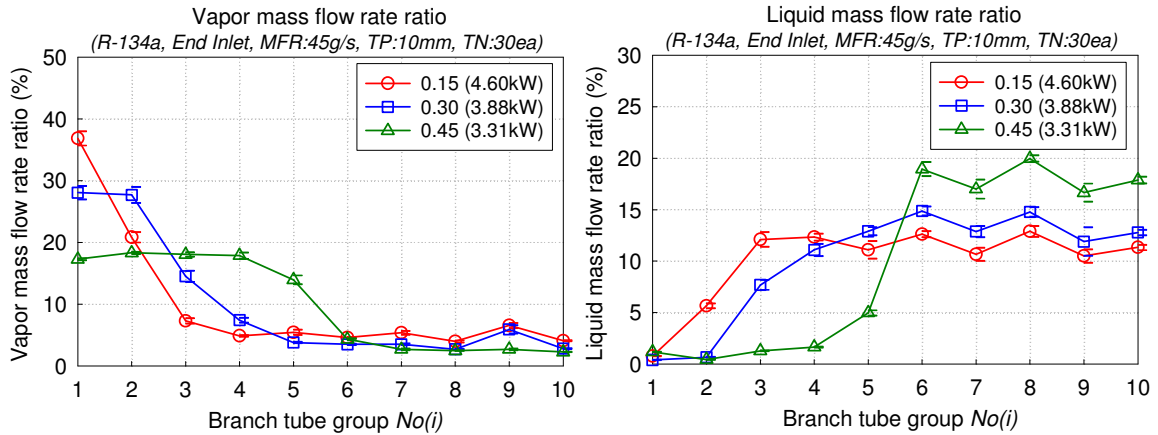


Figure 4.24 Vapor and liquid mass flow rate ratio at varying inlet quality for R-134a with the end inlet (Tube pitch: 10 mm, Tube group No: 10 ea, $\dot{m}_{dm,in} = 45$ g/s)

4.3.3.3 Pressure drop measurements

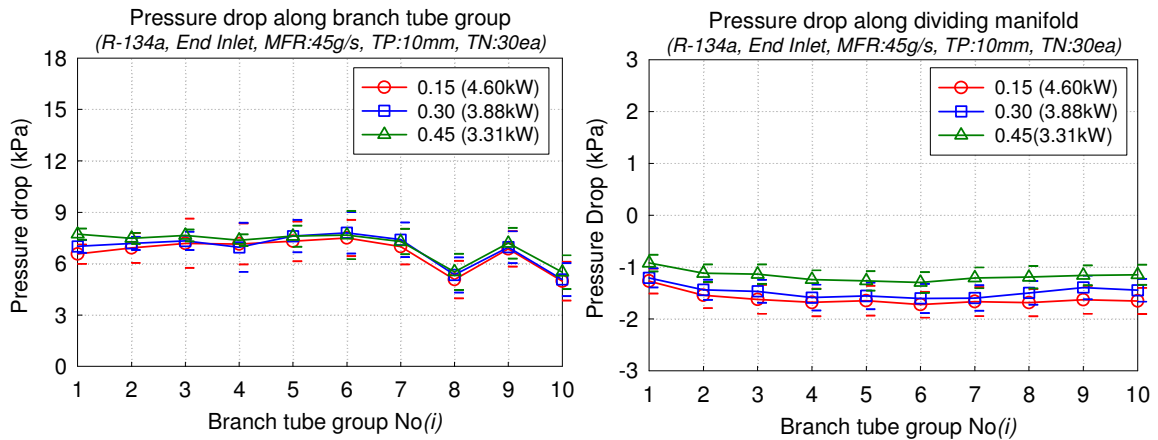


Figure 4.25 Pressure drops along the branch tube groups and the manifold at varying inlet quality for R-134a, end inlet

(Tube pitch: 10 mm, Tube group No.: 10 ea, $\dot{m}_{dm,in} = 45$ g/s)

Figure 4.25 shows the pressure drop measurements along the branch tube groups and the dividing manifold, respectively at varying manifold inlet vapor quality for R-134a, $\dot{m}_{dm,in} = 45$ g/s, and the end inlet as a function of the branch tube group number. As

shown in Figure 4.25, the pressure drop along the branch tube group is affected insignificantly by the inlet vapor quality. As explained earlier in section 4.3.1.3, for the pressure drop along the dividing manifold, it is shown that the pressure in the manifold is higher than the manifold inlet pressure.

4.3.3.4 Power input and temperature measurements

Figure 4.26 shows the power input for the main heaters and the branch tube outlet temperature at varying inlet vapor quality for R-134a, $\dot{m}_{dm,In} = 45 \text{ g/s}$, and the end inlet as a function of the branch tube group number. As manifold inlet vapor quality increases, the number of the branch tube groups with the lower power input is increasing because of less cooling capacity due to the higher manifold inlet vapor quality. In the same way, as manifold inlet vapor quality increases, the number of the branch tube groups with the cut-off temperature is increasing.

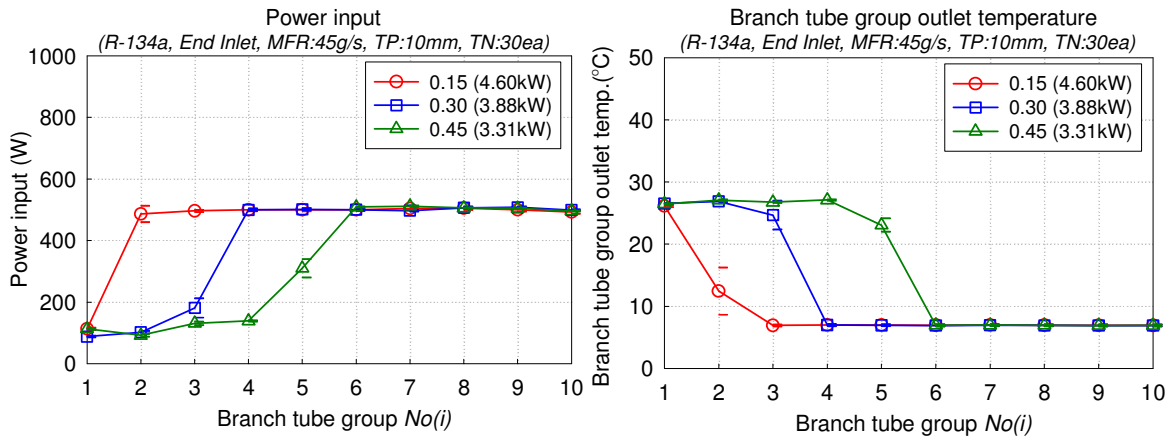


Figure 4.26 Power input and the branch tube outlet temperature with varying inlet quality for R-134a, end inlet

(Tube pitch: 10 mm, Tube group No: 10 ea, $\dot{m}_{dm,In} = 45 \text{ g/s}$)

4.3.4 Effect of branch tube number (Manifold length with fixed tube pitch)

In this section, test results of the dividing manifold with 10 mm tube pitch at varying branch tube number, which means varying manifold length with fixed tube pitch, for R-410A are described. As shown in Figures 3.4 and 3.5, the branch tube number (or manifold length) with fixed tube pitch was adjusted by blocking a certain number of the branch tubes using dead blocks. In Figure 4.27, TN30, TN24 and TN18 represent that the number of tubes is 30, 24 and 18, respectively. In addition, 30, 24 and 18 tubes represent 10, 8 and 6 tube groups, respectively.

4.3.4.1 The branch tube inlet and outlet vapor quality

Figure 4.27 shows the branch tube group inlet vapor quality with various branch tube numbers (or various manifold lengths) for R-410A and 5 kW heat load as a function of the branch tube group number. Figure 4.27 (a) and (b), and (c) and (d) show the branch tube inlet vapor quality for $\dot{m}_{dm,in} = 30$ g/s and 55 g/s, respectively, as a function of the branch tube group number. As shown in the Figure, for the reduced branch tube numbers (or for the reduced manifold length), in overall, the vapor quality profile for both inlet locations is similar to that for the 30 tubes (10 tube groups, which is base line). For the end inlet, the vapor phase is distributed into the first tube groups, and the liquid phase is distributed into the tube groups close to the end of the manifold. In addition, for the side inlet, the inlet vapor quality profile is almost symmetric, and the inlet vapor quality near the inlet is higher than that for the branch tube groups located close to the ends of the manifold.

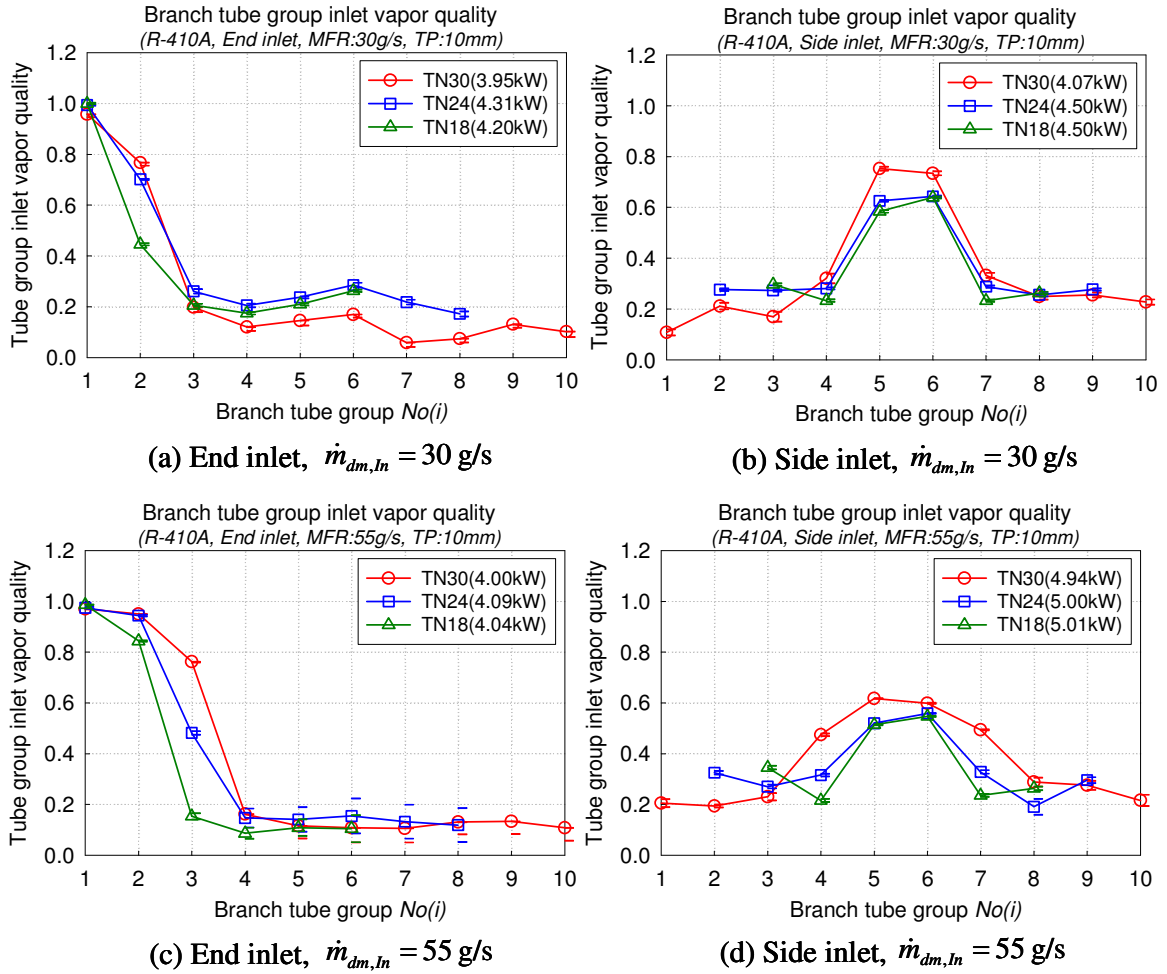


Figure 4.27 Branch tube group inlet vapor quality with various branch tube group number (or various manifold lengths) for R-410A (Tube pitch: 10 mm, Heat load: 5 kW)

4.3.4.2 Refrigerant distribution

Figure 4.28 shows the mass flow rate ratio with various branch tube numbers (or various manifold lengths) for R-410A and 5 kW heat load as a function of the branch tube group number. Figure 4.28 (a) and (b), and (c) and (d) show the mass flow rate ratio for $\dot{m}_{dm,in} = 30 \text{ g/s}$ and 55 g/s , respectively, as a function of the branch tube group number. As can be expected for both inlet cases, it is shown that as branch tube number decreases,

the mass flow rate ratio increases because of the reduced tube number for the fixed manifold inlet mass flow rate. For $\dot{m}_{dm,in} = 55 \text{ g/s}$ with the end inlet, it is shown that for the reduced tube numbers, the mass flow rate ratio for the tube groups close to the end of manifold is higher than that for the tube groups near the inlet.

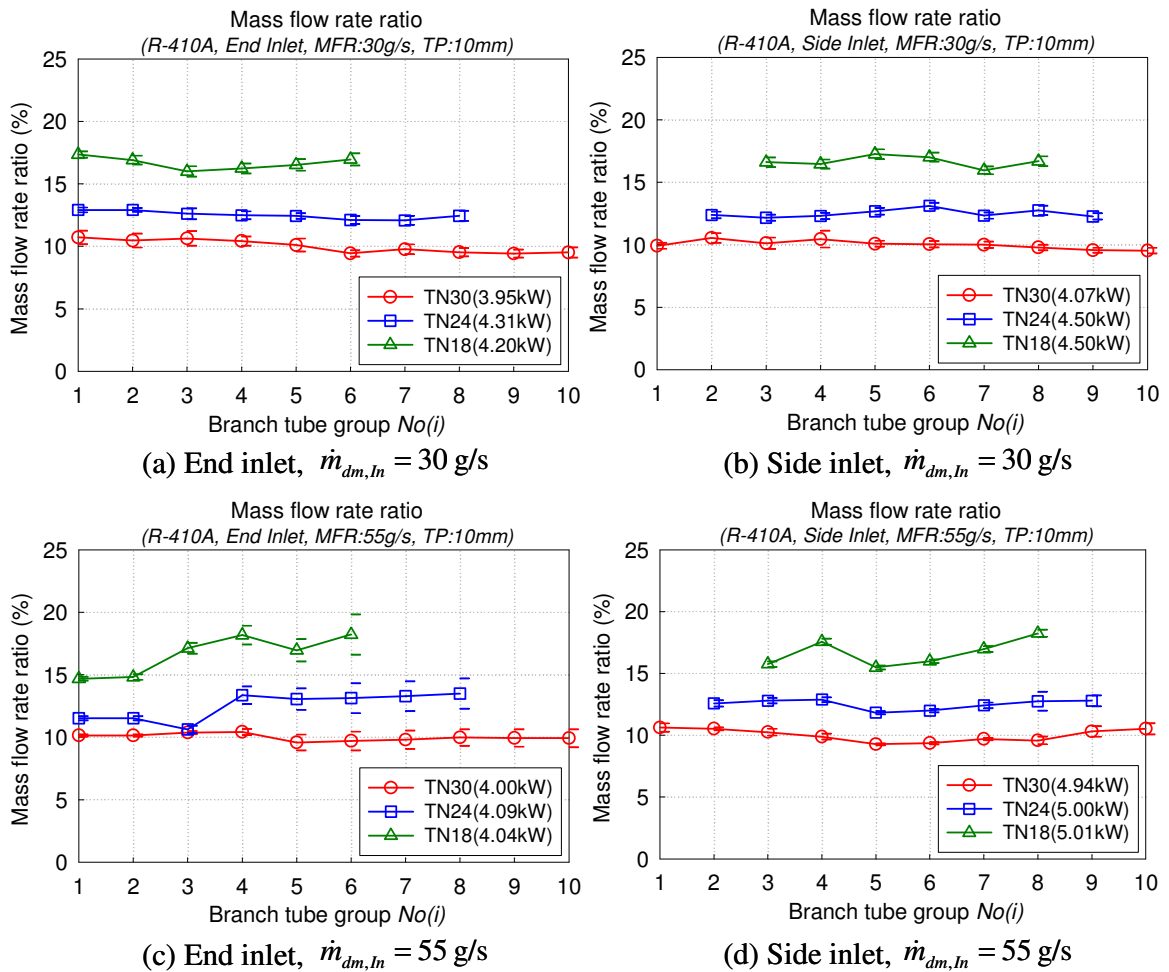


Figure 4.28 Mass flow rate ratio with various branch tube group numbers for R-410A (Tube pitch: 10 mm, Heat load: 5 kW)

Figure 4.29 shows the vapor mass flow rate ratio with various branch tube numbers (or various manifold lengths) for R-410A and 5 kW heat load as a function of the branch

tube group number. Figure 4.29 (a) and (b), and (c) and (d) show the vapor mass flow rate ratio for $\dot{m}_{dm,In} = 30$ g/s and 55 g/s, respectively, as a function of the branch tube group number. In overall, as the branch tube number decreases, the vapor mass flow rate ratio increases, especially for the branch tube groups near the inlet.

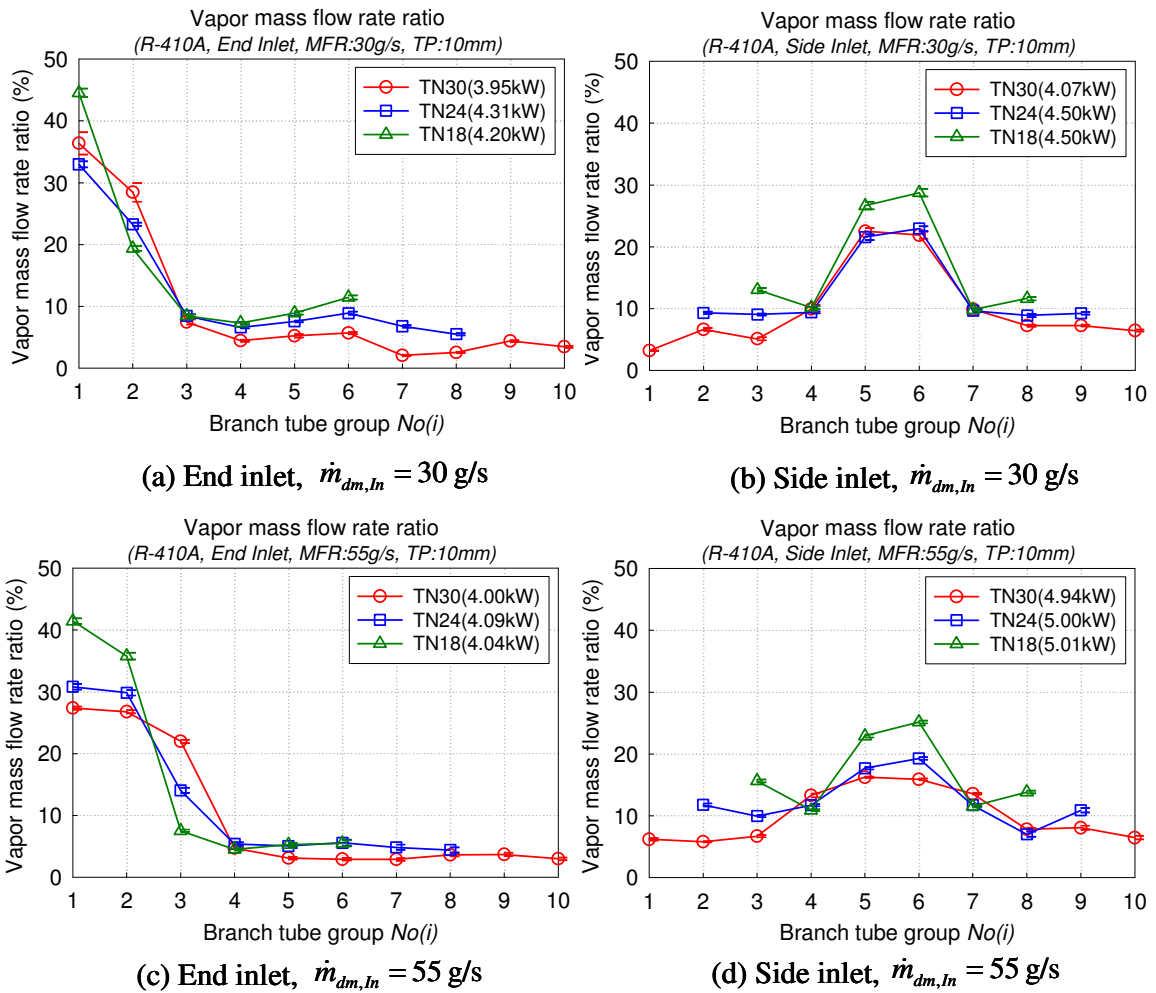


Figure 4.29 Vapor mass flow rate ratio with various branch tube group numbers for R-410A (Tube pitch: 10 mm, Heat load: 5 kW)

Figure 4.30 shows the normalized vapor mass flow rate ratio using Equation 4.3 with various branch tube numbers (or various manifold lengths) for R-410A and 5 kW heat

load as a function of the branch tube group number. Figure 4.30 (a) and (b), and (c) and (d) show the normalized vapor mass flow rate ratio for $\dot{m}_{dm,In} = 30$ g/s and 55 g/s, respectively, as a function of the branch tube group number. In Figure 4.30, the unity indicates equal distribution. Based on that, it is shown that maldistribution of the vapor is more severe for the 30 tubes than that for other tube numbers.

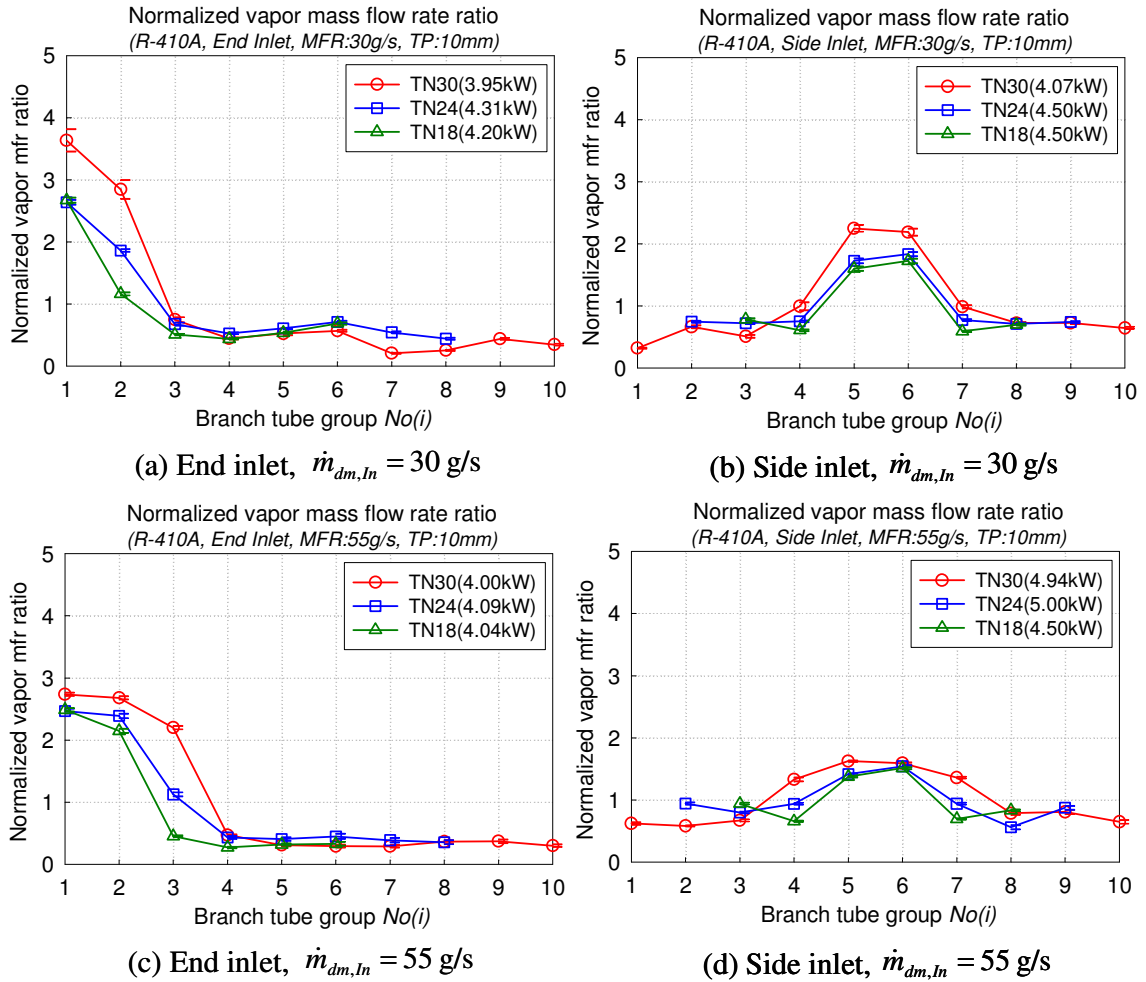


Figure 4.30 Normalized vapor mass flow rate ratio with various branch tube group numbers for R-410A (Tube pitch: 10 mm, Heat load: 5 kW)

Figure 4.31 shows the liquid mass flow rate ratio with various branch tube numbers (or various manifold lengths) for R-410A and 5 kW heat load as a function of the branch tube group number. Figure 4.31 (a) and (b), and (c) and (d) show the liquid mass flow rate ratio for $\dot{m}_{dm,In} = 30$ g/s and 55 g/s, respectively, as a function of the branch tube group number. As shown in Figure 4.31, it is clearly shown that as the branch tube number decreases, the liquid mass flow rate ratio increases for both inlet locations and the two manifold inlet mass flow rates.

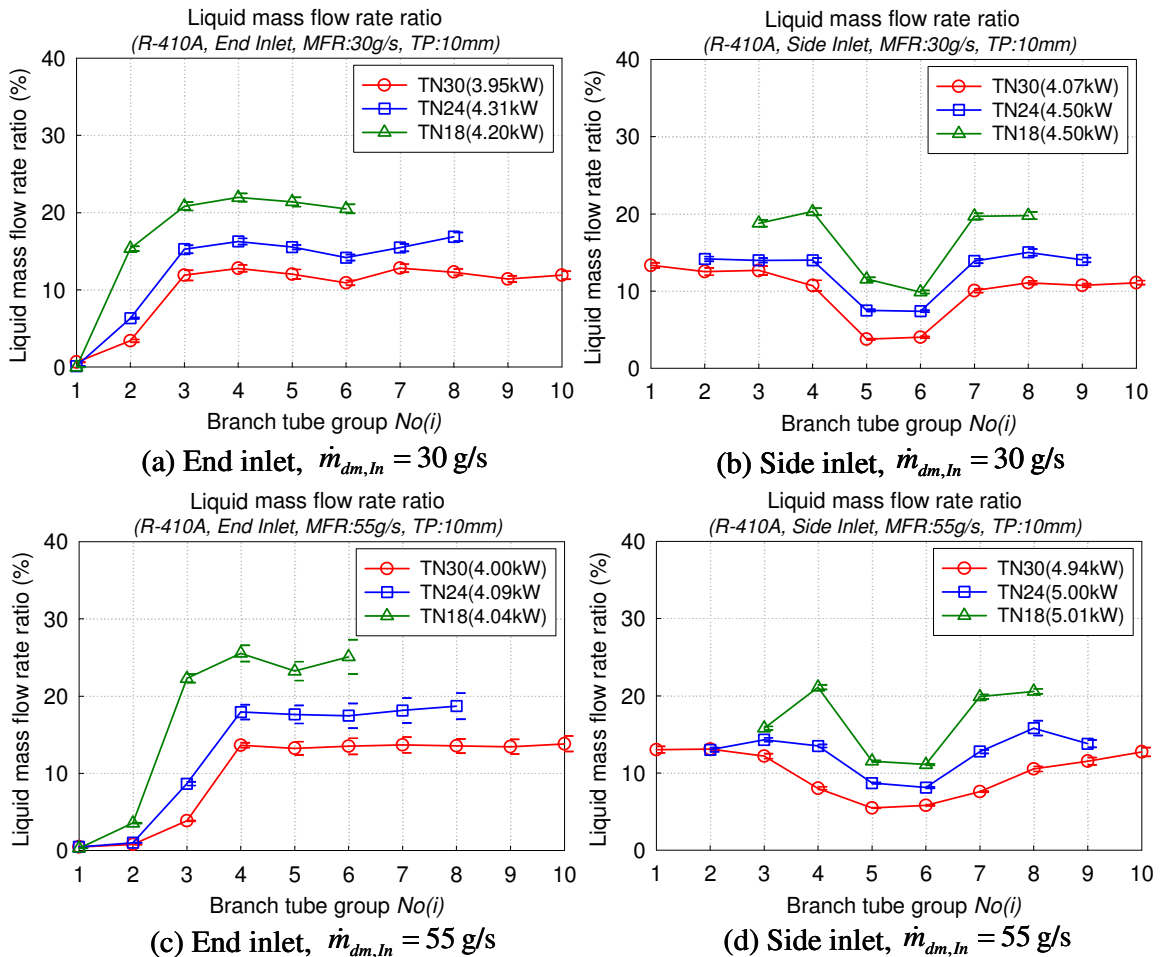


Figure 4.31 Liquid mass flow rate ratio with various branch tube group numbers for R-410A (Tube pitch: 10 mm, Heat load: 5 kW)

Figure 4.32 shows the normalized liquid mass flow rate ratio using Equation 4.3 with various branch tube numbers (or various manifold lengths) for R-410A and 5 kW heat load as a function of the branch tube group number. Figure 4.32 (a) and (b), and (c) and (d) show the normalized liquid mass flow rate ratio for $\dot{m}_{dm,In} = 30$ g/s and 55 g/s, respectively, as a function of the branch tube group number. In Figure 4.32, the unity indicates equal distribution of liquid phase. Based on that, it is shown that near the inlet, the normalized liquid mass flow rate ratio for the three tube numbers is approximately the same.

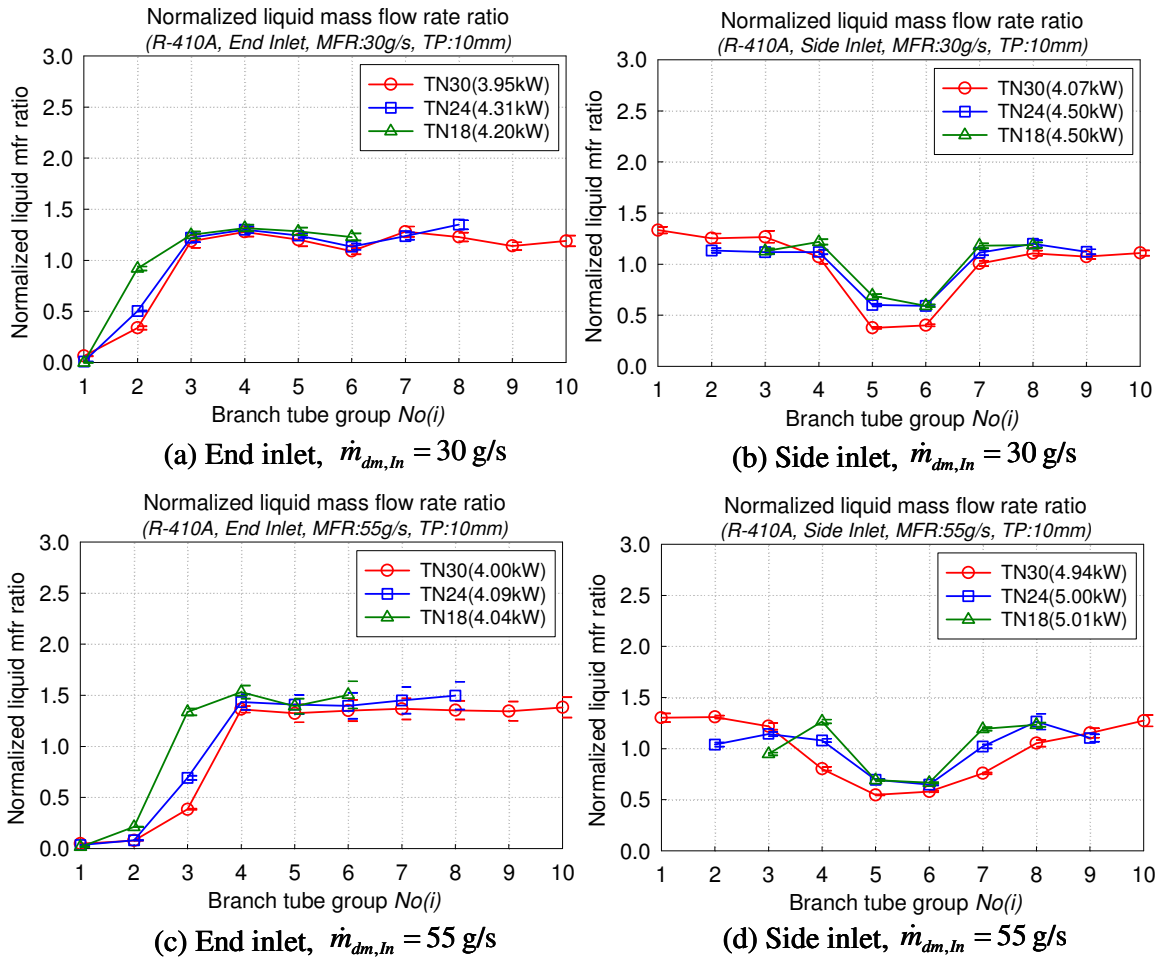


Figure 4.32 Normalized liquid mass flow rate ratio with various branch tube group numbers for R-410A (Tube pitch: 10 mm, Heat load: 5 kW)

In order to analyze quantitatively the degree of maldistribution for the three tube numbers, the normalized standard deviation of the mass flow rate at the branch tube groups for the vapor phase and liquid phase was evaluated by using the following equations :

$$STD_{\dot{m}_{bt,vap}} = \frac{\sqrt{\frac{\sum_{i=1}^{N_{bt}} (\dot{m}_{bt,vap}(i) - AMFR_{vap})^2}{N_{bt}}}}{AMFR_{vap}} \quad (4.4)$$

$$STD_{\dot{m}_{bt,liq}} = \frac{\sqrt{\frac{\sum_{i=1}^{N_{bt}} (\dot{m}_{bt,liq}(i) - AMFR_{liq})^2}{N_{bt}}}}{AMFR_{liq}} \quad (4.5)$$

Using Equations 4.4 and 4.5, for the three tube numbers, the normalized standard deviation of the mass flow rate at the branch tube groups for the vapor phase and liquid phase was calculated, and is shown in Table 4.2.

Table 4.2 Normalized standard deviation of the mass flow rate at the branch tube groups for the vapor and liquid phase for various branch tube group numbers ($\dot{m}_{dm,in} = 30$ g/s , and 55 g/s)

$\dot{m}_{dm,in} = 30$ g/s	End inlet		Side inlet	
	$STD_{\dot{m}_{bt,vap}}$	$STD_{\dot{m}_{bt,liq}}$	$STD_{\dot{m}_{bt,vap}}$	$STD_{\dot{m}_{bt,liq}}$
Tube group no.: 10 ea	1.144	0.408	0.638	0.320
Tube group no.: 8 ea	0.751	0.450	0.452	0.235
Tube group no.: 6 ea	0.785	0.466	0.473	0.256

$\dot{m}_{dm,in} = 55$ g/s	End inlet		Side inlet	
	$STD_{\dot{m}_{bt,vap}}$	$STD_{\dot{m}_{bt,liq}}$	$STD_{\dot{m}_{bt,vap}}$	$STD_{\dot{m}_{bt,liq}}$
Tube group no.: 10 ea	1.016	0.549	0.402	0.286
Tube group no.: 8 ea	0.856	0.595	0.302	0.202
Tube group no.: 6 ea	0.938	0.631	0.329	0.249

For the normalized standard deviation of the mass flow rate at the branch tube groups for the vapor phase and liquid phase, the smaller the value is, the more uniform the phase is. As shown in Table 4.2, the normalized standard deviation for the side inlet case is smaller than that for the end inlet case, and for the end inlet case, the normalized standard deviation for $\dot{m}_{dm,in} = 30$ g/s is smaller than that for 55 g/s. For the side inlet case, the normalized standard deviation of the $\dot{m}_{dm,in} = 55$ g/s case is smaller than that for 30 g/s case. In overall, the vapor and liquid distribution for the 30 tubes is less uniform than those for two other tube numbers. However, in general, the effect of branch tube number on the refrigerant distribution is not severe.

4.3.4.3 Pressure drop measurements

Figure 4.33 shows the pressure drop measurements along the branch tube groups with various branch tube numbers (or various manifold lengths) for R-410A and 5 kW heat load as a function of the branch tube group number. Figure 4.33 (a) and (b), and (c) and (d) show the pressure drop measurements along the branch tube groups for $\dot{m}_{dm,in} = 30$ g/s and 55 g/s, respectively, as a function of the branch tube group number. As shown in Figure 4.33, in overall, as the branch tube number decreases, the pressure drop along the branch tube groups increases because of the increased mass flow rate due to the reduced branch tube group number for the fixed manifold inlet mass flow rate.

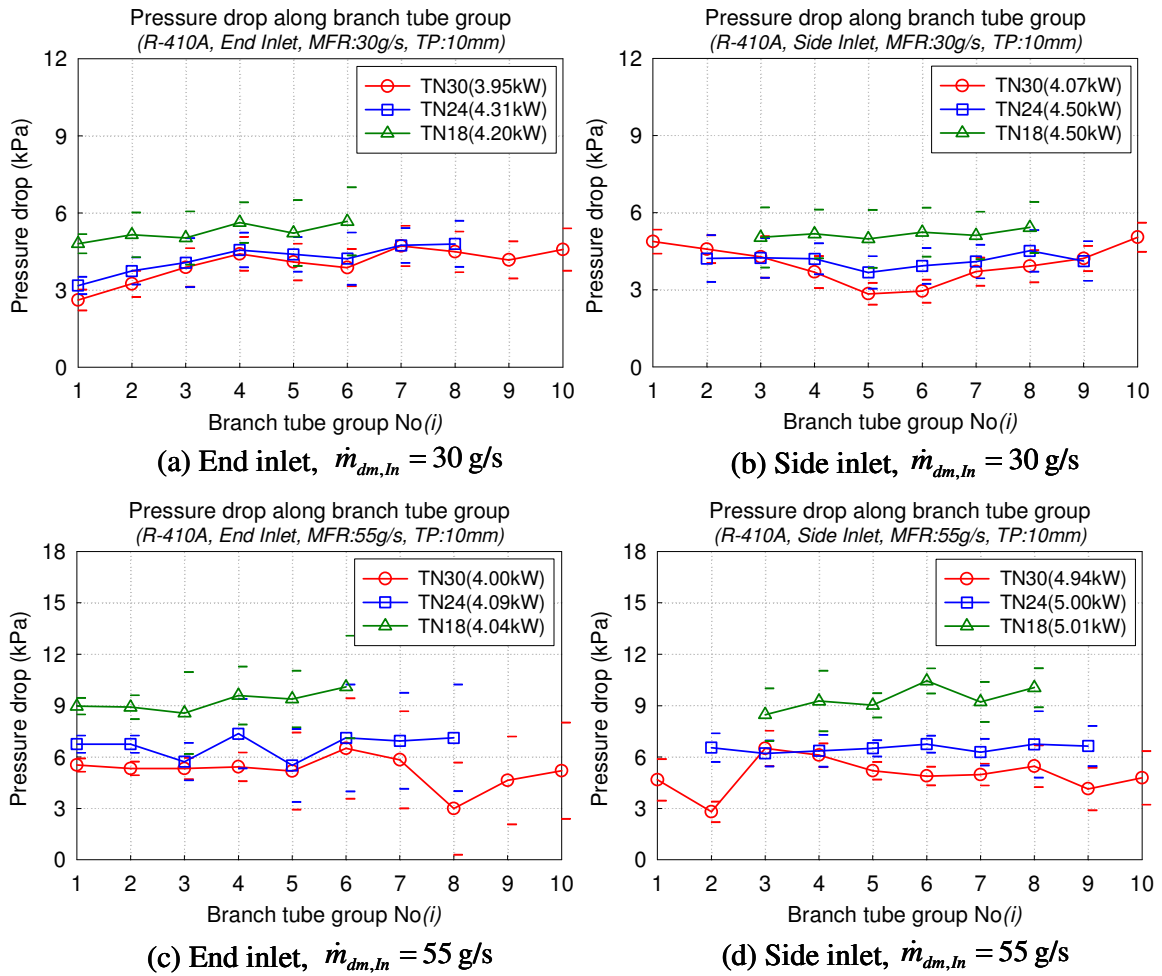


Figure 4.33 Pressure drop along the branch tube group with various branch tube group numbers for R-410A (Tube pitch: 10 mm, Heat load: 5 kW)

4.3.4.4 Power input and temperature measurements

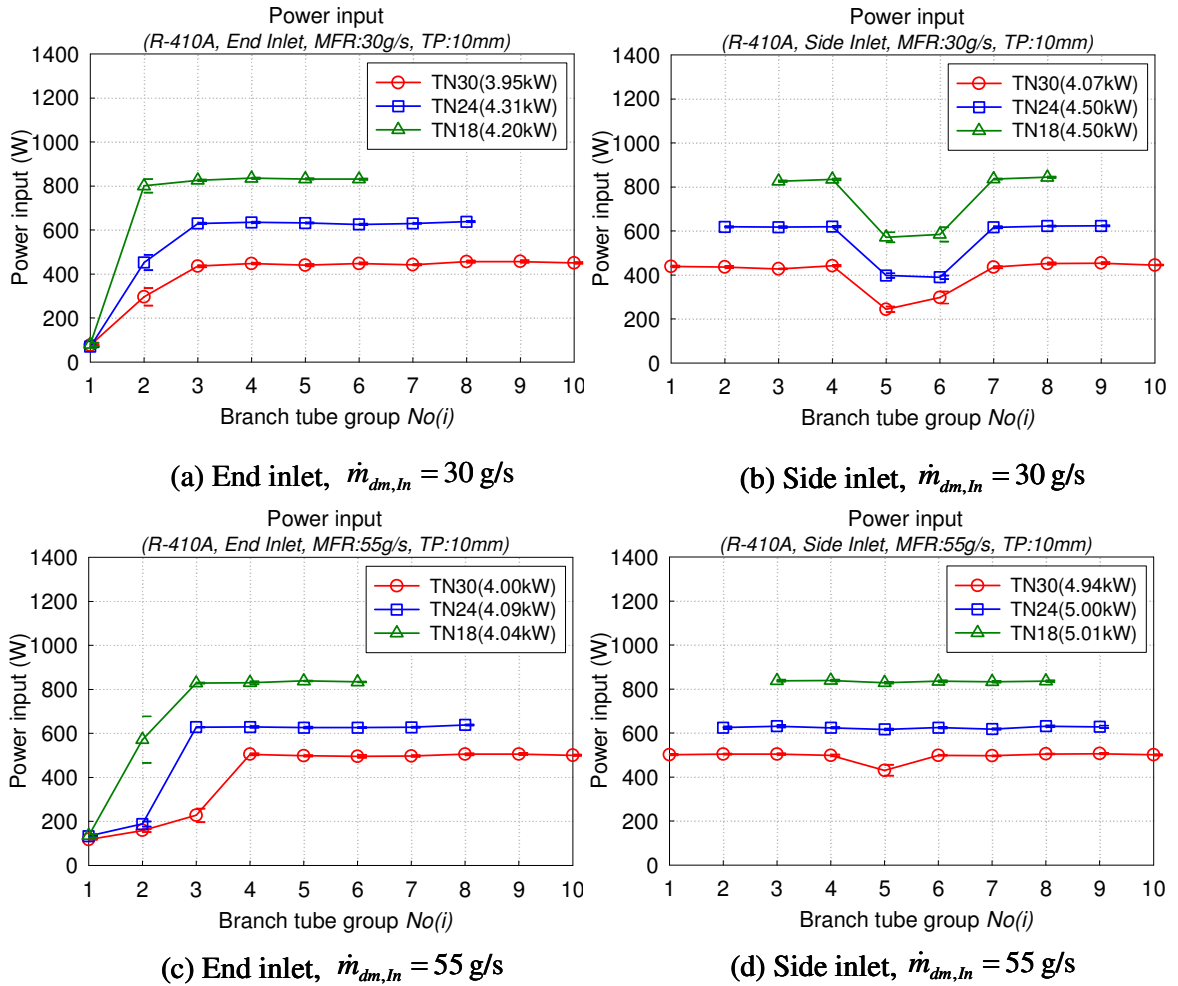


Figure 4.34 Power input with various branch tube group numbers for R-410A

(Tube pitch: 10 mm, Heat load: 5 kW)

Figure 4.34 shows the power input for the main heaters installed on the branch tubes with various branch tube numbers (or various manifold lengths) for R-410A and 5 kW heat load as a function of the branch tube group number. Figure 4.34 (a) and (b), and (c) and (d) show the power input for the main heaters for $\dot{m}_{dm,in} = 30 \text{ g/s}$ and 55 g/s , respectively, as a function of the branch tube group number. While conducting experiments, the given test condition for the total power input on the branch tubes was kept constant. Therefore,

as the number of the branch tube groups decreases, the provided power input for the individual tube groups increases. The power input for the tube groups with higher inlet vapor quality was reduced by the control because of the reduced cooling capacity due to the higher branch tube inlet vapor quality. However, for $\dot{m}_{dm,in} = 55 \text{ g/s}$ with the side inlet, the originally provided power was almost absorbed by the refrigerant in the tube groups near the inlet for the specific branch inlet vapor quality because of the larger cooling capacity of the increased mass flow rate compared to $\dot{m}_{dm,in} = 30 \text{ g/s}$.

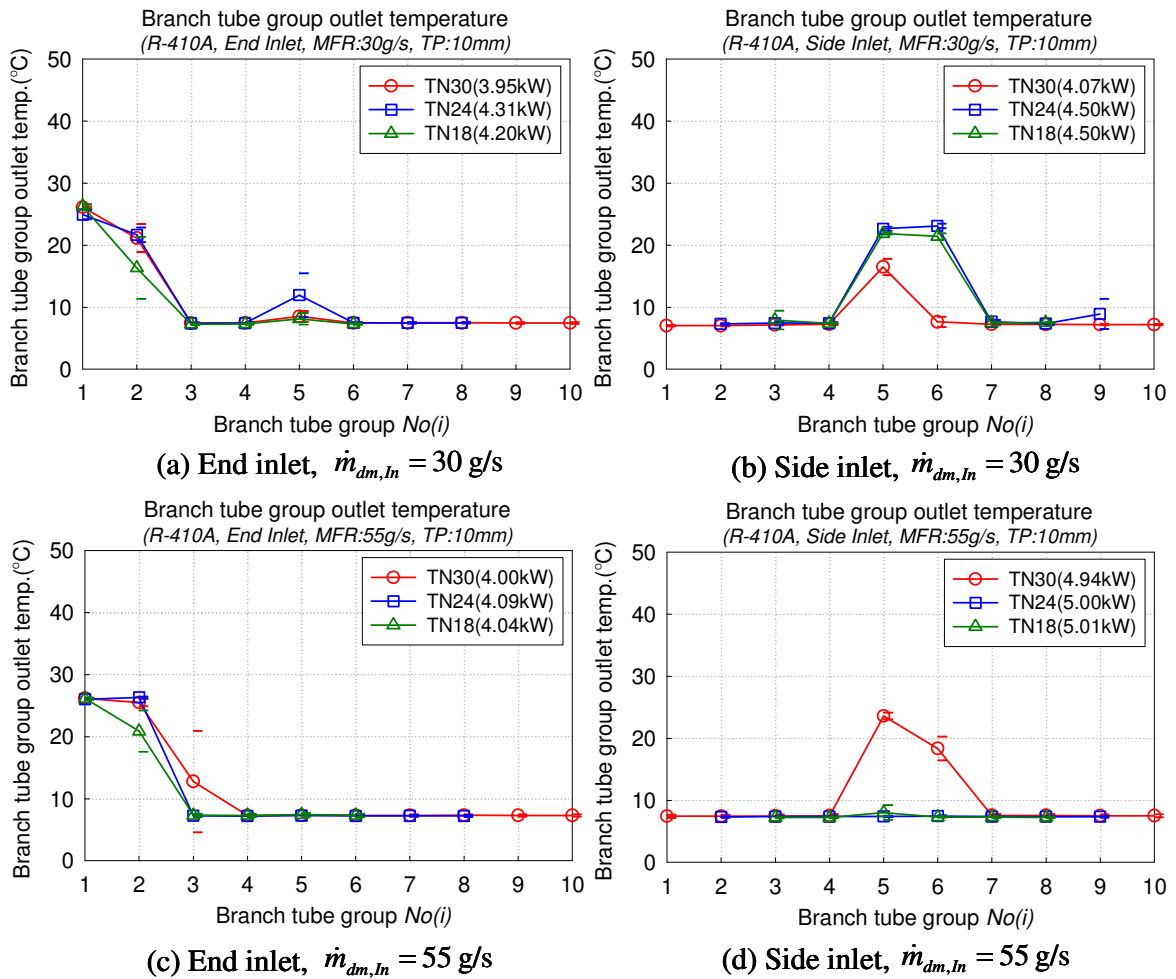


Figure 4.35 Branch tube outlet temperature with various branch tube group numbers for R-410A (Tube pitch: 10 mm, Heat load: 5 kW)

Figure 4.35 shows the branch tube outlet temperature with various branch tube numbers (or various manifold lengths) for R-410A and 5 kW heat load as a function of the branch tube group number. Figure 4.35 (a) and (b), and (c) and (d) show the branch tube outlet temperature for $\dot{m}_{dm,in} = 30$ g/s and 55 g/s, respectively, as a function of the branch tube group number. The temperature profile reflects the power input profile explained earlier. In overall, the temperature for the tube groups near the inlet is close to the cut-off temperature depending on the tube group number.

4.3.5 Effect of tube pitch

In this section, test results of the dividing manifold with 10 tube groups with various tube pitches for R-410A are presented.

4.3.5.1 Refrigerant distribution

Figure 4.36 shows the mass flow rate ratio with various tube pitches for R-410A and 5 kW heat load as a function of the branch tube group number. Figure 4.36 (a) and (b), and (c) and (d) show the mass flow rate ratio for $\dot{m}_{dm,in} = 30$ g/s and 55 g/s, respectively, as a function of the branch tube group number. As shown in Figure 4.36, in overall, the mass flow rate ratio has the same trend for those tube pitches. For $\dot{m}_{dm,in} = 30$ g/s and the end inlet, the mass flow rate ratio for the tube groups near the inlet is higher than that for the tube groups close to the end of the manifold.

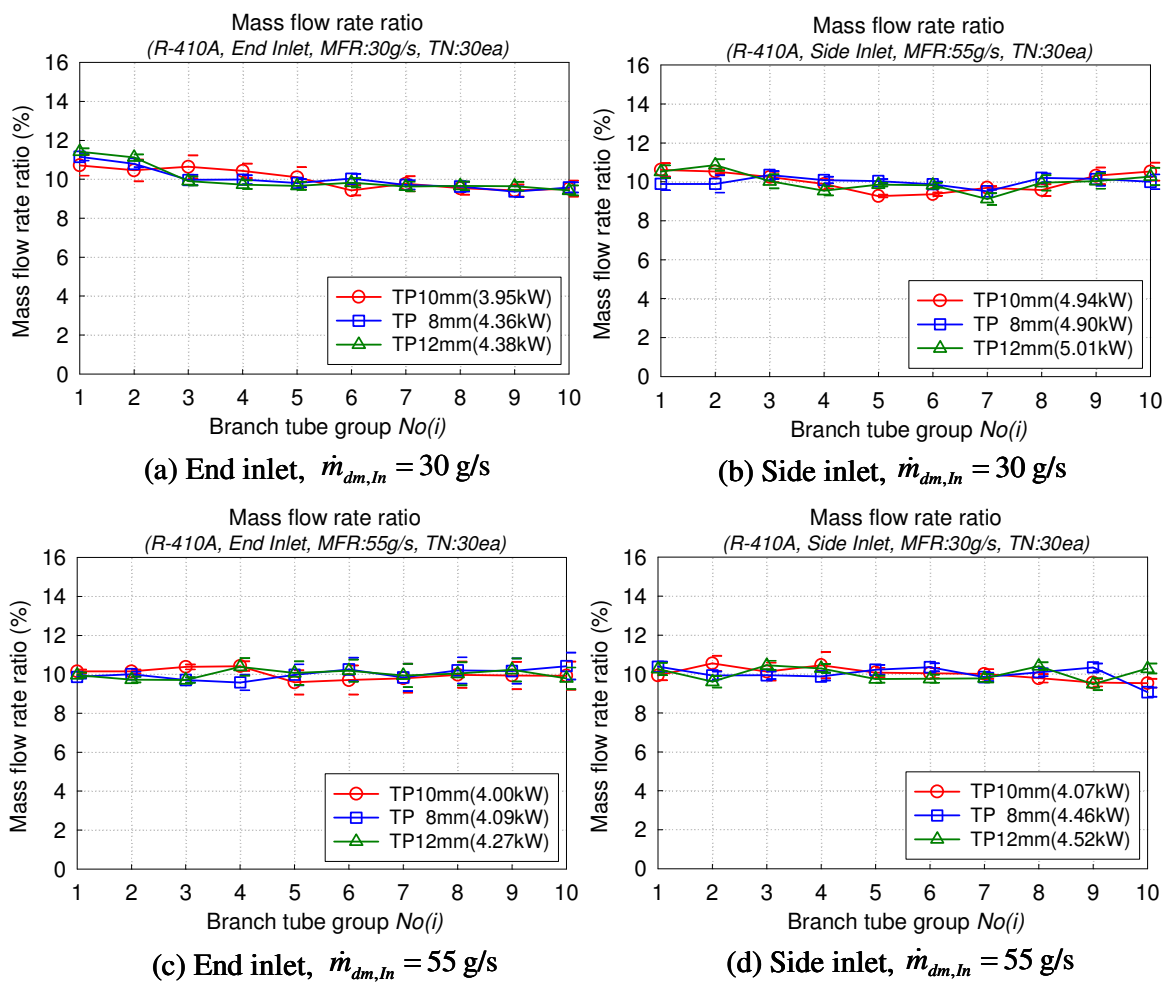


Figure 4.36 Mass flow rate ratio with various tube pitches for R-410A

(Tube number: 30 ea, Heat load: 5 kW)

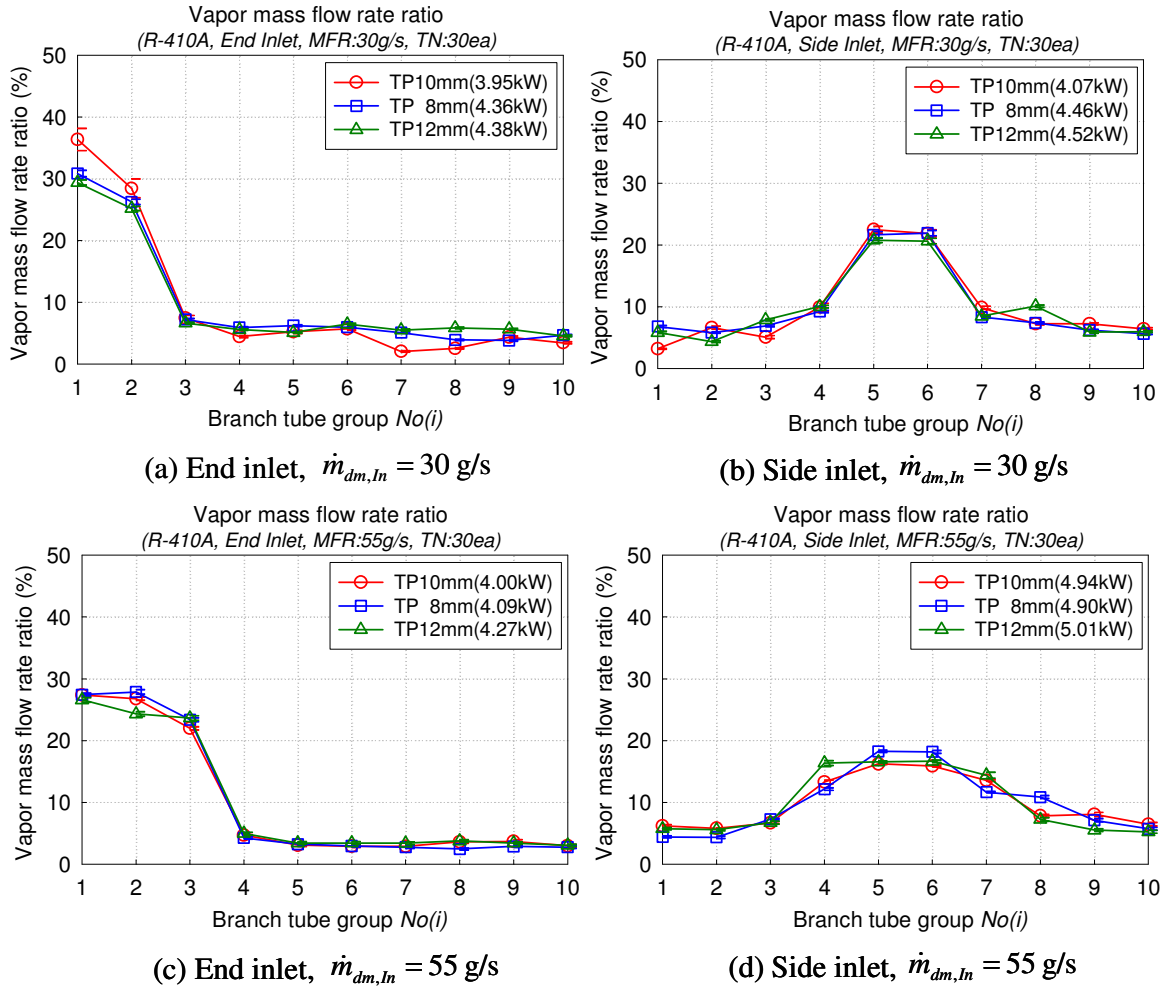


Figure 4.37 Vapor mass flow rate ratio with various tube pitches for R-410A

(Tube number: 30 ea, Heat load: 5 kW)

Figure 4.37 shows the vapor mass flow rate ratio with various tube pitches for R-410A and 5 kW heat load as a function of the branch tube group number. Figure 4.37 (a) and (b), and (c) and (d) show the vapor mass flow rate ratio for $\dot{m}_{dm,in} = 30 \text{ g/s}$ and 55 g/s , respectively, as a function of the branch tube group number. In overall, the vapor mass flow rate ratio is little affected by tube pitch variation. This is well matched with the flow visualization as shown in Figure 4.4.

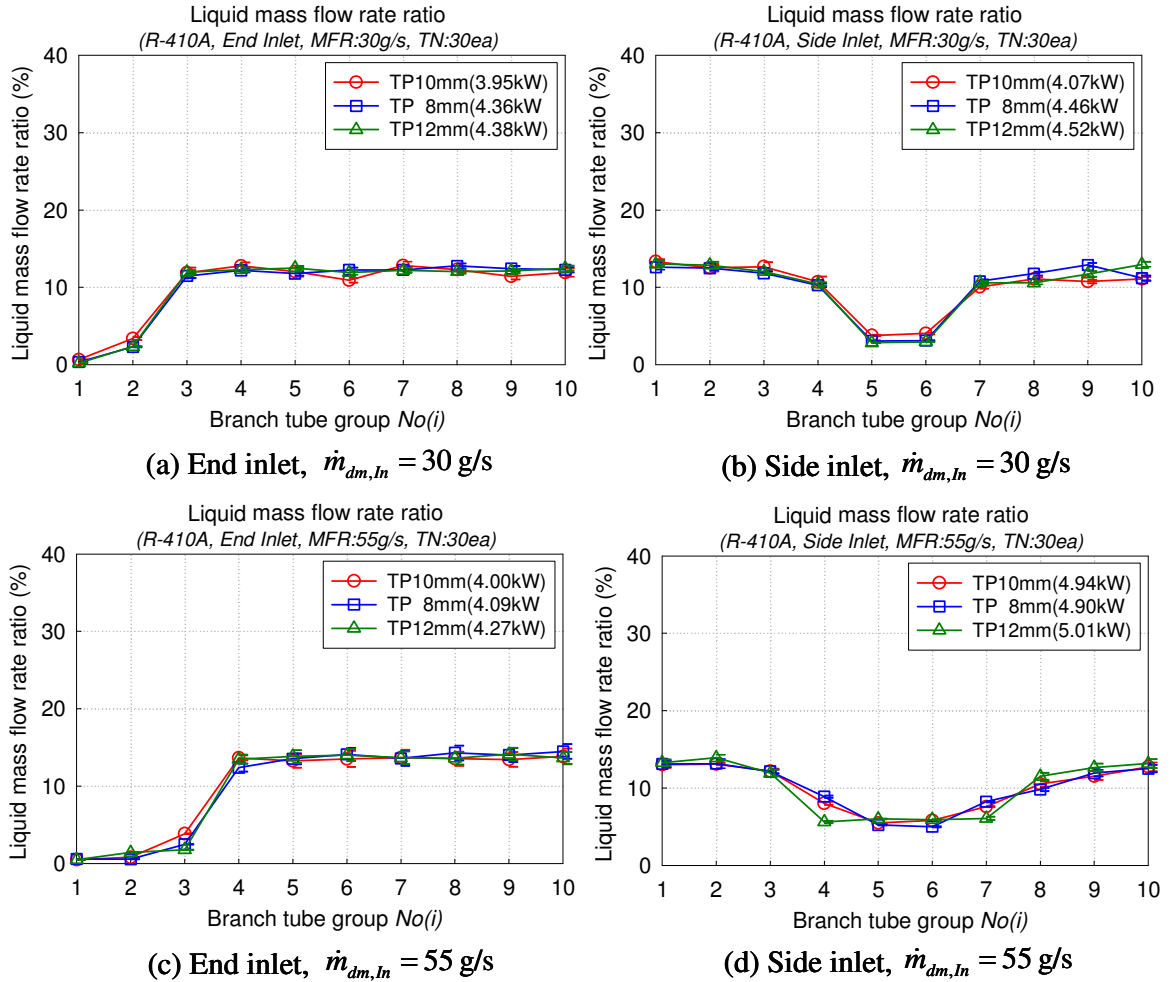


Figure 4.38 Liquid mass flow rate ratio with various tube pitches for R-410A
(Tube number: 30 ea, Heat load: 5 kW)

Figure 4.38 shows the liquid mass flow rate ratio with various tube pitches for R-410A and 5 kW heat load as a function of the branch tube group number. Figure 4.38 (a) and (b), and (c) and (d) show the liquid mass flow rate ratio for $\dot{m}_{dm,in} = 30 \text{ g/s}$ and 55 g/s , respectively, as a function of the branch tube group number. In Figure 4.38, it is shown that the liquid mass flow rate ratio is little affected by tube pitch variation. Compared to the liquid mass flow rate ratio profile of the tube pitch 10 mm, which is base line, the profiles for the tube pitch 8 mm and 12 mm are almost similar to that of the tube pitch 10

mm for both inlet locations. For the end inlet, the liquid mass flow rate ratio of the first few tube groups near the inlet is comparatively lower than that for the tube groups close to the end of the manifold, and for the side inlet, the liquid mass flow rate ratio profile is symmetric, and the liquid mass flow rate ratio for the tube groups near the inlet is comparatively lower. In order to figure out quantitatively the degree of maldistribution for the three tube pitches, the normalized standard deviation of the mass flow rate at the branch tube groups for the vapor phase and the liquid phase was calculated using Equations 4.4 and 4.5, and is shown in Table 4.3.

Table 4.3 Normalized standard deviation of the mass flow rate at the branch tube groups for the vapor and liquid phase with various branch tube pitches ($\dot{m}_{dm,in} = 30$ g/s , and 55 g/s)

$\dot{m}_{dm,in} = 30$ g/s	End inlet		Side inlet	
	$STD_{\dot{m}_{bt,vap}}$	$STD_{\dot{m}_{bt,liq}}$	$STD_{\dot{m}_{bt,vap}}$	$STD_{\dot{m}_{bt,liq}}$
Tube pitch: 10 mm	1.144	0.408	0.638	0.320
Tube pitch: 8 mm	0.938	0.438	0.599	0.354
Tube pitch: 12 mm	0.872	0.439	0.565	0.368

$\dot{m}_{dm,in} = 55$ g/s	End inlet		Side inlet	
	$STD_{\dot{m}_{bt,vap}}$	$STD_{\dot{m}_{bt,liq}}$	$STD_{\dot{m}_{bt,vap}}$	$STD_{\dot{m}_{bt,liq}}$
Tube pitch: 10 mm	1.016	0.549	0.402	0.286
Tube pitch: 8 mm	1.069	0.580	0.490	0.294
Tube pitch: 12 mm	0.976	0.576	0.496	0.341

As shown in Table 4.3, it can be said that in overall, the vapor and liquid distribution in the manifold is little affected by the variation of tube pitch.

4.3.5.2 Pressure drop measurements

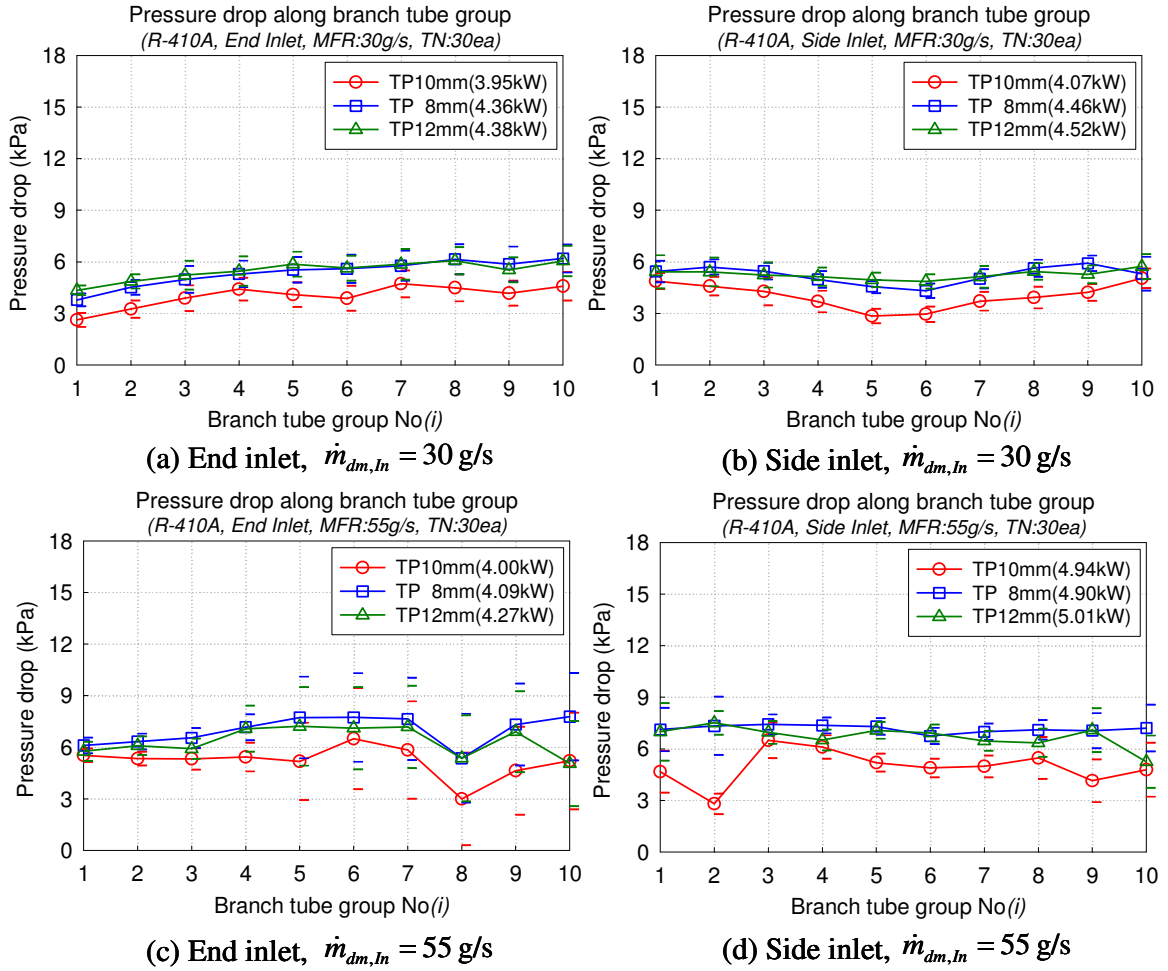


Figure 4.39 Pressure drop along the branch tube group with various tube pitches for R-410A (Tube number: 30 ea, Heat load: 5 kW)

Figure 4.39 shows the pressure drop measurements along the branch tube groups with various tube pitches for R-410A and 5 kW heat load as a function of the branch tube group number. Figure 4.39 (a) and (b), and (c) and (d) show the pressure drop measurements along the branch tube groups for $\dot{m}_{dm,in} = 30 \text{ g/s}$ and 55 g/s , respectively, as a function of the branch tube group number. As shown in the Figure 4.39, for $\dot{m}_{dm,in} = 30 \text{ g/s}$, the pressure drop for the tube groups near the inlet is lower than that for

the tube groups close to the end of manifold. The pressure drop profile for tube pitch 8 and 12 mm is almost the same for both inlet locations, and the pressure drop for tube pitch 10mm is a little lower than that for the other two tube pitches. For $\dot{m}_{dm,In} = 55 \text{ g/s}$, the pressure drop measurements have bigger uncertainty compared to $\dot{m}_{dm,In} = 30 \text{ g/s}$, especially for the tube groups at the far end. In overall, the pressure drop profile for tube pitch 8 and 12 mm is almost same for both inlet locations, and the pressure drop for tube pitch 10 mm is a little lower than that for the two tube pitches.

4.3.5.3 Power input and temperature measurements

Figure 4.40 shows the power input for the main heaters installed on the branch tubes with various tube pitches for R-410A and 5 kW heat load as a function of the branch tube group number. Figure 4.40 (a) and (b), and (c) and (d) show the liquid mass flow rate ratio for $\dot{m}_{dm,In} = 30 \text{ g/s}$ and 55 g/s , respectively, as a function of the branch tube group number. As explained earlier, it is shown that the power input for the tube groups with higher inlet vapor quality was reduced by the control because of less cooling capacity due to the higher branch tube inlet vapor quality. For $\dot{m}_{dm,In} = 30 \text{ g/s}$, the power input for the tube pitch 10 mm is 10% less than that for the other two tube pitches. This is not because of heater cut-off, but because of different heater control scheme. In the beginning of the test, the heaters were controlled by time fraction on-off using Q-basic program to provide the exact power inputs because the installed heaters have 1.4 kW per tube group. After testing a few cases, the heater control was changed to the control by the voltage transformers for accurate control. However, as shown in the heat load effect discussion, this difference does not affect this parametric study. Other than that, the power input

profiles for the tube pitch 8 and 12 mm are almost similar to that for the tube pitch 10 mm, which is base line, for both inlet locations.

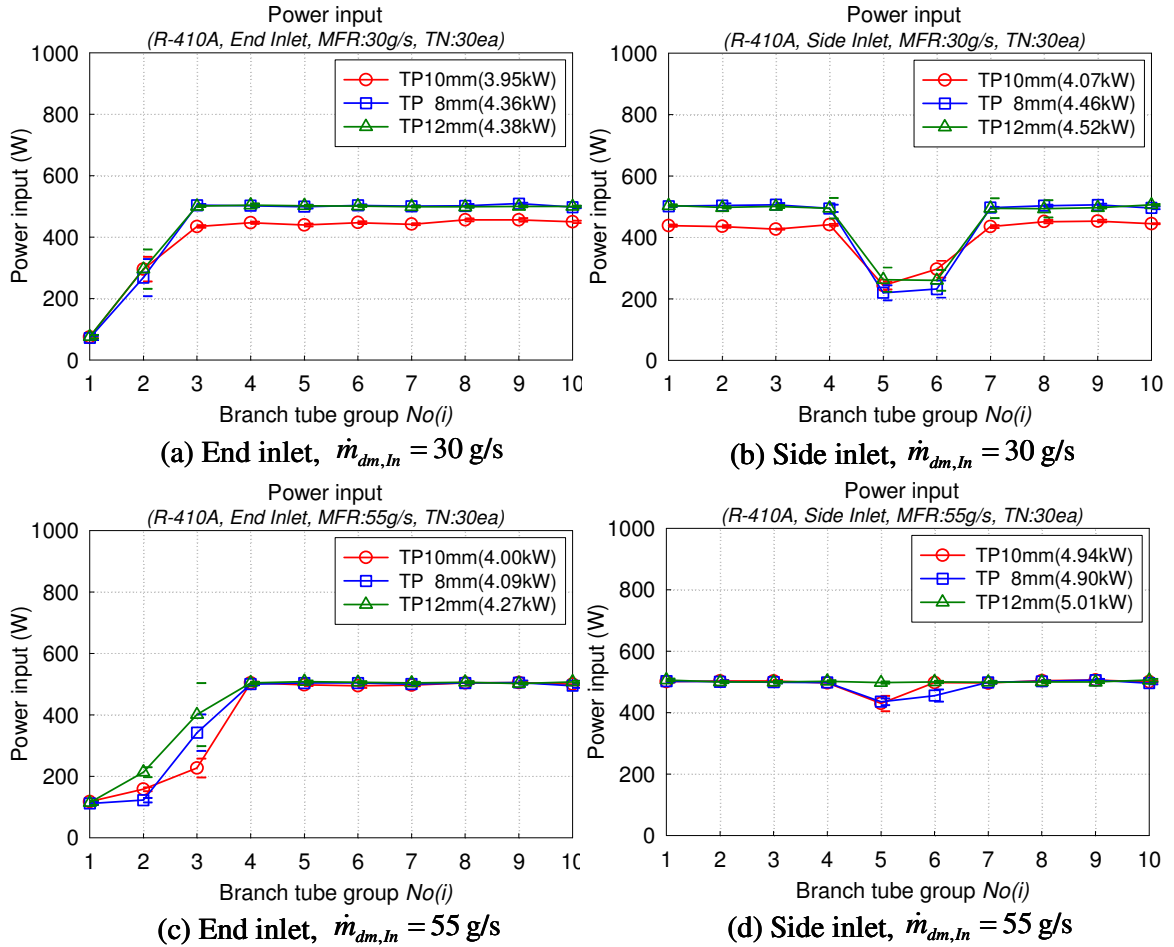


Figure 4.40 Power input for various tube pitches for R-410A

(Tube number: 30 ea, Heat load: 5 kW)

Figure 4.41 shows the branch tube outlet temperature for various tube pitches for R-410A and 5 kW heat load as a function of the branch tube group number. Figure 4.41 (a) and (b), and (c) and (d) show the branch tube outlet temperature for various tube pitches for $\dot{m}_{dm,in} = 30 \text{ g/s}$ and 55 g/s , respectively, as a function of the branch tube group number.

The temperature profile reflects the power input profile explained before. Especially, for the end inlet, the outlet temperatures for the three tube pitches at the tube group No. 2 for $\dot{m}_{dm,in} = 30 \text{ g/s}$ and the outlet temperatures at the tube group No. 3 for 55 g/s are different among them because the tube group No. 2 and No. 3 is vapor-liquid interface for the mass flow rates.

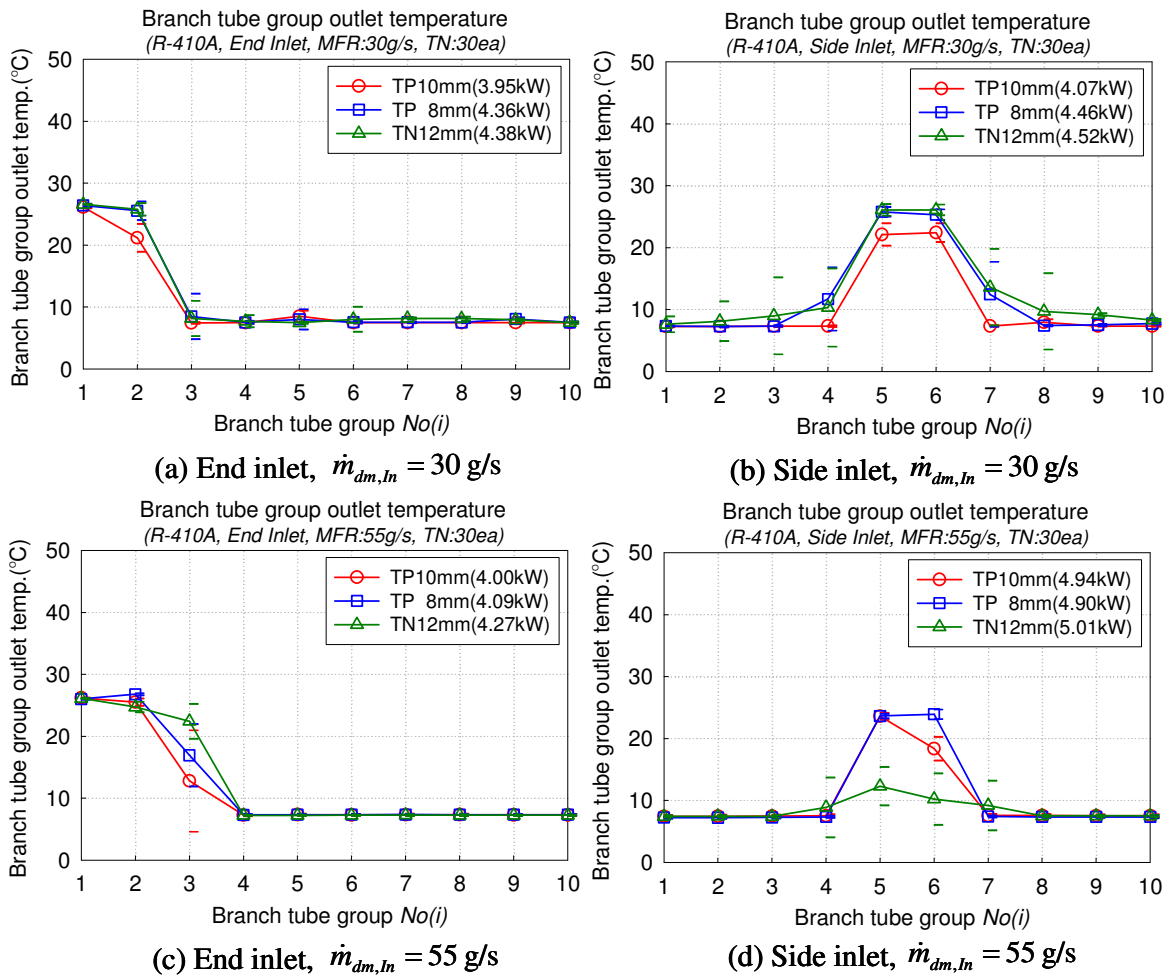


Figure 4.41 Branch tube outlet temperature with various tube pitches for R-410A

(Tube number: 30 ea, Heat load: 5 kW)

4.3.6 Effect of oil mass fraction

In this section, the effect of Oil Mass Fraction for the R-410A is presented. The OMF (Oil Mass Fraction) is defined as Equation 4.6.

$$OMF = \frac{\dot{m}_{oil}}{\dot{m}_{oil} + \dot{m}_{ref}} \quad (4.6)$$

Several tests were conducted with POE (Polyol Ester) oil for the end inlet case to investigate the oil mass fraction effect. The calculated oil mass fraction is about 2 wt.% based on the density measurements. For measuring the mixture density for the R-410A and the POE oil, the Coriolis-type mass flow meter which was used for measuring manifold inlet mass flow rate was used. The density measurement accuracy is ± 0.5 kg/m³.

4.3.6.1 The branch tube inlet vapor quality

Figure 4.42 shows the branch tube group inlet vapor quality with 0 and 2 wt.% OMF for R-410A and $\dot{m}_{dm,In} = 45$ g/s as a function of the branch tube group number. In the Figure, it is shown that at the near inlet, the branch tube group inlet vapor quality with both inlet locations for the 2 wt.% OMF is almost same as that for the oil-free case, but at the other tube groups, the branch tube group inlet vapor quality with both inlet locations for the 2 wt.% OMF is about 15 ~ 20% higher than that for the oil-free case. As shown in Figure 4.42, the uncertainty of the branch tube inlet vapor quality for the 2 wt.% OMF is much higher than that for the oil-free case. At the tube groups near the inlet for the 2 wt.%

OMF case, the uncertainty is comparatively smaller than that for the tube groups close to the end of the manifold, even though the uncertainty is bigger than that for the oil-free case. In order to figure out the bigger uncertainty source of the branch tube inlet vapor quality for the 2 wt.% OMF, the mass flow rate measurements were reviewed since the vapor quality calculation was based on the mass flow rate, temperature, and pressure measurements. Figure 4.43 shows the mass flow rate at the tube group No. 10 for both 0 wt.% and 2 wt.% OMF cases with time variation. In Figure 4.43, it is clearly shown that the mass flow rate for the 2 wt.% OMF has much higher standard deviation. Even though enough degree of superheating (greater than 50 K) for the post heater section was kept, the mass flow rate measurements was affected by adding oil because a gas mass flow meter was used for the measurements. Therefore, the vapor mass flow rate summation of the whole tube groups for the 2 wt.% OMF case deviated far from the manifold inlet vapor mass flow rate. For most of oil-free cases, the vapor mass flow rate summation of the whole tube groups is within 100 ~ 125% of the manifold inlet vapor mass flow rate. However, for the 2 wt.% OMF cases, the vapor mass flow rate summation of the whole tube groups is within 147 ~ 150% of the manifold inlet vapor mass flow rate. Based on the flow visualization and consideration of both mass balance and uncertainty of the measurements, it is expected that the refrigerant distribution is little affected by adding 2 wt.% OMF even though the measured tube inlet vapor quality of the tube groups close to the end of the manifold was bigger than that for the oil-free case.

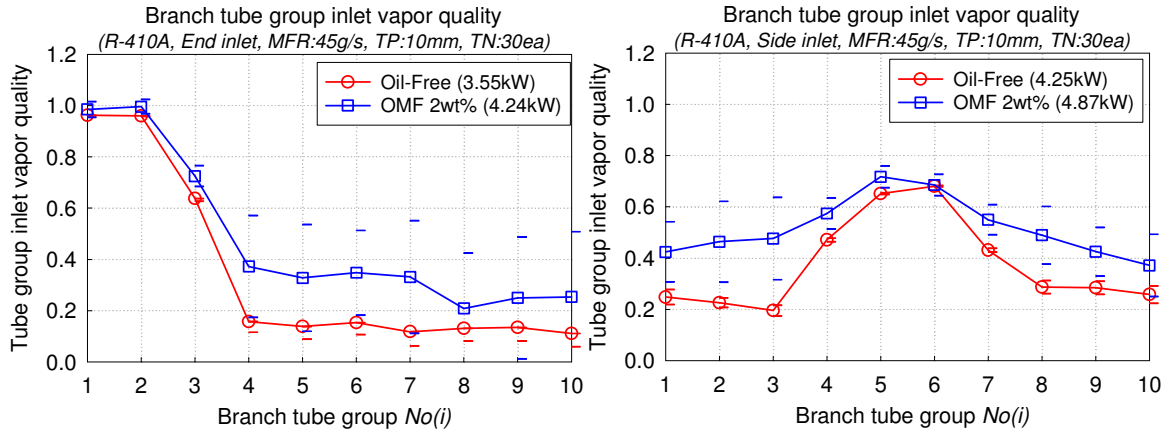


Figure 4.42 Branch tube group inlet vapor quality with 0 and 2wt% OMF for R-410A ($\dot{m}_{dm,in} = 45 \text{ g/s}$, Tube number: 30 ea, Heat load: 5 kW)

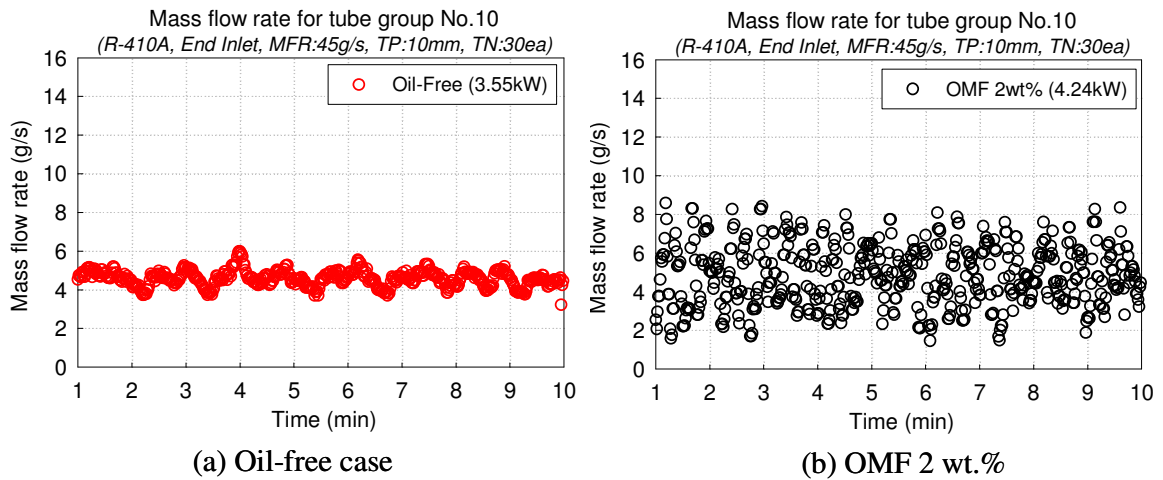


Figure 4.43 Mass flow rate for the tube group No.10 with 0 and 2 wt.% OMF for R-410A, end inlet ($\dot{m}_{dm,in} = 45 \text{ g/s}$, Tube number: 30 ea, Heat load: 5 kW)

4.3.6.2 Refrigerant distribution

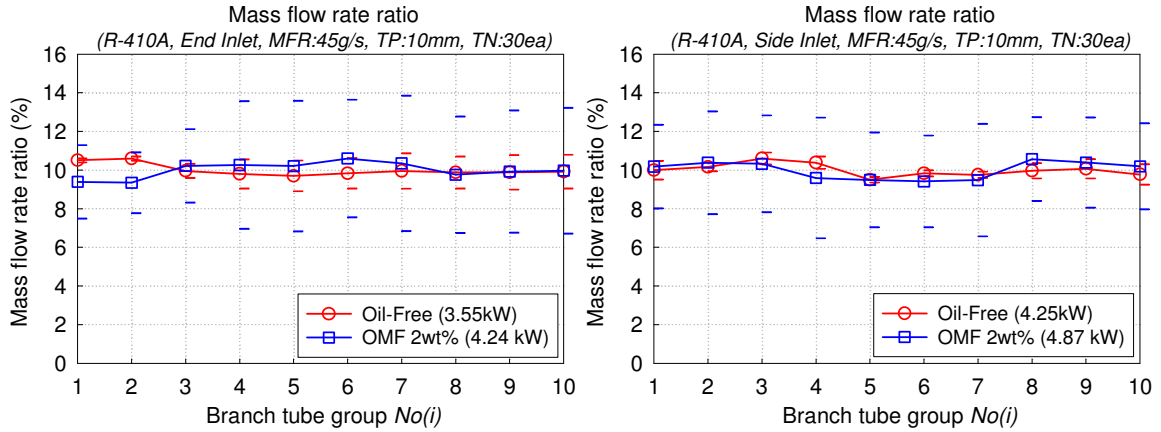


Figure 4.44 Mass flow rate ratio with 0 and 2 wt.% OMF for R-410A

$$(\dot{m}_{dm,in} = 45 \text{ g/s}, \text{ Tube number: } 30 \text{ ea}, \text{ Heat load: } 5 \text{ kW})$$

Figure 4.44 shows the mass flow rate ratio with 0 and 2 wt.% OMF for R-410A and $\dot{m}_{dm,in} = 45 \text{ g/s}$ as a function of the branch tube group number. As shown in Figure 4.44, in overall, the mass flow rate ratio has the same trend for both oil-free case and 2 wt.% OMF case. However, as explained before, the uncertainty for the 2 wt.% OMF case is much higher than that for the oil-free case.

Figure 4.45 shows the vapor mass flow rate ratio with 0 and 2 wt.% OMF for R-410A and $\dot{m}_{dm,in} = 45 \text{ g/s}$ as a function of the branch tube group number. As expected, based on the mass flow rate and the branch tube group inlet vapor quality, the vapor mass flow rate ratio at the tube groups near the inlet for the 2 wt.% OMF case is lower than that for the oil-free case because the measured branch tube inlet vapor quality at the tube groups located far away from the inlet is higher than that for the oil-free case.

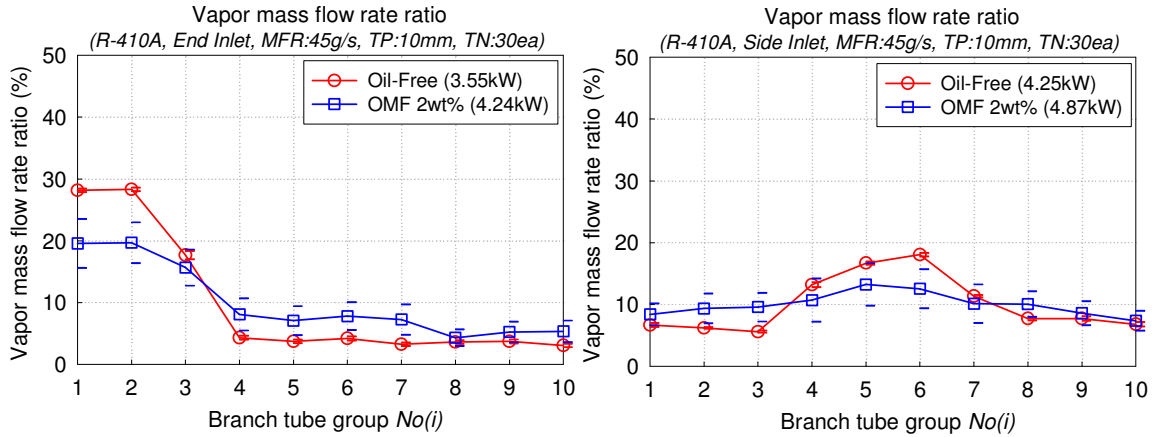


Figure 4.45 Vapor mass flow rate ratio with 0 and 2 wt.% OMF for R-410A

$$(\dot{m}_{dm,In} = 45 \text{ g/s} , \text{ Tube number: } 30 \text{ ea, Heat load: } 5 \text{ kW})$$

Figure 4.46 shows the liquid mass flow rate ratio with 0 and 2 wt.% OMF for R-410A and $\dot{m}_{dm,In} = 45 \text{ g/s}$ as a function of the branch tube group number. The profile for both cases has the same trend even though the vapor mass flow rate ratio profile for both cases was different. The liquid mass flow rate ratio was less affected by the mass flow rate measurements and the branch tube inlet vapor quality because the liquid phase has 70% of manifold inlet mass flow rate compared to 30% for the vapor phase.

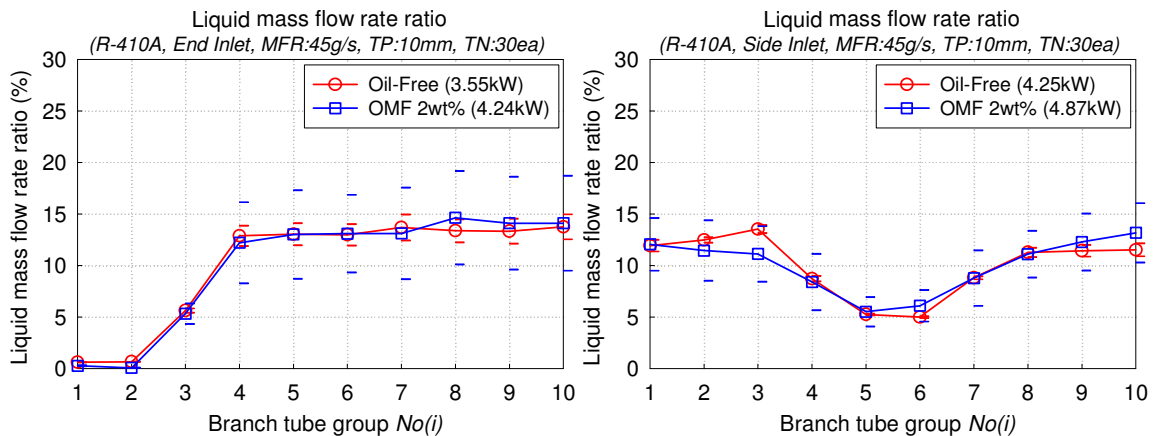


Figure 4.46 Liquid mass flow rate ratio with 0 and 2wt% OMF for R-410A

$$(\dot{m}_{dm,In} = 45 \text{ g/s} , \text{ Tube number: } 30 \text{ ea, Heat load: } 5 \text{ kW})$$

4.3.6.3 Pressure drop measurements

Figure 4.47 shows the pressure drop measurements along the branch tube groups with 0 and 2 wt.% OMF for R-410A and $\dot{m}_{dm,In} = 45 \text{ g/s}$ as a function of the branch tube group number. The pressure drop for the 2 wt.% OMF is 2 ~ 4 kPa higher than that for the oil-free case. In addition, as expected, the uncertainty of the pressure drop for the 2 wt.% OMF is $\pm 0.5 \sim \pm 1.5 \text{ kPa}$ higher than that for the oil-free case.

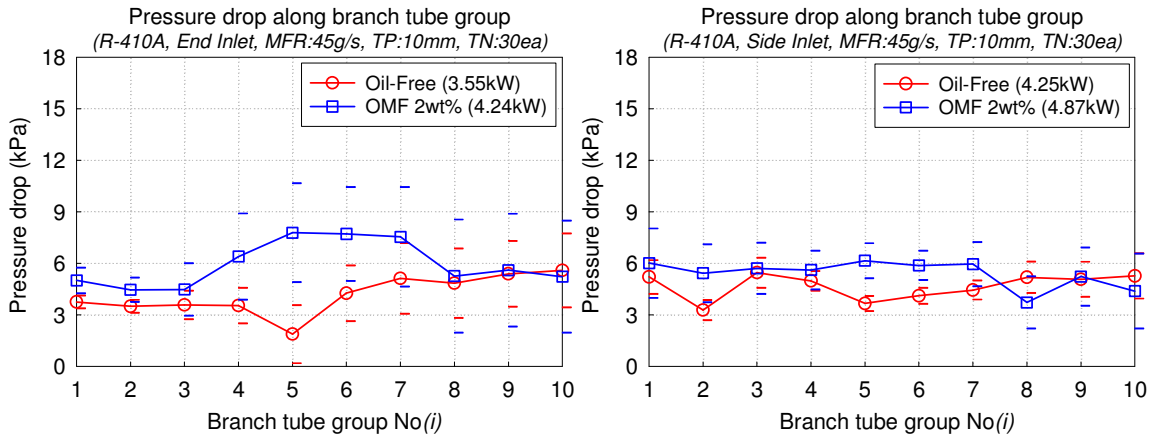


Figure 4.47 Pressure drop along the branch tube group with 0 and 2 wt.% OMF for R-410A ($\dot{m}_{dm,In} = 45 \text{ g/s}$, Tube number: 30 ea, Heat load: 5 kW)

4.3.6.4 Power input and temperature measurements

Figure 4.48 shows the power input for the main heaters installed on the branch tubes with 0 and 2 wt.% OMF for R-410A and $\dot{m}_{dm,In} = 45 \text{ g/s}$ as a function of the branch tube group number. It is cleared that the power input for the tube groups with higher inlet vapor quality was reduced by the control because of less available cooling capacity due to the higher branch tube inlet vapor quality. The power input at the tube groups far away from the inlet for the oil-free case is 10% less than that for the 2 wt.% OMF case. This is not

because of heater cut-off, but because of different heater control scheme. However, as shown in the heat load effect in section 4.3.2, this difference does not affect flow distribution.

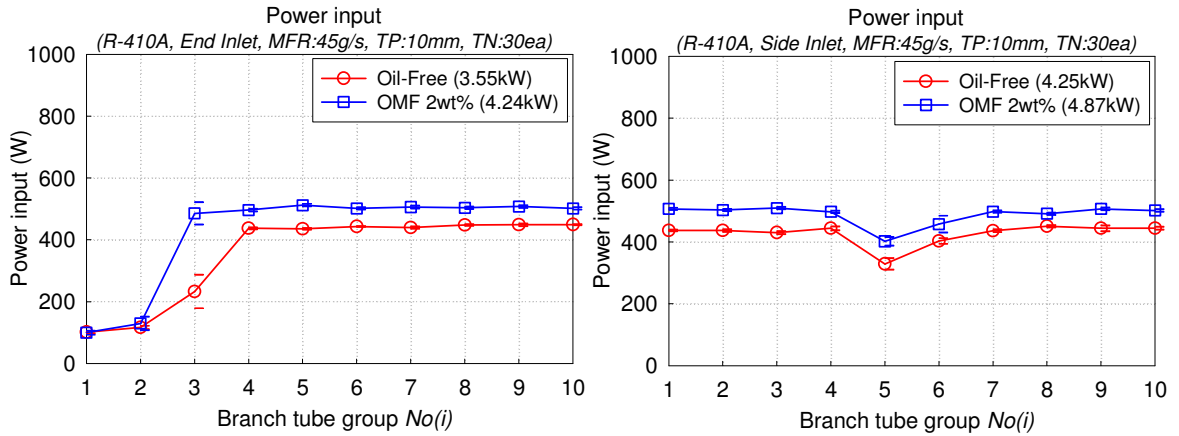


Figure 4.48 Power input with 0 and 2wt% OMF for R-410A

($\dot{m}_{dm,In} = 45 \text{ g/s}$, Tube number: 30 ea, Heat load: 5 kW)

Figure 4.49 shows the branch tube outlet temperature with 0 and 2 wt.% OMF for R-410A and $\dot{m}_{dm,In} = 45 \text{ g/s}$ as a function of the branch tube group number. The temperature profile reflects the power input profile explained before. Especially, for the end inlet case, the temperatures at the tube group No. 3 for both cases are different each other, and have bigger uncertainties because the vapor-liquid interface is located at the tube group No. 3. Therefore, the temperature is fluctuating a lot with time variation.

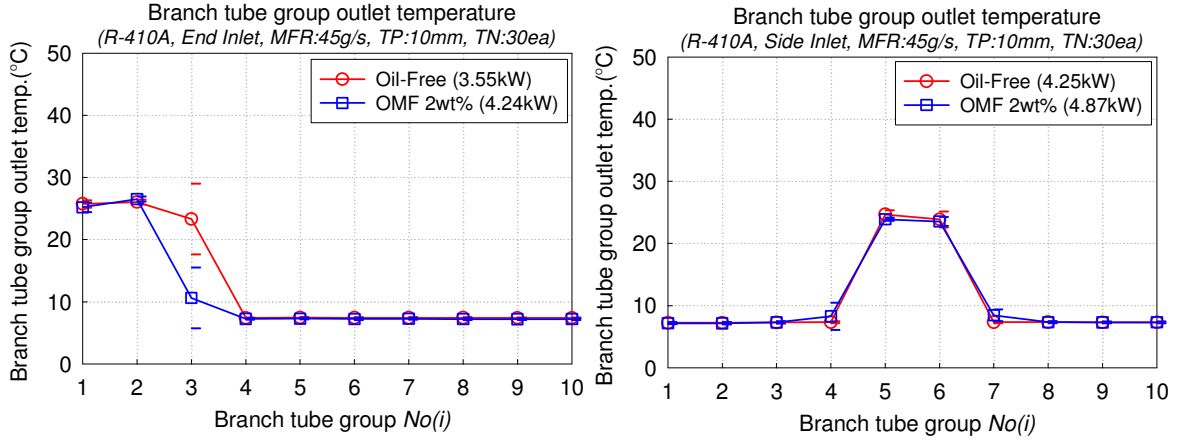


Figure 4.49 Branch tube outlet temperature with 0 and 2wt% OMF for R-410A

($\dot{m}_{dm,In} = 45 \text{ g/s}$, Tube number: 30 ea, Heat load: 5 kW)

4.4 Flow Pattern Map

In this section, flow pattern maps based on Thome, J. R. and Hajal, J. E. (2002) are given. Many researchers mentioned that the flow pattern at the inlet of a manifold and along the manifold length significantly affected the two-phase flow distribution. Figures 4.50 and 4.51 show flow pattern map based on Thome, J. R. and Hajal, J. E. (2002) for R-134a and R-410A, respectively. The flow properties at the inlet of T-junctions are included in Figures 4.50 and 4.51. Based on Figures 4.50 and 4.51, the flow patterns at most of the inlets of T-junctions in the manifold are stratified flow or stratified-wavy flow.

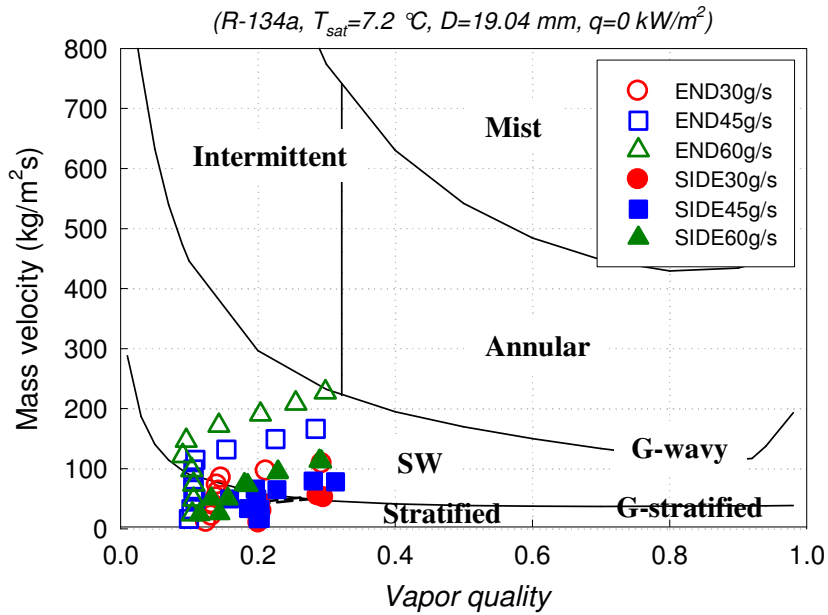


Figure 4.50 Flow pattern map for R-134a based on Thome, J. R. and Hajal, J. E. (2002)

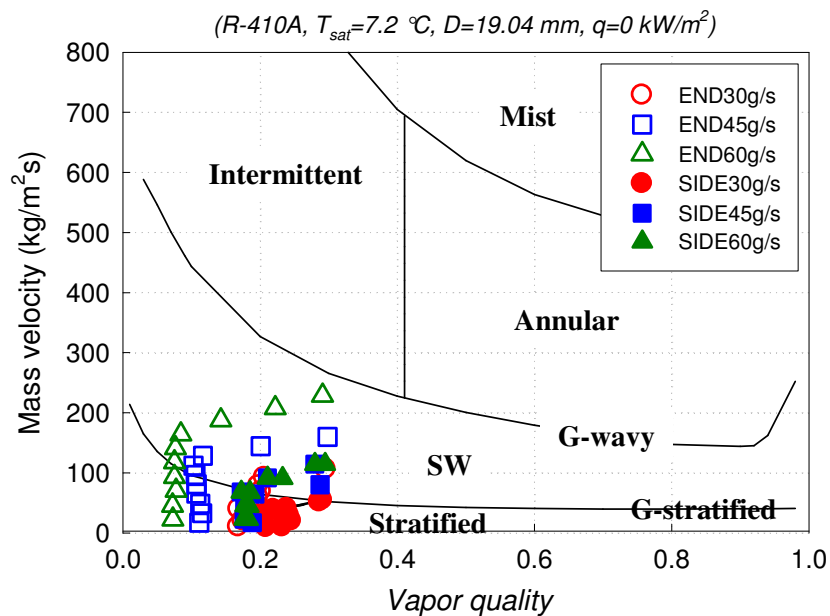


Figure 4.51 Flow pattern map for R-410A based on Thome, J. R. and Hajal, J. E. (2002)

5. MODELING OF REFRIGERANT DISTRIBUTION

5.1 Overview

In this section, modeling of refrigerant distribution using the experimental results is discussed, and test results are compared to two-phase flow distribution models in T-junctions and empirical correlations in manifolds. In addition, new correlations based on the test results are proposed.

5.2 Modeling of Refrigerant Distribution

To simulate the effects of refrigerant flow distribution in microchannel tube heat exchangers (or multiport tube heat exchangers), correlations for the flow distribution in manifolds are needed. Many approaches have been proposed for correlations of flow distribution. One method which can be used for analyzing refrigerant distribution in manifolds is to consider a manifold as a series of successive T-junctions. For using such method to analyze refrigerant distribution, the local properties for the individual tube group along the dividing manifold are needed. The mass flow rates for the dividing manifold inlet ($\dot{m}_{dm,in}$) and the individual branch tube group (\dot{m}_{bt}) were measured. In addition, the vapor qualities for the manifold inlet ($x_{dm,in}$) and the individual tube group ($x_{bt,in}$) were calculated based on the measurements. For better understanding of notations, the related schematic diagram is shown in Figure 5.1.

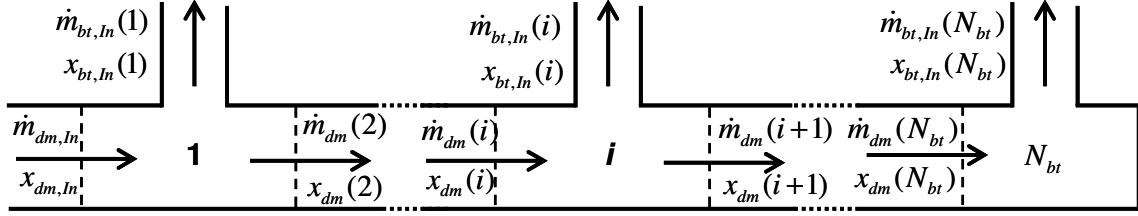


Figure 5.1 Schematic diagram of the dividing manifold

While using the T-junction method for modeling of refrigerant distribution, a correction procedure was introduced in order to consider deviation from the mass balance between the measured manifold inlet mass flow rate ($\dot{m}_{dm,ln}(meas)$) and the sum of the measured branch tube group mass flow rates ($\sum_{i=1}^{N_{bt}} \dot{m}_{bt,ln}(i)(meas)$) due to uncertainties of measurements. A correction factor for the branch tube group mass flow rates is defined as follows;

$$cf\dot{m}_{bt} = \frac{\dot{m}_{dm,ln}(meas)}{\sum_{i=1}^{N_{bt}} \dot{m}_{bt,ln}(i)(meas)} \quad (5.1)$$

Therefore, the corrected branch mass flow rates ($\dot{m}_{bt,ln}(i)$) can be written as Equation 5.2.

$$\dot{m}_{bt,ln}(i) = cf\dot{m}_{bt} \times \dot{m}_{bt,ln}(i)(meas) \quad (5.2)$$

Accordingly, the branch tube inlet vapor quality ($x_{bt,ln}(i)$) was corrected such that the sum of the branch tube group vapor mass flow rates was equal to the manifold inlet vapor

mass flow rate. A correction factor for vapor mass flow rates at the branch tube group ($cf\dot{m}_{bt,vap}$) was defined as follows;

$$cf\dot{m}_{bt,vap} = \frac{\dot{m}_{dm,ln}(meas)x_{dm,ln}(meas)}{\sum_{i=1}^{N_{bt}} [\dot{m}_{bt,ln}(i)x_{bt,ln}(i)(meas)]} \quad (5.3)$$

Therefore, the corrected vapor mass flow rate for the branch tube group can be written as Equation 5.4.

$$\dot{m}_{bt,ln,vap}(i) = cf\dot{m}_{bt,vap}\dot{m}_{bt,ln}(i)x_{bt,ln}(i)(meas) \quad (5.4)$$

Accordingly, the corrected branch tube inlet vapor quality can be calculated as follows:

$$x_{bt,ln}(i) = \frac{\dot{m}_{bt,ln,vap}(i)}{\dot{m}_{bt,ln}(i)} \quad (5.5)$$

Based on the mass conservation, the mass flow rates along the dividing manifold are calculated as follows:

$$\dot{m}_{dm}(i+1) = \dot{m}_{dm}(i) - \dot{m}_{bt,ln}(i) \quad (5.6)$$

In addition, the vapor quality at the local position in the dividing manifold can be calculated by Equation (5.7).

$$x_{dm}(i+1) = \frac{(x_{dm}(i)\dot{m}_{dm}(i) - x_{bt,ln}(i)\dot{m}_{bt,ln}(i))}{\dot{m}_{dm}(i+1)} \quad (5.7)$$

5.3 Comparison To Existing Two-Phase Distribution Model

In this section, the test results are compared to existing two-phase distribution models in T-junctions and in manifolds.

5.3.1 Comparison to models using h/h_b

In this section, the test results are compared to existing two-phase distribution models which use the value of h/h_b representing two major control parameters, liquid level and the vapor flow rate. Smogle et al. (1987) model, Schrock et al. (1986) model and Castiglia and Giardina (2002a) model belong to this type of model. As explained in section 2.6, the models are shown in Equation 2.3, 2.5, and 2.6, respectively.

(1) Smogle et al. (1987) model

$$x = 1 - \left(\frac{1.15}{1 + \sqrt{\rho_l/\rho_g}} \right)^{2\frac{h}{h_b}} \left[1 - \frac{1}{2} \frac{h}{h_b} \left(1 + \frac{h}{h_b} \right) \left(\frac{1.15}{1 + \sqrt{\rho_l/\rho_g}} \right)^{1-\frac{h}{h_b}} \right]^{0.5} \quad (2.3)$$

(2) Schrock et al. (1986) model

$$x_{br} = \left(\frac{h}{h_b} \right)^{3.25 \left(1 - \frac{h}{h_b} \right)^2} \quad (2.4)$$

(3) Castiglia and Giardina (2002a) model

$$\frac{h}{h_b - h} = K \left(\frac{x_3}{1 - x_3} \right)^n \quad (2.5)$$

To compare the test results with such models, it is need to calculate the value of h (distance between the branch tube inlet and the liquid level). To calculate the value of h , it is necessary to estimate void fraction in the manifold. Recently, Thome and El Hajal (2002) have simplified implementation of the map by bringing the Rouhani-Axelsson void fraction equation into the method to remove its iterative solution scheme. Therefore, in the current study, the Rouhani and Axelsson (1970) void model shown in Equation 5.8 was used.

$$\alpha = \frac{1}{\pi} \left[(1 + 0.12(1 - x)) \left(\frac{x}{\rho_g} + \frac{1 - x}{\rho_l} \right) + \frac{1.18(1 - x) [g \sigma (\rho_l - \rho_g)]^{\frac{1}{4}}}{G \rho_l^{0.5}} \right] \quad (5.8)$$

Figure 5.2 and 5.3 show comparison of the void fraction for R-134a and R-410A, respectively. At low vapor quality, the void fraction calculated by the Rouhani and Axelsson (1970) void model is a little higher than that by the Zivi model (1964). In addition, the void fraction for R-134a is higher than that for R-410A.

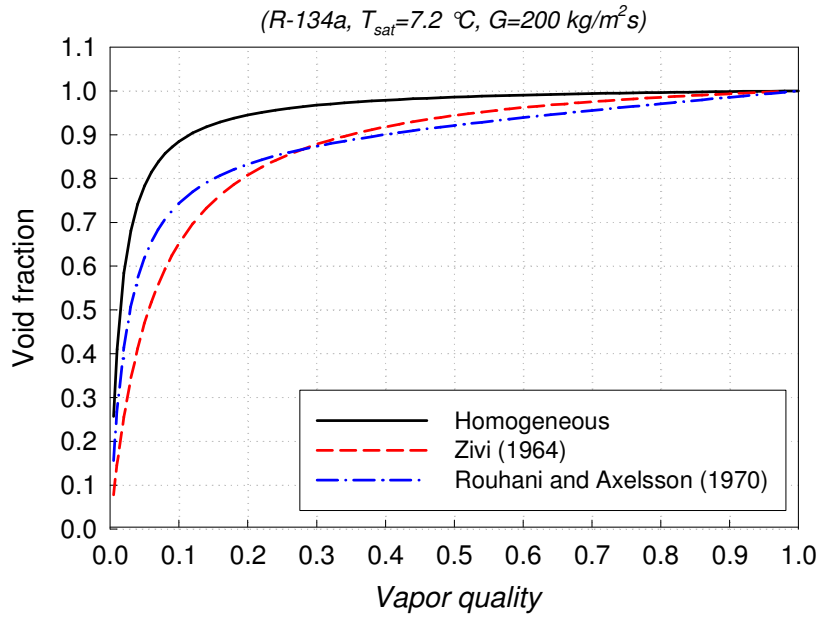


Figure 5.2 Comparison of void fraction for R-134a

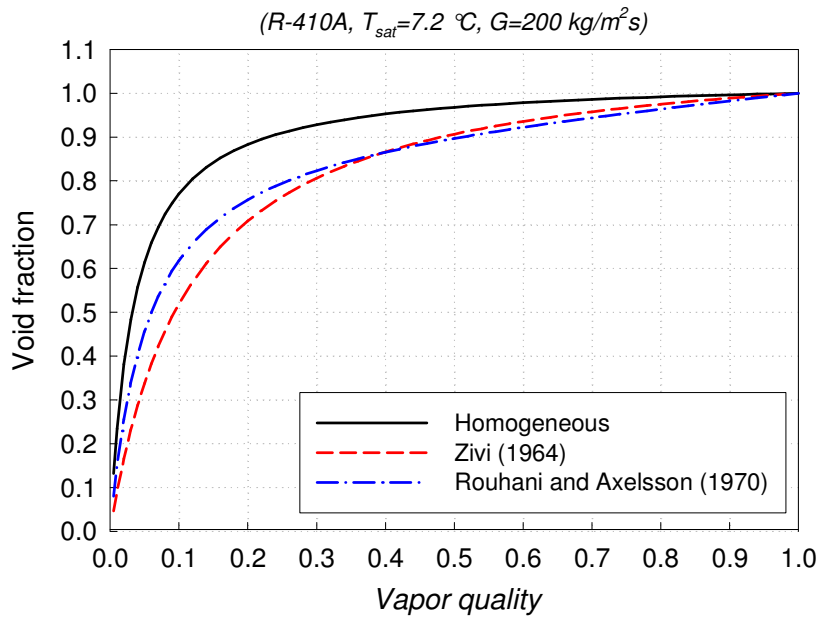


Figure 5.3 Comparison of void fraction for R-410A

Figure 5.4 shows comparison of the two-phase distribution model which use the normalized parameter, h/h_b . The branch tube inlet vapor quality is shown in Figure 5.4 as a function of the normalized parameter, h/h_b . As the normalized parameter, h/h_b increases, the branch tube inlet vapor quality increases. The predicted branch tube inlet quality by the Smoglie et al. (1987) is much higher than other two models at lower value of h/h_b .

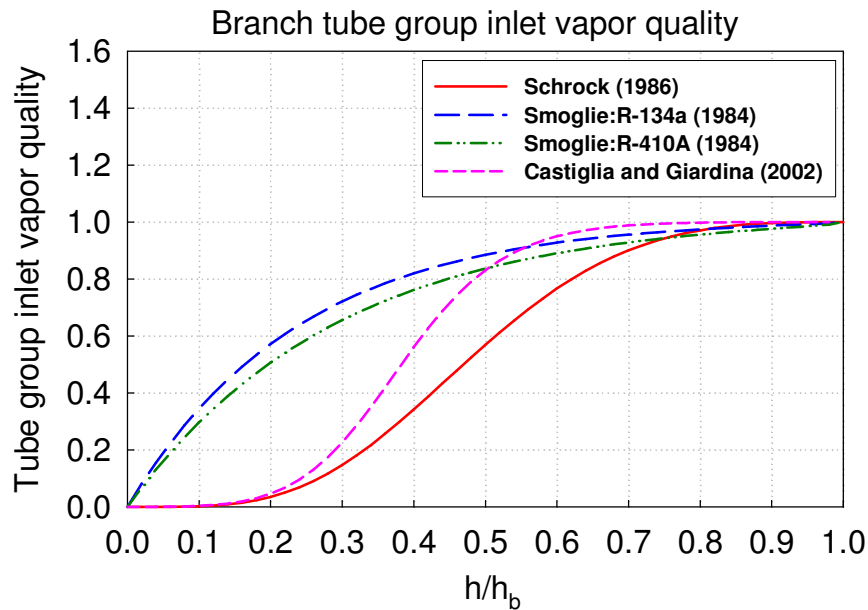


Figure 5.4 Comparison of T-junction models (branch tube vapor quality vs. h/h_b)

Figures 5.5 and 5.6 show comparison of test results for R-134a with T-junction models for $\dot{m}_{dm,in} = 30$ g/s and 60 g/s, respectively. The branch tube group inlet vapor quality is shown in Figures 5.5 and 5.6 as a function of branch tube group number. As shown in Figures 5.5 and 5.6, the predicted tube inlet vapor quality by the T-junction models deviates a lot from the test results. Based on the comparison, it is observed that the poor prediction occurs due to different geometry and operating conditions.

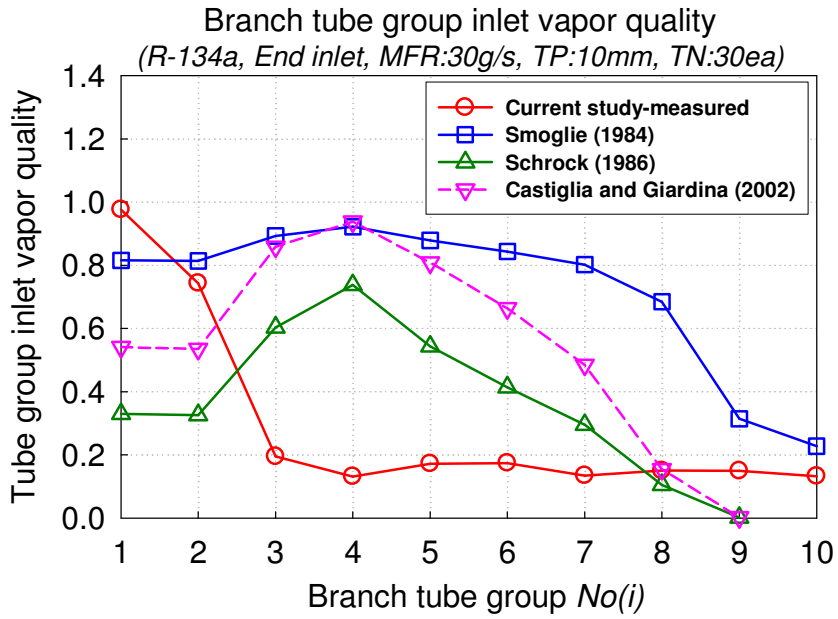


Figure 5.5 Comparison of test results with T-junction models

(R-134a, End inlet, $\dot{m}_{dm,In} = 30$ g/s)

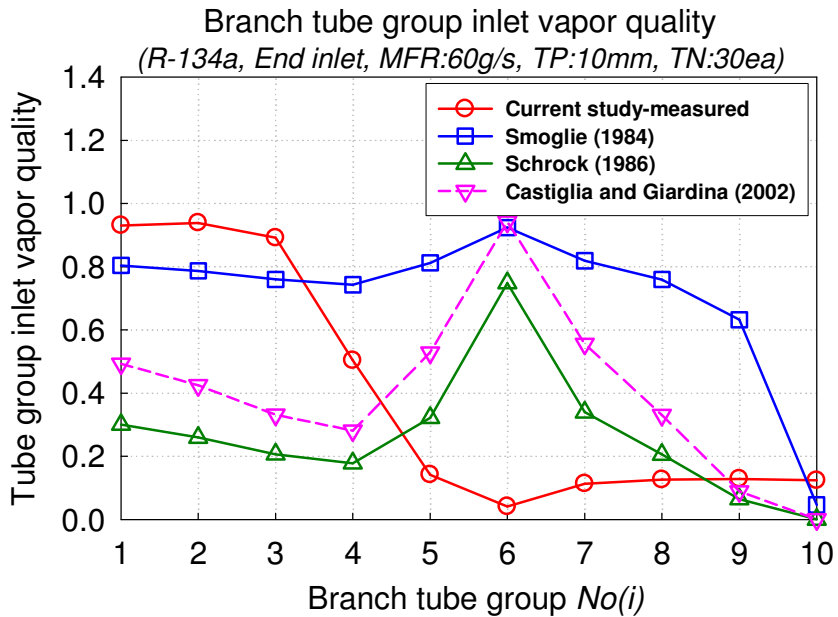


Figure 5.6 Comparison of test results with T-junction models

(R-134a, End inlet, $\dot{m}_{dm,In} = 60$ g/s)

5.3.2 Comparison to Seeger et al. model and Sivert Vist model

In this section, the test results are compared to Seeger et al. (1985) model and Sivert Vist (2003) model. As explained in section 2.6, Seeger et al. (1985) model is shown in Equation 2.1.

$$x_3/x_1 = (G_3/G_1)^{-0.8} \quad (2.1)$$

As explained in section 2.7, Sivert Vist (2003) model is shown in Equations 2.10, 2.11, and 2.12.

$$CLTF = (\dot{m}_{l,t} / \dot{m}_{l,m})_{const} = -1.055 + e^{\frac{1.450}{A_c \times 10^5 + 7.248}} \quad (2.10)$$

$$G_{g,m,lim} = 4.471 + e^{\frac{103.4}{A_c \times 10^5 + 18.07}} \quad (2.11)$$

$$G_{g,m} < G_{g,m,lim} : x_t = \frac{G_{g,m}}{G_{g,m,lim}} \quad (2.12)$$

$$G_{g,m} > G_{g,m,lim} : x_t = 1$$

Figures 5.7 and 5.8 show comparison of test results for R-134a with Seeger et al. (1985) model and Sivert Vist (2003) model for $\dot{m}_{dm,in} = 30$ g/s and 60 g/s, respectively. The branch tube group inlet vapor quality is shown in Figures 5.7 and 5.8 as a function of branch tube group number. As shown in Figures 5.7 and 5.8, the predicted tube inlet

vapor quality by the two models deviates from the test results. Figures 5.9 and 5.10 show comparison of test results for R-410A with Seeger et al. (1985) model and Sivert Vist (2003) model for $\dot{m}_{dm,in} = 30$ g/s and 60 g/s, respectively. The branch tube group inlet vapor quality is shown in Figures 5.9 and 5.10 as a function of branch tube group number. As shown in Figures 5.9 and 5.10, the predicted tube inlet vapor quality by the two models deviates from the test results. Based on the comparison, it is observed that the deviation occurs due to different geometry and operating conditions.

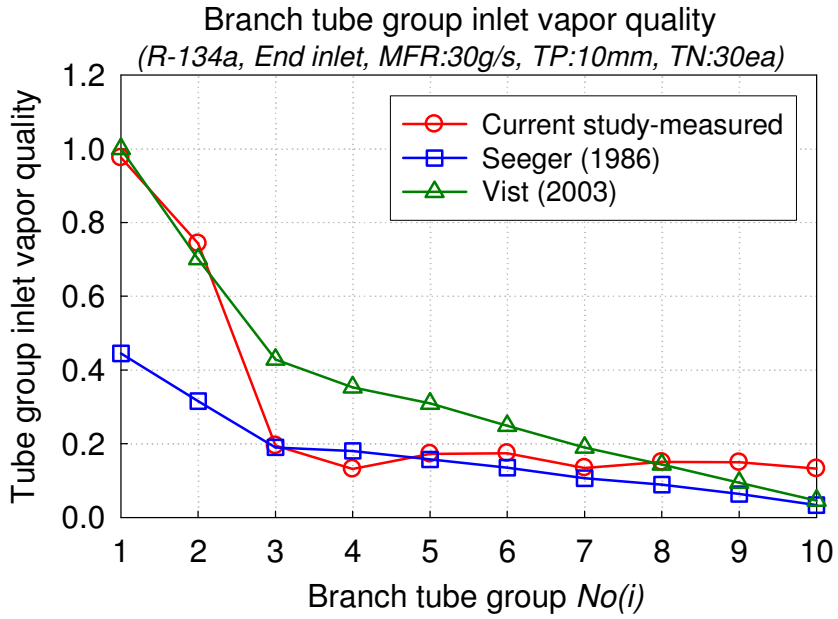


Figure 5.7 Comparison of test results with Seeger model and Vist model

(R-134a, End inlet, $\dot{m}_{dm,in} = 30 \text{ g/s}$)

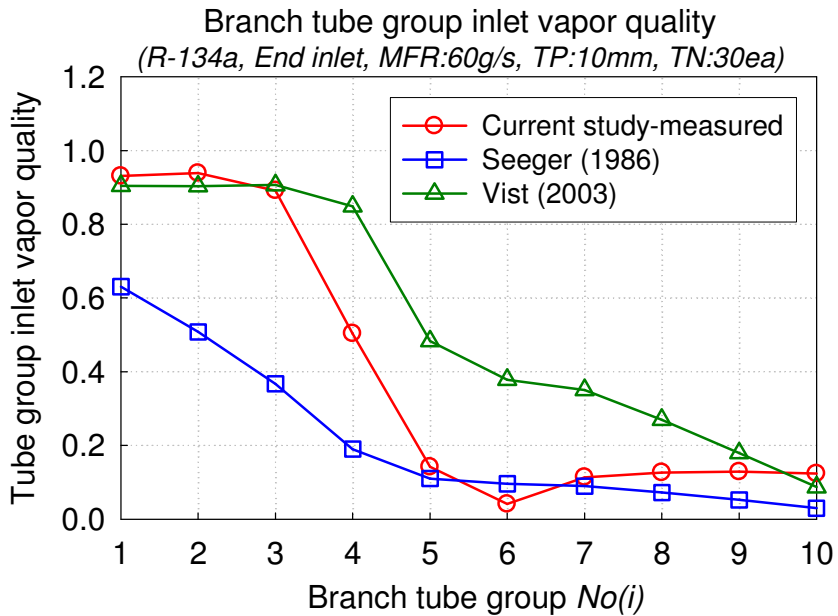


Figure 5.8 Comparison of test results with Seeger model and Vist model

(R-134a, End inlet, $\dot{m}_{dm,in} = 60 \text{ g/s}$)

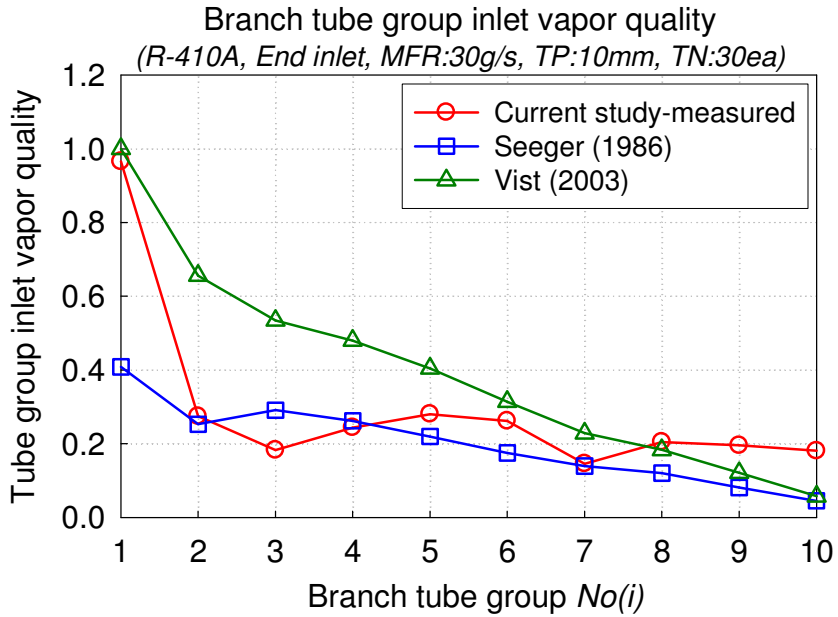


Figure 5.9 Comparison of test results with Seeger model and Vist model

(R-410A, End inlet, $\dot{m}_{dm,In} = 30 \text{ g/s}$)

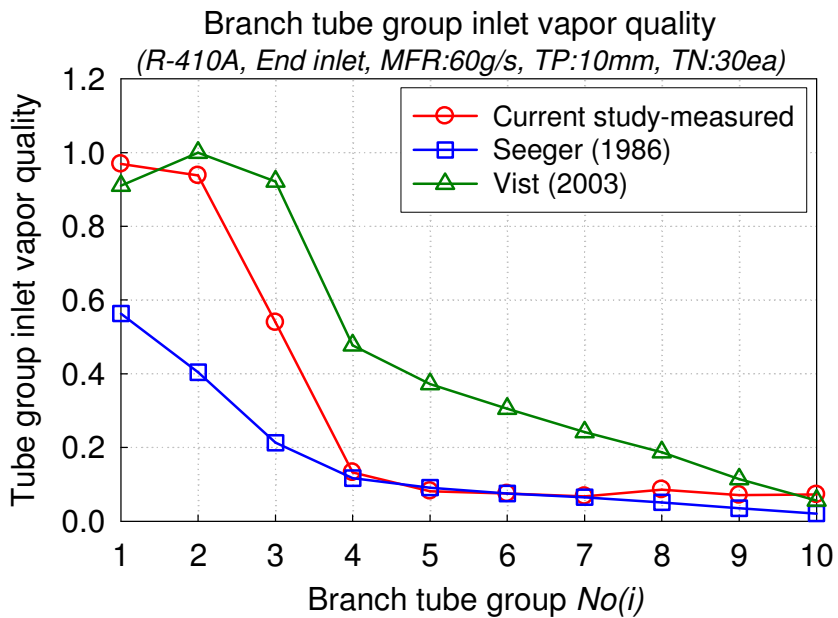


Figure 5.10 Comparison of test results with Seeger model and Vist model

(R-410A, End inlet, $\dot{m}_{dm,In} = 60 \text{ g/s}$)

5.3.3 Comparison to the model of Watanabe

In this section, the test results of the current study are compared to Watanabe et al. (1995) model. As explained in section 2.8, Watanabe et al. (1995) developed an empirical correlation based on the experiments in a 20 mm inner diameter manifold with four upward 6 mm inner diameter branch tubes using R-11. The correlation is shown in Equations 2.7 and 2.8.

$$G_{bt,In,vap}(i) = 6.07G_{dm,vap}(i) \quad (2.7)$$

$$\frac{\dot{m}_{bt,In,liq}(i)}{\dot{m}_{dm,liq}(i)} = 2.74 \times 10^{-5} \eta^2 - 0.0124\eta + 1.37, \text{ where } \eta = \sqrt{\text{Re}_{dm,vap}(i)} \quad (2.8)$$

Even though the heat exchanger geometry which was used in the current study is different from their geometry, the test results in the manifold with 10 mm tube pitch and 30 tubes (10 tube groups) were compared with the empirical model. For better understanding of the manifold geometry for the Watanabe's study and the current study, the geometries are compared in Table 5.1. The tube number and the cross sectional area of the branch tube for the Watanabe's study are smaller than those for the current study when the branch tubes for the current study are considered as the branch tube groups.

Table 5.1 Comparison of manifold geometry

		Watanabe's study	Current study
Manifold inner diameter (mm)		20	19.05
Branch tube	Geometry	Round Tube	Multiport Tube
	Number (ea)	4	30 (10 tube groups)
	Cross sectional area (mm ²) per tube	28.3	18.7 (per tube) 56.1 (per tube group)
	Tube pitch (mm)	40	10 (per tube) 30 (per tube group)

5.3.3.1 Comparison of test results in the manifold for the side inlet

Since two inlet locations were used in this study, first, the test results in the manifold for the side inlet are compared to the Watanabe model in this section. Figures 5.11 and 5.12 show the branch tube vapor mass flux ($G_{bt,In,vap}(i)$) as a function of the vapor mass flux at the inlet of the manifold T-junction ($G_{dm,vap}(i)$) for R-410A and R-134a, respectively, for the side inlet test. Test results for 0 and 5 kW are shown in Figures 5.11 and 5.12, and the dashed line in the Figures represents the prediction from the Watanabe correlation. In the Figures, data points having the highest manifold vapor mass flux are the data of the branch tube group No. 1, and data points with decreasing manifold vapor mass flux represent the data of the successive branch tube groups. As shown in the Figures, the relationship between the branch tube vapor mass flux and the manifold vapor mass flux at the inlet of T-junctions shows linear relation between the two vapor mass fluxes for the two refrigerants. For the Watanabe's study, the data range of the manifold vapor mass flux is 0 ~ 37 kg/m²s. Based on that, the data range of the manifold vapor mass flux is almost similar for both Watanabe's study and the side inlet cases of the current study. However, for both refrigerants, the slope of the prediction by Watanabe correlation is

steeper than that for this side inlet case of the current study. Based on these results, it is seen that the relationship between the two vapor mass fluxes is affected by both the local vapor mass flux at the inlet of T-junctions and the manifold inlet flow conditions, which are the manifold inlet vapor mass flux and the inlet geometry. As shown in Figures 5.11 and 5.12, the slopes of the linear relation between the branch tube vapor mass flux and the manifold vapor mass flux at the inlet of T-junctions for the two refrigerants are almost similar.

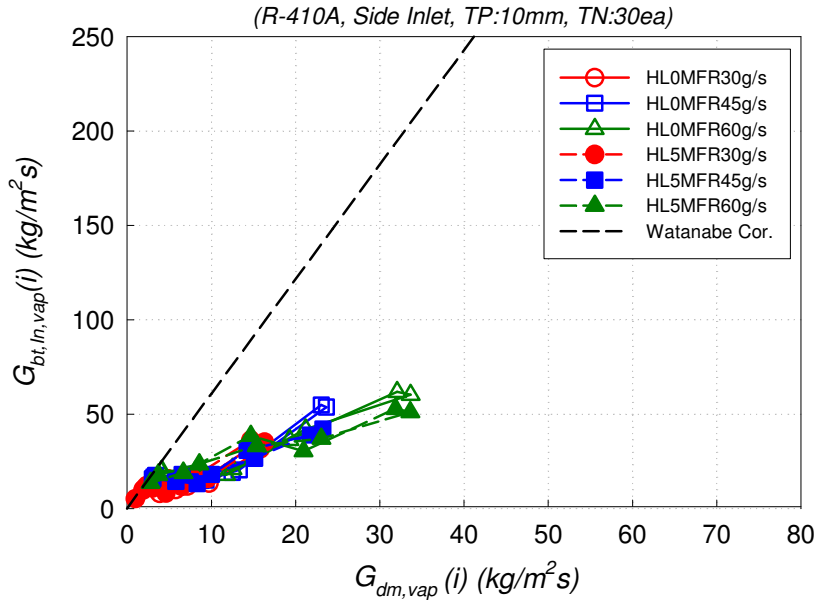


Figure 5.11 Branch vapor mass flux ($G_{bt,In,vap}(i)$) vs. the vapor mass flux at the inlet of the manifold T-junctions ($G_{dm,vap}(i)$) for R-410A, side inlet (Measurements for heat load 0 kW and 5 kW are shown, and the prediction of Watanabe correlation is shown for comparison.)

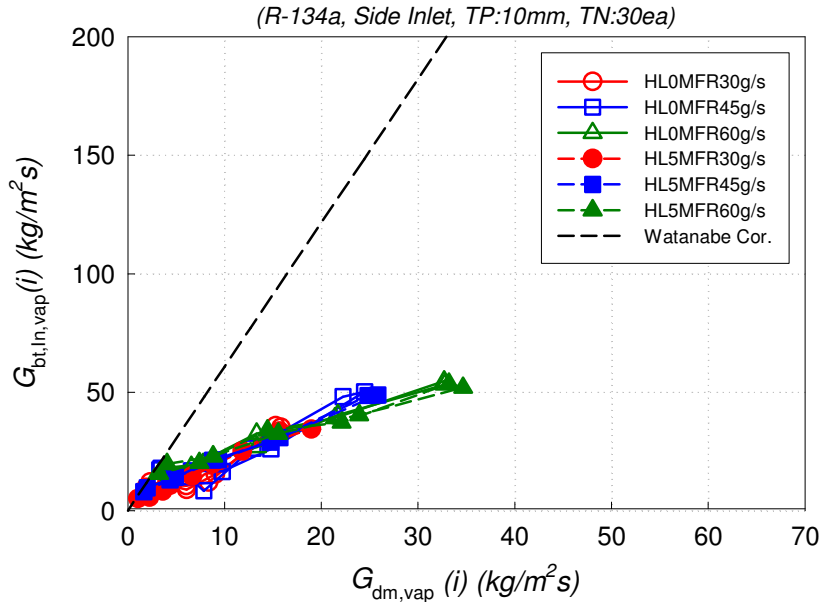


Figure 5.12 Branch vapor mass flux ($G_{bt,In,vap}(i)$) vs. the vapor mass flux at the inlet of the manifold T-junctions ($G_{dm,vap}(i)$) for R-134a, side inlet (Measurements for heat load 0 kW and 5 kW are shown, and the prediction of Watanabe correlation is shown for comparison.)

Figures 5.13 and 5.14 show the branch tube liquid fraction taken off ($\dot{m}_{bt,ln,liq}(i) / \dot{m}_{dm,liq}(i)$) as a function of the vapor Reynolds number at the inlet of T-junctions in the manifold ($\sqrt{\text{Re}_{dm,vap}(i)}$) for R-410A and R-134a, respectively, for the side inlet test. Test results for 0 and 5 kW are shown in the Figures, and the dashed line in the Figures represents the prediction from the Watanabe correlation. For the Watanabe's study, the data range of the vapor Reynolds number in the manifold ($\sqrt{\text{Re}_{dm,vap}(i)}$) is 0 ~ 220. Based on that, the data range of the vapor Reynolds number in the manifold ($\sqrt{\text{Re}_{dm,vap}(i)}$) is almost similar for both Watanabe's study and the side inlet case of the current study. In Figures 5.13 and 5.14, the branch tube liquid fraction taken off ($\dot{m}_{bt,ln,liq}(i) / \dot{m}_{dm,liq}(i)$) is found to decrease with increasing vapor Reynolds number in the manifold ($\sqrt{\text{Re}_{dm,vap}(i)}$). The trend for the test results in this study is quite similar to the prediction from the Watanabe model. Based on this comparison, it is assumed that the branch tube liquid fraction taken off for the side inlet case of the current study can be correlated as a function of the vapor Reynolds number at the inlet of the manifold T-junctions in the manifold. As shown in Figures 5.13 and 5.14, the trend of the relationship between the branch tube liquid fraction taken off ($\dot{m}_{bt,ln,liq}(i) / \dot{m}_{dm,liq}(i)$) and the vapor Reynolds number at the inlet of T-junctions in the manifold ($\sqrt{\text{Re}_{dm,vap}(i)}$) for the two refrigerants is almost similar.

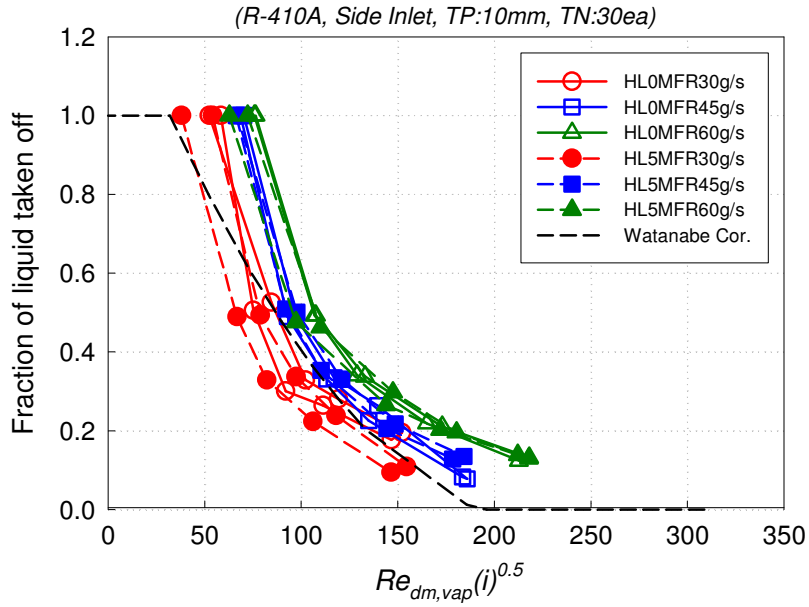


Figure 5.13 Branch tube liquid fraction taken off ($\dot{m}_{bt,In,liq}(i)/\dot{m}_{dm,liq}(i)$) vs. $\sqrt{Re_{dm,vap}(i)}$ for R-410A, side inlet (Measurements for heat load 0 kW and 5 kW are shown, and the prediction of Watanabe correlation is shown for comparison.)

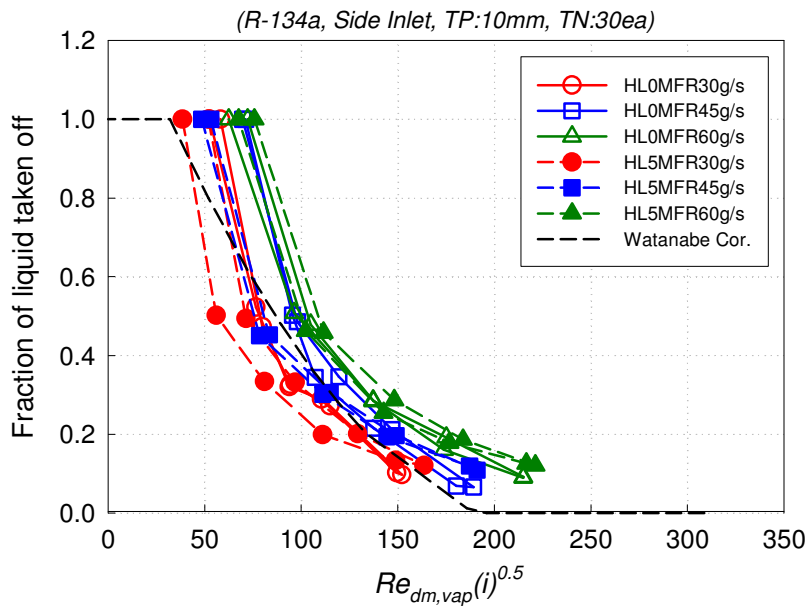


Figure 5.14 Branch tube liquid fraction taken off ($\dot{m}_{bt,In,liq}(i)/\dot{m}_{dm,liq}(i)$) vs. $\sqrt{Re_{dm,vap}(i)}$ for R-134a, side inlet (Measurements for heat load 0 kW and 5 kW are shown, and the prediction of Watanabe correlation is shown for comparison.)

5.3.3.2 Comparison of test results in the manifold for the end inlet

In this section, the test results in the manifold for the end inlet are compared to the Watanabe model. Figures 5.15 and 5.16 show the branch tube vapor mass flux ($G_{bt,In,vap}(i)$) as a function of the vapor mass flux at the inlet of the manifold T-junctions ($G_{dm,vap}(i)$) for R-410A and R-134a, respectively, for the end inlet conditions. Test results for 0 and 5 kW are shown in the Figures, and the dashed lines in the Figures represent the prediction from the Watanabe correlation. In the Figures, data points having the highest manifold vapor mass flux are the data of the branch tube group No. 1, and data points with decreasing manifold vapor mass flux represent the data of the successive branch tube groups. Unlike the side inlet case, for the end inlet case of the current study, there exist non-linear regions between the branch tube vapor mass flux ($G_{bt,In,vap}(i)$) and the vapor mass flux at the inlet of the manifold T-junctions ($G_{dm,vap}(i)$). In addition, the prediction by Watanabe correlation deviates a lot from the test results. However, Figures 5.15 and 5.16 show a relationship between the branch tube inlet vapor mass flux and the manifold vapor mass for the current study, which means that there are three regions depending upon the manifold vapor mass flux. In a region above a certain manifold vapor mass flux depending upon the manifold inlet mass flow rate, the branch tube inlet vapor mass flux is almost constant. At a region below a certain manifold vapor mass flux, the branch tube inlet vapor mass flux is almost constant. For a region in between the two regions, the branch tube inlet vapor mass flux is proportional to the manifold inlet vapor mass flux similar to Watanabe's correlation. In general, the trend is quite different from that for the Watanabe model. At high manifold vapor mass flux, the relationship between the two vapor mass fluxes deviates from the linear relation predicted by Watanabe's

model. This can be explained by the difference of test conditions. For the Watanabe's study, the data range of the manifold vapor mass flux is 0 ~ 37 kg/m²s, but for the current study, the data range is 0 ~ 67 kg/m²s. Based on that, the manifold vapor mass flux for Watanabe's data covers a narrower data region than that for the current study. That's why the relation by the model does not show any nonlinear behavior. In addition to that, it is known that based on the comparison of test results between both inlet locations, the vapor flow distribution is strongly affected by flow regime. In addition, at low manifold vapor mass flux, the behavior is different between the model and the current study.

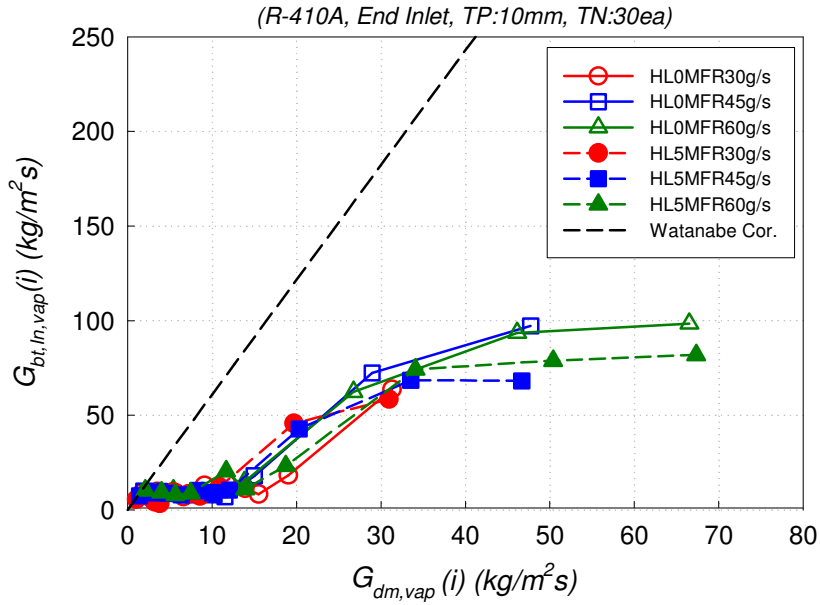


Figure 5.15 Branch tube vapor mass flux ($G_{bt,in,vap}(i)$) vs. the vapor mass flux at the inlet of the manifold T-junction ($G_{dm,vap}(i)$) for R-410A, end inlet (Measurements for heat load 0 kW and 5 kW are shown, and the prediction of Watanabe correlation is shown.)

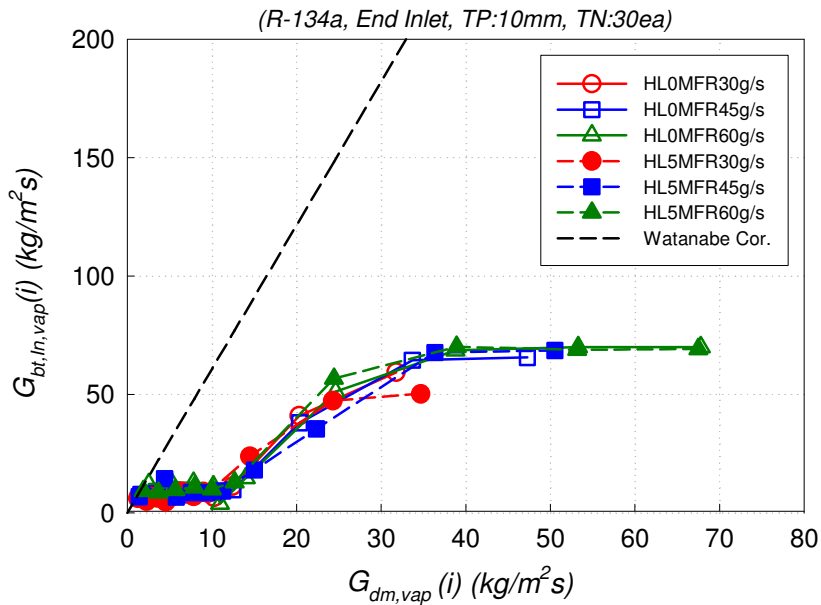


Figure 5.16 Branch tube vapor mass flux ($G_{bt,in,vap}(i)$) vs. the vapor mass flux at the inlet of the manifold T-junction ($G_{dm,vap}(i)$) for R-134a, end inlet (Measurements for heat load 0 kW and 5 kW are shown, and the prediction of Watanabe correlation is shown.)

Figures 5.17 and 5.18 show the branch tube liquid fraction taken off ($\dot{m}_{bt,In,liq}(i)/\dot{m}_{dm,liq}(i)$) as a function of the vapor Reynolds number at the inlet of T-junctions in the manifold ($\sqrt{\text{Re}_{dm,vap}(i)}$) for R-410A and R-134a, respectively, for the end inlet test. Test results for 0 kW and 5 kW are shown in the Figures 5.17 and 5.18, and the dashed line in Figures 5.17 and 5.18 represents the prediction from the Watanabe correlation. In Figures 5.17 and 5.18, the branch tube liquid fraction taken off ($\dot{m}_{bt,In,liq}(i)/\dot{m}_{dm,liq}(i)$) decreases with increasing vapor Reynolds number in the manifold ($\sqrt{\text{Re}_{dm,vap}(i)}$). For the Watanabe's study, the data range of the vapor Reynolds number in the manifold ($\sqrt{\text{Re}_{dm,vap}(i)}$) is 0 ~ 220, but for the current study, the data range of the vapor Reynolds number in the manifold ($\sqrt{\text{Re}_{dm,vap}(i)}$) is 0 ~ 320. However, as shown in Figures 5.17 and 5.18, the trend for the test results in the current study is quite similar to the prediction from the Watanabe model. Based on this comparison, it is assumed that the branch tube liquid fraction taken off for the end inlet case of the current study can be correlated as a function of vapor Reynolds number at the inlet of the manifold T-junctions too. As shown in Figures 5.17 and 5.18, the trend of the relationship between the branch tube liquid fraction taken off ($\dot{m}_{bt,In,liq}(i)/\dot{m}_{dm,liq}(i)$) and the vapor Reynolds number at the inlet of T-junctions in the manifold ($\sqrt{\text{Re}_{dm,vap}(i)}$) for the two refrigerants is almost similar.

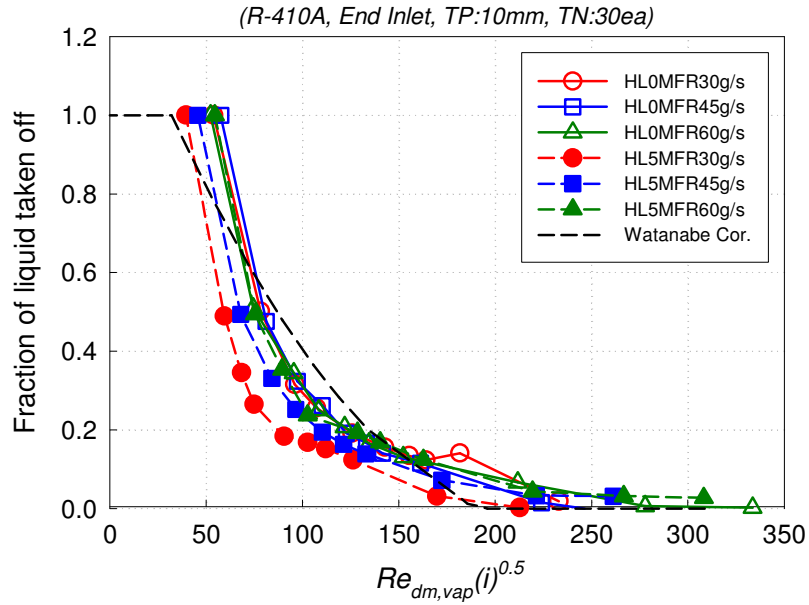


Figure 5.17 Branch tube liquid fraction taken off ($\dot{m}_{bt,In,liq}(i)/\dot{m}_{dm,liq}(i)$) vs. $\sqrt{Re_{dm,vap}(i)}$ for R-410A, end inlet (Measurements for heat load 0 and 5 kW are shown, and the prediction of Watanabe correlation is shown for comparison.)

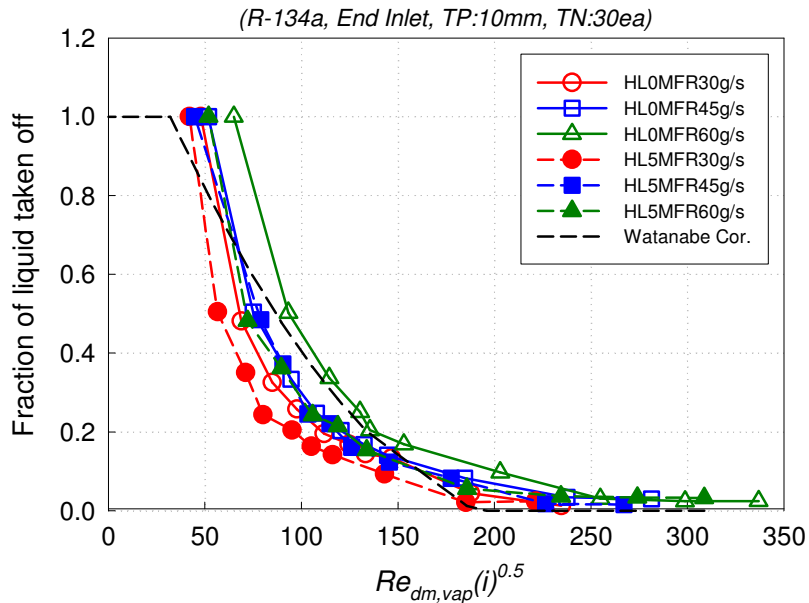


Figure 5.18 Branch tube liquid fraction taken off ($\dot{m}_{bt,In,liq}(i)/\dot{m}_{dm,liq}(i)$) vs. $\sqrt{Re_{dm,vap}(i)}$ for R-134a, end inlet (Measurements for heat load 0 kW and 5 kW are shown, and the prediction of Watanabe correlation is shown for comparison.)

5.4 Model

In the previous section 5.3.3, it was shown that both vapor fraction taken off and the liquid fraction taken off could be correlated with the vapor flow properties in the manifold. The relationships between the branch tube vapor mass flux and manifold vapor mass flux, and between the liquid fraction of taken off and the vapor Reynolds number had different relationships for different inlet cases. Using the same T-junction approach with Watanabe's, the correlation for the refrigerant distribution in the manifold is proposed as follows for each inlet.

5.4.1 Model for the side inlet conditions

First, the correlation for the side inlet conditions was developed. As shown in Figures 5.11 and 5.12, the relationship between the branch tube vapor mass flux and the manifold vapor mass flux at the inlet of T-junctions showed linear relation between the two vapor mass fluxes for the two refrigerants. Therefore, first, the correlation using the relationship between the branch tube vapor mass flux and the manifold vapor mass flux at the inlet of T-junctions was tested. Figures 5.19 and 5.20 show the comparison of correlation with measured data based on the relationship between the branch vapor mass flux ($G_{bt,In,vap}(i)$) and the vapor mass flux at the inlet of the manifold T-junctions ($G_{dm,vap}(i)$) for R-410A and R-134a, respectively, for the side inlet case. Figures 5.19 and 5.20 show the branch vapor mass flux ($G_{bt,In,vap}(i)$) as a function of the vapor mass flux at the inlet of the manifold T-junctions ($G_{dm,vap}(i)$) for R-410A and R-134a, respectively, for the side inlet case. As shown in Figures 5.19 and 5.20, the prediction deviates substantially from the

measured data for the two refrigerants at a region, where the manifold vapor mass flux ($G_{dm,vap}(i)$) is smaller than $10 \text{ kg/m}^2\text{s}$. For proposing better correlation for the vapor phase, the relationship between the measured branch tube inlet vapor quality and the manifold vapor mass flux at the inlet of T-junctions in the manifold was considered. In addition, considering the inlet flow conditions, the normalized manifold vapor mass flux ($G_{dm,vap}(i)/G_{dm,in,vap}$) was introduced. To develop the correlation for the vapor phase with the side inlet, the measured branch tube inlet vapor quality is plotted for the R-410A and R-134a, respectively, in Figures 5.21 and 5.22 as a function of the normalized manifold vapor mass flux at the inlet of T-junctions in the manifold.

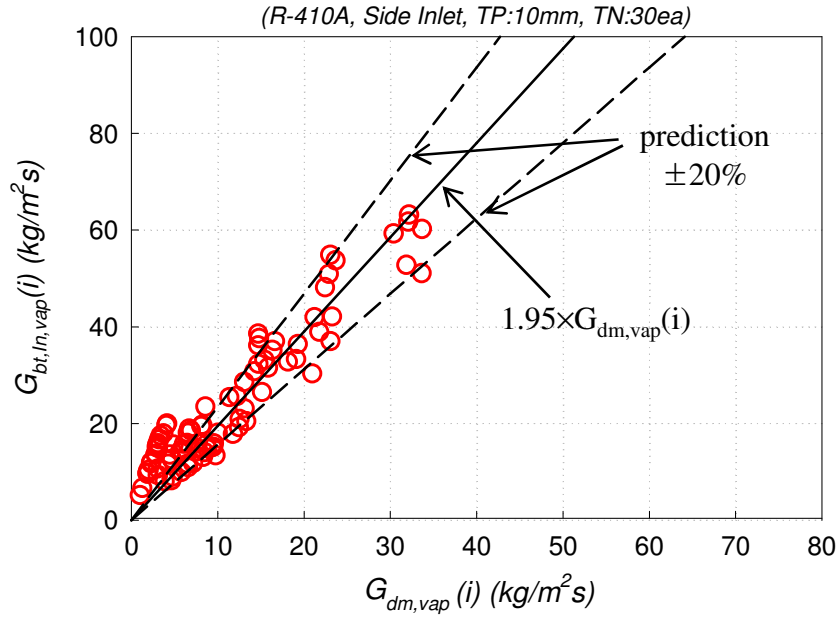


Figure 5.19 Comparison of correlation with measured data based on the relationship between the branch vapor mass flux ($G_{bt,In,vap}(i)$) and the vapor mass flux at the inlet of the manifold T-junctions ($G_{dm,vap}(i)$) for R-410A, side inlet

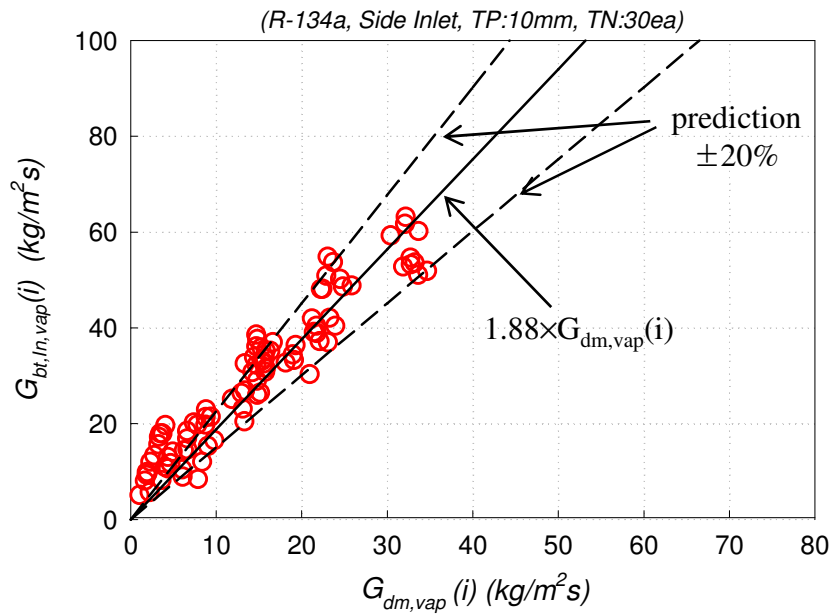


Figure 5.20 Comparison of correlation with measured data based on the relationship between the branch vapor mass flux ($G_{bt,In,vap}(i)$) and the vapor mass flux at the inlet of the manifold T-junctions ($G_{dm,vap}(i)$) for R-134a, side inlet

As shown in Figures 5.21 and 5.22, there exists a constant inlet vapor quality region below 0.2 of the normalized manifold vapor mass flux. In addition, for a region above 0.2, the measured branch tube inlet vapor quality increases as the normalized manifold vapor mass flux increases. After considering these observations, simple correlations are proposed in a modified form of Watanabe model for the side inlet in Equation 5.9 as follows;

$$\begin{aligned}
 \text{For } R-410A; \quad G_{dm,vap}(i)/G_{dm,In,vap} \leq 0.2 \quad & x_{bt,In}(i) = 0.205 \\
 0.2 < G_{dm,vap}(i)/G_{dm,In,vap} & \\
 x_{bt,In}(i) = 1.389 \times G_{dm,vap}(i)/G_{dm,In,vap} - 0.073 & \\
 & (5.9)
 \end{aligned}$$

$$\begin{aligned}
 \text{For } R-134a; \quad G_{dm,vap}(i)/G_{dm,In,vap} \leq 0.2 \quad & x_{bt,In}(i) = 0.188 \\
 0.2 < G_{dm,vap}(i)/G_{dm,In,vap} & \\
 x_{bt,In}(i) = 1.341 \times G_{dm,vap}(i)/G_{dm,In,vap} - 0.012 &
 \end{aligned}$$

In addition, for comparison, the predicted branch tube inlet vapor quality is shown in Figures 5.21 and 5.22. For the R-410A test with the side inlet, as can be seen in Figures 5.21, 70% of the measured branch tube inlet vapor quality data are within the branch tube inlet vapor quality ± 0.05 , and 91% of the measured branch tube inlet vapor quality are within the predicted branch tube inlet vapor quality ± 0.1 . For the R-134a test with the side inlet, as can be seen in Figures 5.22, 67% of the measured branch tube inlet vapor quality data are within the branch tube inlet vapor quality ± 0.05 , and 92% of the measured branch tube inlet vapor quality are within the predicted branch tube inlet vapor quality ± 0.1 .

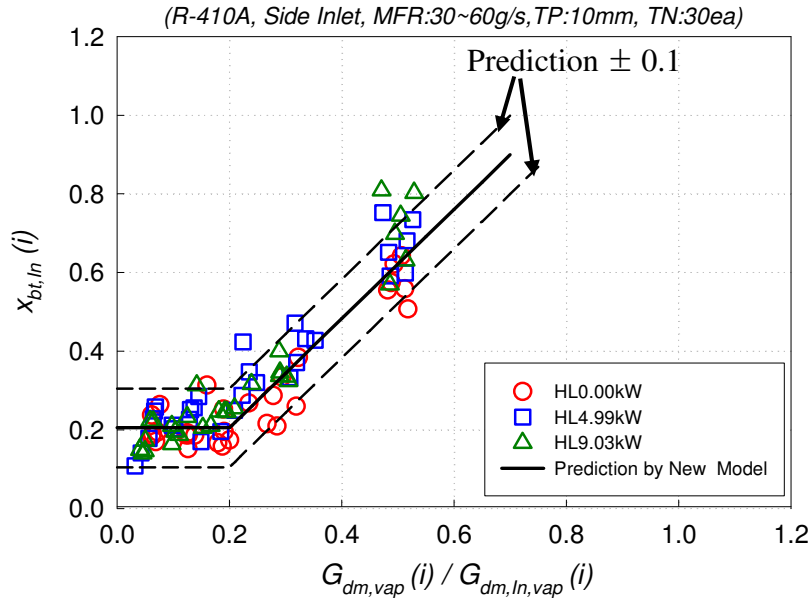


Figure 5.21 Measured branch tube inlet vapor quality ($x_{bt,In}(i)$) vs. the normalized vapor mass flux ($G_{dm,vap}(i) / G_{dm,In,vap}(i)$) for R-410A, side inlet

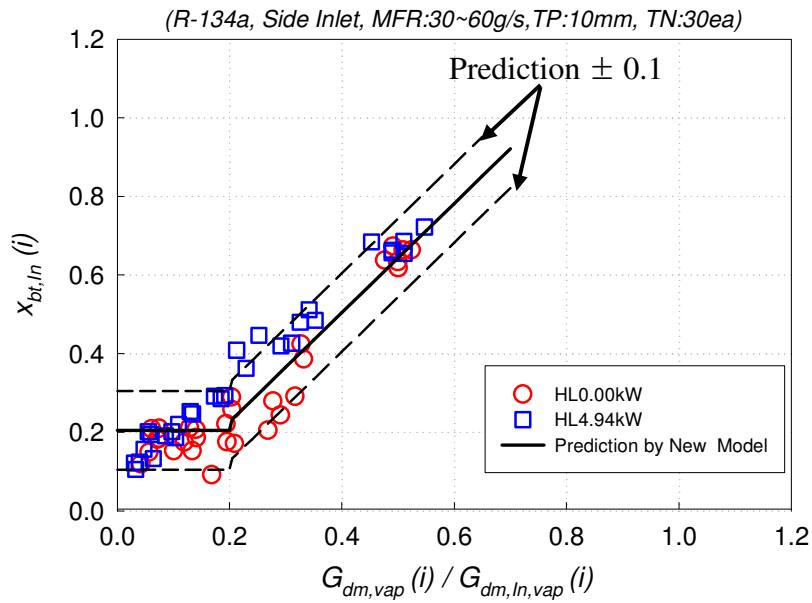


Figure 5.22 Measured branch tube inlet vapor quality ($x_{bt,In}(i)$) vs. the normalized vapor mass flux ($G_{dm,vap}(i) / G_{dm,In,vap}(i)$) for R-134a, side inlet

For the liquid fraction taken off, the liquid fraction taken off is plotted for the R-410A and R-134a, respectively, in Figures 5.23 and 5.24 as a function of the normalized vapor Reynolds number at the inlet of T-junctions in the manifold. Figures 5.23 and 5.24 show the clear relationship between the liquid fraction taken off and the normalized vapor Reynolds number, that is, at a region below a certain normalized vapor Reynolds number, the liquid fraction taken off equals unity, and at a region above the normalized vapor Reynolds number, the liquid fraction taken off decreases with increasing normalized vapor Reynolds number. Based on the relationship, simple equations for the liquid fraction taken off are proposed for R-410A and R-134a in Equation 5.10.

$$\begin{aligned}
 &x \leq 0.22; \quad y = 1 \\
 &x > 0.22; \quad y = \left(a + \frac{b}{x^{1.5}} \right) \\
 &\text{where } y = \dot{m}_{bt,In,liq}(i) / \dot{m}_{dm,liq}(i), \quad x = \sqrt{\text{Re}_{dm,vap}(i)} / \sqrt{\text{Re}_{dm,In,vap}} \quad (5.10) \\
 &\text{For R-410A; } a = -0.046, \quad b = 0.113 \\
 &\text{For R-134a; } a = -0.021, \quad b = 0.099
 \end{aligned}$$

In addition, for comparison, the predicted fraction of liquid taken off is shown in Figures 5.23 and 5.24. For the R-410A test with the side inlet, as can be seen in Figure 5.23, 69% of the measured fraction of liquid taken off data are within the predicted fraction of liquid taken off ± 0.05 , and 86% of the measured fraction of liquid taken off data are within the predicted fraction of liquid taken off ± 0.1 . For the R-134a test with the side inlet, as can be seen in Figure 5.24, 67% of the measured fraction of liquid taken off data are within the predicted fraction of liquid taken off ± 0.05 , and 85% of the measured fraction of liquid taken off data are within the predicted fraction of liquid taken off ± 0.1 .

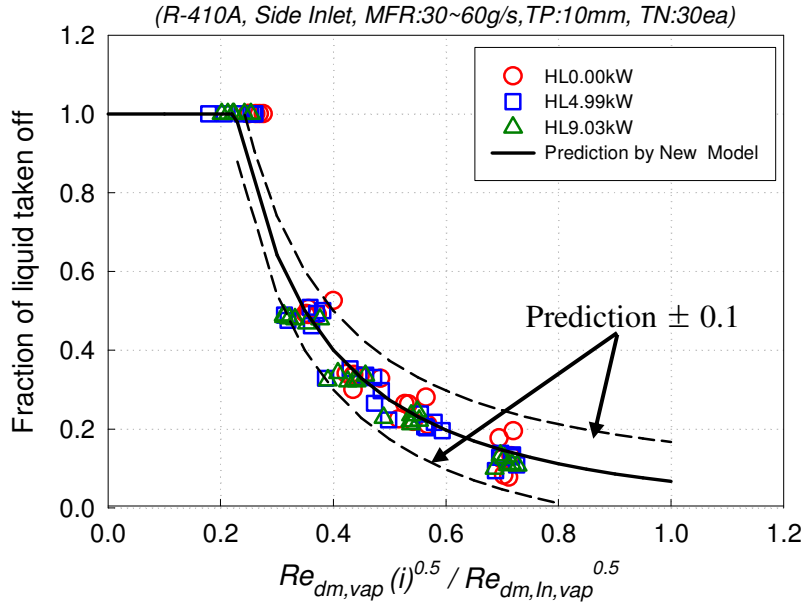


Figure 5.23 Branch tube liquid fraction taken off ($\dot{m}_{bt,ln,liq}(i) / \dot{m}_{dm,liq}(i)$) vs. the normalized Reynolds number ($\sqrt{Re_{dm,vap}(i)} / \sqrt{Re_{dm,ln,vap}}$) for R-410A, side inlet

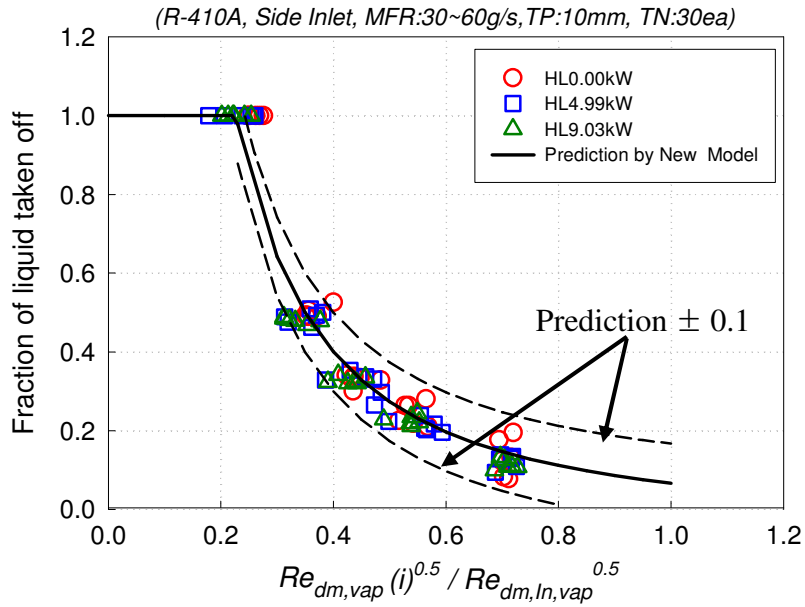


Figure 5.24 Branch tube liquid fraction taken off ($\dot{m}_{bt,ln,liq}(i) / \dot{m}_{dm,liq}(i)$) vs. the normalized Reynolds number ($\sqrt{Re_{dm,vap}(i)} / \sqrt{Re_{dm,ln,vap}}$) for R-134a, side inlet

5.4.2 Model for the end inlet conditions

In Figures 5.15 and 5.16, for the vapor phase, it was shown that the branch tube inlet vapor mass flux is almost constant at a region above a certain manifold vapor mass flux, and at a region below a certain manifold vapor mass flux. In addition, in between the two regions, the branch tube inlet vapor mass flux is proportional to the manifold vapor mass flux at the inlet of T-junctions. In order to design such a behavior, in the same way as the side inlet case, the measured branch tube inlet vapor quality versus the normalized manifold vapor mass flux at the inlet of T-junctions in the manifold is plotted for the R-410A and R-134a, respectively, in Figures 5.25 and 5.26. As shown in the Figures, there exist constant inlet vapor quality regions above 0.7, and below 0.2 of the normalized manifold vapor mass flux. After considering these observations, simple correlations are proposed in a modified form of Watanabe model for the end inlet in Equation 5.11 as follows;

$$\begin{aligned}
 G_{dm,vap}(i) / G_{dm,In,vap} \leq 0.2 & \quad x_{bt,In}(i) = 0.123 \\
 0.2 < G_{dm,vap}(i) / G_{dm,In,vap} < 0.7 & \\
 \text{For } R-410A & \quad x_{bt,In}(i) = 1.674 \times G_{dm,vap}(i) / G_{dm,In,vap} - 0.212 \\
 \text{For } R-134a & \quad x_{bt,In}(i) = 1.902 \times G_{dm,vap}(i) / G_{dm,In,vap} - 0.297 \\
 0.7 \leq G_{dm,vap}(i) / G_{dm,In,vap} & \quad x_{bt,In}(i) = 0.96
 \end{aligned} \tag{5.11}$$

As shown in Equation 5.11, the normalized manifold vapor mass flux is used instead of manifold vapor mass flux because the vapor phase distribution is affected by the manifold inlet vapor mass flux as well as the local vapor mass flux at the inlet of T-

junction in the manifold. In addition, for comparison, the predicted branch tube inlet vapor quality is shown in Figures 5.25 and 5.26. For R-410A, 87% of the measured branch tube inlet vapor quality data are within the predicted branch tube inlet vapor quality ± 0.1 . For R-134a, 92% of the measured branch tube inlet vapor quality data are within the predicted branch tube inlet vapor quality ± 0.1 .

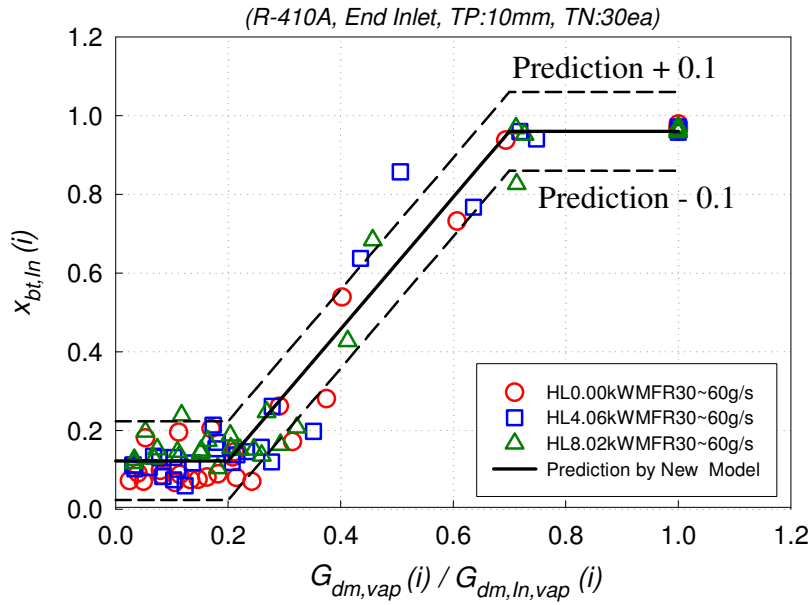


Figure 5.25 Measured branch tube inlet vapor quality ($x_{bt,ln}(i)$) vs. the normalized vapor mass flux ($G_{dm,vap}(i)/G_{dm,ln,vap}(i)$) for R-410A, end inlet

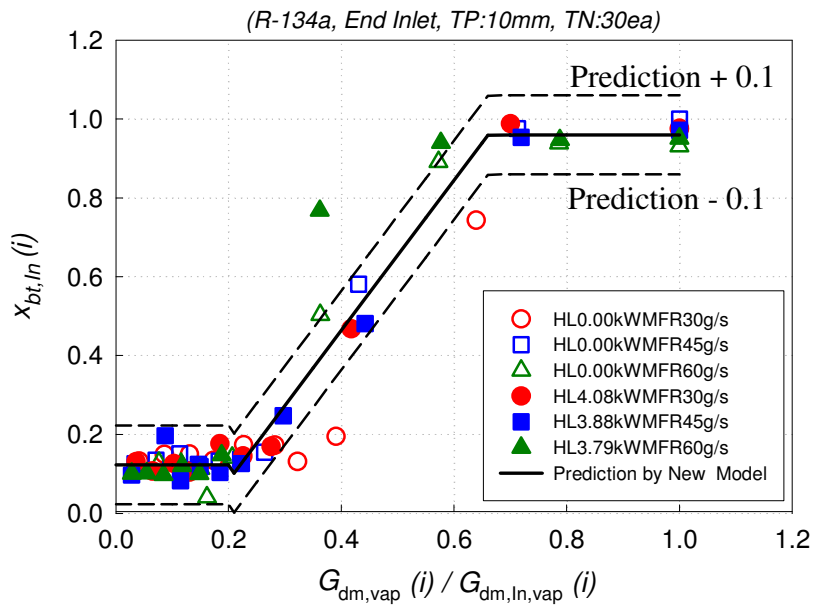


Figure 5.26 Measured branch tube inlet vapor quality ($x_{bt,ln}(i)$) vs. the normalized vapor mass flux ($G_{dm,vap}(i)/G_{dm,ln,vap}(i)$) for R-134a, end inlet

For the liquid fraction taken off, in the same way used for the side inlet case, the liquid fraction taken off versus the normalized vapor Reynolds number at the inlet of T-junctions in the manifold is plotted for the R-410A and R-134a, respectively, in Figures 5.27 and 5.28. The Figures show the clear relationship between the liquid fraction taken off and the normalized vapor Reynolds number, that is, at a region below a certain normalized vapor Reynolds number, the liquid fraction taken off equals unity, and at a region above the normalized vapor Reynolds number, the liquid fraction taken off decreases as the normalized vapor Reynolds number increases. Based on this relationship, simple equations for the liquid fraction taken off are proposed for R-410A and R-134a in Equation 5.12.

$$\begin{aligned}
 &x \leq 0.18; \quad y = 1 \\
 &x > 0.18; \quad y = \left(a + \frac{b}{x^{1.5}} \right) \\
 &\quad \text{For R-410A; } a = -0.063, \quad b = 0.080 \\
 &\quad \text{For R-134a; } a = -0.075, \quad b = 0.081 \\
 &\text{where } y = \dot{m}_{bt,ln,liq}(i) / \dot{m}_{dm,liq}(i), \quad x = \sqrt{\text{Re}_{dm,vap}(i)} / \sqrt{\text{Re}_{dm,ln,vap}}
 \end{aligned} \tag{5-12}$$

As shown in Equation 5.12, the normalized vapor Reynolds number at the inlet of T-junctions in the manifold is used for considering the effect of both the manifold inlet vapor Reynolds number and the local vapor Reynolds number at the inlet of T-junctions. In addition, for comparison, the predicted fraction of liquid taken off is shown in Figures 5.27 and 5.28. For the R-410A test with the end inlet, as can be seen in Figure 5.27, 75% of the measured fraction of liquid taken off data are within the predicted fraction of liquid

taken off ± 0.05 , and 90% of the measured fraction of liquid taken off data are within the predicted fraction of liquid taken off ± 0.1 . For the R-134a test with the end inlet, as can be seen in Figure 5.28, 85% of the measured fraction of liquid taken off data are within the predicted fraction of liquid taken off ± 0.05 , and 95% of the measured fraction of liquid taken off data are within the predicted fraction of liquid taken off ± 0.1 .

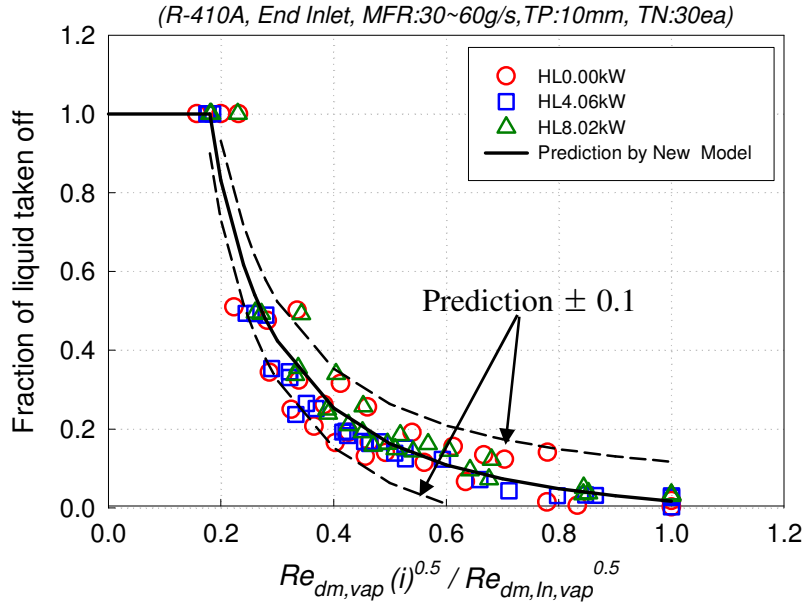


Figure 5.27 Branch tube liquid fraction taken off ($\dot{m}_{bt,ln,liq}(i) / \dot{m}_{dm,liq}(i)$) vs. the normalized Reynolds number ($\sqrt{Re_{dm,vap}(i)} / \sqrt{Re_{dm,ln,vap}}$) for R-410A, end inlet

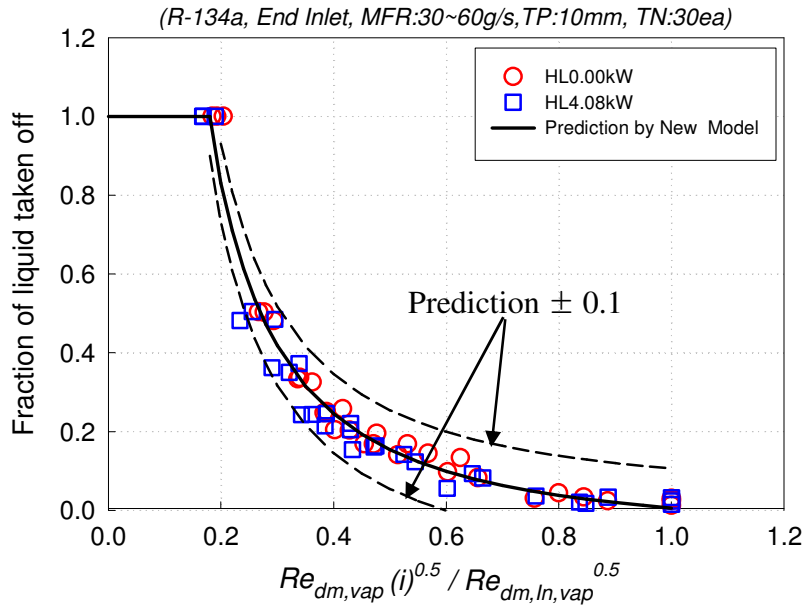


Figure 5.28 Branch tube liquid fraction taken off ($\dot{m}_{bt,ln,liq}(i) / \dot{m}_{dm,liq}(i)$) vs. the normalized Reynolds number ($\sqrt{Re_{dm,vap}(i)} / \sqrt{Re_{dm,ln,vap}}$) for R-134a, end inlet

5.4.3 Effect of inlet location (or inlet geometry)

To investigate the effect of inlet location (or inlet geometry), for R-410A, test results for the manifold inlet mass flow rate 30 g/s with the end inlet are compared with test results for the manifold inlet mass flow rate 60 g/s with the side inlet. For the side inlet, the refrigerant flows into the dividing manifold from the middle located at the rear side. The incoming refrigerant impinges on the inner wall of the manifold, and is divided symmetrically near the inlet. Therefore, for 60 g/s with the side inlet, the test results for half of the manifold are compared with the test results of the entire manifold for 30 g/s with the end inlet. For the two inlet locations, the inlet vapor and liquid mass flux are almost same because the test results for half of the manifold for the side inlet are considered. To investigate the effect of inlet location, first, correlations of the vapor phase for the two inlet locations were developed. To develop the correlations of the vapor phase for both inlet locations, the measured branch tube inlet vapor quality is plotted for 30 g/s with the end inlet and for 60 g/s with the side inlet, respectively, in Figures 5.29 and 5.30 as a function of the normalized manifold vapor mass flux at the inlet of T-junctions in the manifold. As shown in Figures 5.29 and 5.30, there exists a constant inlet vapor quality region below 0.4 of the normalized manifold vapor mass flux. In addition, for a region above 0.4, the measured branch tube inlet vapor quality increases as the normalized manifold vapor mass flux increases. After considering these observations, simple correlations are proposed in a modified form of Watanabe model for 30 g/s with the end inlet and for 60 g/s with the side inlet in Equation 5.13 as follows;

For R – 410A, $\dot{m}_{dm,In} = 30$ g/s , end inlet;

$$\begin{aligned} G_{dm,vap}(i) / G_{dm,In,vap} &\leq 0.4 & x_{bt,In}(i) &= 0.174 \\ 0.4 < G_{dm,vap}(i) / G_{dm,In,vap} & & & \\ x_{bt,In}(i) &= 1.321 \times G_{dm,vap}(i) / G_{dm,In,vap} - 0.35 \end{aligned} \quad (5.13)$$

For R – 410A, $\dot{m}_{dm,In} = 60$ g/s , side inle

$$\begin{aligned} G_{dm,vap}(i) / G_{dm, half-In,vap} &\leq 0.4 & x_{bt,In}(i) &= 0.188 \\ 0.4 < G_{dm,vap}(i) / G_{dm, half-In,vap} & & & \\ x_{bt,In}(i) &= 0.653 \times G_{dm,vap}(i) / G_{dm, half-In,vap} - 0.073 \end{aligned}$$

In addition, for comparison, the predicted branch tube inlet vapor quality is shown in Figures 5.29 and 5.30. For the manifold inlet mass flow rate 30 g/s with the end inlet, as can be seen in Figures 5.29, 87% of the measured branch tube inlet vapor quality data are within the predicted branch tube inlet vapor quality ± 0.1 . For the manifold inlet mass flow rate 60 g/s with the side inlet, as can be seen in Figures 5.30, 93% of the measured branch tube inlet vapor quality data are within the predicted branch tube inlet vapor quality ± 0.1 . In Figures 5.29 and 5.30, unity of the normalized manifold vapor mass flux represents the manifold inlet region and 0 of the normalized manifold vapor mass flux represents a region close to the end of the manifold. As seen in Figures 5.29 and 5.30, at a region below 0.4 of the normalized manifold vapor mass flux, the developed correlations show that the branch inlet vapor quality is almost constant for both inlet locations. However, at a region above 0.4 of the normalized manifold vapor mass flux, the developed correlations show different trends for both inlet locations. At the inlet of the manifold, the branch tube inlet vapor quality for the end inlet is almost 100%, but the branch tube inlet vapor quality for the side inlet is almost 60%. As shown in Figures 5.29 and 5.30, at a region above 0.4 of the normalized manifold vapor mass flux, the branch

tube inlet vapor quality for the end inlet is more drastically varied along the manifold. Based on that, it can be said that the vapor phase distribution is strongly affected by the inlet location (or inlet geometry), especially at a region near the inlet. For developing correlations of the liquid fraction taken off, the liquid fraction taken off is plotted for the manifold inlet mass flow rate 30 g/s with the end inlet and for the manifold inlet mass flow rate 60 g/s with the side inlet, respectively, in Figures 5.31 and 5.32 as a function of the normalized vapor Reynolds number at the inlet of T-junctions in the manifold. Figures 5.31 and 5.32 show that at a region below a certain normalized vapor Reynolds number, the liquid fraction taken off equals unity, and at a region above the normalized vapor Reynolds number, the liquid fraction taken off decreases with increasing normalized vapor Reynolds number. Based on the relationship, simple equations for the liquid fraction taken off are proposed for 30 g/s with the end inlet and for 60 g/s with the side inlet in Equation 5.14. In addition, for comparison, the predicted fraction of liquid taken off is shown in Figures 5.31 and 5.32. For the manifold inlet mass flow rate 30 g/s with the end inlet, as can be seen in Figure 5.31, 90% of the measured fraction of liquid taken off data are within the predicted fraction of liquid taken off ± 0.10 . For the manifold inlet mass flow rate 60 g/s with the side inlet, as can be seen in Figure 5.32, 93% of the measured fraction of liquid taken off data are within the predicted fraction of liquid taken off ± 0.1 .

For R – 410A, $\dot{m}_{dm,In} = 30$ g/s , end inlet;

$$x \leq 0.20; y = 1$$

$$x > 0.20; y = \left(a + \frac{b}{x^{1.5}} \right)$$

$$a = -0.073, b = 0.098$$

where $y = \dot{m}_{bt,In,liq}(i) / \dot{m}_{dm,liq}(i)$, $x = \sqrt{\text{Re}_{dm,vap}(i)} / \sqrt{\text{Re}_{dm,In,vap}}$

For R – 410A, $\dot{m}_{dm,In} = 60$ g/s , side inlet; (5.14)

$$x \leq 0.32; y = 1$$

$$x > 0.32; y = \left(a + \frac{b}{x^{1.5}} \right)$$

$$a = -0.061, b = 0.189$$

where $y = \dot{m}_{bt,In,liq}(i) / \dot{m}_{dm,liq}(i)$, $x = \sqrt{\text{Re}_{dm,vap}(i)} / \sqrt{\text{Re}_{dm,half-In,vap}}$

As seen in Figures 5.31 and 5.32, unity of the normalized vapor Reynolds number represents the manifold inlet region and 0 of the normalized vapor Reynolds number represents a region close to the end of the manifold. Figures 5.31 and 5.32 show that at a region below 0.2 of the normalized vapor Reynolds number at the inlet of T-junctions, the fraction of liquid taken off for both inlet locations is unity. In Figures 5.31 and 5.32, in overall, it is shown that at a region above 0.2 of the normalized vapor Reynolds number at the inlet of T-junctions, the fraction of liquid taken off for the end inlet case is lower than that for the side inlet case.

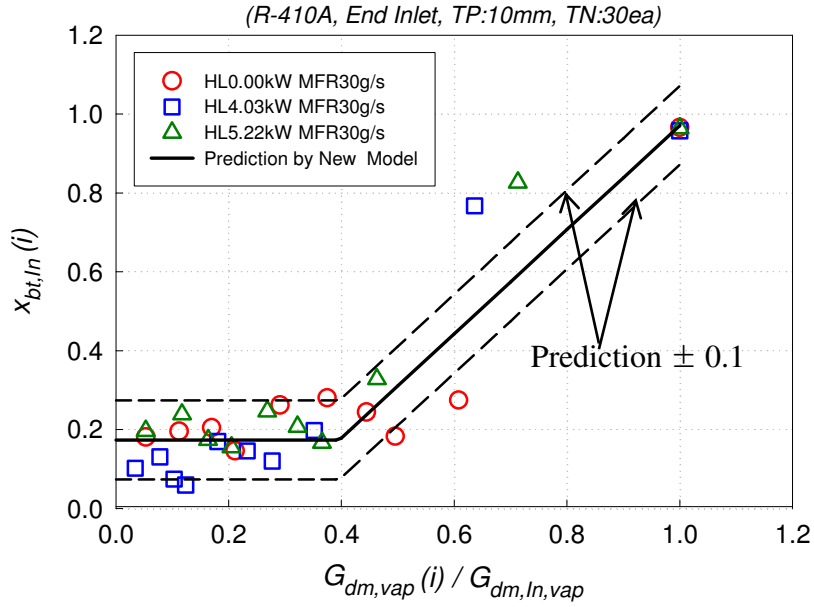


Figure 5.29 Measured branch tube inlet vapor quality ($x_{bt,ln}(i)$) vs. the normalized vapor mass flux ($G_{dm,vap}(i) / G_{dm,ln,vap}$) for R-410A and $\dot{m}_{dm,ln} = 30$ g/s , end inlet

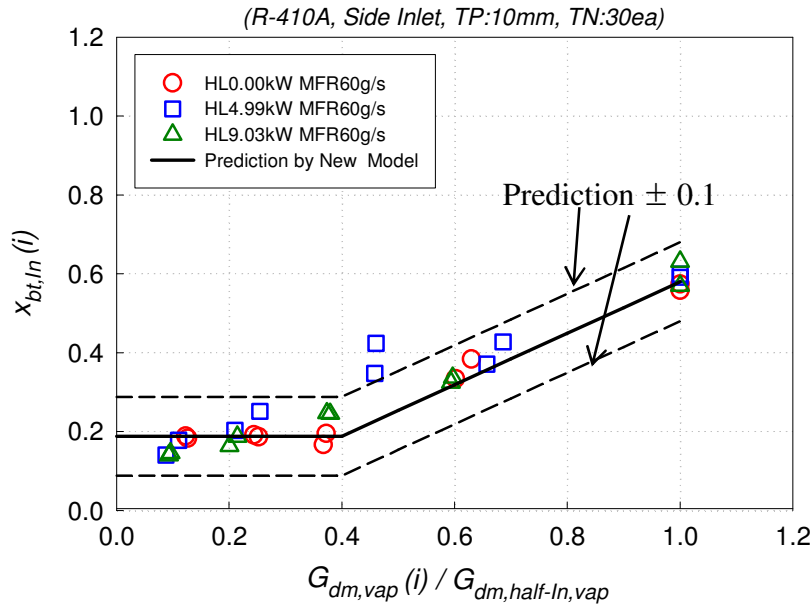


Figure 5.30 Measured branch tube inlet vapor quality ($x_{bt,ln}(i)$) vs. the normalized vapor mass flux ($G_{dm,vap}(i) / G_{dm,half-ln,vap}$) for R-410A and $\dot{m}_{dm,ln} = 60$ g/s , side inlet

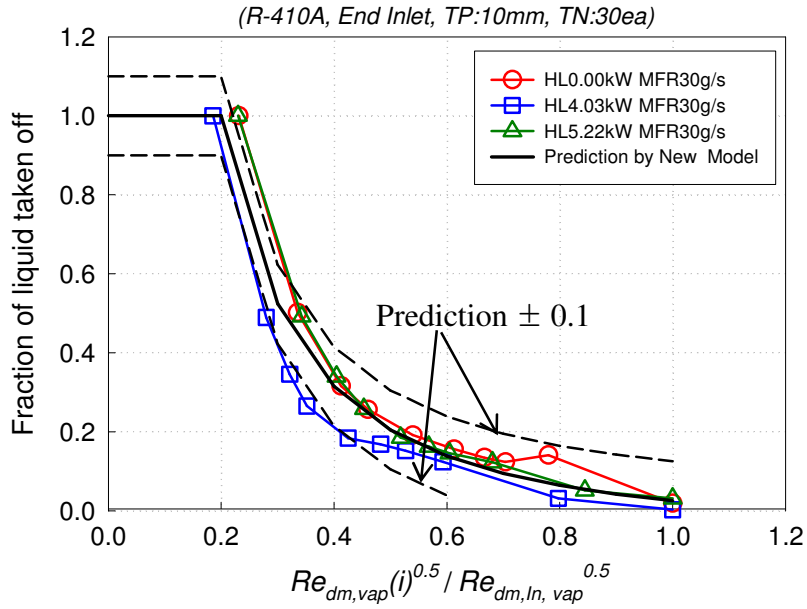


Figure 5.31 Branch tube liquid fraction taken off ($\dot{m}_{bt,ln,liq}(i) / \dot{m}_{dm,liq}(i)$) vs. the normalized Reynolds number ($\sqrt{Re_{dm,vap}(i)} / \sqrt{Re_{dm,ln,vap}}$) for R-410A and $\dot{m}_{dm,ln} = 30$ g/s , end inlet

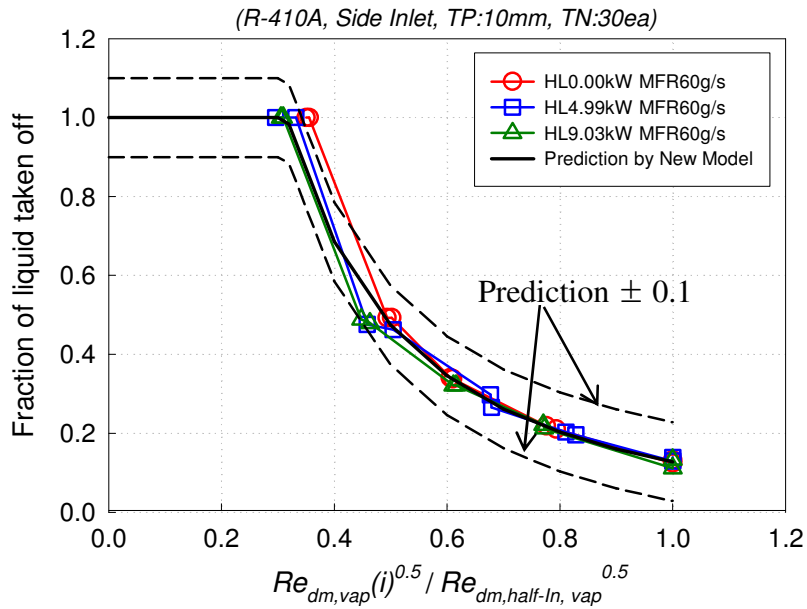


Figure 5.32 Branch tube liquid fraction taken off ($\dot{m}_{bt,ln,liq}(i) / \dot{m}_{dm,liq}(i)$) vs. the normalized Reynolds number ($\sqrt{Re_{dm,vap}(i)} / \sqrt{Re_{dm, half-ln, vap}}$) for R-410A and $\dot{m}_{dm,ln} = 60$ g/s , side inlet

5.5 Parameters Affecting Refrigerant Flow Distribution

Based on the test results and the analysis of the refrigerant distribution in the manifold using a T-junction method, the effects of parameters on the flow distribution were evaluated. Three major parameters affecting refrigerant flow distribution are summarized as follows;

5.5.1 Manifold mass flux

As shown in section 5.4, for the end inlet, the branch tube inlet vapor quality is almost constant at high vapor mass flux and at low vapor mass flux. In between the two vapor mass fluxes, the branch tube inlet vapor quality is proportional to the manifold vapor mass flux in the inlet of T-junction in the manifold. For the side inlet, there is no such high vapor mass flux region where the branch tube inlet vapor quality is almost constant, which is close to 100% because of the reduced manifold vapor mass flux due to the inlet location and/or inlet geometry. At the same range of the normalized manifold vapor mass flux, the branch inlet vapor quality distribution shows different behaviors depending on the inlet location and/or inlet geometry. The branch tube inlet vapor quality for the end inlet case is more sensitive to the normalized manifold vapor mass flux than for the side inlet case. Therefore, it can be said that the vapor phase distribution is affected by the manifold vapor mass flux in the inlet of the T-junction in the manifold as well as inlet flow conditions including inlet geometry.

5.5.2 Momentum flux ratio between vapor and liquid

Due to the difference in the momentum flux for the vapor and the liquid, the liquid is traveling farther towards the end of manifold than the vapor. Therefore, the vapor phase is flowing through the first branch tubes near the inlet, while the liquid phase is flowing through the last branch tubes of the manifold. Through the flow visualization, it was seen that the liquid level increased along the dividing manifold.

5.5.3 Inlet location and/or inlet geometry

For the end inlet, the refrigerant is coming from the left to the manifold inlet. At the near inlet, the liquid is flowing at the lower part of the dividing manifold, and the vapor is flowing at the upper part of the manifold due to the gravitational effect. Therefore, it is shown that the branch tube inlet quality for the first tubes near the inlet is close to 100% even though the number of tube groups having 100% vapor quality is depending upon the manifold inlet mass flux. In addition, it is shown that the liquid level increases along the dividing manifold up to a certain length of it because the liquid is traveling farther than the vapor due to inertia difference, and at the far right end, the liquid level is kept almost constant. For the side inlet, it was shown that the incoming refrigerant impinges on the inner side wall of the manifold, and is divided symmetrically near the inlet. The interface between the vapor and the liquid has a V-shaped form near the inlet. Due to the difference in the inlet geometry, the different flow distribution from that for the end inlet is shown even though the manifold inlet flow conditions are the same.

6 HEAT EXCHANGER SIMULATIONS

In order to investigate the effect of refrigerant maldistribution on the performance of the tested heat exchanger, heat exchanger simulations were conducted. Based on the developed refrigerant correlations, a heat exchanger simulation program (CEEE, 2006) was used for the heat exchanger simulations. In order to consider realistic operating conditions for the low manifold inlet mass flow rates, it was needed to reduce either the heat exchanger length or frontal air velocity for the fixed of degree of superheating at the outlet of heat exchanger. In the current study, for the low manifold inlet mass flow rates, the heat exchanger simulations were performed by reducing frontal air velocity with the fixed heat exchanger geometry (which is tested heat exchanger). Table 6.1 shows the heat exchanger geometry and operating conditions for the heat exchanger simulations.

Table 6.1 Heat exchanger geometry and operating conditions for heat exchanger simulations

No	Refrigerant	TP (mm)	TN	$x_{dm,In}$	HEX Length (m)	Inlet	MFR (g/s)
1	R-410A	10	30	0.3	1	End	30, 45, 60
2						Side	30, 45, 60

To calculate the air-side heat transfer coefficient and pressure drop, Chang-Wang louver fin correlation was used. The dimension of the louver fin chosen for calculation is as follows: 1) louver angle: 30° 2) fin thickness: 0.1mm 3) Number of fins per inch: 18 fpi 4) Fin height: 7.2 mm 5) louver depth: 1 mm. For calculating refrigerant side heat transfer coefficient, Gnielinski correlation and Kandlikar correlation were chosen for single phase and two-phase, respectively. For the calculation of the refrigerant pressure

drop, Blasius correlation and Friedel correlation were used for single phase and two-phase, respectively.

Table 6.2 Heat exchanger simulations results

$\dot{m}_{dm,in}$ (g/s)	30		
Air Velocity (m/s)	0.5		
Inlet Temperature (°C)	7.2		
Air-Side HTC (W/m ² K)	71.9		
Refrigerant Distribution	Uniform distribution	Maldistribution - End inlet	Maldistribution - Side inlet
Capacity (W)	4,708 (100%)	4,520 (96%)	4,449 (94.5%)

$\dot{m}_{dm,in}$ (g/s)	45		
Air Velocity (m/s)	1.0		
Inlet Temperature (°C)	7.2		
Air-Side HTC (W/m ² K)	102.4		
Refrigerant Distribution	Uniform distribution	Maldistribution - End inlet	Maldistribution - Side inlet
Capacity (W)	7,203 (100%)	6,800 (94.4%)	6,654 (92.4%)

$\dot{m}_{dm,in}$ (g/s)	60		
Air Velocity (m/s)	1.2		
Inlet Temperature (°C)	7.2		
Air-Side HTC (W/m ² K)	112.4		
Refrigerant Distribution	Uniform distribution	Maldistribution - End inlet	Maldistribution - Side inlet
Capacity (W)	9,257 (100%)	7,836 (84.6%)	8,721 (94.2%)

Table 6.2 shows some heat exchanger simulations results. As shown in Table 6.2, for the end inlet case, as the manifold inlet mass flow rate increases, the performance degradation increases. For $\dot{m}_{dm,In} = 30$ g/s and 45 g/s, the capacity degradation for both inlet locations is almost similar compared to the uniform refrigerant distribution. However, for the end inlet case with $\dot{m}_{dm,In} = 60$ g/s, the capacity degradation is about 15%. Therefore, for $\dot{m}_{dm,In} = 60$ g/s, the side inlet design is preferred. Figures 6.1, 6.2, and 6.3 show the simulated cooling capacity as a function of branch tube group for $\dot{m}_{dm,In} = 30$ g/s, 45 g/s, and 60 g/s, respectively. For both inlets, the cooling capacity for the tube groups near the inlet is smaller than that for other tube groups because of higher inlet vapor quality.

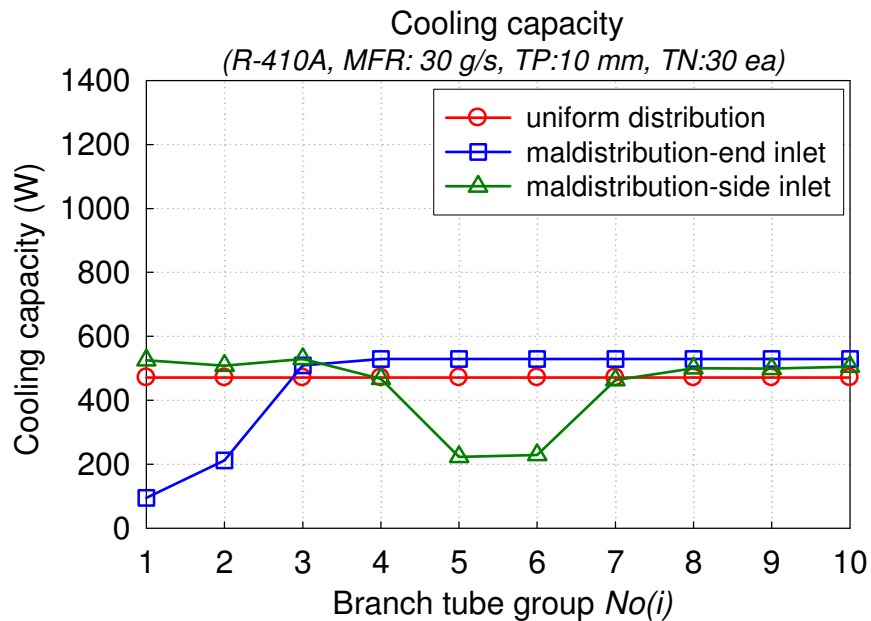


Figure 6.1 Simulated cooling capacity vs. branch tube group number for R-410A and $\dot{m}_{dm,In} = 30$ g/s

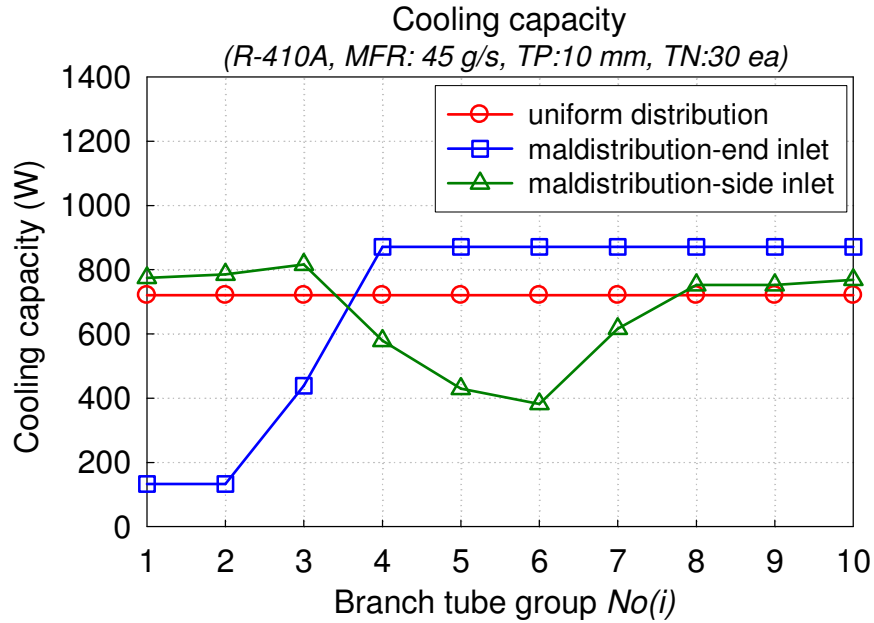


Figure 6.2 Simulated cooling capacity vs. branch tube group number for R-410A and $\dot{m}_{dm,In} = 45$ g/s

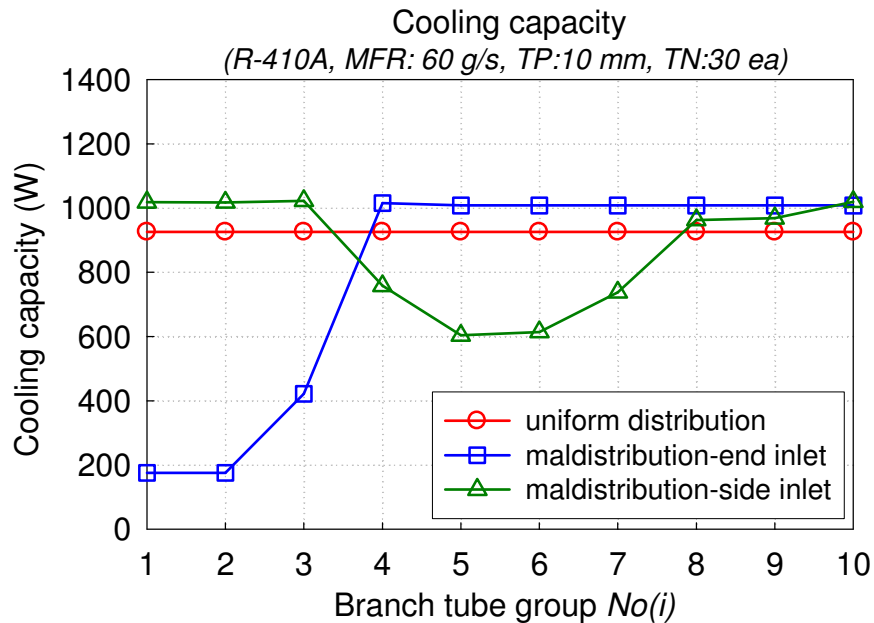


Figure 6.3 Simulated cooling capacity vs. branch tube group number for R-410A and $\dot{m}_{dm,In} = 60$ g/s

7 CONCLUSIONS

In order to provide essential design information of microchannel evaporators, an experimental study was conducted for the effects of geometry, operating conditions, and fluid properties on the distribution of refrigerant and pressure drops in the horizontal evaporator manifold. From the experimental data and simulation results, the following conclusions are deduced.

- An experimental facility with a visualization section for mimicking a real heat exchanger manifold geometry was developed. Measurements for refrigerant distribution were conducted under realistic operating conditions.
- Based on the observations on experimental data, the two-phase refrigerant was not uniformly distributed. For the entire test conditions, both non-uniform distribution of the mass flow rate and non-uniform distribution of the individual phases were found.
 - In the current study, the degree of non-uniform distribution of the vapor and liquid phase was more severe than that of the mass flow rate.
- Based on the heat exchanger simulation results using test results for the refrigerant distribution, for the side inlet case, the capacity degradation as compared to the uniform distribution at the tested inlet manifold mass flow rates (at 30, 45 and 60 g/s) is 5 ~ 8%. For the end inlet case, as the inlet manifold mass flow rate increases, the capacity degradation as compared to the uniform distribution is larger. The capacity degradation ranges from 4% to 15% as a function of the manifold inlet mass flow rate.

- Based on the observations of the effects of geometry, operating conditions and fluid properties on the flow distribution, the following characteristics were observed.
 - The differences between R-410A and R-134a were minor.
 - The refrigerant distribution is little affected by the variation of heat load, tube pitch, and tube group number.
 - The refrigerant distribution is strongly affected by the manifold inlet locations and/or inlet geometry and manifold inlet vapor mass flux. For the end inlet case, the profile of the branch tube inlet vapor quality is of a “stepwise” shape. There exist two almost constant value regions, one of about 100% vapor quality, one of about 20% vapor quality with a very short transition region. Near the inlet, the branch tube inlet vapor quality is almost 100%, and near the end of the manifold, the branch tube inlet vapor quality is about 12%. In between two regions, there is a short transition area. For the end inlet case, as the manifold inlet mass flow rate increases, the number of branch tube groups having almost 100% tube inlet vapor quality is increasing because the vapor-liquid interface is moving farther towards the end of the manifold due to the increased momentum. At the manifold inlet mass flow rate 30 g/s, 10% of the number of branch tubes has almost 100% tube inlet vapor quality. At 60 g/s, about 30% of the number of branch tubes has almost 100% tube inlet vapor quality. However, for the side inlet case, there is no such region having 100% branch tube inlet vapor quality. For the side inlet case, the profile of the branch tube inlet vapor quality is symmetric. Near the inlet, the branch tube inlet vapor quality is about 60 ~ 70%, and near the end of the manifold, the branch tube inlet vapor quality is about 20%. In between two

regions, the branch tube inlet vapor quality decreases monotonously along the manifold.

- In overall, based on the test results, the side inlet location is preferred for a wide range of mass flow rate compared to the end inlet location.

- Based on the flow visualization and test results, gravitational forces affect phase separation in the horizontal manifold. In addition, the momentum difference between vapor and liquid has effects on the refrigerant distribution, that is, low momentum vapor is easily taken off in the branch tubes near the inlet, while high momentum liquid is traveling farther towards the far end of the manifold.
- Based on the test results, a set of empirical correlations for the refrigerant distribution in the dividing manifold were developed using a T-junction concept in the modified forms of the Watanabe model.

8 FUTURE WORK

The current study has investigated two-phase refrigerant distribution in horizontal manifolds with vertically upward branch tubes for the representative geometrical and operational parameters. For better understanding of two-phase refrigerant distribution in manifolds with other geometrical and operational parameters, the recommended future research effort is:

(1) Number of refrigerant inlets

In the current study, one inlet was used for refrigerant flow distribution. For the end inlet case, it was shown that as the manifold inlet mass flow rate increased, the vapor-liquid interface for the transition region was traveling farther towards the end of the manifold. Therefore, the capacity degradation for the higher mass flow rate as compared to a uniform distribution was larger because of the increased number of tube groups having higher inlet vapor quality. For improving refrigerant flow maldistribution, it is of considerable interest to investigate refrigerant distribution in the manifolds with two or more inlets depending on the geometry and manifold length. Based on the measurements for the manifold inlet mass flow rate 60 g/s with the end inlet, about 30% of the branch tube groups near the inlet have almost 100% vapor quality. For instance, if two inlets are used in the manifolds instead of one inlet, it is expected that the degree of maldistribution is getting smaller due to the reduced manifold inlet mass flow rate.

(2) Location of the dividing manifold

In the current study, the dividing manifold was located at the bottom, while the collecting manifold was located at the top in the heat exchanger. Therefore, the refrigerant flow

direction in the branch tubes was vertically upward. Since the dividing manifold was located at the bottom, the liquid was flowing at the lower part of the manifold, while the vapor was flowing at the upper part of the manifold due to gravitational effect. Therefore, it was very difficult to distribute the liquid into the branch tubes near the inlet. However, if the dividing manifold is in the top of the heat exchanger, gravity will assist liquid distribution into the branch tubes near the inlet. Therefore, it is recommended to investigate two-phase refrigerant distribution in horizontal manifolds with vertically downward branch tubes for better understanding of flow distribution with the different location of the dividing manifold. In addition, in some evaporators for specific applications, there is more than one pass using baffles in the manifolds for better refrigerant distribution or reducing refrigerant pressure drop. In such evaporators, the refrigerant flow is reversing multiple times in the headers, which means the role of header is not fixed but alternatively changing as a dividing manifold and then collecting manifold. Therefore, for the complete analysis of refrigerant flow distribution in such evaporators, it is needed to investigate experimentally refrigerant distribution in the manifold with vertically downward branch tubes.

(3) Inclined heat exchanger

In the current study, the investigation of two-phase refrigerant distribution was conducted in horizontal manifolds with vertically upward branch tubes. In some application, the evaporators are inclined, which means the branch tubes have a slope. In such evaporators, the effect of gravity might be reduced, and the different pressure drop profile along the branch tubes may lead to different refrigerant distribution results. Therefore, it will be very interesting to investigate refrigerant distribution in the microchannel evaporators

with different slope. In addition, in the inclined heat exchanger, the air velocity distribution is not uniform either. This may lead to different refrigerant distribution results too.

(4) Fundamental modeling

In the current study, the new model for the refrigerant distribution in the manifolds with vertically upward branches was proposed based on the test results. Since large number of geometrical and operational parameters is involved, it is impractical to develop empirical models with general applicability. Therefore, many researchers have attempted to develop physically based mechanistic models with better prediction capability and wide range or validity and operating conditions. In such models, it is needed to identify involved governing mechanisms and to apply appropriate conservation laws and closure equations. It was reported that such models produced big deviations from test results in some cases, and brought stability and convergence problems in the solution procedure due to the large set of equations involved. However, such physically based mechanistic models provide very valuable insight of fundamental mechanism for the flow distribution. Therefore, for better understanding of refrigerant flow distribution in the manifold, it is recommended to perform fundamental modeling for the present and similar geometries.

9 REFERENCES

1. American Society of Heating, Refrigerating, and Air-Conditioning Engineers, Inc., 2001, Fundamentals, *ASHRAE Handbook*.
2. Anjun, J., Yanzhong, L., and Chunzheng, C., 2003, "Experimental Investigation on Fluid Flow Maldistribution in Plate-Fin Heat Exchangers," *Heat Transfer Engineering*, Vol. 24, No. 4, pp. 25-31.
3. Asoh, M., Hirao, Y., Watanabe, Y., and Fukano, T., 1991, "Phase separation of refrigerant two-phase mixture flowing downward into three thin branches from a horizontal manifold pipe," *ASME/JSME Thermal Engineering Proceedings*, Vol. 2, pp. 159–164.
4. Azzopardi, B. J., and Whalley, P. B., 1982, "The effect of flow pattern on two phase flow in a T junction," *International Journal of Multiphase Flow*, Vol. 8, pp. 481-507.
5. Azzopardi, B. J., and Smith, P. A., 1992, "Flow split at a T-junction: effect of branch tube orientation and downstream geometry," *International Journal of Multiphase Flow*, Vol. 18, pp. 861-875.
6. Azzopardi, B. J., 2000, "Phase separation at T-junctions," *Multiphase Science and Technology*, Vol. 11, pp. 223-329.

7. Bajura, R. A., 1971, "A model for flow distribution in manifolds," *Journal of Engineering for Power*, pp. 7–12.
8. Bajura, R. A., and Jones Jr, E. H., 1976, "Flow distribution manifolds," *Transactions of the ASME, Paper No. 76-FE-7 in Gas Turbine and Fluids Engineering Conference, New Orleans*, pp. 654-666.
9. Bassiouny, M. K., and Martin, H., 1984, "Flow Distribution and Pressure Drop in Plate Heat Exchangers – I. U-type Arrangement," *Chemical Engineering Science*, Vol. 39, pp. 693-700.
10. Beaver, A. C., Hrnjak, P. S., Yin, J. M., and Bullard, C. W., 2000, "Effects of distribution in headers of microchannel evaporators on transcritical CO₂ heat pump performance," *Proceedings of the ASME Advanced Energy Systems Division*, Vol. 40.
11. Carey, V. P., 1992, *Liquid-vapor phase change phenomena*, Taylor & Francis.
12. Castiglia, F., and Giardina, M., 2002a, "Mass discharge through branches in horizontal two-phase flow," 12th International Heat Transfer Conference, Grenoble, France, August 18-23.

13. Castiglia, F., and Giardina, M., 2002b, "Modelling two-phase flow discharge through lateral branches in large horizontal pipes with stratified flow," 8th International Conference of Multiphase flow in Industrial Plants, Alba, Italy, September 18-20.
14. Çengel, Y. A., and Boles, M. A., 2002, Thermodynamics, McGraw-Hill.
15. Center for Environmental Energy Engineering (CEEE), 2006, Coil-Designer: Heat exchanger simulation software.
16. Cho, H., and Cho., K., 2004, "Mass flow rate distribution and phase separation of R-22 in multi-microchannel tubes under adiabatic condition," Microscale Thermophysical Engineering, Vol. 8, pp. 129-139.
17. Cho, H., Cho, K., Youn, B., and Kim, Y. S., 2002, "Flow maldistribution in microchannel evaporator," Ninth International Refrigeration and Air Conditioning Conference, Purdue.
18. Coleman, J. W., and Garimella, S., 2000, "Visualization of Refrigerant Two-Phase Flow During Condensation," Proceedings of 34th National Heat Transfer Conference, Pittsburgh, PA.
19. Collier, J. G., and Thome, J. R., 1994, Convective Boiling and Condensation, 3rd ed., Oxford University Press, Oxford.

20. Datta, A. B., and Majumdar, A. K., 1983, "A calculation procedure for two phase flow distribution in manifolds with and without heat transfer," *International Journal of Heat and Mass Transfer*, Vol. 26, No. 9, pp. 1321-1328.
21. Fei, P., Chandrak, D., and Hrnjak, P., 2002, "Refrigerant distribution in the inlet header of plate evaporators," *SAE World Congress*, Paper 2002-01-0948.
22. Heggs, P. J., Ingham, D. B., and Sanderson, P. D., 1996, "Thermal Performance of Plate Heat Exchangers with Flow Maldistribution, Looped Configuration," 2nd European Thermal-Science and 14th UIT national Heat Transfer Conference, pp. 1279-1286.
23. Holman, J. P., 2001, *Experimental Methods for Engineers*, 7th Edition, Chapter 3, McGrawHill.
24. Hrnjak, P., 2004, "Flow Distribution Issues in Parallel Flow Heat Exchangers," *ASHRAE Transactions*, Vol. 110, No. 1.
25. Huang, X., and Van Sciver, S. W., 1995, "Pressure drop and void fraction of two-phase helium flowing in horizontal tubes, *Cryogenics*, Vol. 35, pp. 467-474.

26. Hwang, S. T., Soliman, H. M., Lahey Jr, R. T., 1988, "Phase Separation in Dividing Two-Phase Flows," *International Journal of Multiphase Flow*, Vol. 14, No. 4, pp. 439-458.
27. Kandlikar, S. G., 1990, "A General Correlation for Saturated Two-Phase Flow Boiling Heat Transfer Inside Horizontal and Vertical Tubes," *Journal of Heat Transfer*, Vol. 112, pp. 219-228.
28. Kandlikar, S. G., 2002, "Two-Phase Flow Patterns, Pressure Drop, and Heat Transfer during Boiling in Minichannel Flow Passages of Compact Evaporators," *Heat Transfer Engineering*, Vol 23, pp. 5-23.
29. Katsaounis, A., Papanikas, D. G., Fertis, D. K., and Margaris, D. P., 1997, "Dynamic T-Junction Separator for Multiphase Transport Pipelines," *Experimental Heat Transfer, Fluid Mechanics and Thermodynamics*, pp. 1045-1052.
30. Kattan, N., Thome, J. R., and Favrat, D., 1998, "Flow Boiling in Horizontal Tubes, Part 1: Development of a Diabatic Two-Phase Flow Pattern Map," *Journal of Heat Transfer*, Vol. 120, pp. 140-147.
31. Kattan, N., Thome, J. R., and Favrat, D., 1998, "Flow Boiling in Horizontal Tubes: Part 2-New Heat Transfer Data for Five Refrigerants," *International Journal of Heat Transfer*, Vol. 120, pp. 148-155.

32. Kim, Jong-Soo, Lee, Ki-Taek, Kim, Jae-Hong, Ha, Soo-Jung, and Im, Yong-Bin, 2004, "A relation between two-phase pressure drop and flow distribution in a compact heat exchanger header," Second International Conference on Microchannels and Minichannels, Rochester, NY, Paper Number ICMM2004-2363, pp. 413-420.
33. Kim, S., Choi, E., and Cho, Y. I., 1995, "The effect of header shapes on the flow distribution in a manifold for electronic packaging applications," International Communications in Heat and Mass Transfer, Vol. 22, No. 3, pp. 329-341.
34. Kitto Jr, J. B., and Robertson, J. M., 1989, "Effects of Maldistribution of Flow on Heat Transfer Equipment Performance," Heat Transfer Engineering, Vol. 10, No. 1, pp. 18-25.
35. Kubo, T., and Ueda, T., 1969, "On the Characteristics of Divided Flow and Confluent Flow in Headers," Bulletin of the JSME, Vol. 12, No. 52, pp. 802-807.
36. Kubo, T., and Ueda, T., 1973, "On the Characteristics of Confluent Flow of Gas-Liquid Mixtures in Headers," Bulletin of the JSME, Vol. 16, No. 99, pp. 1376-1384.
37. Kulkarni, T., Bullard, C., and Cho, K., 2004, "Header design tradeoffs in microchannel evaporators," Applied Thermal Engineering, Vol. 24, pp. 759-776.

38. Lahey, R. T., 1986, "Current understanding of phase separation mechanisms in branching conduits," Nuclear Engineering and Design, Vol. 95, pp. 145-161.
39. Liaw, J. S., Wang, C. C., Liao, C. C., and Fang, L. J., 1997, "Flow Distribution in Dividing manifolds at Low Reynolds Number," Experimental Heat Transfer, Fluid Mechanics and Thermodynamics, pp. 1649-1653.
40. Maciaszek, T., and Micaelli, J. C., 1990, "CATHARE phase separation modeling for small breaks in horizontal pipes with stratified flow," Nuclear Engineering and Design, Vol. 124, pp. 247-256.
41. Mcquillan, K. W., and Whalley, P. B., 1985, "Flow Patterns in Vertical Two-Phase Flow," International Journal of Multiphase Flow, Vol. 11, No. 2, pp. 161-175.
42. Moon, Y. M., and No, H. C., 2003, "Off-take and Slug Transition at T-junction of Vertical-up Branch in the Horizontal Pipe," Journal of Nuclear Science and Technology, Vol. 40, No. 5, pp. 317-324.
43. Moran, M. J., and Shapiro, H. N., 1993, Fundamentals of Engineering Thermodynamics,
John Wiley & Sons, Inc.

44. Mueller, A.C., and Chiou, J.P., 1988, "Review of Various Types of Flow Maldistribution in Heat Exchangers," *Heat Transfer Engineering*, Vol. 9, pp. 36-50.
45. Munson, B. R., Young, D. F., and Okiishi, T. H., 2002, *Fundamentals of fluid mechanics*, 4th Edition, John Wiley & Sons, Inc.
46. Oh, S. J., and Lee, K. S., 2001, "Optimal Shape of Header Part in a Parallel-Flow Heat Exchanger," *Korean Journal of Air-Conditioning and Refrigeration Engineering*, Vol. 13, No. 10, pp. 1017–1024.
47. Osakabe, M., Hamada, T., and Horiki, S., 1999, "Water flow distribution in horizontal header contaminated with bubbles," *International Journal of Multiphase Flow*, Vol. 25, pp. 827-840.
48. Peng, F., and Shoukri, M., 1997, "Modelling of Phase Redistribution of Horizontal Annular Flow Divided in T-junctions," *The Canadian Journal of Chemical Engineering*, Vol. 75, pp. 264-271.
49. Penmatcha, V. R., Ashton, P. J., and Shoham, O., 1996, "Two-phase stratified flow splitting at a T-junction with an inclined branch arm," *International Journal of Multiphase Flow*, Vol. 22, No. 6, pp. 1105-1122.

50. Reimann, J., Seeger, W., 1986, "Two-Phase Flow in a T-junction with a Horizontal Inlet - Part ii: pressure differences," *International Journal of Multiphase Flow*, Vol. 12, pp. 587-608.
51. Rong, X., Kawaji, M., and Burgers, J. G., 1995, "Two-Phase Flow Distribution in a Stacked Plate Heat Exchanger," *ASME/JSME Fluid Engineering and Laser Anemometry Conference and Exhibition*.
52. Rouhani, Z., and Axelsson, E., 1970, "Calculation of void volume fraction in the subcooled and quality boiling regions," *International Journal of Heat and Mass Transfer*, Vol. 13, pp. 383-393.
53. Sa, Y. C., Jang, D. Y., Ko, Oh, S.K., Oh, S.Y., and Chung, B.Y., 2003, "Flow maldistribution of flat tube evaporator," *The 4th international Symposium on HVAC*, Beijing, China.
54. Saba, N., Lahey, R.T., 1984, "The analysis of phase separation phenomena in branching conduits," *International Journal of Multiphase Flow*, Vol. 10, pp. 1-20.
55. Seeger, W., Reimann, J., Muller, U., 1986, "Two-phase flow in a T-junction with a horizontal inlet - Part i: phase separation," *International Journal of Multiphase Flow*, Vol. 12, pp. 575-585.

56. Smoglie, C., Reimann, J., Muller, U., 1987, "Two-phase flow through small breaks in a horizontal pipe with stratified flow," *Nuclear Engineering and Design*, Vol. 99, pp. 117-130.
57. Stacey, T., Azzopardi, B. J., and Conte, G., 2000, "The split of annular two-phase flow at a small diameter T-junction," *International Journal of Multiphase Flow*, Vol. 26, pp. 845-856.
58. Tae, S. J., and Cho, K., 2003, "Effect of geometric and dynamic parameters on the two-phase flow distribution of R-22 in branch tubes," *International Congress of Refrigeration*, Washington, D.C.
59. Taitel, Y., and Dukler, A. E., 1976, "A model for predicting flow regime transitions in horizontal and near-horizontal gas-liquid flow," *AIChE Journal*, Vol. 22, pp. 47-55.
60. Thome, J. R., El Hajal, J., 2002, "Two-phase flow pattern map for evaporation in horizontal tubes: Latest version," *Heat Transfer Engineering*, Vol. 24, pp. 3-10.
61. Thome, J. R., 2005, "Condensation in Plain Horizontal Tubes: Recent Advances in Modelling of Heat Transfer to Pure Fluids and Mixtures," *Journal of the Braz. Soc. of Mech. Sci. & Eng.*, Vol. 27, pp. 23-30.

62. Tompkins, D.M., Yoo, T., Hrnjak, P., Newell, T., and Cho, K., 2002, "Flow Distribution and Pressure Drop in Microchannel Manifolds," Proceedings of 7th International Refrigeration and Air Conditioning Conference, West Lafayette, IN.
63. Vist, S., and Pettersen, J., 2002, "Two-phase flow distribution in compact heat exchanger manifolds," Compact Heat Exchanger Symposium, A Festschrift on the 60th Birthday of R.K. Shah, August 24, Grenoble, France.
64. Vist, S., 2003, "Two-phase flow distribution in heat exchanger manifolds," Ph.D Thesis, Norwegian University of Science and Technology, Norway.
65. Vist, S., and Pettersen, J., 2004, "Two-phase flow distribution in compact heat exchanger manifolds," Experimental Thermal and Fluid Science, Vol. 28, pp. 209-215.
66. Vist, S., 2004, "Two-phase Refrigerant Distribution in Round Tube Manifolds," ASHRAE Winter Meeting, Paper Number AN-04-1-3.
67. Wallis, G. B., 1969, One-dimensional two-phase flow, McGraw-Hill, New York.
68. Walters, L. C., Soliman, H. M., and Sims, G. E., 1998, "Two-phase pressure drop and phase distribution at reduced tee junctions," International Journal of Multiphase Flow, Vol. 24, pp. 775-792.

69. Wang, L., and Sunden, B., 2001, "Design Methodology for Multistream Plate-Fin Heat Exchangers in Heat Exchanger Networks," *Heat Transfer Engineering*, Vol. 22, pp. 3-11.
70. Wang, X. A., and Yu, P., 1989, "Isothermal Flow Distribution in Header Systems," *International Journal of Solar Energy*, Vol. 7, pp. 159-169.
71. Watanabe, M., Katsuta, M., and Nagata, K., 1995, "Two-phase flow distribution in multi-pass tube modeling serpentine type evaporator," *Proceedings of the ASME/JSME Thermal Engineering Conference*, Vol. 2, pp. 35-42.
72. Watanabe, M., Katsuta, M., and Nagata, K., 1995, "General Characteristics of Two-phase Flow Distribution in a Multipass Tube," *Heat Transfer, Japanese Research*, Vol. 24, pp. 32-44.
73. Wen, J., and Li, Y., 2004, "Study of Flow Distribution and its Improvement on the Header of Plate-Fin Heat Exchanger," *Cryogenics*, Vol. 44, No. 11, pp. 823-831.
74. Whalley, P. B., 1987, *Boiling, condensation and gas-liquid flow*, Clarendon Press, Oxford.

75. Winkler, C. M., and Peters, J.E., 2002, "Refrigerant Droplet Size Measurements in Conjunction with a Novel Method for Improving Flow Distribution in Evaporators," *Aerosol Science and Technology*, Vol. 36, pp. 734-741.
76. Wojtan, L., Ursenbacher, T., and Thome, J. R., 2004, "Interfacial measurements in stratified types of flow, Part II: Measurements for R-22 and R-410A," *International Journal of Multiphase Flow*, Vol. 30, pp. 125-137.
77. Yang, C., and Webb, R. L., 1996, "Friction pressure drop of R-12 in small hydraulic diameter extruded aluminum tubes with and without micro fins," *International Journal of Heat and Mass Transfer*, Vol. 39, No. 4, pp. 801-809.
78. Yang, C., and Shieh, C., 2001, "Flow pattern of air-water and two-phase R-134a in small circular tubes," *International Journal of Multiphase Flow*, Vol. 27, pp. 1163-1177.
79. Yin, J. M., Bullard, C. W., and Hrnjak, P. S., 2002, "Single-Phase Pressure Drop Measurements in a Microchannel Heat Exchanger," *Heat Transfer Engineering*, Vol. 23, pp. 3-12.
80. Zietlow, D. C., Campagna, M., and Dias, J. F., 2002, "Innovative experimental apparatus to measure liquid flow distribution in two-phase flow occurring in the manifolds of compact heat exchangers," *ASHRAE Transactions*, Vol. 108, No. 2.

81. Zivi, S. M., 1964, "Estimation of steady-state steam void fraction by means of the principle of minimum entropy production," ASME, Vol. 86, pp. 247-252.

82. Zürcher, O., Favrat, D., Thome, J. R., 1999, "Evaporation of ammonia in a smooth horizontal tube: heat transfer measurements and predictions," Journal of Heat Transfer, Vol. 121, pp. 89-101.